UNIVERSITY COLLEGE LONDON

PhD Thesis

Confinement Effects on Non-Reactive and Reactive Transport Processes: Insights from Molecular Dynamics Simulations

Author:

Tran Thi Bao Le

Supervisor:

Prof. Alberto Striolo

A dissertation submitted in fulfilment of the degree

of Doctor of Philosophy

in the

Department of Chemical Engineering

June 2020

Declaration of Authorship

I, Tran Thi Bao Le, declare that this thesis titled, “Confinement Effects on Non-reactive and Reactive Transport Processes: Insights from Molecular Dynamics Simulations” and the works presented in it are my own. Where information has been derived from other sources, I confirm that they have been properly indicated in the thesis.

Signed: _____

Date: _____

Abstract

Exploring the thermodynamic, structural and transport properties, coupled with the reactivity of complex geo-fluids in porous systems is vital in geochemistry, and it also has repercussions in a variety of fields, most importantly the manufacturing of chemicals in the industry. Experimental and computational studies can shed light on the behaviour of fluids in confinement, thereby providing insights for industrial applications in various areas such as catalysis, gas recovery, separations, and adsorption. This thesis seeks to obtain some fundamental understanding of the behaviour of fluids confined in narrow pores as well as the role of pores in reactive-transport processes by implementing the atomistic molecular dynamics (MD) simulation techniques. In collaboration with experimentalists, validation has been achieved for selected systems. The systems were simulated as confined within a realistic cylindrical pore of diameter ~16 Å carved out of amorphous silica. A series of MD simulations implementing classical force fields were conducted to examine the effect of bulk pressure and water loading on the mobility of propane confined within cylindrical silica pores. The transport properties of propane were found to depend on pressure, as well as on the amount of water present. At high H_2O loading, propane transport is hindered by "molecular bridges" formed by water molecules. The results are in quantitative agreement with neutron scattering data conducted for propane-water systems confined in MCM-41–type materials. To investigate the effect of narrow pores on the possible abiotic synthesis of methane in sub-surface conditions, MD simulations implementing the reactive force field (ReaxFF) formalism were performed. Although the ReaxFF force fields were successfully parameterized to describe dynamics of complex reactive chemical systems, the simulation results reveal that they can also be able to reliably predict bulk properties of nonreactive pure fluids (CH_4, CO_2, H_2O, and H_2). However, the agreement with both simulations implementing classical force fields and experiments depends strongly on fluids and thermodynamics conditions considered. When ReaxFF molecular dynamics simulations were conducted for CO_2 in the presence of excess H_2 within the amorphous silica nanopores, no CH_4 was obtained at the conditions considered; however, CO was found to be a stable product, suggesting that the silica pore surface facilitates the partial reduction of CO_2 to CO. Because the results could be important for CCUS applications, we investigated the wetting properties of calcite in the presence of water and CO_2, at various pressures and salt content.

Comparison with experiments suggests that much fundamental research is still needed to design safe and reliable geological storage repositories.

Impact Statement

Due to the depletion of conventional hydrocarbon sources and the rise in global energy consumption, unconventional oil and gas reservoirs (e.g., shale oil, shale gas, tight oil, and gas hydrates) have received considerable attention in recent years. Shale gas and oil, the most commercialized resources, are produced directly from shale rocks, which have poor permeability and low porosity. Hydrocarbons exist in shale rocks as free, dissolved or adsorbed fluids that retain or accumulate within the reservoirs without migrating. In order to optimize the production of shale oil from these low permeability reservoirs, innovative techniques including horizontal drilling and hydraulic fracturing are required. The main drawbacks of hydraulic fracturing technique are the large amount of water used, and the composition of the 'flowback' water, which can contain large amounts of salts and sometimes naturally occurring radioactive material (NORM), depending on the geological formation. Because the interactions between hydrocarbons and water trapped within nanopores and microfactures are responsible for determining well productivity, this thesis focuses on detailed molecular-level observations for the behaviour of fluids confined within narrow porous matrices such as those found in shale formations. The results provide useful insights into the impact of water on gas storage and transport in shale systems, thereby helping reduce the environmental impact connected with the energy sector. Furthermore, analysis of confined fluid behaviours (e.g., structure, dynamics and reactivity) could help interpret and/or predict complex geochemical phenomena occurring at subsurface environments, including shedding light on possible abiotic mechanisms responsible for the generation of hydrocarbons. The results could also help design innovative strategies for carbon capture, utilization and storage (CCUS) applications.

Atmospheric concentrations of carbon dioxide, a potent greenhouse gas that drives climate change, have significantly increased since the start of the industrial revolution. Among other technologies, the thermochemical CO_2 splitting approach has a great potential for the chemical utilization of CO_2. Our fundamental insights into CO_2 reduction within silica nanopores could help in the design of catalysts which promotes CO_2 adsorption and activation. To store CO_2 in geological formations, it is imperative to quantify the wetting properties of the rocks as a function of CO_2 pressure: our results provide the foundation for extensive future studies in this field as well.

Acknowledgements

Frist of all, I would like to express my deep and sincere gratitude towards my supervisor Professor Alberto Striolo, for his constant support, guidance and inspiration throughout my PhD study. There would never be any way for me to complete my study without his valuable expertise, creative thoughts and insightful suggestions. I am truly grateful for all the learning opportunities he has offered to build me up to a self-sufficient and confident learner. Thank you very much!

I would like to extend my sincere gratitude to our collaborator, Professor David R. Cole from the Ohio State University, USA, for his constructive comments and invaluable suggestions throughout my research.

I would like to give immense appreciation to Dr. Cuong Luu for supporting and encouraging me through the ups and downs in the years. I would also like to give thanks to Dr. Thu Le for helping me to understand molecular dynamics simulation when I started my research.

Furthermore, special thanks to my dear friends, Dr. Sada Namsami, Dr. Benjamin Tam and Mr Kai Bin Yu for their personal friendships that have helped me through all those tough times in research and life.

This thesis is especially dedicated to my parents and my brother, who are always the unique motivation for me to overcome all difficulties. Thank you for always believing in me and loving me unconditionally.

Last of all, my sincere thanks to everyone in Professor Striolo's group, especially Dr. Sakiru Badmos and Ms Abeer Khedr for their support and advices in my personal life.

Publications

The work presented in this thesis has been published in the following articles.

1. **Tran Thi Bao Le**, Alberto Striolo, and David R. Cole. Propane–water mixtures confined within cylindrical silica nanopores: Structural and dynamical properties probed by molecular dynamics. *Langmuir*, 33(42):11310–11320, 2017.

2. **Tran Thi Bao Le**, Alberto Striolo, and David R. Cole. Structural and dynamical properties predicted by reactive force fields simulations for four common pure fluids at liquid and gaseous non-reactive conditions. *Molecular Simulation*, 44(10):826–839, 2018.

3. **Tran Thi Bao Le**, Alberto Striolo, and David R. Cole. Partial CO_2 reduction in amorphous cylindrical silica nanopores studied with reactive molecular dynamics simulations. *Journal of Physical Chemistry C*, 123(43):26358–26369, 2019.

4. Siddharth Gautam, **Tran Thi Bao Le**, Gernot Rother, Niina Jalarvo, Tingting Liu, Eugene Mamontov, Sheng Dai, Zhen-An Qiao, Alberto Striolo, and David Cole. Effects of water on the stochastic motions of propane confined in MCM-41-S pores. *Physical Chemistry Chemical Physics*, 21(45):25035–25046, 2019.

5. **Tran Thi Bao Le**, Alberto Striolo, and David R. Cole. Supercritical CO_2 effects on calcite wettability: A molecular perspective. *Journal of Physical Chemistry C*, 124(34):18532–18543, 2020.

Contents

List of Figures

List of Tables

Chapter 1. Introduction

This thesis focuses on attempting to better understand various molecular phenomena occurring in narrow pores at subsurface environments by implementing molecular dynamics (MD) simulations. This simulation technique is widely applied and especially popular in the investigation of dynamic properties and processes at the atomic level in the fields of chemical physics, materials science, and biophysics. Using MD simulations, one is able to study phenomena that are difficult or impossible to capture experimentally under any circumstances.

When fluids are entrapped or confined in nano-channel or nanopores, the geometric constraints are imposed on fluid molecules as well as interactions between fluids molecules and channels or pore walls, thereby affecting the free thermal motion of these molecules. This would result in significant changes in physical and chemical properties of confined fluids as compared to those of bulk fluids. The physical properties of fluids confined in various environments are of considerable interest, given that they could provide information on glass transition [1, 2], migration [3, 4] and adsorption [5-7], phenomena that are relevant to geology, biology, and engineering. Keith Gubbins and his group pioneered the use of molecular simulations for better understanding the behavior of confined fluids [8]. He addressed many important topics, such as phase separations in confinement [9], freezing and melting in confinement [10], and also the development of realistic models for the porous adsorbents [11].

Nanoporous materials have attracted great interest due to their unique properties, such as a high specific surface area, large specific pore volume, uniform pore size, and rich surface chemistry. Nanoporous materials are classified on the basis of pore sizes [12] into micropore (< 2 nm), mesopore (2 – 50 nm), and macropore (> 50 nm). Apart from dimension-based classification, nanoporous materials can be divided into two broad categories, based on their origin: natural nanomaterials, and synthetic (engineered) nanomaterials [13]. The behaviour of confined fluids has been studied using these nanoporous materials as substrates. Silica was chosen as one of the main solid substrates for simulations presented in this thesis. Several authors have studied structure and dynamics of fluids confined in nanoporous silica materials with different geometries (slit pores [14-19] or cylindrical pores [20-24]). For example,

Gautam et al. [19] reported a direct comparison of MD simulations of propane in 20 nm slit pore of silica against quasielastic neutron scattering (QENS) experiments on propane in mesoporous silica aerogel of pore size 15–20 nm. The time scales of the decay of the intermediate scattering functions calculated from the simulation data agree well with those obtained from the QENS experiment, thereby confirming the anomalous pressure dependence of the diffusion coefficient. The simulation results suggest that the rotational motion of propane molecules is isotropic throughout the silica pore; however, it is too fast to be captured by the QENS instrument used in the experiment. Milischuk et al. [23] used MD simulations to study water in approximately cylindrical silica nanopores of varying diameters at full hydration and room temperature. They found that water molecules form two distinct molecular layers at the interface and the water density becomes uniform further into the centre of the pore. Both water translational and rotational motions are strongly dependent on the proximity to the interface. The studies on structure and dynamics of confined fluids provide insights for applications ranging from nanofiltration [25], separation [26], and catalysis [27], among others. Our contribution attempts to understand the migration of fluids through narrow porous media in the sub-surface where the presence of water might affect the adsorption and diffusion of confined fluids. In **Chapter 3**, equilibrium MD simulations were conducted to study the fluid systems composed of propane and water confined within a cylindrical pore of diameter ∼16 Å carved out of amorphous silica. The main goal of this chapter is to elucidate not only structure and dynamics of confined fluids but also the effect of water on the transportation of propane. The simulation results were qualitatively compared to experimental quasielastic neutron scattering data.

The discovery of biological communities unexpectedly thriving around submarine hydrothermal vents in the late 1970s has prompted intensive studies on the possibility of abiotic synthesis of organic compounds in these environments. This exciting research field arises, in part, from the high concentrations of methane and other organic compounds found in hydrothermal fluids, suggesting that the abiotic synthesis may have provided essential ingredients from which life emerged on the Earth [28, 29]. The abiotic synthesis of organic compounds involves the reduction of inorganic carbon sources such as CO_2 and CO by H_2. High hydrogen concentrations could derive from either the oxidation of ferrous iron in basalt or the serpentinization of ultramafic minerals (for example, olivine and pyroxene) [30, 31]. As an example of a recent contribution to this discussion, Ménez et al. [32] reported evidence for the occurrence of aromatic amino acids formed abiotically at depth in oceanic crust.

These authors suggest that the amino acid formation could have been catalyzed by an iron-rich saponite clay. It appears that iron catalysts play an important role. In fact, Muchowska et al. [33] recently showed that ferrous iron promotes a purely chemical reaction network by which CO_2 reduction yields many intermediates of the biological Krebs cycle.

To address the question concerning the potential of abiotic synthesis as well as the role of pores and micro-fractures in the reactive-transport processes, one would need to directly analyse the system compositions in the pores, which is not experimentally achievable. Le et al. [34] recently implemented the reaction ensemble Monte Carlo (RxMC) approach [35, 36] to quantify the potential effect of confinement on the equilibrium composition for the CO_2 methanation reaction (Reaction 1.1).

$$CO_2 + 4H_2 \leftrightarrow CH_4 + 2H_2O \tag{1.1}$$

From a purely thermodynamic point of view, the authors compared the equilibrium composition of a reactive system composed of CO_2 and H_2 in confinement vs. that in the bulk phase at similar thermodynamics conditions. The results emphasize the possible existence of pathways for the abiotic organic synthesis within hydrothermal vent systems and indicate the preferential shift of equilibrium composition towards methane formation at moderate temperature and low pressure. The RxMC approach is an advanced technique for studying the equilibrium behaviour of chemically reactive systems. However, the approach does not assess the mechanism of reaction. Compared to the RxMC approach, reactive molecular dynamics simulations allow researchers to monitor the kinetics of a chemical reaction and to identify the role of various catalysts. For example, reactive MD simulations conducted within the ReaxFF formalism were successfully employed to describe complex reactive chemical systems [37, 38]. In the ReaxFF parameterization, the bond order concept is implemented to determine interatomic interactions between all atoms within a chemical system. Therefore, when appropriately parameterized, ReaxFF provides an accurate description of the formation and dissociation of covalent bonds during dynamic simulations. ReaxFF captures short-lived molecular fragments and intermediates, which may not be considered in the RxMC approach, and could be difficult to detect, even experimentally. ReaxFF parameters are obtained by fitting against training datasets containing quantum mechanical simulation results and experimental data. Accurate ReaxFF parameterizations have been applied to a wide range of reactive systems, including combustion processes [39-42], the shock-induced chemistry of high-energy materials [43-45], nanomaterials [46-50], catalysts [51-54], and also

electrochemical phenomena [55-57]. These studies address the ability of the reactive force fields to provide important insights into systems that undergo chemical reactions, which is the primary reason these force fields were developed. However, they do not help to understand the limits of reactive force fields with respect to structural and transport properties of molecular systems. To test this, in **Chapter 4**, we attempted to replicate the bulk properties of the common pure fluids by implementing ReaxFF parameters. The chosen compounds are involved in Reaction 1.1, including CO_2, H_2, CH_4, and H_2O. The pure fluids are not expected to undergo chemical reactions at the conditions chosen for these simulations. The ReaxFF parameters were taken from the 'combustion' ReaxFF [39] developed to study hydrocarbon combustion and from the 'aqueous' ReaxFF [58] developed to study aqueous systems. Radial distribution functions, self-diffusion coefficients, and second virial coefficients are chosen as yardsticks to assess the reliability of reactive force fields in estimating the bulk properties of selected molecular systems. The results were then compared to data obtained implementing usually reliable classical force fields, including those from the transferable potentials for phase equilibria (TraPPE), the optimized potentials for liquid simulations (OPLS), and the simple point charge (SPC) families.

Another question that needs to be addressed is whether the CO_2 methanation reaction (Reaction 1.1) could occur within silica nanopores when the ReaxFF MD simulation approach is implemented. In **Chapter 5**, the ReaxFF potential developed for the Si/C/H/O system [59] was employed to simulate CO_2 reduction in either the bulk phase or for fluid systems confined in cylindrical silica pores. The reliability of reactive force field in describing CO_2 reduction and the effects on the reaction were then reported.

An extended work was presented in the **Chapter 6** where MD simulations were conducted to study the wettability behaviour of reservoir rocks (e.g. calcite) which plays a vital role in determining CO_2 storage capacity and containment security. Several experimental studies characterized the wettability of CO_2/brine/rock systems for a wide range of realistic conditions. To develop a fundamental understanding of the molecular mechanisms responsible for such observations, the results of molecular dynamics simulations, conducted at atomistic resolution, are reported in **Chapter 6** for representative systems in a wide range of pressure and temperature conditions. The results presented could be relevant for predicting the longevity of CO_2 sequestration in geological repositories. Note that this is the first work in the new project of reservoir wettability.

Chapter 2. Simulation Methodology

2.1. Introduction

Molecular dynamics, first developed by Alder and Wainwright in the late 1950s and later Rahman in the early 1960s [60], is a computer simulation technique for studying many-body systems modelled at atomic level. The time evolution of a set of *N* interacting particles is determined by numerically solving the Newton's equations of motion.

$$\mathbf{F}_i = m_i \frac{d^2\mathbf{r}_i}{dt^2} \tag{2.1}$$

Where $\boldsymbol{r}_i(t)=(x_i(t), y_i(t), z_i(t))$ is the position vector of *i*th particle and $\boldsymbol{F}_i$ is the force acting upon the *i*th particle at time *t* due to the interactions with the other particles and m_i is the mass of particle. The force acting on *i*th particle is determined by the gradient of the potential energy *U* with respect to the particle positions:

$$\mathbf{F}_i(\mathbf{r}_1, \dots, \mathbf{r}_N) = -\nabla_i U(\mathbf{r}_1, \dots, \mathbf{r}_N) = -\left(\frac{\partial U}{\partial x_i}, \frac{\partial U}{\partial y_i}, \frac{\partial U}{\partial z_i}\right) \tag{2.2}$$

Once the potential energy is calculated, the equation of motion is used to update the position and velocity of each particle. The trajectories describing the time evolution of the system in phase space are defined by both position and velocity vectors. Various macroscopic properties are obtained from the trajectory.

MD simulation can be used to solve the dynamic evolution of the system in a given equilibrium and non-equilibrium state. Equilibrium molecular dynamics (EMD) simulations have been successfully applied to predict the thermodynamic, transport, and structural properties from equilibrium trajectories. At equilibrium, the system may still undergo fluctuations with time, but important properties should no longer change systematically with simulation time. In non-equilibrium molecular dynamics (NEMD) simulations, the system is driven away from thermodynamic equilibrium state, e.g. by imposing a steady heat flux that generates a fixed temperature gradient. NEMD has become popular for its effectiveness in computing the thermal conductivity and shear viscosity of fluids when steady state is reached. Like an equilibrium system, in the steady state the system does not display net macroscopic

change over time. Unlike an equilibrium system, a constant input of energy is required to maintain the system in its steady state.

2.2. Hamiltonian mechanics

The Hamiltonian, H, for a system of *N* interacting particles is determined by Equation 2.3:

$$\mathrm{H}(\mathbf{p},\mathbf{r}) \equiv \mathrm{H}(\mathbf{p}_1,\ldots,\mathbf{p}_\mathrm{N},\mathbf{r}_1,\ldots,\mathbf{r}_\mathrm{N}) = \sum_{\mathrm{i}=1}^{\mathrm{N}} \frac{\mathbf{p}_\mathrm{i}^2}{2\mathrm{m}_\mathrm{i}} + \mathrm{U}(\mathbf{r}_1,\ldots,\mathbf{r}_\mathrm{N}) \tag{2.3}$$

The equations of motion can be derived from Equation 2.3 according to Hamilton's equations,

$$\dot{\mathbf{r}}_\mathrm{i} = \frac{\partial \mathrm{H}}{\partial \mathbf{p}_\mathrm{i}} = \frac{\mathbf{p}_\mathrm{i}}{\mathrm{m}_\mathrm{i}} \tag{2.4}$$

$$\dot{\mathbf{p}}_\mathrm{i} = -\frac{\partial \mathrm{H}}{\partial \mathbf{r}_\mathrm{i}} = -\frac{\partial \mathrm{U}}{\partial \mathbf{r}_\mathrm{i}} = \mathbf{F}_\mathrm{i}(\mathbf{r}_1,\ldots\mathbf{r}_\mathrm{N}) \tag{2.5}$$

Where $\boldsymbol{p}_1$, ..., $\boldsymbol{p}_\mathrm{N}$ are the momenta vector of the particles. The Newton's equations of motion (Equation 2.1) are yielded by taking the time derivative of both sides of the first of Hamilton's equations and substituting into the second.

The full set of positions and momenta collected into a single vector $\mathbf{X} = (\mathbf{p}_1,\ldots, \mathbf{p}_\mathrm{N}, \mathbf{r}_1,\ldots, \mathbf{r}_\mathrm{N})$ is called the phase space vector. A single point in the phase space specifies a mechanical state at a given time, and corresponds to a microstate of the system. The phase space is the union of all possible microstates of a system. A macrostate is specified by a few thermodynamic variables (e.g., temperature, pressure, volume). Many different microstates correspond to one single macrostate.

One of the important properties of the equations of motion is that they are time reversible, i.e., they take the same form when the transformation $\mathrm{t} \rightarrow -\mathrm{t}$ is made. In consequence of time-reversal symmetry, the microscopic physics is independent of the direction of time. Another important property of the equations of motion is that they conserve the Hamiltonian which is given in Equation 2.3.

$$\frac{\mathrm{dH}}{\mathrm{dt}} = \sum_{\mathrm{i}=1}^{\mathrm{N}} \left[\frac{\partial \mathrm{H}}{\partial \mathbf{r}_\mathrm{i}}\dot{\mathbf{r}}_\mathrm{i} + \frac{\partial \mathrm{H}}{\partial \mathbf{p}_\mathrm{i}}\dot{\mathbf{p}}_\mathrm{i}\right] = \sum_{\mathrm{i}=1}^{\mathrm{N}} \left[\frac{\partial \mathrm{H}}{\partial \mathbf{r}_\mathrm{i}}\frac{\partial \mathrm{H}}{\partial \mathbf{p}_\mathrm{i}} - \frac{\partial \mathrm{H}}{\partial \mathbf{p}_\mathrm{i}}\frac{\partial \mathrm{H}}{\partial \mathbf{r}_\mathrm{i}}\right] = 0 \tag{2.6}$$

The conservation of the Hamiltonian is equal to the conservation of the total energy of the system.

2.3. Atomic force fields

The interatomic forces acting between the atoms and associated potential energies are described by atomic force fields. An atomic force field composes of the functional forms along with parameters which are derived from experiments and/or quantum mechanical calculations. The choice of appropriate force fields for representing the physics and chemistry phenomena of the system of interest determines the validity of simulations results.

2.3.1. Classical force field

A common expression for a classical force field employed in MD simulations can be given in the following form:

$$U(r_1, \dots, r_N) = \sum_{\text{bonds}} \frac{a_i}{2}(l_i - l_{i0})^2 + \sum_{\text{angles}} \frac{b_i}{2}(\theta_i - \theta_{i0})^2 + \sum_{\text{torsions}} \frac{c_i}{2}[1 + \cos(n\omega - \gamma_i)] + \sum_{\text{atom pairs}} 4\varepsilon_{ij}\left[\left(\frac{\sigma_{ij}}{r_{ij}}\right)^{12} - \left(\frac{\sigma_{ij}}{r_{ij}}\right)^{6}\right] + \sum_{\text{atom pairs}} \frac{q_i q_j}{4\pi\varepsilon_0\varepsilon_r r_{ij}} \quad (2.7)$$

The first three terms refer to the bonded interactions defined by the covalent structure of molecules in the system, and the last two terms describe the non-bonded interactions of all the pairs of atoms.

In details, the first two terms describe energies of deformation of the bond lengths l_i and bond angles θ_i from equilibrium values l_{i0} and θ_{i0}, respectively. The harmonic form of these terms (with respective force constant a_i and b_i) preserves the basic chemical structure of molecules, and does not describe bond breaking and forming in chemical processes.

For molecules with more than three atoms, the third term describes the energy of a torsional rotation around covalent bonds. The torsional potential is usually represented by a cosine function such as the one expressed in Equation 2.7, where force constants (c_i) determines the height of the potential barrier, multiplicity (n) refers to the number of potential energy minima over a period of 360° rotation, ω is the torsional angle, and the phase angle (γ_i) defines the position of the energy minima. The torsional potential is most commonly classified into proper dihedral angle potential and improper torsion. The proper dihedral angle potential depending on four atoms in three consecutive covalent bonds is mostly

applied to constrain the rotation around a bond. The improper torsion depending on three unconnected atoms bonded to a central atom is used to maintain the planarity in a molecular structure.

The fourth term represents the Van der Waals (VdW) repulsive and attractive interactions between neutral atoms *i* and *j* separated by a distances r_{ij} in the form of a 12-6 Lennard-Jones (LJ) potential, where σ is the distance at which the potential is zero and ε is the depth of the potential energy well.

The last term is the electrostatic interactions between two partial atomic charges q_i and q_j, which are described with the Coulomb potential, where ε_0 is the permittivity of free space and ε_r is the relative dielectric constant.

2.3.2. Reactive force field – ReaxFF

Unlike classical force fields having fixed bond topologies, ReaxFF is an empirical force field based on a chemical bond order/bond length relationship that allows bonds to dynamically dissociate and form. In the ReaxFF formalism [61], the instantaneous bond order, which is calculated and updated at every iteration from interatomic distances, is used to define all of the connectivity-dependent interactions (for example, valence and torsion angles). The bond orders depend on sigma, pi, and double-pi bonds. The energies and forces associated with all bonded interactions disappear once the bonds dissociate. The general expression for the energy of the system, E_{system}, is given by Equation 2.8 [61]:

$$E_{system} = E_{bond} + E_{val} + E_{tors} + E_{over} + E_{under} + E_{lp} + E_{vdwaals} + E_{coulomb} \quad (2.8)$$

The partial contributions to the total energy include bond energy (E_{bond}), valence angle energy (three-body) (E_{val}), torsion angle energy (four-body) (E_{tors}), overcoordination energy penalty (E_{over}), undercoordination stability (E_{under}), lone-pair energy (E_{lp}), nonbonded van der Waals ($E_{vdwaals}$), and Coulomb ($E_{coulomb}$) interactions.

The bond order BO'_{ij} which determines the number of atomic orbitals involved in the formation of a chemical bond between two atoms is calculated directly from the interatomic distances r_{ij} as given in Equation 2.9 and plotted in **Figure 2.1**.

$$BO'_{ij} = \exp\left[p_{bo1}.\left(\frac{r_{ij}}{r_0^{\sigma}}\right)^{p_{bo2}}\right] + \exp\left[p_{bo3}.\left(\frac{r_{ij}}{r_0^{\pi}}\right)^{p_{bo4}}\right] + \exp\left[p_{bo5}.\left(\frac{r_{ij}}{r_0^{\pi\pi}}\right)^{p_{bo6}}\right] \quad (2.9)$$

where r_0^{σ}, r_0^{π}, $r_0^{\pi\pi}$ are the covalent radius of sigma bond, pi bond and double pi bond, respectively. The bond parameters (p_{bo1} and p_{bo2}), (p_{bo3} and p_{bo4}) and (p_{bo5} and p_{bo6}) correspond to the sigma bond, pi bond and second double pi bond, respectively.

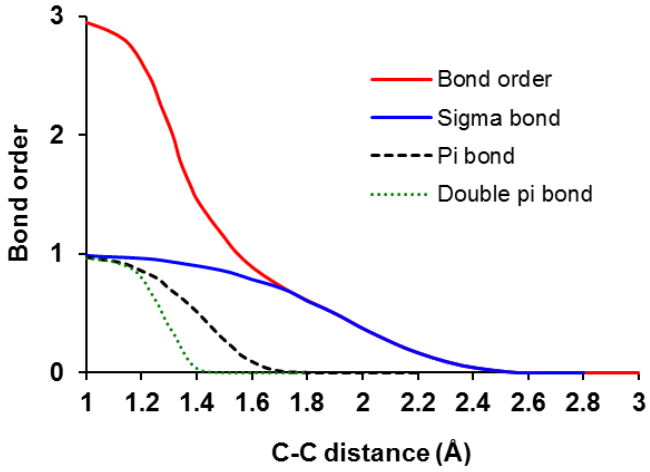

Figure 2.1. Interatomic distance dependency of the carbon-carbon bond order

The total bond order is divided into sigma-bonds, pi-bonds and double pi-bonds.

$$\mathrm{BO}'_{ij} = \mathrm{BO}^{\sigma}_{ij} + \mathrm{BO}^{\pi}_{ij} + \mathrm{BO}^{\pi\pi}_{ij} \tag{2.10}$$

The difference between the total bond orders around the atom and its valency Val_i is calculated by an uncorrected overcoordination Δ'_i as shown in Equation 2.11:

$$\Delta'_i = \sum_{j=1}^{\mathrm{neighbours(i)}} \mathrm{BO}'_{ij} - \mathrm{Val}_i \tag{2.11}$$

The bond order BO'_{ij} is then corrected using the uncorrected overcoordination as given in Equation 2.12:

$$\mathrm{BO}_{ij} = \mathrm{BO}'_{ij}.\mathrm{f}_1\left(\Delta'_i, \Delta'_j\right).\mathrm{f}_4\left(\Delta'_i, \mathrm{BO}'_{ij}\right).\mathrm{f}_5\left(\Delta'_j, \mathrm{BO}'_{ij}\right) \tag{2.12}$$

All connected interactions in ReaxFF are incorporated with the bond order. Equation 2.13 is used to determine the bond energies from the corrected bond order BO_{ij}.

$$\mathrm{E}_{\mathrm{bond}} = -\mathrm{D}^{\sigma}_{e}.\mathrm{BO}^{\sigma}_{ij}.\exp\left[\mathrm{p}_{\mathrm{be1}}\left(1-\left(\mathrm{BO}^{\sigma}_{ij}\right)^{\mathrm{p}_{\mathrm{be2}}}\right)\right] - \mathrm{D}^{\pi}_{e}.\mathrm{BO}^{\pi}_{ij} - \mathrm{D}^{\pi\pi}_{e}.\mathrm{BO}^{\pi\pi}_{ij} \tag{2.13}$$

where D_e^{σ}, D_e^{π}, and $D_e^{\pi\pi}$ are dissociation energy of the sigma bond, pi bond and double pi bond, respectively; p_{be1} and p_{be2} are bond energy parameters.

The valence angle energy contribution is expressed as Equation 2.14:

$$E_{val} = f_7(BO_{ij}).f_7(BO_{ik}).f_8(\Delta_j).\{p_{val1} - p_{val1}\exp[-p_{val2}(\Theta_0 - \Theta_{ijk})^2]\} \quad (2.14)$$

where ($\Theta_0 - \Theta_{ijk}$) term is the deviation of valence angle Θ_{ijk} from its equilibrium value Θ_0; p_{val1} and p_{val2} are valence angle parameters.

The energy of torsion angle ω_{ikjl} is determined by Equation 2.15:

$$\begin{aligned} E_{tors} = f_{10}(BO_{ij}, BO_{jk}, BO_{kl}).\sin\Theta_{ijk}.\sin\Theta_{jkl}.\Big[&\frac{1}{2}V_1.(1+\cos\omega_{ijkl}) \\ &+ \frac{1}{2}V_2.\exp\left\{p_{tor1}.\left(BO_{jk}^{\pi} - 1 + f_{11}(\Delta_j,\Delta_k)\right)^2\right\}.(1-\cos2\omega_{ijkl}) \\ &+ \frac{1}{2}V_3.(1+\cos3\omega_{ijkl})\Big] \end{aligned} \quad (2.15)$$

where p_{tor1} is the torsion angle parameter; V_1, V_2, and V_3 are the torsion barriers.

The lone pair energy is determined by Equation 2.16:

$$E_{lp} = \frac{p_{lp2}.(n_{lp,opt} - n_{lp,i})}{1 + \exp[-75.(n_{lp,opt} - n_{lp,i})]} \quad (2.16)$$

where $n_{lp,opt}$ and n_{lp} are the optimal number of lone pairs and the number of lone pairs around an atomic center, respectively. The number of lone pairs around an atom is determined by Equation 2.17:

$$\begin{aligned} n_{lp,i} = \operatorname{int}&\left(\frac{\sum_{j=1}^{neighboirs(i)} BO_{ij} - Val_i^e}{2}\right) \\ &+ \exp\left[-p_{lp1}.\left(2 + \left\{\sum_{j=1}^{neighboirs(i)} BO_{ij} - Val_i^e\right\}\right.\right. \\ &\left.\left. - 2.\operatorname{int}\left\{\frac{\sum_{j=1}^{neighboirs(i)} BO_{ij} - Val_i^e}{2}\right\}\right)^2\right] \end{aligned} \quad (2.17)$$

where Val_i^e is the total number of outer shell electrons around an atom; p_{lp1} the valency angle/lone pair parameter.

An energy penalty is applied on the system when the atom is overcoordinated ($\Delta_i > 0$) and it is expressed as Equation 2.18:

$$E_{over} = \frac{\sum_{j=1}^{nbond} p_{ovun1} \cdot D_e^{\sigma} \cdot BO_{ij}}{\Delta_i^{lpcorr} + Val_i} \cdot \Delta_i^{lpcorr} \cdot \left(\frac{1}{1 + \exp(p_{ovun2} \cdot \Delta_i^{lpcorr})} \right) \quad (2.18)$$

where p_{ovun1} is overcoordination penalties; p_{ovun2} is the valence angle parameter and Δ_i^{lpcorr} is an uncorrected overcoordination, as calculated in Equation 2.19:

$$\Delta_i^{lpcorr} = \Delta_i - \frac{\Delta_i^{lp}}{1 + p_{ovun3} \cdot \exp\left(p_{ovun4} \cdot \left\{\sum_{j=1}^{neighbours(i)} \left(\Delta_j - \Delta_j^{lp}\right) \cdot (BO_{ij}^{\pi} + BO_{ij}^{\pi\pi})\right\}\right)} \quad (2.19)$$

where p_{ovun3} and p_{ovun4} are overcoordination parameters.

For an under-coordinated atom ($\Delta_i < 0$), the energy contribution for the resonance of the π–electron between attached under-coordinated atomic centers is given by Equation 2.20:

$$E_{under} = -p_{ovun5} \cdot \frac{1 - \exp\left(p_{ovun6} \cdot \Delta_i^{lpcor}\right)}{1 + \exp(-p_{ovun2} \cdot \Delta_i^{lpcor})} \times \frac{1}{1 + p_{ovun7} \cdot \exp\left[p_{ovun8} \cdot \left\{\sum_{j=1}^{neighbour(i)} \left(\Delta_j - \Delta_j^{lp}\right) \cdot (BO_{ij}^{\pi} + BO_{ij}^{\pi\pi})\right\}\right]} \quad (2.20)$$

Where p_{ovun5} is the undercoordination energy; p_{ovun6}, p_{ovun7} and p_{ovun8} are the undercoordination parameters.

Because bonds are breaking and forming during dynamics, non-bonded interactions (van der Waals and Coulomb) must be included between all atom pairs, irrespective of the instantaneous connectivity. All excessive short-range non-bonded interactions are prevented by the introduction of shielding terms so that these interactions become constant as $r_{ij} \rightarrow 0$. A distance-corrected Morse-potential is employed to account for the van der Waals interactions, as given in Equation 2.21:

$$E_{vdWaals} = D_{ij} \cdot \left\{\exp\left[\alpha_{ij} \cdot \left(1 - \frac{f_{13}(r_{ij})}{r_{vdW}}\right)\right] - 2 \cdot \exp\left[\frac{1}{2}\alpha_{ij} \cdot \left(1 - \frac{f_{13}(r_{ij})}{r_{vdW}}\right)\right]\right\} \quad (2.21)$$

where D_{ij} is the van der Waals dissociation energy; r_{vdw} is the VdW radius and α_{ij} is the VdW parameter.

Meanwhile, the Electron Equilibration Method (EEM) approach [62] is implemented to describe electrostatic interactions expressed as Equation 2.22. This geometry-dependent charge calculation method enables ReaxFF to handle the polarization of a system.

$$E_{Coulomb} = C.\frac{q_i q_j}{\left[r_{ij}^3 + (1/\gamma_{ij})^3\right]^{1/3}} \tag{2.22}$$

where *C* is the dispersion parameter and γ_{ij} is the EEM shielding.

2.4. Statistical ensemble

A statistical ensemble is a virtual collection of all possible systems which have different microstates but belong to the same macrostate. An average over all possible microstates of a system is called an ensemble average. Statistical ensembles are usually characterized by fixed values of thermodynamic variables such as energy (*E*), temperature (*T*), pressure (*P*), volume (*V*), particle number (*N*) or chemical potential (μ). The fundamental ensemble is called the microcanonical ensemble which is characterized by constant particle number, constant volume, and constant total energy, and is denoted as the NVE ensemble. This corresponds to an isolated system since energy is conserved. Other examples include the canonical ensemble (NVT), the isothermal-isobaric ensemble (NPT), and the grand canonical ensemble (μVT).

The averaged quantity of a macroscopic system over a period of time is determined as a time average. When the system is ergodic, the ensemble average is equivalent to the time average. Ergodicity implies that the system will explore all possible microstates in the phase space when it is allowed to evolve for a long period of time.

2.5. Integration method

Due to a tremendous number of atoms in the system, the Newton's equations of motion (Equation 2.1) have to be solved numerically by using an appropriate integration algorithm. The basic criteria for a good integration algorithm for MD simulations are as follows:

(i) The algorithm should be accurate for large time steps.

(ii) It should reproduce properties of the classical equations of motion (i.e., time reversible).

(iii) It should conserve energy and the area/volume of the phase space (i.e., symplectic).

Several simple symplectic integrators [63] have been proposed for integrating the Newton's equations of motion (e.g., explicit Euler [63], Verlet [64], and Leap-frog [65] algorithms). Symplectic methods are constructed so that the linear symplectic structure of phase space is preserved. These algorithms offer distinct advantages such as long-term conservation of energy and good approximate conservation of integrals of motion.

2.5.1. Forward Euler algorithm

The forward Euler algorithm is the simplest numerical integrator, which is based on a truncated Taylor series expansion.

$$\vec{r}(t+\delta t) = \vec{r}(t) + \vec{v}(t)\delta t + \frac{1}{2}\frac{\vec{F}(t)}{m}\delta t^2 + o(\delta t^3) \tag{2.23}$$

$$\vec{v}(t+\delta t) = \vec{v}(t) + \frac{\vec{F}(t)}{m}\delta t + o(\delta t^2) \tag{2.24}$$

This is an explicit integration method, i.e., $\vec{r}(t+\delta t)$ is given explicitly in terms of known quantities such as $\vec{r}(t)$ and $\vec{v}(t)$. However, the forward Euler algorithm is neither time reversible nor symplectic. Moreover, it yields very large energy drift and hence rather unfavourable.

2.5.2. Verlet algorithm

In the studies implementing ReaxFF family, we applied the Verlet algorithm to solve Newton's equations of motion. This integration algorithm yields positions and dynamics properties (e.g., velocities and accelerations) at time *t* in the following forms:

$$\vec{r}(t+\delta t) = \vec{r}(t) + \vec{v}(t)\delta t + \frac{1}{2}\frac{\vec{F}(t)}{m}\delta t^2 \tag{2.25}$$

$$\vec{r}(t-\delta t) = \vec{r}(t) - \vec{v}(t)\delta t + \frac{1}{2}\frac{\vec{F}(t)}{m}\delta t^2 \tag{2.26}$$

Summing these two equations, one obtains:

$$\vec{r}(t+\delta t) = 2\vec{r}(t) - \vec{r}(t-\delta t) + \frac{\vec{F}(t)}{m}\delta t^2 \tag{2.27}$$

The velocities at time *t* can be approximated at the cost of accuracy by Equation 2.28:

$$\vec{v}(t) = \frac{\vec{r}(t+\delta t) - \vec{r}(t-\delta t)}{2\delta t} + o(\delta t^2) \tag{2.28}$$

The Verlet algorithm uses position and acceleration at time *t* and the position from time $t - \delta t$ to calculate new positions at time $t + \delta t$. Notice that the explicit form of velocities is not used for the computation of the new positions. The advantages of the Verlet algorithm are that it is simple, straightforward, and low storage requirements. The disadvantage is that the algorithm is of moderate precision.

2.5.3. Leap-frog algorithm

For the studies using non-reactive force fields, we applied the Leap-frog algorithm to solve Newton's equations of motions. This algorithm gives positions and velocities at time *t* in the following forms:

$$\vec{v}\left(t+\frac{1}{2}\delta t\right) = \vec{v}\left(t-\frac{1}{2}\delta t\right) + \frac{\vec{F}(t)}{m}\delta t \tag{2.29}$$

$$\vec{r}(t+\delta t) = \vec{r}(t) + \vec{v}\left(t+\frac{1}{2}\delta t\right)\delta t \tag{2.30}$$

In this algorithm, the velocities are initially calculated at time $t + 1/2\delta t$ and then used to calculate the positions, *r*, at time $t + \delta t$. Therefore, the velocities leap over the positions and then the positions leap over the velocities. The velocities at time *t* can be computed approximately by averaging the velocities at $(t + \frac{1}{2}\delta t)$ and $(t - \frac{1}{2}\delta t)$ as shown in Equation 2.31:

$$\vec{v}(t) = \frac{1}{2}\left[\vec{v}\left(t+\frac{1}{2}\delta t\right) + \vec{v}\left(t-\frac{1}{2}\delta t\right)\right] \tag{2.31}$$

The advantage of this algorithm is that the velocities are explicitly calculated and it is more accurate than the Verlet algorithm; however, the disadvantage is that velocities and the positions are not calculated at the same time.

The Leap-frog and Verlet algorithms are time reversible and they preserve the phase-space volume. Although they do not conserve the total energy, the long-term energy drift is not very large provided a small time step is used.

2.6. Constraint algorithm

Many algorithms have been proposed for solving the nonlinear problem of resetting coupled constraints after an unconstrained update. The SHAKE algorithm [66] is a straightforward modification of the Verlet algorithm to impose constraints on bond lengths and bond angles through fixed interatomic distances. SHAKE is numerically stable and most widely used for large molecules. It resets all bonds (angles) to prescribed values until all constraints are satisfied to within a relative tolerance. Unlike SHAKE, the LINCS constraint method [67] is non-iterative, as it operates in two steps. The projections of the new bonds on the old bonds are set to zero, and then a correction which prevents the lengthening of the bonds due to rotation is implemented. This method is three to four times faster than SHAKE algorithm at the same accuracy. For the special case of rigid water models, SETTLE [68] is a fast algorithm which resets the positions and velocities to satisfy the holonomic constraints on models.

2.7. Force calculation and long-range interaction

The positions and velocities of each atom must be updated by recalculating the forces that are acting upon the atoms at each step. A summation of non-bonded interactions including van der Waal and electrostatic interactions has to be performed to account for all non-bonded pairs. As a result, the calculation of non-bonded interactions in the system costs tremendous computational time. To deal with the limited computer memory as well as to speed up the calculations, the cutoff distance is imposed. This indicates that the non-bonded interactions between atoms separated by a distance greater than a certain cutoff value are ignored. Such an approach, called the Cutoff Method (CM), treats well for the van der Waal interactions; however, it is not applicable for the systems with charged atoms due to the long-range nature of electrostatic interactions. Multiple efficient techniques have been developed for the treatment of the electrostatic interactions such as the one which is to divide the electrostatic interactions into a long-range and short-range component. While rapidly varying electrostatic interactions at short-range is computed in real space, the slowly decaying potential at long-range is calculated in reciprocal space using different approaches, for example, Ewald summation [69], Particle Mesh Ewald (PME) [70], and Particle-Particle Particle-Mesh methods (PPPM) [65]. These approaches help greatly improve the efficiency of the computation. In our simulations, we employed the PPPM and PME algorithms to account for the long-range electrostatic interactions. In these methods, the point charges are interpolated

onto a regular grid, and then converted to their equivalent space structure factors through a fast Fourier transform.

2.8. Thermostat

The central idea behind MD simulations using the Newtonian equations of motion is to study the time evolution of a statistical ensemble of microstates characterized by the NVE ensemble. Because the total energy is conserved, but not the kinetic and potential energy contributions, the simulated system will reach equilibrium while the temperature changes. It is therefore appropriate to require a means to modulate the temperature of the system. Furthermore, in order to simulate or mimic experiments performed in laboratory conditions, sampling from the NVT ensemble or the NPT ensemble is desirable.

The temperature of a simulated system is typically computed from kinetic energies using the equipartition theorem defined by Equation 2.32:

$$\frac{3}{2}\mathrm{N}k_{\mathrm{B}}\mathrm{T} = \langle \sum_{\mathrm{i}=1}^{\mathrm{N}} \frac{1}{2}\mathrm{m_i}\mathrm{v_i}^2 \rangle \tag{2.32}$$

where k_B is Boltzmann's constant, m_i and v_i are the mass and velocity of atom i, respectively, and N is the total number of atoms. The angular brackets indicate that the temperature is a time-averaged quantity. Equation 2.32 can be used to define an instantaneous temperature at time t from the average over all velocities of atoms. As the system evolves toward an equilibrium state, the instantaneous temperature will drift. Even after equilibrium is reached, the instantaneous temperature will fluctuate around the target temperature.

To maintain a constant temperature during the course of a simulation, a variety of thermostat algorithms have been developed. Thermostat algorithms work either by altering the velocities of the atoms or by modifying the Newtonian equations of motion. One of the easiest thermostats to implement is so called 'simple velocity rescaling' [71], which relies on rescaling all the atomic velocities by a factor $\sqrt{\frac{\mathrm{T_0}}{\mathrm{T}}}$ in order to drive the instantaneous temperature of the system, T to the desired temperature, T_0. However, this thermostat is also one of the most non-physical thermostats. It has been shown that the simple velocity rescaling does not properly sample the isokinetic ensemble except in the limit of infinitesimal time steps [72]. This algorithm was found to introduce artifacts in the structural, dynamic, and energetic properties of the system, so it is not recommended [73].

A similar approach to temperature control was proposed by Berendsen [74], consisting of a weak coupling of the system to an external heat bath. The Berendsen thermostat uses an exponential decay of the temperature towards the desired temperature as shown in Equation 2.33:

$$\frac{dT}{dt} = \frac{1}{\tau}(T_0 - T) \tag{2.33}$$

where τ is the coupling constant. Although the Berendsen thermostat is quite efficient in relaxing the system to the desired temperature, it samples neither the canonical distribution nor the isokinetic distribution. In practice, it is recommended to equilibrate the system using the Berendsen thermostat with a small coupling constant in order to attain quickly the desired temperature.

A widely used thermostat that samples the correct canonical ensemble was originally developed by Nóse [75] and subsequently improved by Hoover [76]. In the Nóse-Hoover thermostat, the equation of motion is modified by introducing a friction parameter through which the motion of particles is controlled until the system temperature, T approaches the target value T_0. The modified equation of motion is expressed as Equation 2.34:

$$\frac{d^2\vec{\mathbf{r}}_i}{dt^2} = \frac{\vec{F}_i}{m_i} - \frac{p_\zeta}{Q}\frac{d\vec{r}_i}{dt} \tag{2.34}$$

where the friction variable ζ is a dynamic quantity which controls the motion of particles until the temperature T approaches the target value T_0, Q determines the relaxation of the dynamics of the friction and its own momentum p_ζ is expressed as Equation 2.35:

$$\frac{dp_\zeta}{dt} = T - T_0 \tag{2.35}$$

Unlike the Berendsen thermostat, the Nosé-Hoover thermostat takes longer time to relax the system towards the target temperature. It is preferable to switch to the Nosé-Hoover thermostat for production as the simulated system has reached equilibrium.

2.9. Barostat

The pressure is commonly measured using the virial which is the product of the positions and the derivative of the potential energy function. This product changes quickly with r which causes the pressure to fluctuate much more than other quantities (e.g., temperature in the

NVT ensemble and energy in the NVE ensemble) during the course of simulation. As is the case with thermostat, a barostat algorithm will be needed to maintain the pressure in a simulation. The approaches used for controlling the pressure are analogous to those that are used for controlling the temperature. Barostat algorithms work by scaling or rescaling the coordinates in the system or by modifying the Newton equations of motion. A plethora of barostat exits, including Parrinello-Rahman [77], Nosé-Hoover [78, 79], Berendsen [74], Andersen [80]. The Berendsen barostat maintains the pressure by coupling the system to a weakly interacting pressure bath. This bath scales the volume of the system such that the instantaneous pressure approaches the target pressure. In Andersen barostat the system is coupled to a fictitious pressure bath, by introducing an additional degree of freedom to the equations of motion. The Parrinello-Rahman barostat works by scaling the size and shape of the simulation box. Unlike the Andersen barostat, the Parrinello-Rahman barostat can be used to apply anisotropic pressures to parts of the system. In this thesis, the Nóse-Hoover barostat was applied to all MD simulations in the NPT ensemble. The Nóse-Hoover barostat is an extended system algorithm which is coupled with a Nóse-Hoover thermostat. This is similar to the Andersen thermostat. The additional degree of the freedom acting as a piston is added to the Hamiltonian of the system which results in the following equations of motion:

$$\frac{d\mathbf{r}(t)}{dt} = \mathbf{v}(t) + \eta(t)[\mathbf{r}(t) - R_{COM}] \tag{2.36}$$

$$\frac{d\mathbf{v}(t)}{dt} = \frac{\mathbf{F}(t)}{M} - [\chi(t) + \eta(t)]\mathbf{v}(t) \tag{2.37}$$

$$\frac{d\chi(t)}{dt} = \frac{1}{\tau_T^2}\left(\frac{T}{T_0} - 1\right) \tag{2.38}$$

$$\frac{d\eta(t)}{dt} = \frac{1}{Nk_B T_0 \tau_P^2} V(t)(P - P_0) \tag{2.39}$$

$$\frac{dV(t)}{dt} = 3\eta(t)V(t) \tag{2.40}$$

where R_{COM} is the coordinates of the center of mass of the system, η is the barostat friction coefficient, τ_T is the thermostat time constant for temperature fluctuations, τ_P is the barostat

time constant for pressure fluctuations, χ is the volume scaling, V is the volume of the simulation box, P_0 and T_0 are desired pressure and temperature, respectively.

2.10. Periodic boundary condition

In order to minimize the boundary effects caused by finite size and to simulate more closely bulk properties with finite size systems, periodic boundary conditions (PBC) are usually employed in MD. With the use of PBC, the finite simulation box is replicated throughout space to form an infinite lattice. The central simulation box is enclosed in green as shown in **Figure 2.2**. It is surrounded by its periodic images in all directions resulting in each particle in the central box having interactions not only with other particles in the same box, but also with the particles in the adjacent boxes. Thus, the particles in the computational box encounter the forces in the same way that they do in infinite system. Further, when a molecule leaves the central computational box, one of its periodic images in the replicated boxes having the same momenta will enter from the opposite side of the box. Therefore, there are no walls at the boundary of the central box avoiding the surface effects. In our studies, periodic boundary conditions in all directions were employed.

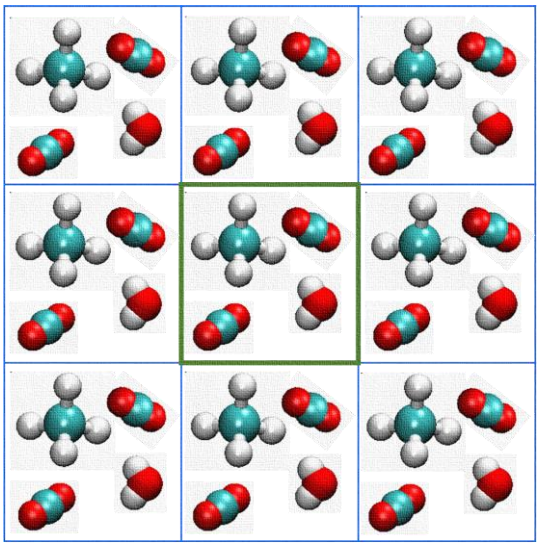

Figure 2.2. Periodic boundary condition in MD simulations

Periodic boundary conditions are usually used in conjunction with the minimum image convention in which each atom interacts with the closest images of other atoms in the simulation. The minimum image convention ensures that only one pairwise interaction for each pair of atoms is calculated. A cutoff distance is thus introduced but not allowed to exceed half of the simulation box size to prevent violation of the minimum image convention.

Chapter 3. Propane-Water Confined within Cylindrical Silica Nano-Pores: Structural and Dynamical Properties Probed by Molecular Dynamics

The material presented in this Chapter was published in 2017 in volume 33, pages 11310−11320 of Langmuir.

3.1. Introduction

Fluids confined in porous media exhibit significantly different behaviour from conventional bulk fluid [81]. While molecules in bulk fluid phases show isotropic properties, the behaviour of molecules under confinement can be considerably different due to strong molecule-substrate interactions, preferential adsorption, and crowding effects when other molecules are present near the interfaces [82, 83]. Despite the multiple length and time scales over which fluid-mineral interactions occur, interfacial phenomena control the exchange of matter and impact the nature of multiphase flow, as well as the reactivity of C–O–H fluids in geologic systems. In general, the properties of confined fluids, and their influence on porous geologic phenomena are much less well understood compared to those of bulk fluids. Attempts have been made to study the dynamics of single species confined in porous materials [19, 21, 84-86]. Several fluids, however, are often found confined in porous rocks in natural environment at the same time, and consequently, the presence of one fluid may affect the dynamics of the other. Micro- and mesoporous silica materials have been widely used for systematic studies of fluids in confined environments, in part because silica is one of the most abundant subsurface materials. When pure silica comes in contact with water, its outer layer is expected to be hydroxylated. The hydrophilic character of the resultant pore surface significantly affects the confined fluids, as it has been documented in the case of interfacial water both in terms of structure and dynamics [22, 23, 87-89]. The nature of the interactions between water, guest molecules, and the solid substrate must be better understood to elucidate molecular phenomena that occur in narrow pores at subsurface conditions. Toward this goal, Professor Alberto Striolo's research group previously reported molecular dynamics (MD) simulations that documented the effect of density and composition of CO_2−hydrocarbon mixtures on adsorption and mobility of the confined mixtures [4, 18].

Those simulation results, which seem to be in agreement with experimental observations [85, 90, 91], suggest that the preferential CO_2 adsorption to the pore walls weakens the adsorption of hydrocarbons, and enhances the self-diffusion of hydrocarbons via lowering the activation energy for diffusion. The present work in this Chapter stems from recent quasi-elastic neutron scattering experiments conducted for systems containing propane confined in MCM-41-S materials [92, 93]. These experimental results showed that propane mobility decreases as the D_2O content increases. To probe a system similar to the experimental one, in this thesis, propane–water mixtures confined inside a 16 Å diameter cylindrical silica pore were considered. The geometry of the pore and its reduced size, the amorphous nature of the pore surface, and the preferential interactions between water and the surface −OH groups as opposed to the weaker interactions between propane and the silica substrate are expected to yield significant differences compared to the results reported previously for CO_2-hydrocarbon mixtures in slit-shaped pores carved out of crystalline cristobalite. The simulations were conducted at moderate temperature–pressure conditions (T = 300 K, P_{bulk} = ∼0.6–3 MPa). Our attention focused on the effect of the bulk pressure of C_3H_8 loading as well as on the effect of adding water on the dynamics of confined C_3H_8. The simulation results provide extensive insights into the structural and dynamic properties of all components considered.

The remainder of this Chapter is organized as follows: We start by reviewing both simulation models and algorithms, we then present our main simulation results, we compare the results with those from other mixed fluid-porous matrix interactions, and we finally conclude via summarizing our main results.

3.2. Simulation methods and algorithms

3.2.1. Preparation of the amorphous silica pore

To create a model of bulk amorphous silica, we started from the β-cristobalite structure in a system composed of 12,288 atoms within a 57.28 Å × 57.28 Å × 57.28 Å simulation box with periodic boundary conditions. The amorphous system was prepared following the annealing cycle proposed by Leroch et al. [94]. In this procedure, the crystalline sample is melted at 7000K, then equilibrated in the liquid phase, and finally quenched to room temperature at a rate of 4K/ps. The annealing simulations were conducted first in the NPT ensemble at a pressure of 1 bar, which allows for adaptations of the simulation cell volume during phase transition to maintain the desired pressure. At the end of annealing process, the amorphous

silica block was equilibrated under NVT conditions. The final cubic dimension of the simulation box was of 56.9 Å on all sides.

Following Leroch et al., for the annealing simulations we implemented the Morse-type potential developed by Demiralp et al. [95]. In this force field, a two-body Morse–Stretch term describes nonelectrostatic interactions, and the atomic charges depend on the local atomic configuration. The interaction potential is described as Equation 3.1:

$$U_{ij}(R_{ij}) = \frac{q_i q_j}{R_{ij}} + D_0 \left\{ \exp\left[\gamma\left(1 - \frac{R_{ij}}{R_0}\right)\right] - 2\exp\left[\frac{1}{2}\gamma\left(1 - \frac{R_{ij}}{R_0}\right)\right]\right\} \quad (3.1)$$

In Equation 3.1 q_i and q_j represent the charges of atoms *i* and *j*, respectively. In our approach, for Si atoms $q_{Si} = +1.3e$ and for O atoms $q_O = -0.65e$. In Equation 3.1 R_{ij} denotes the interatomic distance between atoms *i* and *j*. D_0, R_0 and γ represent bond strength, bond length, and dimensionless force, respectively. It has been shown that the potential of Equation 3.1 closely reproduces the melting temperature of cristobalite, the glass phase transition temperature of silica glass, and the density of silica after the annealing cycle [96-98], in some cases better than BKS [99] or TTAM [100] potentials. In **Table 3.1** we report the Morse potential parameters used in this study.

Table 3.1. Morse potential parameters taken from Ref [98]

Interaction	R_0 (Å)	D_0 (kcal/mol)	γ
O–O	3.7910	0.5363	10.4112
Si–Si	3.7598	0.17733	15.3744
Si–O	1.6280	45.9970	8.6342

From the bulk amorphous silica volume prepared as described above, a cylindrical channel of 16 Å in diameter was carved out by removing all atoms located within a distance of 8 Å from the X axis, i.e., all atoms whose *y* and *z* coordinates obey the relation:

$$\sqrt{y^2 + z^2} < 8 \quad (3.2)$$

The resulting SiO_2 substrate was composed of 11,613 atoms. The surface of the cylindrical pore is rough at the atomic level, reflecting the amorphous nature of the substrate. The dangling silicon and oxygen atoms in the interfacial region were saturated with hydroxyl groups and hydrogen atoms, respectively, yielding two kinds of silanol groups: Si–$(OH)_2$ (germinal) and Si–OH (single silanol). The resultant hydroxyl density was of 3.8/nm^2,

which is in good agreement with experimental data (from 2.6 to 4.6 OH/nm^2) measured on flat amorphous silica surfaces [101]. The final number of atoms in the solid substrate was 11,694.

Within the periodic boundary conditions implemented, the cylindrical pore was aligned parallel to the X direction, along which it was effectively infinite. This model substrate was used to sample transport and structural properties for the confined fluid systems.

To prepare a model of propane–water mixtures confined inside the pore at equilibrium with a bulk reservoir, we followed the procedure previously implemented for other substrates [17, 102], and briefly described below.

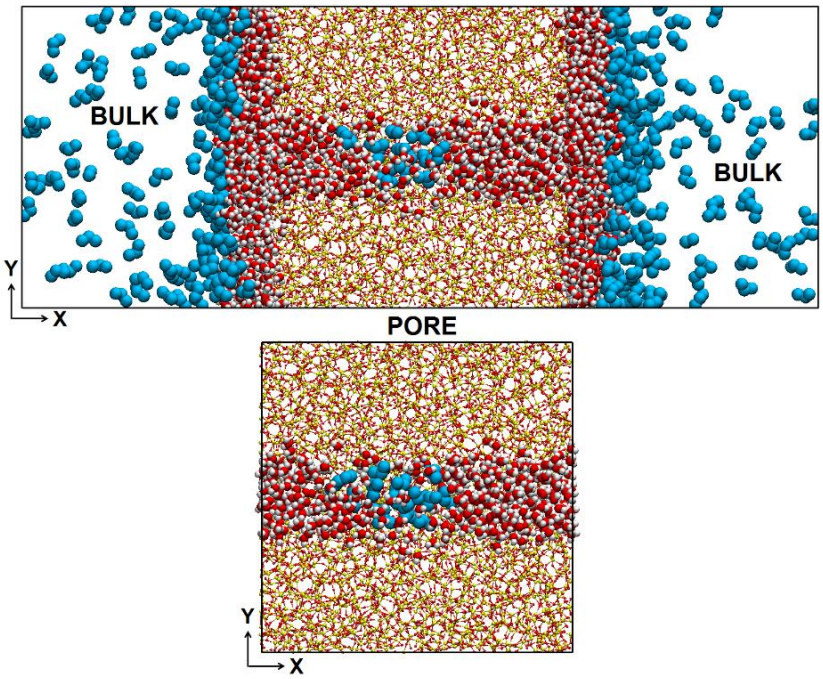

Figure 3.1. Side view of representative simulation snapshots for setups following System A (top) and System B (bottom), as described in the text. Yellow, red, white and cyan spheres represent silicon, oxygen, hydrogen atoms, and propane molecules, respectively. The silica substrate contains 3,847 silicon, 7,745 oxygen, and 102 hydrogen atoms. Note that only a portion of the simulation box is shown for clarity.

Once the amorphous pores were prepared, subsequent simulations concerning fluid-pore systems were conducted implementing CLAYFF for the solid substrate, as described below. Two systems were prepared and used in our simulations. In one (System A), the solid substrate was in contact with an external "bulk" fluid reservoir. In the other (System B), the pore was infinitely long because of periodic boundary conditions.

In **Figure 3.1** we report a schematic of the two simulation scenarios. The two corresponding simulation box sizes were of 150.0 × 56.9 × 56.9 and 56.9 × 56.9 × 56.9 $Å^3$, respectively. In both cases, periodic boundary conditions were implemented along the X, Y, and Z directions. The X dimension of the simulation box for System A simulations allowed for a "bulk" region of thickness ~93 Å. The X dimension of the simulation box for System B simulations, 56.9 Å, is large enough to prevent unphysical interactions between replicas of the simulated molecules along the X direction. It is worth repeating that we employed System A to determine how much propane is adsorbed within the pore by varying the thermodynamic conditions of bulk propane. The final configuration obtained from simulations of System A was then used to prepare System B, which was employed to quantify the transport and the structural properties of the fluid systems confined in the pore. In a recent work, Le et al. [6] showed that the approach followed within the System A algorithm yields adsorption isotherms for propane in narrow slit-shaped silica pores that are in fair agreement with experimental data. It has shown that the pore geometry affects the interactions between the particles and the pore walls, thereby controlling the shape of adsorption isotherms [103]. However, Cracknell et al. [104] reported that the adsorption isotherms based on slit-shaped and cylindrical structures show fairly similar trends. Therefore, the approach is expected to yield reasonable amounts of propane adsorbed within the pores for the scope of the present work. One alternative approach would be to use grand canonical Monte Carlo simulations to obtain the initial configurations for the simulations conducted within the System B.

The initial configuration for simulations conducted within this framework consists of a desired number of water and propane molecules placed at each side of the cylindrical pore, in the "bulk" region, along the X direction. As simulations proceeded, water and propane spontaneously filled the pore and were distributed across both pore and bulk volumes. To fill the pore completely with water we require 2,141 water molecules. An increasing amount of propane (from 76 to 350 molecules) is placed in the bulk region. This propane controls the pressure of the system. As the simulations progress, some propane adsorbs in the hydrated pore. Once equilibrium is reached, the propane density in the bulk was calculated from density profiles such as those shown in **Figure 3.2b**. These representative results show that, for each simulated system, propane accumulates near the substrate and penetrates the pore, while a constant propane density is maintained away from the solid substrate. The portion of each data set where the propane density is constant (from X = 0 to X ~20 Å in **Figure 3.2**) was used to extract the bulk propane density. The bulk pressure for each system was then

estimated from the bulk pure propane density in gas phase by using the Peng–Robinson (PR) equation of state [105]. The accuracy of the PR equation of state depends on the parameters modelling the intermolecular attraction force [106]. Additional simulations under the NVT ensemble would be an alternative approach to determine the bulk propane pressures according to the propane densities. A schematic of the process is provided in **Figure 3.2**. The estimated bulk pressures for five C_3H_8–H_2O mixtures of different compositions are given in **Table 3.2**.

System A

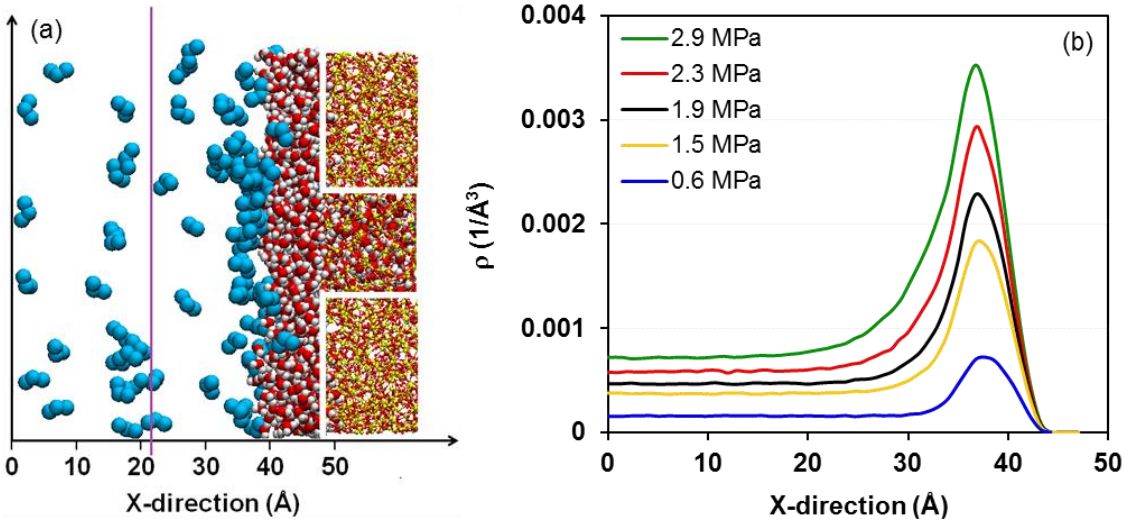

Figure 3.2. Detail of a simulation snapshot revealing the distribution of propane away from the solid substrate (a), and propane molecular density profiles along the X direction of the simulation box, in the region outside the cylindrical pore (b). In this representation, the solid substrate is located at $x > \sim 46$ Å. Note that the density profiles show accumulation of propane near the substrate, as visualized in the snapshot. The vertical line in panel (a) identifies the bulk region within which the propane density is constant. The white lines on the right of panel (a) help identify the silica substrate, which yields a cylindrical pore filled with water (red and white for O and H atoms, respectively).

Table 3.2. Bulk propane pressures estimated for five propane–water systems simulated within the System A model at T = 300 K, and the composition of the corresponding systems simulated with System B models

Number	System A composition	Estimated bulk pressure (MPa)	System B composition
1	76 C_3H_8–2,141 H_2O	0.60 ± 0.05	11 C_3H_8–387 H_2O
2	176 C_3H_8–2,141 H_2O	1.5 ± 0.1	15 C_3H_8–379 H_2O
3	221 C_3H_8–2,141 H_2O	1.9 ± 0.1	17 C_3H_8–383 H_2O
4	281 C_3H_8–2,141 H_2O	2.30 ± 0.02	21 C_3H_8–373 H_2O
5	350 C_3H_8–2,141 H_2O	2.90 ± 0.05	22 C_3H_8– 371 H_2O

System B

To quantify the properties of confined fluids, the resulting configurations obtained from the simulations conducted using the System A setups were modified by removing the region outside of the pores (along the X direction), and by rendering the cylindrical pores effectively infinite. For each system, the number of propane and water molecules inserted inside the pore corresponded to those obtained from the System A simulations. In **Table 3.2** we report the number of fluid molecules confined within the corresponding System B pores.

To further quantify the impact of water on the diffusion of confined propane, we conducted additional simulations in which (a) 45 propane molecules were confined within the cylindrical pore (no H_2O present, corresponding to bulk pressure of ∼0.6 MPa), and (b) starting from system B5 (22 C_3H_8 and 371 H_2O molecules) we systematically reduced the amount of water molecules (three simulations with 321, 271, and 221 water molecules, respectively, while maintaining 22 C_3H_8 molecules confined within cylindrical pores).

3.2.2. Force fields

For all simulations in which fluid molecules were at contact with the solid substrate, the CLAYFF [107] force field was implemented to simulate the silica substrates. CLAYFF is a general force field suitable for fluid-clay and other clay-related systems. In these simulations, the silica frame was kept rigid by freezing the position of the bulk O and Si atoms while only the surface H atoms of silanol groups were allowed to move. Because the simple point charge/extend (SPC/E) model [108] provides acceptable estimates for the structure, the internal energy, the density and the diffusivity for water at ambient conditions [109], it was selected to describe water. Building on prior simulation results from Professor Alberto Striolo's research group [6], the TraPPE-UA force field [110] was employed to model propane. Dispersive forces were described implementing the 12–6 Lennard–Jones potential and electrostatic forces were taken into account for nonbonded interactions. The distance cutoff of interatomic interactions for all simulations was fixed at 14 Å. The particle mesh Ewald (PME) method [111] was used to treat the long-range electrostatic interactions. The Lorentz–Berthelot mixing rule [112] is applied to determine the Lennard-Jones parameters for unlike interactions.

3.2.3. Algorithms

All simulations were carried out using the Groningen Machine for Chemical Simulations (GROMACS) simulation package, version 5.1.2 [113, 114]. The leapfrog algorithm [115] was used to integrate the equations of motion. The temperature of the silica matrix was kept constant at 300 K using the Nosé–Hoover thermostat. The temperature of the confined fluids was also maintained constant at 300 K using the Nosé–Hoover thermostat. It was found that decoupling the two thermostats prevents unrealistic distributions of the kinetic energy between solid and fluid [116]. Both thermostats had a fixed temperature-damping factor of 100 fs. Following the minimization of the energy for the initial configuration, both systems A and B were simulated using molecular dynamics.

For Systems A, we found that equilibration was achieved after ~60–100 ns of simulation time, depending on loading. Equilibration was considered achieved when the propane densities oscillated around constant values, and both system temperature and energy fluctuations remained within 10% of their respective average values. The density profiles of propane and the adsorption isotherm obtained from the last 2 ns of the simulations are presented in **Figure 3.2b** and **Figure 3.4**, respectively as results.

For Systems B, all systems were simulated for 80 ns with a time step of 1 fs. After 78 ns of equilibration time, trajectories from the last 2 ns of simulations were used to analyze transport and structural properties of the fluids. Equilibration was considered achieved when the density profiles of propane and water within the pore and the total energy of the systems converged within the criteria discussed above.

In this study, the diffusive motion of fluid particles was described by their translation. The translational diffusion is often quantified by diffusion coefficients. The self-diffusion coefficients were calculated from the mean square displacement (MSD) $\langle |\mathrm{r_i}(\mathrm{t}' + \mathrm{t}) - \mathrm{r_i}(\mathrm{t}')|^2 \rangle$ by implementing the Einstein equation [117]:

$$\mathrm{D_s} = \lim_{\mathrm{t}\to\infty} \frac{\langle |\mathrm{r_i}(\mathrm{t}' + \mathrm{t}) - \mathrm{r_i}(\mathrm{t}')|^2 \rangle}{2.\,\mathrm{t}.\,\mathrm{d}} \tag{3.3}$$

In Equation 3.3, $r_i(t)$ and $r_i(t')$ are the positions of particle *i* at time *t* and at the time origin *t'*, respectively, *d* is the number of degrees of freedom, and the average $\langle \ldots \rangle$ is taken over possible trajectories of the fluid particles. For sufficiently long observation times, the mean-square displacement of a single particle increases linearly with time. A typical MSD plot for a

homogeneous fluid as a function of time and its relation to the self-diffusion coefficient D_s are shown in **Figure 3.3**.

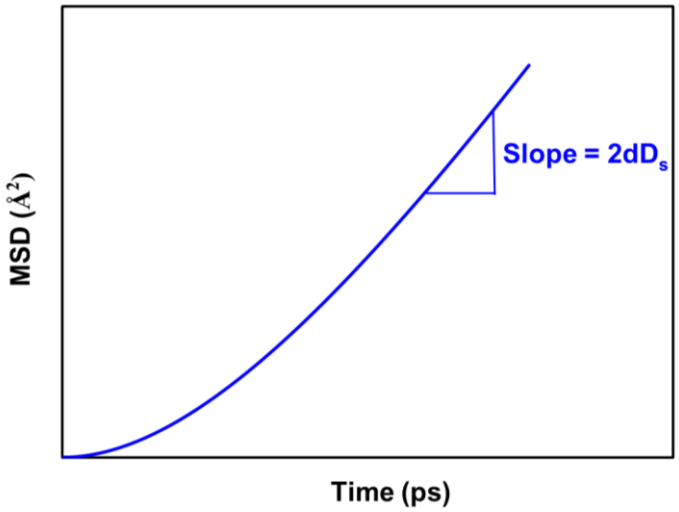

Figure 3.3. Mean square displacement.

The diffusivity of fluids within the pore is considered as a one-dimensional translation (d = 1) along the X direction, because the cylindrical shape of the pores constrains the movement of molecules over long distances along the Y and Z directions.

3.3. Simulation results

3.3.1. Adsorption isotherm

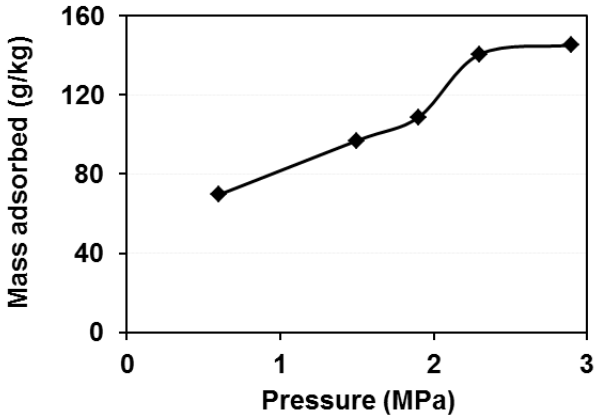

Figure 3.4. Simulated amount of propane adsorbed in the cylindrical pore filled with water as a function of the bulk pressure. The simulations were conducted at 300 K. The amount of propane adsorbed is expressed as grams of propane per kilogram of water inside the pore.

In **Figure 3.4**, we report the simulated amount of propane adsorbed in the cylindrical pores filled with water at 300 K and bulk pressures in the range ~0.6 to 2.9 MPa. For these

simulations, we used the approach described as System A in the Simulation Methods and Algorithms section. The amount of propane adsorbed in the pore increases as the pressure increases. For comparison, the experimental mole fraction solubility of propane in bulk water at 298 K and 1 bar is 2.732×10^{-5} [118], which corresponds to ~0.067 g of propane per kg of water. For completeness, we point out that Ferguson et al. [119] used molecular dynamics to study the solubility of linear alkanes in water in the bulk. They found excellent agreement between simulated and experimental solubility for short alkanes. Ferguson et al. implemented the SPC/E force field to simulate water, and the TraPPE force field to simulate alkanes. Based on these observations, the results in **Figure 3.4** suggest that the amount of propane in confined water is much larger than that which could be expected based on bulk solubility data. However, analysis of the simulation snapshots, discussed below, show that in the case simulated here propane is not solubilized in confined water.

3.3.2. Structural properties: atomic density profiles

Atomic density profiles as a function of distance from the pore axis were calculated for all confined fluid molecules. These simulations were conducted using the approach described as System B in the Simulation Methods and Algorithms section, but they were initiated from data obtained from the final configurations derived from simulations for Systems A. All simulation results described in the remainder of this Chapter were obtained using the System B set up. Representative density profiles are shown in **Figure 3.5**, where the density profiles of silanol group atoms are used to locate the pore surface, and different lines represent density distributions of various compounds. We report the atomic density profiles of O and H atoms of water and the molecular density profile of propane, as obtained from the distribution of the CH_2 group of confined propane. The density profiles of confined water do not change significantly as the amount of propane increases, hence only one data set is shown for O and H atomic density profiles.

The radial density profiles for the O atom of water, shown in **Figure 3.5**, are characterized by one pronounced peak at ~7.4 Å. This peak indicates the formation of one layer of water in proximity of the solid substrate. The formation of this hydration layer seems to be in agreement with experimental neutron scattering data obtained for water confined in MCM-41 [120, 121]. The density profile for H atoms of water provides further information. In particular, two peaks are observed around the position of the pronounced O density peak: one at ~7.1 Å and one at ~8.4 Å. Because the H peak at ~8.4 Å is approximately identical in

intensity as the O peak at ~7.4 Å, the results suggest that the water molecules in the first hydration layer lay with one of their OH vectors toward the surface. The second H peak, located at ~7.1 Å has nearly twice the intensity than the O peak at ~7.4 Å, suggesting that this peak is due to H atoms of water molecules in the first layer plus H atoms of water molecules whose oxygen atoms are in the second hydration layer. The peaks in both O and H density profiles at distances larger than ~8.4 Å represent water molecules that are found within the atomically rough surface.

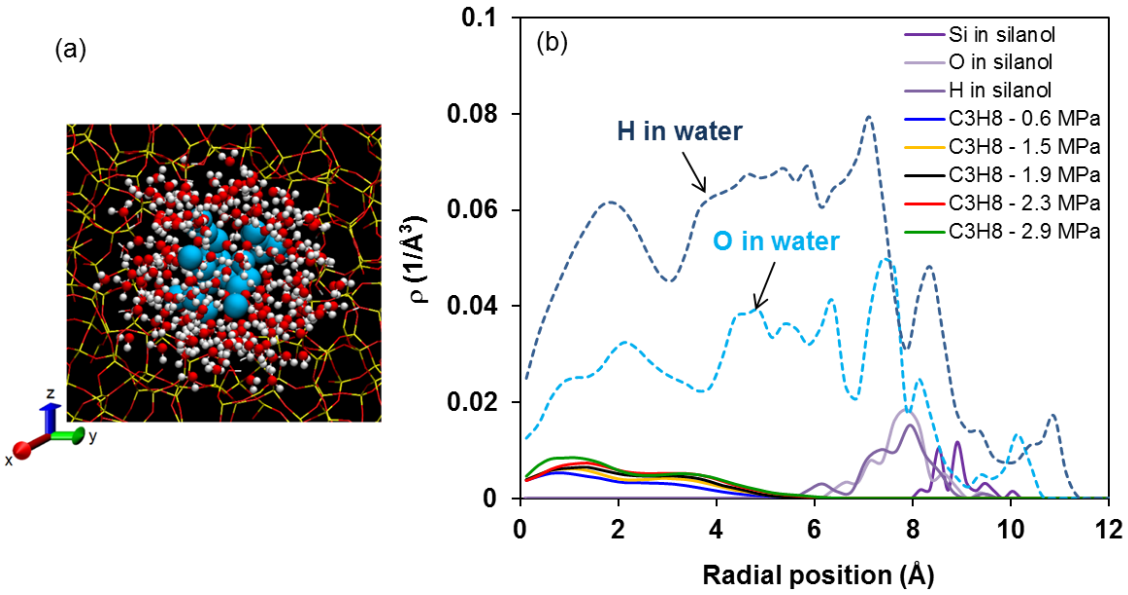

Figure 3.5. (a) Axial view of a representative simulation snapshot illustrating the distribution of fluid molecules confined in the cylindrical silica pore. (b) Radial density profiles calculated for molecules within the cylindrical silica pore. The reference 0 is the central axis of the pore. For water we report the density profiles of both oxygen and hydrogen atoms. These density profiles do not change considerably with pressure, as the amount of water in these systems does not change significantly. For propane, the density profile is obtained from the position of the ethyl pseudoatoms.

The atomic density profiles of confined water show that water does not homogeneously occupy the pore volume, as water seems to be depleted from the pore center. Not far from the pore center, the water density approaches the bulk value (0.033 molecules/Å^3). However, given the small pore and the features already discussed, water in this region probably does not behave as bulk water. Few water molecules are found at r > 8 Å due to the surface roughness of the substrate. These molecules (about 22) are found to penetrate small cavities present within the silica matrix, and are excluded from the calculations of the dynamical properties of confined water presented below. The water atomic density profiles do not

change significantly as the bulk pressure increases, since the number of water molecules within the pore is not considerably different.

On the other hand, increasing the bulk pressure by adding propane molecules to the simulations of System A yields an increase in the molecular density of propane within the pores. Note that propane density peaks, irrespective of the simulated pressure, are always close to the pore center, implying that propane molecules preferentially accumulate in this region, and remain excluded from the hydration layer.

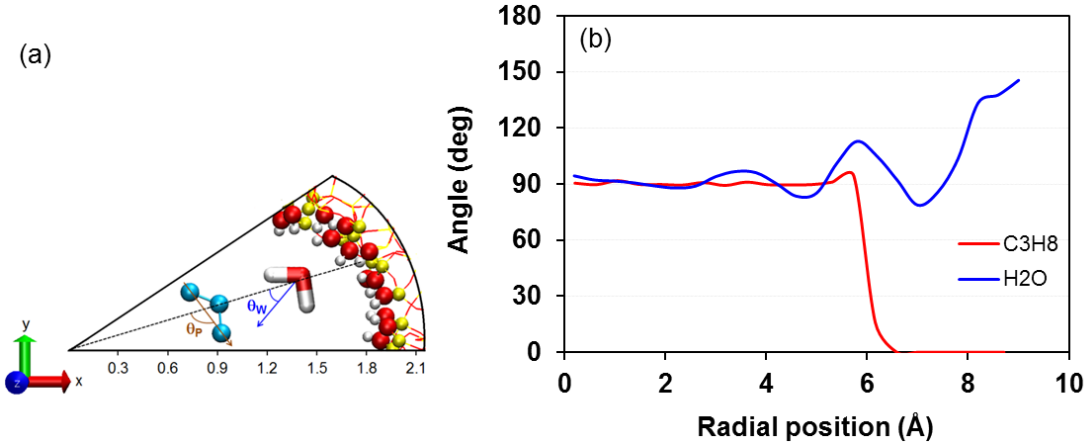

Figure 3.6. Scheme representing the orientation angles θ_w and θ_P as calculated for confined water and propane molecules, respectively (a). Orientation of confined fluids as a function of their distances from the central axis of the pore (b) for a system composed of 11 propane molecules and 387 water molecules.

The preferential orientations of confined molecules with respect to the radial direction are reported in **Figure 3.6**. For propane, we quantified the angle θ_p formed between the CH_3–CH_3 vector identified by each propane molecule, and the vector pointing from the pore surface to the pore center. For water, we quantified the angle θ_w formed between the dipole moment vector of a water molecule and the vector pointing from the pore surface to the pore center. Schematics of these angles are illustrated in **Figure 3.6a**. For propane molecules, when the angle θ_p is 0° or 180°, the CH_3–CH_3 vector is perpendicular to the pore surface, whereas, when θ_p is 90°, the propane lays parallel to the surface. The interpretation for the results on the orientation of the dipole moment of water molecules is analogous. Our results in **Figure 3.6b** show that propane molecules preferentially orient parallel to the pore surface, irrespective of the distance from the surface. Conversely, water molecules show different orientations along the radial distance. In the central region of the pore, the dipole moment of H_2O molecules yields a preferential angle of ~90° with respect to the radial direction, while

the preferential angle shows a strong dependence on radial position near the pore surface. The results obtained for θ_w in the interfacial region suggest that one OH group of the water molecules points generally toward the surface. This result is consistent with the hydrogen-up orientation of water molecules observed for the atomic density profiles of water and discussed above (see **Figure 3.5**).

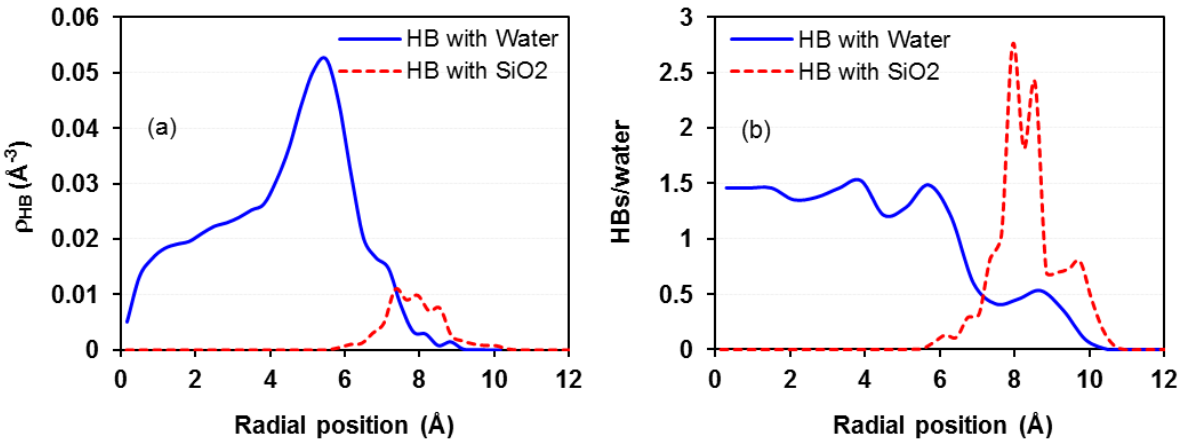

Figure 3.7. (a) Density profile of hydrogen bonds. (b) Average number of hydrogen bonds per water molecule. The data are plotted as a function of the radial distance from the central axis of the pore. Hydrogen bonds are distinguished as forming either among water molecules or between water molecules and surface silanol groups. The results presented in this figure were obtained for a system composed of 15 propane and 379 water molecules.

To quantify the structure formed by water molecules within the cylindrical pore, we computed the number of hydrogen bonds (HBs) that one water molecule forms with other water molecules or with the silica surface. The results are displayed in **Figure 3.7** in the form of the density of HBs (panel a), or of the average number of HBs per water molecule (panel b), wherein both cases are a function of the radial distance. The geometric criterion proposed by Martí [122] was implemented to determine when a HB is formed. According to this criterion, one HB is formed when the distance between the acceptor oxygen and the donor hydrogen is less than 2.4 Å and the H–O···O angle between the atoms involved in the HB is lower than 30°. It was found that changing the amount of propane has little effect on these results. Only one data set is shown for clarity. For reference, when this criterion is used to assess the number of HBs per water molecules in bulk liquid water, it is found that one water molecule forms on average 3.4 HBs [122]. The results for the HB density profile (panel (a) in **Figure 3.7**) show a pronounced peak located at ~5.5 Å. The water molecules in this position (see **Figure 3.6**, panel (b) adopt an angle θ_w of ~113°. This implies that water–water HBs dominate within this region, where water molecules are too far from the surface for

water molecules to form HBs with the surface silanol groups. This is confirmed by the data shown in panel (b) of **Figure 3.7**, which further show that water molecules in this region form an average of ~1.5 HBs per molecule. By contrast, the water molecules in the interfacial region (radial position of ~8 Å) preferentially form HBs with silanol groups, in some cases yielding ~2.8 water-silanol HBs per water molecule. Comparing the data on HB density profiles and those for the preferential orientation of water molecules, we conclude that the oxygen atoms of interfacial water molecules tend to serve as acceptors for HBs formed with the hydrogen atoms provided by the surface silanol groups, which act as donors.

3.3.3. Dynamical properties 1: Translational dynamics of confined propane

Table 3.3. One-dimensional (1D) self-diffusion coefficient estimated for propane confined in silica pores at different pressures. Error bars are estimated as one standard deviation from the average

	D (10^{-10} m^2/s)				
	0.6 MPa	1.5 MPa	1.9 MPa	2.3 MPa	2.9 MPa
confined propane with H_2O	4.1±0.2	3.0±0.2	2.8±0.1	2.4±0.1	1.8±0.1
pure confined propane	94.5±0.8				

The self-diffusion coefficients for propane are summarized in **Table 3.3**. For reference, the self-diffusion coefficient for propane has been simulated by Feng et al. [123] using the OPLS-UA model. At 294 K and 25 MPa, the simulated value was ~9.08×10^{-9} m^2/s, which compares well with the corresponding experimental value of 9.095×10^{-9} m^2/s measured by NMR spin echo by Greiner-Schmid et al. [124]. The results in **Table 3.3** show a drop in propane self-diffusion coefficient as pressure increases. The self-diffusion coefficient for confined pure propane was also computed for comparison, and it is reported in **Table 3.3** as well. The corresponding result, which is comparable to the self-diffusion coefficient for bulk propane, yields a considerably larger 1D self-diffusion coefficient compared to that obtained in the presence of water at the same bulk pressure (by a factor of ~23). These results confirm that the presence of water strongly impedes the transport of propane across the hydrated pores, in qualitative agreement with prior simulations [125], and also with expectations. A similar damping of propane mobility due to presence of D_2O in MCM-41-S has also been observed in quasielastic neutron scattering (QENS) experiments [93]. Unfortunately, only a qualitative comparison can be made, because the experiments were conducted at lower temperatures (i.e., 230 and 250 K) than the simulations presented here.

3.3.4. Dynamical properties 2: Residence times

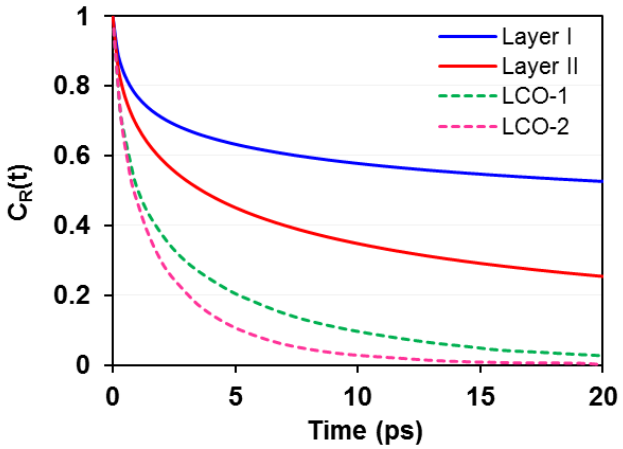

Figure 3.8. Residence autocorrelation functions $C_R(t)$ for oxygen atoms in the first and the second hydration layer of the hydrated silica pores. Solid lines represent results obtained for water confined in the cylindrical amorphous pore considered here, while dashed lines represent results obtained for water on a crystalline flat silica substrate with surface density of 4.54 OH/nm^2 reported by Ho et al. [126] Results indicated as LCO-1 and LCO-2 are for water molecules found within a hydration layer centered at 0.95 and 2.45 Å from the flat surface, respectively. The results for Layer I and Layer II were obtained for a system composed of 17 propane and 383 water molecules.

To quantify the dynamic properties of water in the systems considered, we computed the residence autocorrelation function $C_R(t)$. This quantity allows us to estimate how long a water molecule, found at a specific location away from the surface, remains in that position. The algorithms are described elsewhere [127-129]. In general, the faster $C_R(t)$ decays from 1 to 0 as time progresses, the faster molecules leave the layers considered for these analyses. The analysis is focused on water molecules that reside within two water layers of interest, denoted as layer I (radial position > 6.8 Å) and layer II (5.0 Å < radial position < 6.5 Å). In each case, water found within an annular region of thickness 1.5 Å was considered. The results are reported in **Figure 3.8**. It was found that changing the amount of propane has little effect on these results. Only one data set is shown for clarity. We also report in **Figure 3.8** analogous autocorrelation function results obtained for water molecules on a flat crystalline silica substrate as reported by Ho et al. [126]. Our results show that water molecules in contact with the pore surface stay within the hydration layer (layer I) longer than water molecules found in layer II stay in that region. This is probably due to the preferential interactions between water and silica surface, perhaps via hydrogen bonds. Further, we observe that water molecules reside for longer time in the hydration layer within the cylindrical pore than on the crystalline

flat substrate. These results suggest that the shape and the surface properties of the support strongly affect the dynamical properties of water in the hydration layers.

3.3.5. Dynamical properties 3: Rotational dynamics

The rotational dynamics of molecules can be quantified by calculating vector–vector autocorrelation functions. These calculations reveal changes over time in the orientation of selected molecules. Following previous reports [127-129], we computed reorientation autocorrelation functions defined as Equation 3.4:

$$C_v(t) = \frac{< v_i(t)v_i(0) >}{< v_i(0)v_i(0) >} \quad (3.4)$$

In Equation 3.4, $v(0)$ is either the dipole moment, the hydrogen–hydrogen vector (HH), or the CH_3–CH_3 vector of molecule i at time $t = 0$; $v(t)$ is the same quantity for molecule i, at time t.

The results in **Figure 3.9a** suggest that the CH_3–CH_3 vector autocorrelation functions decay more slowly when increasing bulk pressure, which is attributed to steric hindrance. This observation is in agreement with the results discussed for the diffusivity of propane molecules, which decreases as the bulk pressure increases. We estimate the time required by the CH_3–CH_3 vector autocorrelation function to decay from 1 to 1/e, which was found to be 1.82, 2.62, 3.50, 4.00, and 4.62 ps, respectively, as P increases from ∼0.6 to ∼2.9 MPa. In **Figure 3.9b** and **c**, we report relevant autocorrelation functions estimated for confined water. It was found that these results do not depend strongly on the amount of propane present (the exception being the dipole–dipole autocorrelation function in which case some difference was observed). For brevity, only the results from one system are shown. Both dipole–dipole and HH vector autocorrelation functions in layer I decay more slowly than they do in layer II. These results indicate that those water molecules found in layer I, which are highly associated with surface hydroxyl groups, have a slow rotation, while water molecules in layer II have higher reorientation freedom. These results are qualitatively consistent with those reported by Milischuk et al. [23]. Clearly, solid–water interactions strongly impact the rotation of water molecules. We further note that the reorientation autocorrelation function of the HH vector decays faster than that of the dipole moment vector, suggesting that the rotation of water in the layers considered is anisotropic. Finally, the reorientation dynamics of water molecules confined within the cylindrical pore considered here are found to be much slower than that observed for hydration water on a crystalline flat silica substrate [14]. This is surprising, since

in the crystalline flat substrate the OH bonds in the substrate were treated as rigid, while they are allowed to vibrate in the present work. This suggests that the cylindrical morphology of the surface effectively enhances the strength of the preferential interactions between water molecules and the solid substrate. This is consistent with the high number of HBs formed per water molecule at the interface with the solid substrate (see **Figure 3.7**).

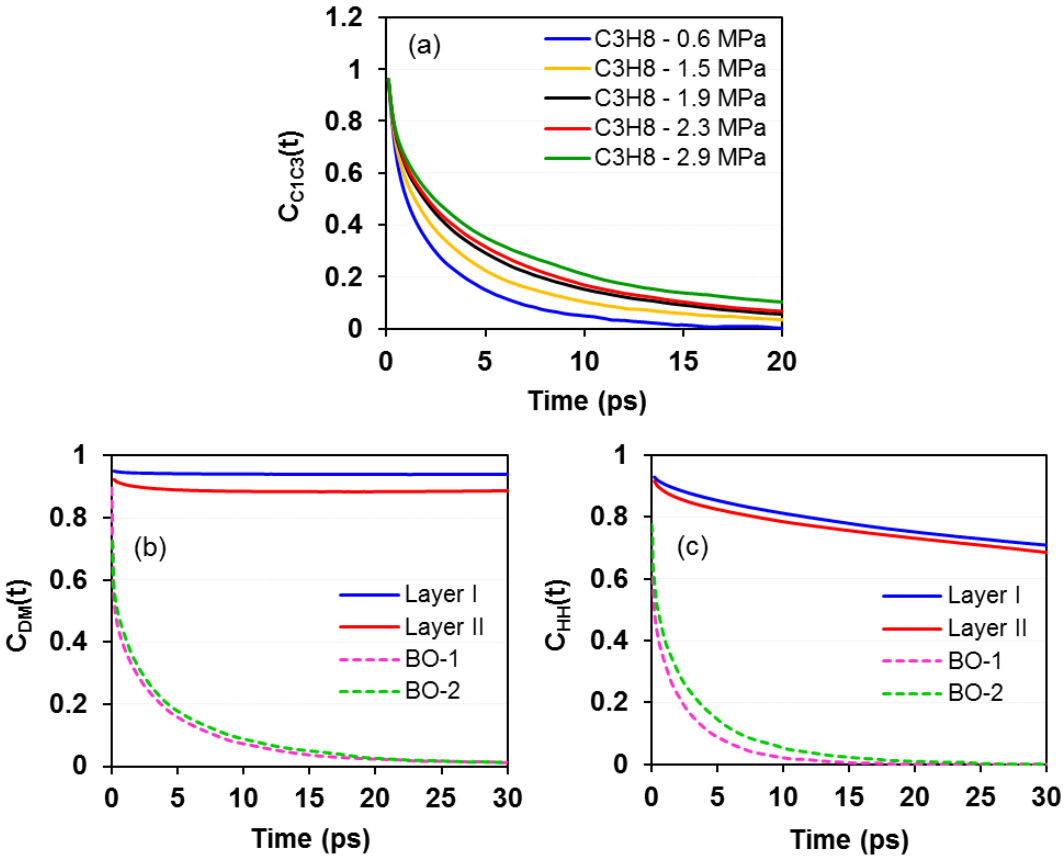

Figure 3.9. CH_3–CH_3 vector autocorrelation function for confined propane molecules at different bulk pressures (a), dipole moment (b), and hydrogen–hydrogen vector (c) autocorrelation functions for water molecules in layer I and layer II within the hydrated silica pores. Solid lines represent results obtained for water in the cylindrical pores considered here for a system composed of 15 propane and 379 water molecules. Dashed lines represent results obtained for water on a flat crystalline silica substrate with hydroxyl surface density of 4.54 OH groups per nm^2 reported by Argyris et al. [14]. Results indicated as BO-1 and BO-2 are for water molecules found within a hydration layer centered at 2.15 and 3.05 Å from the flat surface, respectively.

3.3.6. Hydrogen bond network: Dynamical properties

We assessed the average lifetime of HBs as a function of the position within the cylindrical pore by calculating the HB autocorrelation function, defined as Equation 3.5 [130]:

$$C_{HB}(t) = \frac{< h(t)h(0) >}{< h(0)h(0) >} \quad (3.5)$$

In Equation 3.5 the variable $h(0)$ equals 1 when a HB is found at time $t = 0$. If the tagged HB remains formed as the time t progresses, then $h(t)$ remains equal to 1. The quantity $h(t)$ switches to 0 when the HB breaks, and it remains 0 afterward. The results presented in **Figure 3.10** are averages of 5 calculations. It was found that changing the amount of propane has little effect on the results obtained for confined water. Only one data set is shown for clarity. They show that the HB autocorrelation function for water molecules in layer I decays more slowly at short time intervals than that obtained for water molecules in layer II. This indicates that the water–water HBs near the pore surface remain intact longer compared to those further from the surface.

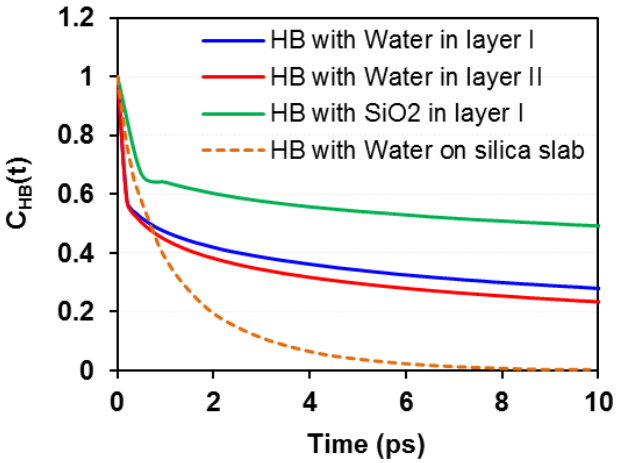

Figure 3.10. Hydrogen bond–hydrogen bond autocorrelation function for water molecules found within layer I and layer II in the cylindrical pores considered here (solid lines). These results were obtained for a system composed of 21 propane and 373 water molecules. The dashed orange line corresponds to hydrogen bond–hydrogen bond autocorrelation function of hydrogen bonds formed between water molecules on the partially hydroxylated slab pore surface with a total surface density of 6.8 −OH/nm^2 reported by Argyris et al. [127].

Similarly, we found a significantly slow decay for the HBs established between water and surface silanol groups (within layer I). This result suggests that water molecules in layer I prefer to form stable HBs with the pore surface rather than with other water molecules. This is expected when considering that interfacial water molecules show slower $C_R(t)$ and rotational diffusion when compared to those further from the pore surface, as discussed above. The results for HB–HB autocorrelation function of the HBs formed between water molecules near a crystalline flat substrate reported previously by Argyris et al. [127] are also

shown in **Figure 3.10**. Consistent with the dynamical results obtained so far, our data suggest that water–water HBs last longer when water is near the cylindrical pore surface than near the flat substrate. Because the density of −OH groups is much larger on the crystalline substrate considered by Argyris et al. than it is for the cylindrical pore considered here, it seems that the cylindrical pore geometry has a stronger effect on these autocorrelation functions than the density of −OH groups.

3.3.7. Effect of H_2O loading on transport of confined propane

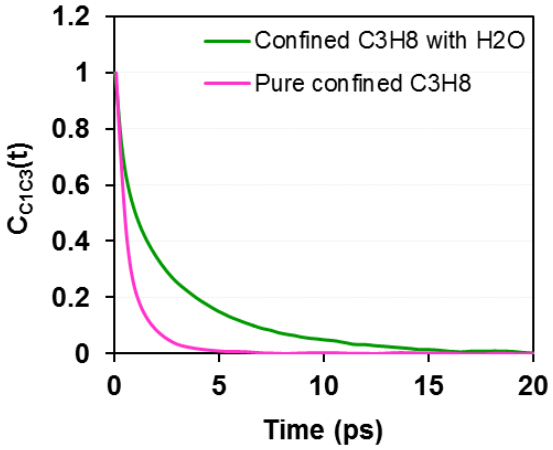

Figure 3.11. CH_3–CH_3 vector autocorrelation functions for propane molecules. When only propane is present, 45 molecules are considered, while when the pore is hydrated we considered 11 propane molecules and 387 water molecules.

Both dynamical and structural features used to quantify the properties of confined fluids suggest the formation of a stable, packed hydration layer (radial distance > 6.8 Å), with a more diffuse and perhaps sparsely filled region of water near the center of the pore. Our results suggest that propane molecules accumulate in this region, near the center of the pore, where water molecules can be depleted. The results for the transport properties of confined propane (see **Table 3.3**) suggest that the translational diffusion is much slower in the hydrated pores than in pores filled only by propane. In **Figure 3.11** we compare the CH_3–CH_3 autocorrelation function for propane calculated when propane is the only fluid in the pores, and when water is also present. The results suggest a significant difference between the rotational diffusion of confined propane. The time required for the CH_3–CH_3 vector autocorrelation function to decay from 1 to 1/e in the hydrated pore is ∼3 times longer than that obtained in the dry pore. It is perhaps interesting to point out that this delay in the rotation of propane molecules is not due to its interactions with the solid matrix, but rather to its interactions with water molecules found within the pore.

The results presented so far suggest that the transport properties of confined propane are controlled by the large number of water molecules present in the pore. To test this hypothesis, we assessed the effect of water loading. We calculated atomic density profiles and self-diffusion coefficients for both water and propane for systems in which the propane loading was maintained constant and the amount of water was reduced. The atomic density profiles are shown in **Figure 3.12**. In each simulation, water density profiles show that water always accumulates near the silica substrate, yielding a hydration layer consistent with layer I in the analysis above. The peak density for water within the hydration layer decreases as the water content is reduced. In other words, as more water fills the pore, the first hydration layer builds up. At low hydration levels, almost no water molecules are found near the pore center. In all cases, the density profiles for propane accumulate near the pore center, suggesting that reducing H_2O loading does not promote the adsorption of propane on the silica surface at least for the systems considered here. This was expected, given the low amount of propane, the large amount of water, and the preferential interactions between the silanol surface groups and the water molecules.

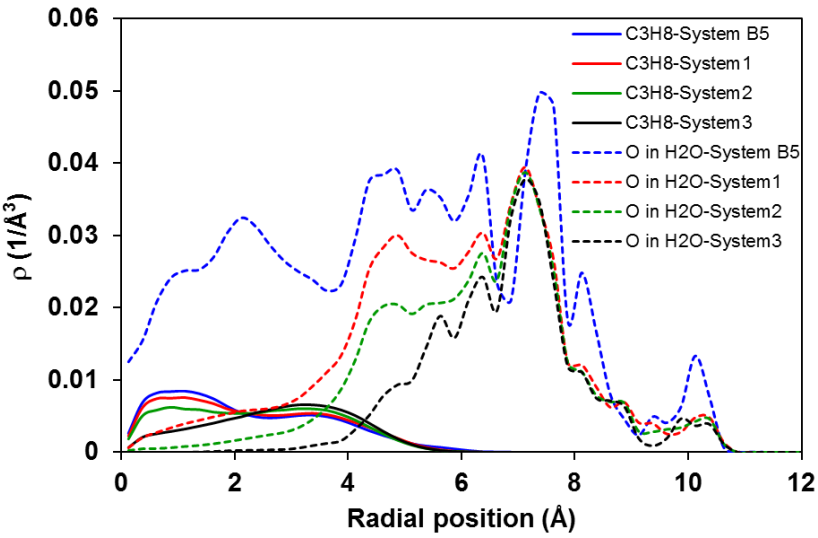

Figure 3.12. Radial density profiles of molecules confined within the amorphous cylindrical silica pore. Systems 1, 2, and 3 contain 321, 271, and 221 water molecules, respectively. In all cases, the number of propane molecules is kept constant at 22.

We report in **Table 3.4** the one-dimensional self-diffusion coefficients for the systems considered in **Figure 3.12**. We computed the self-diffusion coefficients for only those water molecules found in the middle region of the pore (radial distance < 6 Å), since the water molecules in the hydration layer form stable HBs with the surface.

Table 3.4. 1D self-diffusion coefficient estimated for confined fluids in silica pores for four systems with different water loading

System	System composition	Self-diffusion coefficient (10^{-10} m^2/s)	
		C_3H_8	H_2O
B5	22 C_3H_8–371 H_2O	1.8 ± 0.1	1.55 ± 0.05
1	22 C_3H_8–321 H_2O	8.7 ± 0.1	2.0 ± 0.1
2	22 C_3H_8–271 H_2O	27.9 ± 0.5	1.48 ± 0.13
3	22 C_3H_8–221 H_2O	64.2 ± 0.8	0.6 ± 0.1

The self-diffusion coefficient of confined propane was found to decrease as the water loading increases; conversely, the self-diffusion coefficient of confined water was found to increase, reach a maximum, and then decrease. Analysis of sequences of simulation snapshots confirms that the reduced propane diffusion is due to the formation of "molecular bridges" formed by water molecules across the silica pore, which hinder the free flow of propane transport. In **Figure 3.13** we report a snapshot for such a molecular bridge.

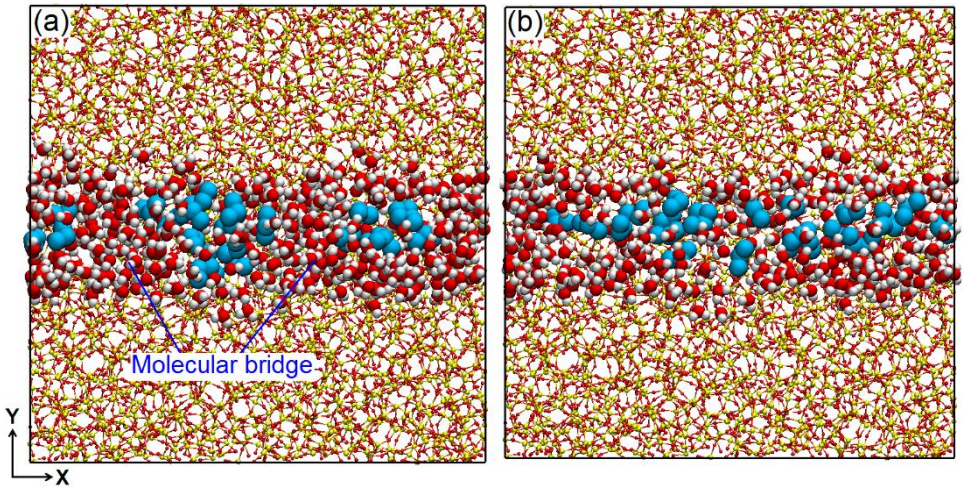

Figure 3.13. Simulation snapshots representing the flow patterns of water molecules across the pores. Panel (a) shows bridges of water molecules formed within the pore filled 22 propane molecules and 371 water molecules. Panel (b) shows the dissolution of the molecular bridges within the pore filled with 22 propane and 271 water molecules.

For the systems considered in **Table 3.4**, the molecular bridges are not present when 321 or fewer water molecules are present, but they form when 371 water molecules are simulated. Further, a decrease in self-diffusion coefficient of water as water loading decreases below 321 corroborates the formation of stable hydration layer near the pore surface as discussed above. The significant decrease in self-diffusion coefficient when water loading increases from 321 to 371 is therefore mostly due to the formation of water bridges, which hinder the

translational diffusion of water molecules found near the pore center. In fact, these molecules are now hydrogen-bonded to water molecules all around the cylindrical pore.

3.4. Conclusions

A series of atomistic molecular dynamics simulations were performed for systems composed of water and propane confined within cylindrical silica pores. The simulations were designed to study the effect of bulk pressure and water loading on the mobility of confined propane. The pressure was controlled by changing the amount of propane. The pore was a model amorphous cylindrical silica pore designed to resemble the pores in MCM-41 materials. All simulations were conducted at 300 K. The simulation results are quantified by analysis of the composition of the confined fluid systems, molecular density profiles in the radial direction, preferential orientations of the fluid molecules with respect to the pore, and both rotational and translational dynamical properties. Our results reveal that propane accumulates near the pore center, where water can be depleted. Conversely, water molecules tend to form hydrogen bonds with the silanol groups on the pore surface. We found that the self-diffusion coefficient of confined propane decreases as bulk pressure or water loading increase. The significant effect of water on the diffusion of confined propane is due to the formation of water bridges that span the pore volume, thus hindering propane transport. This observation provides molecular-level interpretation for recently reported experimental findings regarding mixtures containing propane and D_2O confined in MCM-41-S. The qualitative agreement between simulations and experiments contribute to our understanding of transport of hydrocarbons in subsurface environments.

Chapter 4. Structural and Dynamics Properties Predicted by Reactive Force Fields Simulations for Four Common Pure Fluids at Liquid and Gaseous Non-Reactive Conditions

The material presented in this Chapter was published in 2018 in volume 44, pages 826–839 of Molecular Simulation.

4.1. Introduction

Many classical (non-reactive) force fields have been developed to describe pure fluids and sometimes their mixtures. In these approaches, chemical bonds are defined at the beginning of a simulation and constrained throughout. Each of the successful classical force fields was developed to match selected properties. For example, the TraPPE force fields were developed with the goal of reproducing vapour–liquid coexistence properties with the objective of allowing researchers to 'transfer' the force fields to molecules with similar chemistry [110, 131-134]. While many thermodynamic and transport properties can be extracted from molecular simulations, arguably, the radial distribution function and the self-diffusion coefficients are fundamental properties that should be obtained reliably from a simulation. If this were not the case, estimating any thermodynamic and transport properties would not be straightforward.

While generally successful at predicting structural and transport properties of non-reactive systems, the classical models cannot describe systems undergoing chemical reactions in a molecular dynamics simulation. Reactive force fields have been developed for this purpose. The ReaxFF inventory of reactive force fields is attracting particular attention [37, 38]. ReaxFF potentials provide an atomistic description of chemical reactions by allowing the formation and dissociation of chemical bonds. In addition, ReaxFF describes van der Waals and Coulombs interactions, thus comprehensively describing physical interactions in molecular systems. The force field parameters are typically optimised against a training set obtained from quantum mechanical calculations. ReaxFF parameter sets have been developed to accurately predict the characteristics and evolution of complex reactive systems such as the

oxidation of hydrocarbons [39], the catalytic formation of nanotubes [135], surface catalytic chemistry [136, 137], and even electrochemical mechanisms [56, 138]. Senftle et al. [37] recently reviewed the historical development of the ReaxFF approach. After the initial attempts to study reactive systems, now several parameterisations are available. Because we are interested in using the ReaxFF formalism to test the recent predictions regarding the effect of confinement on the equilibrium composition of the CO_2 methanation reaction [34], we are particularly interested in the ReaxFF force fields developed to study combustion [39]. This parameterisation is indicated as 'combustion' in what follows. However, we found that to simulate water it is preferable to implement the 'aqueous' ReaxFF parameterisation [139], which is indicated as 'aqueous' in what follows. Raju et al. [139] adapted the aqueous parameterisation to study water adsorption on titania, showing that mixed molecular and dissociative adsorption occurs, and suggesting that water molecules in the second adsorbed layer affect the equilibrium structure of adsorbed water. This is the parameterisation we implement, even though no titania surface is present in our systems. Raju et al. [139] showed that the 'aqueous' parameterisation yields radial distribution function and self-diffusion coefficient for bulk liquid water in excellent agreement with experimental data at 298 K.

Because of the ReaxFF success, attempts have been made to implement it to study structural, transport, and reactive properties of a fluid system, all within a single simulation. For example, Huang et al. [140] simulated water on various TiO_2 surfaces, on which they studied the formation of hydrogen bonds, the layering of interfacial water, and the surface reactivity. The results demonstrated that TiO_2 surfaces display different surface reactivity toward water dissociation. However, because the ReaxFF parameters are derived from quantum mechanical calculations, and have the clear objective of describing bond-forming and bond-breaking, one might not expect a priory that structural and transport properties are reproduced satisfactorily. This should not be surprising. For example, significant deviations are sometimes observed among results obtained for the same fluid at the same thermodynamic conditions when different classical force fields are implemented. For instance, Aimoli et al. [141] compared the ability of seven CO_2 models (Cygan, elementary physical model (EPM2), Zhang, etc.,) and three CH_4 models (TraPPE, OPLS, SAFT-γ) to predict transport properties. Their results show that, e.g. the fully flexible models designated as Cygan and TraPPE-flex reproduce transport properties of CO_2 with accuracy comparable to that obtained with rigid models (Zhang, EPM2, etc.), but underestimate some thermodynamic properties. Among the three rigid three-site models considered, the one developed by Zhang provides the best

representation of CO_2. Within the models tested to describe CH_4, the OPLS model outperformed the single-site TraPPE model concerning viscosity and self-diffusion, whereas the single-site model provided the best estimation of thermodynamic properties and thermal conductivity.

Among the ReaxFF applications, Chenoweth et al. [39] derived parameters to describe gas-phase hydrocarbon oxidation (i.e. combustion). We identify these parameters as the 'combustion' ReaxFF in the remainder of this Chapter. The 'combustion' parameters were developed based on ReaxFF formalism for hydrocarbons [61], and they have been widely implemented by others. For instance, Page and Moghtaderi [142] investigated the chemical mechanism of low-temperature partial oxidation of methane. He et al. [143] combined the 'combustion' ReaxFF and density functional theory to study the intrinsic mechanism of methane explosion. They further combined the 'combustion' ReaxFF simulations with *ab initio* MD calculations with particular attention to the substantial effect of water addition at different reaction stages on gas explosions [144]. Cheng et al. [145] developed an approach to accelerate dynamics while describing the chemical reaction rates and mechanisms for large-scale complex reactions. The promising results of these studies suggest that the 'combustion' ReaxFF is a good candidate to study reactive events related to hydrocarbon compounds.

The goal of this Chapter is to determine whether the 'combustion' ReaxFF parameters are also able to reliably replicate structural and diffusion properties of the pure fluids, when they are not undergoing reactions. To test this, we selected four common pure fluids, CH_4, H_2O, CO_2 and H_2, which are the main components in the reactive systems studied employing the 'combustion' ReaxFF. We compare the properties predicted by simulations implementing models developed within the 'combustion' ReaxFF against those obtained when classical force fields are implemented instead. The criteria used to assess the suitability of the ReaxFF force fields to replicate the bulk properties of the pure fluids considered consist in the similarity between the results obtained from the two simulations (implementing classical or reactive force fields). When possible, the similarity between simulations and correspondent experimental data is also discussed. While data for the radial distribution functions for pure liquids are available, and used here, in the gas phase we use experimental second virial coefficient data.

In the remainder of this Chapter, we first provide an overview of the simulation approaches implemented, and a summary of the main features of the force fields chosen. We then

compare the results obtained, in terms of structure and dynamics of pure fluids, in the gas and liquid phases. We close with generalised observations.

4.2. Methods and algorithms

4.2.1. Molecular dynamics simulations

All of the molecular dynamics (MD) simulations were conducted using the large-scale atomic/molecular massively parallel simulator (LAMMPS) package, version 20160514 [146, 147]. All simulations were conducted at equilibrium conditions for the pure compounds. Below we provide details on the force fields implemented. It should be noted that in the present Chapter the ReaxFF force fields are not trained on DFT data-sets. We use parameters that were developed by others to study combustions and/or aqueous systems.

4.2.2. Reactive force field – ReaxFF

Although the conditions chosen for the simulated systems are such that no chemical reaction is expected to take place for CH_4, CO_2, H_2 and gaseous H_2O, in liquid water proton transfer can occur. Both the 'combustion' and 'aqueous' ReaxFF models yield a system composition in which H_3O^+ molecules are ~0.5% of the H_2O molecules. Several other species are also identified in these simulations, with a combined concentration of up to 8% of the water molecules in the simulations.

4.2.3. Classical force fields – TraPPE, OPLS, EPM2, Zhang, SPC, SPC/E, frost

Several non-reactive force fields were implemented for comparison. The total potential energy in these simulations is determined by the sum of energy terms including short-range pairwise interactions, Coulombic long-range interactions, bond stretch, and angle bending terms [148]. The dispersive interactions are described using Lennard-Jones – type potentials. Whereas the ReaxFF uses all-atom structures to simulate various compounds, conventional force fields use molecular models with different morphologies and number of sites. We selected a few force fields to perform our comparison. The parameters of various non-reactive force fields used to conduct simulations are summarised in **Table 4.1**.

A large number of models have been proposed to calculate thermodynamic properties for methane and carbon dioxide in an extended range of state conditions. Based on the results reported by Aimoli et al. [141], we chose the TraPPE single-site model [110] and the fully

flexible five-site OPLS model [149] for CH_4 simulations. We implemented the rigid three-site models EPM2 [150], TraPPE [151], and the model proposed by Zhang [152] for CO_2.

Table 4.1. Force field parameters implemented in the classical simulations described in this Chapter. Dispersive interactions are described by 12-6 Lennard-Jones (LJ) potentials, while electrostatic interactions are described by Coulombic potentials

Force field	Site	σ (nm)	ε (kJ/mol)	q (e)
TraPPE-UA [110]	CH_4	0.3730	1.23054	0
OPLS [149]	C	0.3500	0.27614	–0.24
	H	0.2500	0.12552	0.06
EPM2 [150]	C	0.2757	0.23388	0.6512
	O	0.3033	0.66937	–0.3256
TraPPE-CO_2 [151]	C	0.2800	0.22449	0.70
	O	0.3050	0.65684	–0.35
Zhang [152]	C	0.27918	0.23983	0.5888
	O	0.3000	0.68724	–0.2944
SPC/E [108]	O	0.3166	0.65020	–0.8476
	H	0.0000	0.00000	0.4238
SPC [153]	O	0.3166	0.65020	–0.8200
	H	0.0000	0.00000	0.4100
Frost et al. [154]	H_2	0.2958	0.30764	0

Many models have been proposed for water [108, 153, 155-158]. Vega et al. [159] reported the TIP4P/ice model yields the best description for densities of all ice phases whereas SPC/E, TIP4P, TIP4P/Ew and TIP5P models overestimate experimental ice densities. These authors also reported that TIP4P model reproduces the phase diagram of water better than SPC/E and TIP5P models. Vega et al. [160] compared several water models (the transferable intermolecular potential three-point model (TIP3P), the TIP four-point model (TIP4P), the TIP five-point model (TIP5P) and the TIP four-point model in its 2005 derivation (TIP4P/2005)) to assess their ability to predict ten different water properties (vapor-liquid equilibrium, critical temperature, surface tension, etc.). They concluded that the TIP5P/2005 is the model that best reproduces experimental data, except for the dielectric constant. While the TIP5P model does not seem adequate to describe reliably the water phase diagram, critical point, density of ices and water behaviour at high pressure, it does predict the melting point, the dielectric constant, diffusivity and the maximum in the density of liquid water at room pressure better than the TIP4P model. The rigid nonpolarizable SPC/E model for water [108] was developed to reproduce reliably the radial distribution function of bulk liquid water at 298 K as obtained by Soper et al. [161] using neutron scattering. Because the SPC/E has been used in many prior publications, and because it yields an excellent structure for liquid

water, we chose this model to simulate water in the present Chapter. The SPC/E model also provides acceptable estimates for the internal energy, the density and the diffusivity for water at ambient conditions [109]. The SPC rigid model [153] was chosen to simulate gas-phase water, because it reproduces the thermodynamic properties of supercritical water [162, 163].

A wide variety of classical force fields are available to describe hydrogen [154, 164-168]. In this Chapter, the model reported by Frost et al. [154] was implemented. In this model the Lennard-Jones parameters for the hydrogen molecule are extracted from experimental data [169]. This model consists of a LJ neutral sphere, which is computationally efficient.

4.2.4. Algorithms

The simulations are conducted within the canonical ensemble (constant number of molecules, constant volume and constant temperature), unless otherwise specified. Transport and structural features are determined following the Einstein relation [117] for the self-diffusion coefficients, and radial distribution functions for structural properties, respectively. In the gas phase, we extracted the second virial coefficients from the radial distribution functions obtained for the pure compounds [170]. Experimental second virial coefficients are available. All simulations using single-site, flexible and rigid models were performed implementing the Nosé-Hoover thermostat with a fixed temperature-damping factor of 100 fs. The velocity-Verlet algorithm was used to integrate all molecular dynamics equations of motion. Each simulation was performed within periodic boundary conditions in a cubic box.

Table 4.2. Thermodynamic conditions, number of molecules simulated, density and time step for each of the system investigated in this work

Fluid	P_c (MPa)	T_c (K)	ρ_c (g/l)	Temperature (K)	Molecules simulated	Density (g/l)	Time step (fs)
CH_4	4.5992[a]	190.55[a]	162.6[a]	150	440	449	0.25
				298	216	0.66	0.1
CO_2	7.38[b]	304.18[b]	468[b]	240	400	1,089	0.5
				273	500	1,105	0.5
				298	100	1.8	0.1
H_2O	22.064[c]	647.14[c]	322[c]	298	550	1,000	0.25
				298	421	1,440	0.25
				500	100	2.2	0.1
H_2	1.3[d]	33.2[d]	31.3[d]	15.2	500	76	0.1
				77.5	100	0.3	0.1

T_c, P_c and ρ_c are experimental critical temperature, pressure and density, respectively.

[a]Ref. [171]; [b]Ref. [172]; [c]Ref. [173]; [d]Ref. [174]

The temperatures, number of molecules, density and time steps used in the simulations are given in **Table 4.2**. The force field parameters implemented here for the various non-reactive simulations are reported in **Table 4.3**. In the case of ReaxFF simulations, several parameters are necessary to describe bond length and bond angle, as for example corrections due to bond order and hybridisation are included. These parameters are not reported here for brevity (for details, please refer to Appendix A). Note that the time step implemented was different for each simulation. We ensured that the time step was adequate for the ReaxFF simulations, and we then employed the same time step in the corresponding non-reactive simulations. The cut-off distance of interatomic interactions for all simulations using classical force fields was fixed at 14 Å. The particle mesh Ewald (PME) [111] method was used to treat the long-range Columbic interactions. The Lorentz-Berthelot mixing rule is applied to determine the Lennard-Jones parameters for unlike interaction from values of like components [112].

Table 4.3. Force fields parameters (bond lengths and angles) for the non-reactive force fields as implemented in this work

Model	Bond length, Å				Angle, deg		
	C–H	C=O	O–H	H–H	H–C–H	O=C=O	H–O–H
TraPPE		1.161				180	
Zhang		1.163				180	
EPM2		1.149				180	
OPLS	1.09				107.8		
SPC/E			1.0				109.47
SPC			1.0				109.47

We used a 0.3 bond order cut-off for simulations implementing the 'combustion' ReaxFF. The system temperature, total energy and structural properties oscillated around a constant value after 5 and 10 ns for liquid- and gas-phase simulations, respectively. These lengths of simulations (5 and 10 ns) were, therefore, considered adequate equilibration periods. For comparison, when water was simulated on titania using the 'aqueous' ReaxFF parameterisation, 0.1 ns were considered sufficient to equilibrate the systems [139]. After equilibration, a production run of 1 ns was conducted here to obtain averages for data analysis. During the production phase all atomic coordinates were recorded very 100 time steps.

The radial distribution function (or pair correlation function) is a probability distribution function that describes how density varies with the radial distance from a reference particle. It is widely used to describe the structure of a system, e.g. fluids and solid. The radial distribution function g(r) of a system of N molecules in volume V is defined by Equation 4.1:

$$g(r) = \frac{\langle \rho(r) \rangle}{\rho} \tag{4.1}$$

where ρ(r) is the local density at a distance r from the central atom $\rho(r) = n(r)/4\pi r^2 dr$, ρ is the system average bulk density $\rho = N/V$. The probability to find the mean number of atoms n(r) in a shell dr at the distance r from an atom chosen as a reference point is shown in **Figure 4.1**.

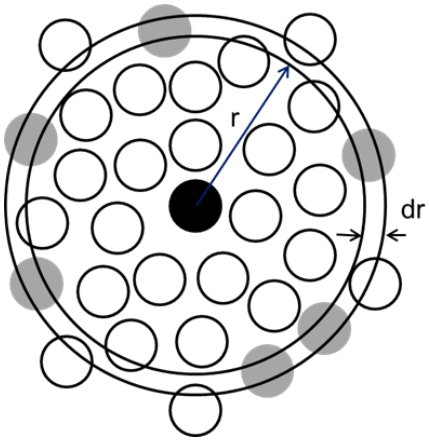

Figure 4.1. The evaluation of the radial distribution function in a molecular system.

4.3. Results

4.3.1. Structure

Intermolecular pair correlation functions were obtained for CH_4, CO_2, H_2 and H_2O at liquid and gaseous conditions. The data obtained from the ReaxFF simulations are compared against those obtained, at the same thermodynamic conditions, using well-known classical non-reactive models. Below is a summary of our findings, which is followed by an analysis of the second virial coefficients obtained from our simulations in the gas phase.

4.3.1.1. Methane

The radial distribution functions, g_{CC}, g_{CH} and g_{HH} are shown in **Figure 4.2**. Note that the TraPPE force field does not take into account the H atoms of CH_4, and therefore g_{CH} and g_{HH} cannot be computed for this model.

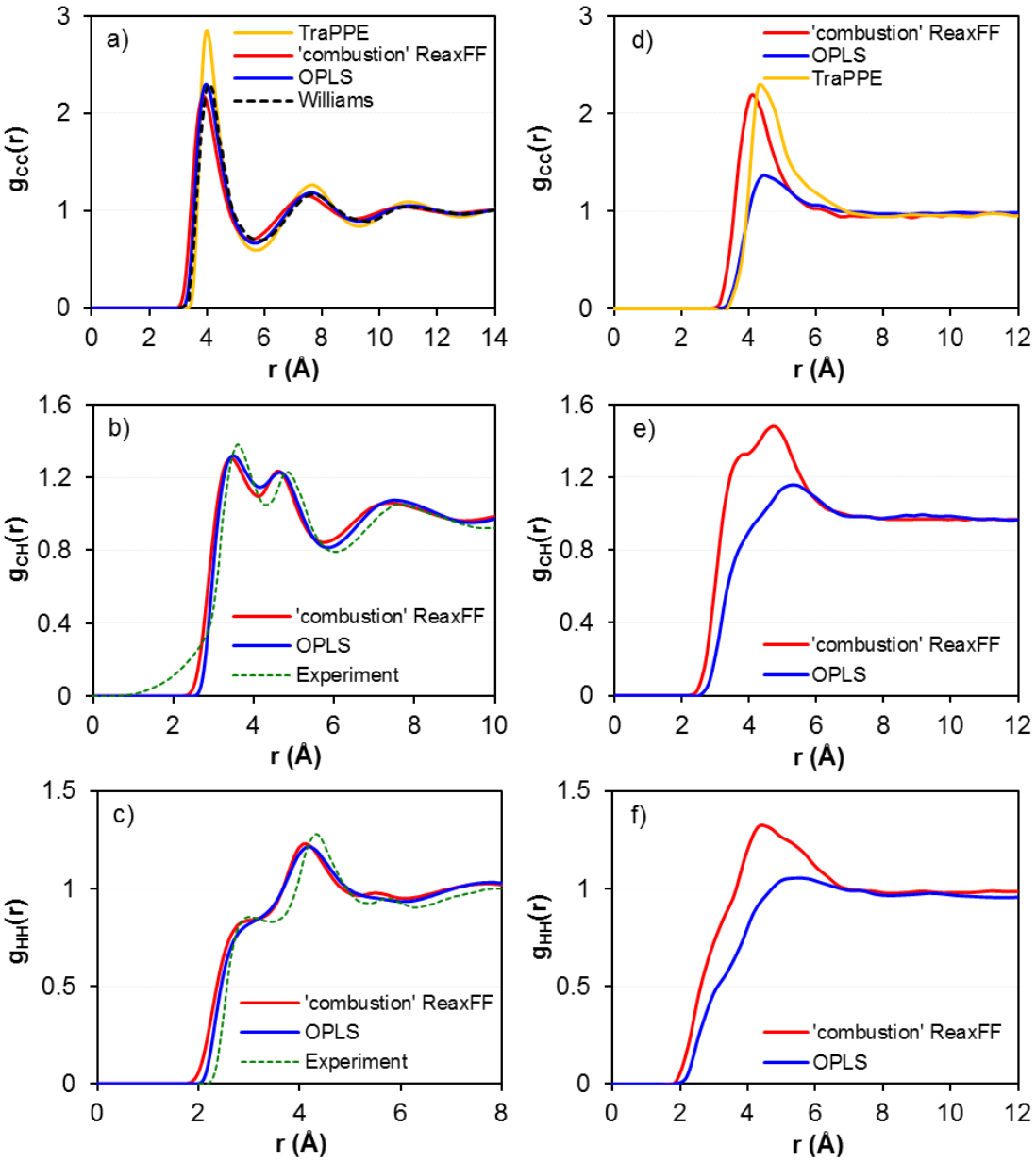

Figure 4.2. Site-site radial distribution functions for CH_4 at 150 K and ρ = 449 g/l (a, b and c), and at 298 K and ρ = 0.66 g/l (d, e and f). Note that the TraPPE force field is united atom, and as such it does not differentiate the H atoms in CH_4.

The pair distribution functions are compared to those considered by Stassen as representative of experimental data [175]. Stassen conducted classical molecular dynamics simulations for liquid methane, although he employed parameters extracted from reverse Monte Carlo to reproduce neutron diffraction data for dense CD_4 [176]. Considering liquid methane at 150 K [**Figure 4.2**(**a**–**c**)], our results show that implementing the 'combustion' ReaxFF yields peaks at shorter distances compared to what is predicted by the TraPPE and OPLS models, and also

compared to experimental data. In addition, the heights of peaks obtained with the 'combustion' ReaxFF are relatively similar to the corresponding ones obtained using OPLS.

The main features of $g_{CC}(r)$ are listed in **Table 4.4** for all models. Although not shown in **Figure 4.2a**, the peak positions and heights of an experimental $g_{CC}(r)$ are included in **Table 4.4**. The $g_{CC}(r)$ obtained for dense fluid methane [177] implementing the site–site exponential-6 model proposed by Williams [178] is illustrated in **Figure 4.2a**. The exponential-6 potential of Williams has been demonstrated to be a good model for predicting the structure of liquid methane [176]. The first minimum in g_{CC} for the 'combustion' ReaxFF appears at ~5.5 Å, which is shifted by ~0.2–0.3 Å towards smaller distances than all the models as well as experiment. The number of neighbours, as estimated by the equation $n = 4\pi \int_0^{r_m} r^2 g(r)\rho dr$, where r_m is the first minimum of $g_{CC}(r)$, is 11.8 for the 'combustion' ReaxFF compared to ~13 from both OPLS and TraPPE simulations and ~12.3 Å from Williams model and experiment.

Table 4.4. Maxima and minima positions and heights of the carbon-carbon pair distribution functions $g_{CC}(r)$ of liquid methane with the investigated potential models. Corresponding plots are shown in **Figure 4.2a**

Model	1st Max	1st Min	2nd Max	2nd Min	3rd Max
'Combustion' ReaxFF	3.9/2.17	5.5/0.70	7.4/1.15	9.1/0.91	10.8/1.04
OPLS	4.0/2.30	5.7/0.67	7.6/1.18	9.3/0.90	11.0/1.05
TraPPE	4.0/2.84	5.7/0.60	7.7/1.26	9.3/0.84	11.0/1.09
Exp-6[a]	4.1/2.35	5.8/0.63	7.7/1.17	9.5/0.85	11.3/1.05
Exp[b]	4.1/2.13	5.8/0.65	7.9/1.13	9.5/0.87	

[a]The simulation results for the exponential-6 model were taken from Table 3 (model H) from Stassen [175]

[b]Data from Stasse [175], as obtained from a potential model adjusted to reproduce experimental neutron diffraction data for CD_4.

The site–site pair distribution functions $g_{CH}(r)$ for 'experimental potential', 'combustion' ReaxFF, and OPLS model shown in **Figure 4.2b** suggest that the first peak contains two maxima separated by the first minimum. Although the shapes of g_{CC} (**Figure 4.2a**) and g_{CH} peaks (**Figure 4.2b**) are in close agreement among all the force fields, the 'combustion' ReaxFF yields a slightly different structure for g_{HH} as compared to OPLS (**Figure 4.2c**). In particular, a shoulder following the first peak is well formed from the 'combustion' ReaxFF and experimental potential, but it is absent from the OPLS model results.

The observed differences are much more pronounced in the gas phase, which are illustrated in **Figure 4.2**(**d**–**f**). The 'combustion' ReaxFF peaks are shifted to shorter distances compared to data obtained from either TraPPE or OPLS models. In general, the magnitude of the g_{CC}, g_{CH} and g_{HH} peaks observed with the 'combustion' ReaxFF is larger than that of the equivalent peaks obtained implementing the OPLS model, and smaller than that of the TraPPE model (TraPPE simulations are only available for g_{CC}). Moreover, there is a small hump at around 3.7 Å in ReaxFF g_{CH} (r), which is absent in the OPLS data-set. Unfortunately, we could not find experimental data to directly compare the simulation results for gaseous CH_4 at the conditions chosen here.

4.3.1.2. Carbon dioxide

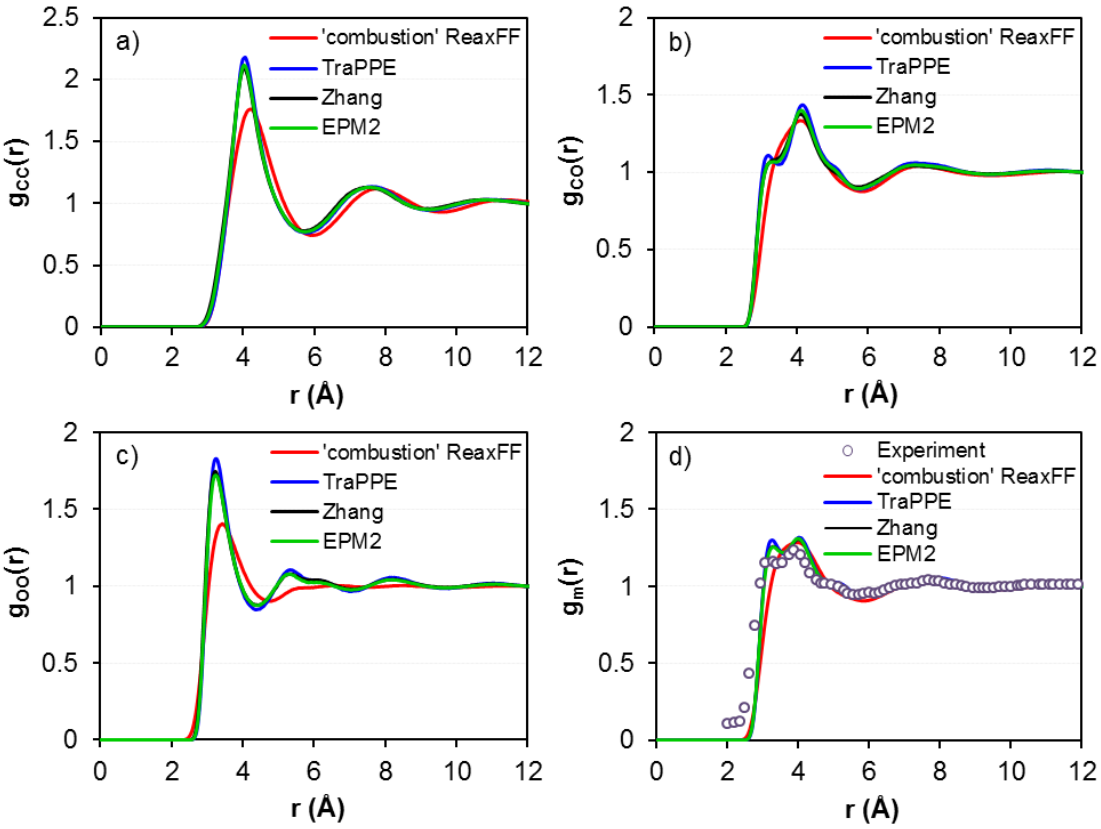

Figure 4.3. Site–site radial distribution functions (a, b and c) and neutron weighted radial distribution functions for CO_2 at 240 K and ρ = 1,089 g/l.

Radial distribution functions obtained for CO_2 are shown in **Figure 4.3** and **Figure 4.4**. The results for liquid CO_2 (**Figure 4.3**) show that the g_{CC}(r) peaks from 'combustion' ReaxFF simulations are shifted to slightly larger distances by about 0.2 Å compared to data obtained implementing classical force fields. The height of the first 'combustion' ReaxFF peak is lower, whereas the second and the third peaks are similar to those obtained by implementing

the Zhang, EPM2 and TraPPE force fields. The number of molecules within the first-neighbour shell is ~13 for the 'combustion' ReaxFF, as opposed to ~12 for the other three classical force fields.

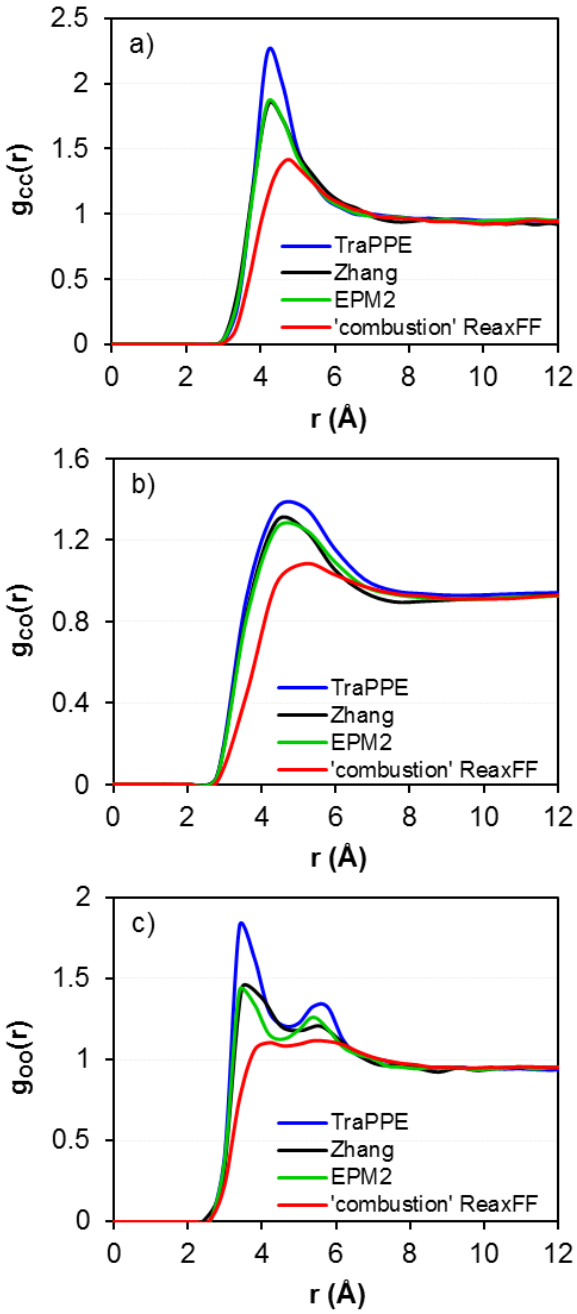

Figure 4.4. Site-site radial distribution functions for CO_2 at 298 K and ρ = 1.8 g/l.

Data for $g_{CO}(r)$ are considerably different when the 'combustion' ReaxFF is compared to the classical force fields wherein the first 'combustion' ReaxFF $g_{CO}(r)$ peak is a singlet, whereas the classical force fields yield a peak at ~3.2 Å as well as one at ~4.1 Å. Also note that the 'combustion' ReaxFF yields a second $g_{CO}(r)$ peak weaker and shifted to slightly larger

distances compared to that computed using classical force fields. Regarding $g_{OO}(r)$, the 'combustion' ReaxFF yields a somewhat broader first peak shifted to slightly larger distances than the corresponding classical simulations results. It should also be noted that the local structure beyond the first peak is missing in the 'combustion' ReaxFF $g_{OO}(r)$.

To compare the simulated liquid structure of CO_2 against experiments, the sum of three radial distribution functions as neutron-weighted distribution function $g_m(r)$ was computed [179]:

$$g_m(r) = 0.403g_{OO}(r) + 0.464g_{CO}(r) + 0.133g_{CC}(r) \quad (4.2)$$

As shown in **Figure 4.3d**, a split of the first peak is observed in the neutron-weighted distribution function obtained from classical models, which qualitatively reproduces the experimental data. This feature almost disappears from the simulation data extracted from the reactive simulations conducted with the 'combustion' ReaxFF parameters.

The characteristics of the site–site pair distribution functions for gaseous CO_2 at 298 K are displayed in **Figure 4.4.** All the $g_{CC}(r)$ from classical models produce a single peak at ~4.2 Å. The single peak obtained from the 'combustion' ReaxFF simulations has lower intensity and is shifted by about 0.5 Å to longer distances. The g_{CO} peak obtained from the 'combustion' ReaxFF appears at larger distances and it is broader than the equivalent peaks obtained implementing TraPPE, Zhang and EPM2 models. With respect to $g_{OO}(r)$, the 'combustion' ReaxFF yields two broad peaks at 4.2 Å and 5.8 Å, which differ in both intensity and location compared with the two correspondent peaks predicted by classical models.

4.3.1.3. Water

We observed an unrealistic phase separation when implementing the 'combustion' ReaxFF to simulate liquid water at ambient conditions. Therefore, we concluded that the 'combustion' ReaxFF parameterisation is not adequate to simulate liquid water at ambient conditions, at least without further training of the parameters. Additional simulations were conducted under the NPT ensemble to determine the density of liquid water at ambient conditions according to the 'combustion' ReaxFF force field. In these simulations, temperature and pressure were controlled by implementing the Nosé-Hoover thermostat and barostat, respectively. The density of ~1,400 g/l was obtained, and used for subsequent simulations for liquid water within the NVT ensemble even though this density is clearly unrealistic. The structure of liquid water estimated using the 'combustion' ReaxFF was then compared to that obtained

from classical simulations that implement the SPC/E model. The results are presented below for completeness.

In **Figure 4.5**, we show g_{OO}, g_{OH} and g_{HH} radial distribution functions determined from 'combustion' ReaxFF simulations and SPC/E or SPC (liquid and gaseous water, respectively). The shapes and peak positions of all intermolecular pair correlation functions from 'combustion' ReaxFF simulations are quite different compared to those predicted by the classical force fields, which is in part due to the higher density at which some of these simulations were conducted compared to that expected for bulk liquid water. We conclude that the 'combustion' ReaxFF is not appropriate for predicting the structural properties of liquid water. Even the gas-phase simulations showed significant aggregation of water when the 'combustion' ReaxFF model was implemented, which yields very pronounced peaks in the radial distribution functions considered.

As described by Senftle et al. [37], the combustion parameterisation was developed to study hydrocarbon oxidation, while the aqueous parameterisation was developed to study aqueous systems. We refer here to the latter ReaxFF parameterisation as 'aqueous', and we implement the parameters developed by Monti et al. [58]. The results from the 'aqueous' ReaxFF parameterisation are in excellent agreement with those obtained from the classical force fields for both liquid and gaseous phases. They are also in reasonable agreement with experimental data, as shown in **Figure 4.5**. Considering liquid water, both SPC/E model and the 'aqueous' ReaxFF yield almost the same positions and magnitudes for the first and the third peaks in g_{OO}(r), both of which are in good agreement with experiments. The second peak for the 'aqueous' ReaxFF is shifted by about 0.2 Å towards smaller distance compared to data obtained from both SPC/E simulations and experiment.

The results for g_{OH}(r) are related to the structure of the hydrogen bond network formed by neighbouring water molecules. The first peak from both SPC/E and 'aqueous' ReaxFF simulations for liquid water appears at ~1.8 Å, and the second peak appears at ~3.3 Å for both 'aqueous' ReaxFF and SPC/E simulations. The positions and most of the magnitudes of all the g_{OH} peaks obtained from both 'aqueous' ReaxFF and SPC/E simulations are in agreement with experimental g_{OH} peaks. A pronounced difference is however found in the magnitude of the first peak. Integrating the radial distribution functions, we calculated that approximately 2 hydrogen atoms are found at a distance lower than ~2.4 Å from each oxygen atom for both SPC/E and 'aqueous' ReaxFF simulations.

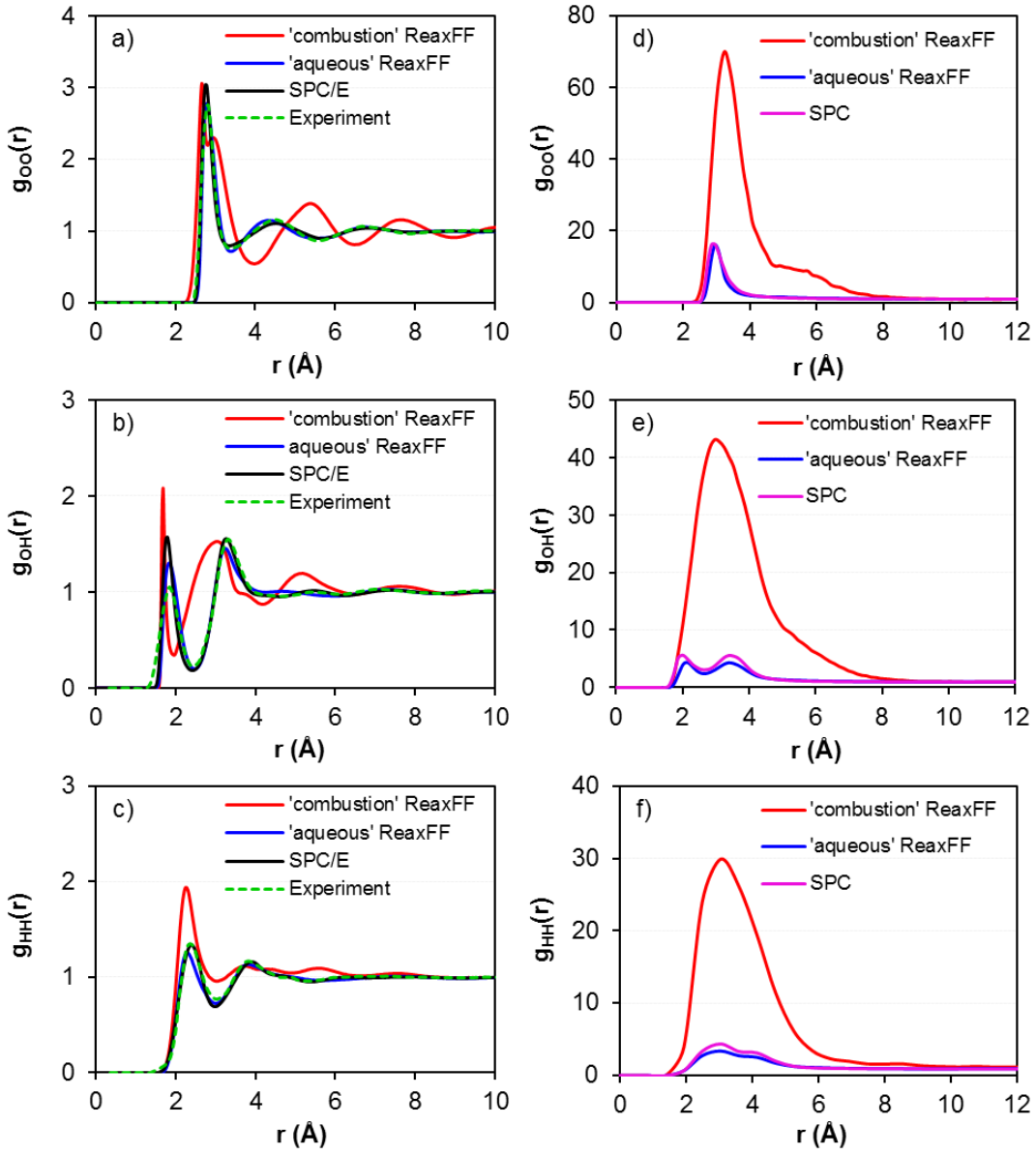

Figure 4.5. Site–site radial distribution functions for H_2O at 298 K (a, b and c), and at 500 K (d, e and f). Notes: The density for 'combustion' ReaxFF simulations in panels (a), (b) and (c) is of 1,440 g/l, and of 2.2 g/l in panels (d), (e) and (f). All other thermodynamic conditions are reported in **Table 4.2**. Neutron diffraction experimental data from Soper et al. [161] are also shown.

Two well-defined peaks in $g_{HH}(r)$ are found at ~2.4 Å and 3.8 Å for both 'aqueous' ReaxFF and SPC/E simulations that are in reasonable agreement with experiments, further suggesting that the 'aqueous' ReaxFF is suitable for describing the structure of liquid water.

Regarding water vapour, our simulation results, **Figure 4.5**(**d**–**f**), further confirm that the 'combustion' ReaxFF parameterisation is inadequate. On the other hand, our results suggest that the 'aqueous' ReaxFF parameterisation is in good agreement with SPC model. Peak

positions and heights of the $g_{OO}(r)$ obtained from both 'aqueous' ReaxFF and SPC simulations are similar. The $g_{HH}(r)$ and $g_{OH}(r)$ have almost identical peak positions for both force fields, albeit 'aqueous' ReaxFF simulations yield smaller intensities than classical simulations implementing the SPC model.

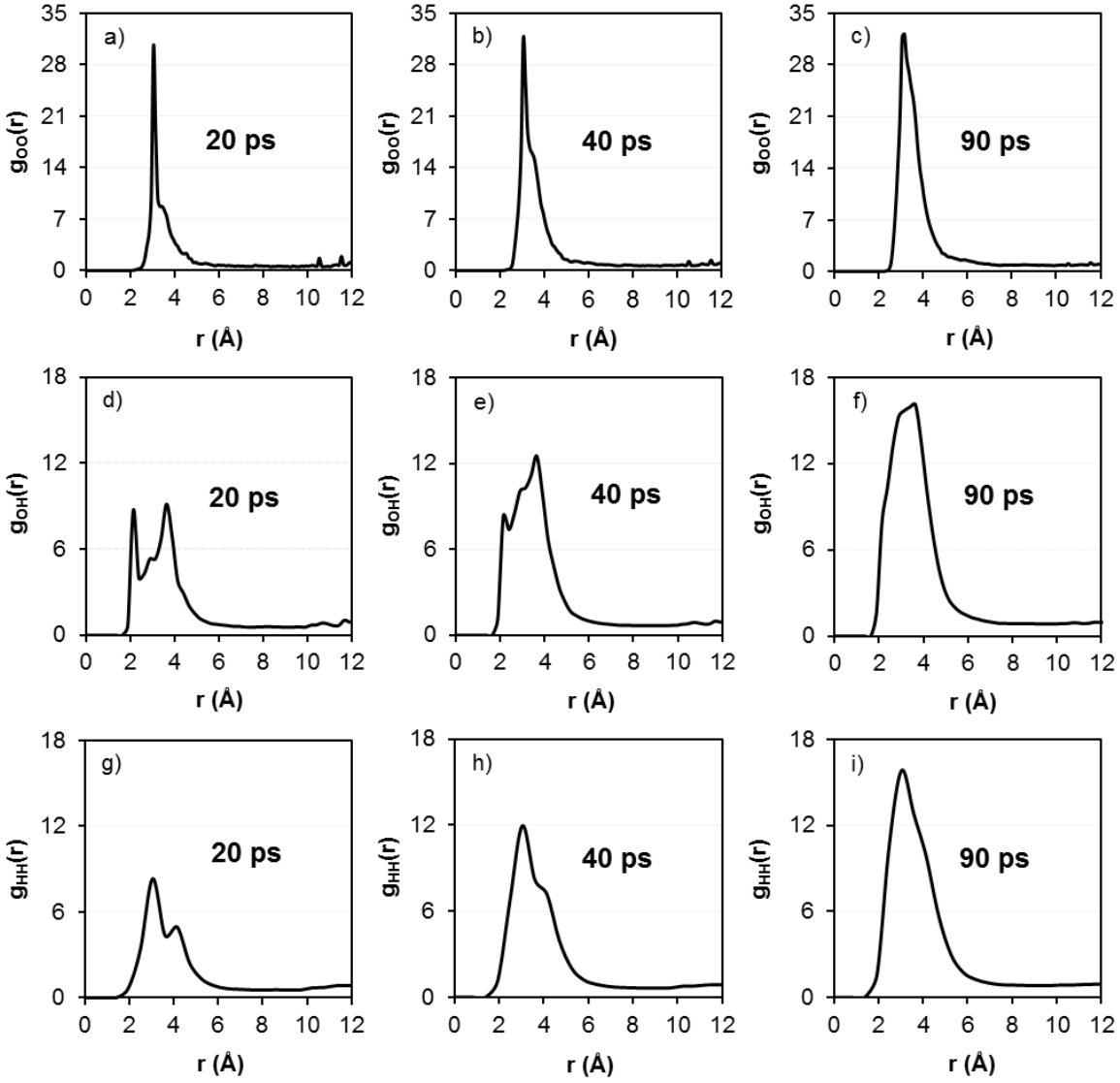

Figure 4.6. Site–site radial distribution functions of gas-phase water molecules as a function of time: $g_{OO}(r)$ (a–c), $g_{OH}(r)$ (d–f), and $g_{HH}(r)$ (g–i).

To investigate the reason why the 'combustion' ReaxFF parameterisation fails in describing the structure of water, the simulation results were analysed at various run times (see **Figure 4.6**). The first important observation is that the structure of water evolves during this analysis, hence equilibrium is not yet reached. This is perhaps not surprising, since these simulations are only 90 ps long, but it should be made clear to avoid confusion. It was found that although $g_{OO}(r)$ maintains the same shape over time (**Figure 4.6**(**a**–**c**)), $g_{OH}(r)$ and $g_{HH}(r)$

change over time. As seen in **Figure 4.6**(**d**–**f**), g_{OH}(r) displays two well-defined peaks, one at 2.1 Å and one at 3.6 Å, after 20 ps. The two peaks vanish after 40 ps, and merge after 90 ps. Similarly, during the initial 20 ps, g_{HH} (**Figure 4.6**(**g**–**i**)) yields two peaks (at 3.0 Å and at 4.1 Å). The second of these peaks is strongly reduced as the simulations progress. Although the 'combustion' ReaxFF seems able to yield a reasonable gas-phase water structure at short simulation times before equilibrium is achieved, after ~90 ps water molecules condense yielding a large cluster. This suggests that the attraction between 'combustion' ReaxFF water molecules in the gas phase is too strong.

4.3.1.4. Hydrogen

In the case of H_2, the 'combustion' ReaxFF parameterisation describes both atoms, while the classical force field is a united-atom approach. To compare the data, we consider the centre of mass of H_2, and we compute the resultant $g_{H2\text{-}H2}$ with the results shown in **Figure 4.7**. Regarding liquid H_2, the first peak position (~3.2 Å) is quite similar in both models, but the 'combustion' ReaxFF yields second, third and fourth peak positions at shorter distances and greater intensities compared to the non-reactive simulations. The number of H_2 first neighbours within the first minimum in the pair correlation function (at 4.4 Å) is ~8 for the 'combustion' ReaxFF. Classical simulations yield ~9.

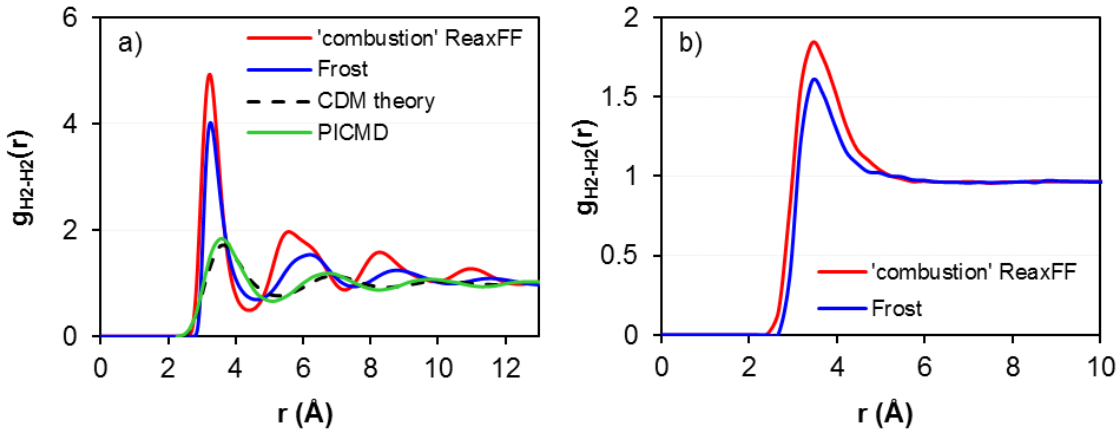

Figure 4.7. Site–site radial distribution functions for H_2 at 15.2 K and ρ = 76 g/l (a) and at 77.5 K and ρ = 0.3 g/l (b). Notes: The result of CDM theory reported by Lindenau et al. [180] was computed for liquid 'para-hydrogen' at 16 K and ρ = 0.021 Å^{-3}.

For comparison purposes, in lieu of experimental data for hydrogen, we used radial distribution functions of liquid 'para-hydrogen' as obtained from correlated density-matrix (CDM) theory [180] and the path-integral-centroid-molecular-dynamics (PICMD) approach [181]. These theoretical results are often considered as reference data for hydrogen. Our

results show a large difference in peaks positions and heights between both 'combustion' ReaxFF and classical simulations predictions and CDM or PICMD data for liquid hydrogen. It should be pointed out, however, that the Frost model was derived to study the gas phase of hydrogen, but it neglects quantum effects. It is likely that the difference between simulation results achieved when the Frost model or the 'combustion' ReaxFF models are implemented as opposed to predictions from the CDM or PICMD models are due to the fact that both CDM and PICMD methods incorporate quantum effects.

Both classical and reactive force fields exhibit a similar peak position at ~3.4 Å in the gas phase. However, the single peak predicted from the 'combustion' ReaxFF is slightly higher and broader than when implementing the model described by Frost et al. [154]. No difference is detected between the two force fields at distances larger than 6 Å.

4.3.2. Second virial coefficients

While it is problematic to directly compare the simulated radial distribution functions in the gas phase to experimental data, experimental data are available for the second virial coefficient, B_2, which is a fundamental thermodynamic quantity. Several approaches can be employed to calculate B_2 for either pure compounds or mixtures. The Mayer sampling method, based on free energy perturbation approaches [182], was implemented to calculate virial coefficients for a variety of potentials [183, 184]. B_2 for small alkanes and inert gases can be extracted from the simulated pair correlation functions [185, 186] or from analytic equations of state [187, 188]. Here, we integrate the radial distribution functions [170]:

$$\mathrm{B_2(T)} = -2\pi \int_0^\infty \mathrm{r^2[g(r) - 1]dr} \tag{4.3}$$

In Equation 4.3, r is the distance between the centres of mass of two molecules and g(r) is the radial distribution function. The second virial coefficients obtained from our simulations, as well as the corresponding experimental values, are reported in **Table 4.5**. In all cases, the results from ReaxFF simulations differ from those obtained using non-reactive force fields.

In the case of methane, the results suggest that the TraPPE force field yields too strong effective attractions compared to experimental observations (the more negative B_2 is, the more attractive the effective interactions are), while the OPLS force field is not attractive enough. The 'combustion' ReaxFF parameters yield an effective interaction between CH_4 molecules that is also too attractive compared to experiments. It is concluded that a

realistic g_{CC} would be in between that obtained for the OPLS and that obtained for the 'combustion' ReaxFF simulations.

In the case of CO_2, none of the simulation results are consistent with the experimental data. The TraPPE force fields are those that yield data in closest agreement with experiments, while all the others, including the 'combustion' ReaxFF, do not yield sufficiently attractive interactions between CO_2 molecules in the gas phase.

Table 4.5. Second virial coefficients for gas-phase molecules estimated from our simulations. For comparison, experimental data are also reported

Molecule	Temperature (K)	Force field	Second virial coefficient (cm^3/mol)	
			This study	Experiment
CH_4	298	TraPPE	–115 ± 14	–43.25[a]
		OPLS	–20 ± 6	
		'combustion' ReaxFF	–75 ± 5	
CO_2	298	TraPPE	–100 ± 20	–121.8[b]
		Zhang	–56 ± 17	
		EPM2	–70 ± 19	
		'combustion' ReaxFF	–16 ± 5	
H_2O	500	SPC	–390 ± 45	–171.97[c]
		'aqueous' ReaxFF	–235 ± 32	
		'combustion' ReaxFF	–5,600 ± 50	
H_2	77.5	Frost	–13 ± 6	–11.1[d]
		'combustion' ReaxFF	–25 ± 7	

[a]Ref. [189]; [b]Ref. [190]; [c]Ref. [191]; [d]Estimated from Ref. [192]

In the case of water, the 'combustion' ReaxFF parameters yield an unrealistically strong attraction, as already discussed in **Figure 4.6.** The 'aqueous' ReaxFF simulations yield a B_2 that is in closer agreement with experimental data than the SPC non-reactive simulations, although all simulations predict an effective attraction that is too strong compared to experiments.

In the case of hydrogen, both non-reactive and 'combustion' ReaxFF simulations yield B_2 data that are slightly too attractive, yet in reasonable agreement with experimental data.

4.3.3. Self-diffusion coefficients

The self-diffusion coefficients were calculated from the mean square displacements by implementing the Einstein equation [117]:

$$\lim_{t\to\infty}\langle|r_i(t'+t)-r_i(t')|^2\rangle = 6D_S t \quad (4.4)$$

In Equation 4.4, $r_i(t)$ and $r_i(t')$ are the positions of molecule *i* at time *t* and at the time origin *t'*, respectively. In these calculations, after the systems are equilibrated, the simulations are conducted for up to 2 ns. The mean square displacements are calculated from at least 5, and sometimes above 10 origins, separated by at least 200 ps but no more than 500 ps. The molecular simulation results of self-diffusion coefficients for all models are compiled in **Table 4.6**, where we also provide experimental data for comparison.

Table 4.6. Self-diffusion coefficients as predicted by all models implemented in this work. For comparison, experimental data are also reported

Molecule	Temperature (K)	Force field	Self-diffusion coefficient		
			This study	Experiment	Unit
CH_4	150	TraPPE	4.40 ± 0.13	6.06[a]	10^{-4} Å^2/fs
		OPLS	6.15 ± 0.11		
		'combustion' ReaxFF	9.39 ± 0.24		
	298	TraPPE	2.46 ± 0.12	2.34[b]	Å^2/fs
		OPLS	2.02 ± 0.02		
		'combustion' ReaxFF	1.93 ± 0.02		
CO_2	273	TraPPE	8.39 ± 0.15	8.42[c]	10^{-4} Å^2/fs
		Zhang	9.57 ± 0.32		
		EPM2	9.13 ± 0.27		
		'combustion' ReaxFF	7.44 ± 0.12		
	298	TraPPE	1.32 ± 0.13	1.13[b]	
		Zhang	1.24 ± 0.18		
		EPM2	1.35 ± 0.11		
		'combustion' ReaxFF	1.20 ± 0.07		
H_2O	298	SPC/E	2.40 ± 0.17	2.30[d]	10^{-4} Å^2/fs
		'aqueous' ReaxFF	2.39 ± 0.05		
		'combustion' ReaxFF	0.52 ± 0.04		
	500	SPC	1.01 ± 0.02	-	Å^2/fs
		'aqueous' ReaxFF	1.04 ± 0.05		
		'combustion' ReaxFF	0.66 ± 0.08 (10^{-3})		
H_2	15.2	Frost	3.88 ± 0.07	4.50[e]	10^{-4} Å^2/fs
		'combustion' ReaxFF	0.41 ± 0.05		
	77.5	Frost	1.38 ± 0.14	1.33[f]	Å^2/fs
		'combustion' ReaxFF	1.29 ± 0.02		

[a]Ref. [124]; [b]Ref. [193]; [c]Ref. [194]; [d]Ref. [195]; [e]Estimated from Ref. [196]; [f]Ref. [197].

It should be remembered that the simulation box size has a strong effect on simulated self-diffusion coefficients. For example, Yeh and Hummer simulated water and a simple Lennard-

Jones fluid [198]. They found that the self-diffusion coefficient increases with the size of the simulation box. They proposed an analytical correction, proportional to $N^{-1/3}$, where N is the number of molecules in the system, to extrapolate the simulation results to the thermodynamic limit. Because of computing-power limitations, we quantified system-size effects only for liquid CO_2 at 273 K. When the number of molecules was increased from 500 to 1,000, and 1,500, the self-diffusion coefficient obtained with the TraPPE force field was found to increase from 8.39 to 8.63, to 8.82 $Å^2$/fs, respectively. When the 'combustion' ReaxFF force field was implemented, the self-diffusion coefficient increased from 7.44 to 7.54, to 7.88 10^{-4} $Å^2$/fs, respectively. Note that the correspondent simulation box size increased from $32.1 \times 32.1 \times 32.1$ $Å^3$, to $40.4 \times 40.4 \times 40.4$ $Å^3$, to $46.3 \times 46.3 \times 46.3$ $Å^3$, respectively. These self-diffusion coefficients, calculated from both ReaxFF and TraPPE models, are shown in **Figure 4.8** as a function of the inverse box size (1/L). The data are fitted using a straight line and used to extrapolate the CO_2 self-diffusion coefficient at infinite box size. These results confirm that D_S increases with the box size for all systems considered. Quantifying for all systems considered here the thermodynamic limit for D_S is beyond the scopes of the present Chapter. Because somewhat similar system size effects are observed for both classical and reactive force fields, such effects do not affect the conclusions of this Chapter.

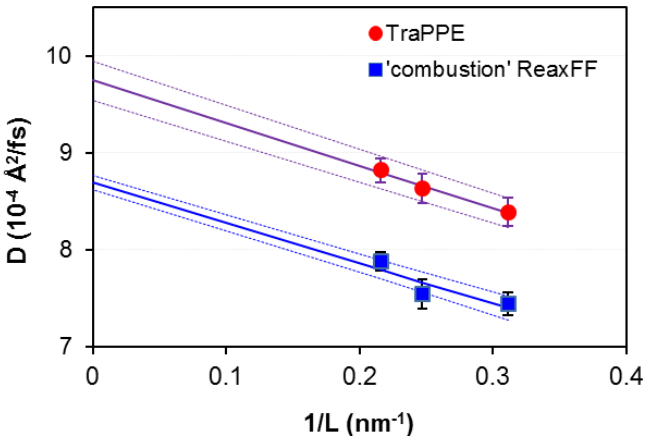

Figure 4.8. Diffusion coefficient of liquid CO_2 as a function of the inverse box size 1/L.
Notes: Symbols are simulation data, continuous lines are fits to the data and extrapolations to the infinite box size. The Error bars are obtained as one standard deviation from the mean of at least three simulation runs. The dotted lines highlight the uncertainty in these extrapolations.

Implementing the 'combustion' ReaxFF yields self-diffusion coefficients for CO_2 in both liquid and gaseous phases that are in reasonable agreement with the non-reactive force field,

and also with available experimental data. The 'combustion' ReaxFF yields reasonable self-diffusion coefficients for gaseous CH_4 and H_2, while it yields self-diffusion coefficients for liquid CH_4 twice as fast as the values predicted by the non-reactive simulations, and for liquid H_2 about 9 times slower than the values predicted by the non-reactive simulations. In the case of water, we report in **Table 4.6** results obtained using both the 'combustion' and 'aqueous' ReaxFF parameterisations. The 'combustion' ReaxFF version under-predicts the self-diffusion coefficient of both vapour and liquid water (by a factor of ~1,500 and ~5, respectively), compared to classical force fields, while the 'aqueous' ReaxFF version provides excellent predictions for the self-diffusion coefficient of liquid water and gaseous water. Raju et al. [139] reported that the self-diffusion coefficient of bulk liquid water at 298 K is ~2.11 10^{-4} $Å^2$/fs, which is in reasonable agreement with our results, as well as with experiments [195, 199].

4.4. Discussion and conclusions

In this Chapter, we calculated structural and dynamic properties of four common pure fluids by conducting equilibrium molecular dynamics simulations implementing reactive and non-reactive force fields. The 'combustion' ReaxFF was considered, as well as several classical non-reactive force fields widely used. The comparison is limited to radial distribution functions, which are related to the ability of a model to predict configurational thermodynamic properties of a fluid, and self-diffusion coefficients, which are related to the ability of a model to predict transport properties. We observed several results in agreement, but also significant differences among the predictions when reactive and non-reactive force fields are implemented. In the liquid phase, experimental data, when available, are in good agreement with the classical simulations, suggesting that the classical models could be good approximations for the properties of pure fluids. For liquid hydrogen, however, neither classical nor ReaxFF simulations reproduce the expected structure. In the gas phase, the second virial coefficient was used to assess the ability of the simulations to reproduce experimental data. Experimental data are indeed available for the second virial coefficient of gases, and this quantity can be readily calculated from radial distribution function data-sets.

It can be seen from the site–site correlation functions for CH_4 molecules in **Figure 4.2**, that the configuration of liquid molecules within the first solvation shell predicted by the 'combustion' ReaxFF calculation is similar to that predicted by TraPPE and OPLS models. Meanwhile, a significant variation is observed between 'combustion' ReaxFF and OPLS

results for CH_4 in the gas phase. Comparing the predicted second virial coefficients to experimental data, we conclude that a realistic g_{CC} should be in between that obtained from the 'combustion' ReaxFF and that obtained from the OPLS non-reactive simulations. All the results for the radial distribution function for liquid methane show a small shift towards shorter distances. A similar trend was also found for gas-phase molecules. The 'combustion' ReaxFF simulations yield a greater self-diffusion coefficient for liquid CH_4 compared to both OPLS and TraPPE models as well as to experimental data. The 'combustion' ReaxFF gas-phase self-diffusion coefficient CH_4 is slightly smaller than that obtained from TraPPE simulations and that measured experimentally, but it is consistent with OPSL model simulations. Thus, we conclude that the 'combustion' ReaxFF yields acceptable values for the diffusivity of pure CH_4 in vapour phases.

The pair correlation functions shown in **Figure 4.3** and **Figure 4.4** suggest that 'combustion' ReaxFF simulations are in slightly better agreement with classical simulations regarding the spatial arrangement of gas-phase CO_2 molecules rather than that of liquid-phase ones. However, the results for the second virial coefficients suggest that none of the force fields implemented yield a sufficiently attractive effective interaction between the CO_2 molecules in the gas phase. In all cases, it was found that 'combustion' ReaxFF calculations yield peak positions shifted to slightly longer distances compared to the respective classical simulations. It was also found that the 'combustion' ReaxFF simulations yield transport properties (i.e. self-diffusion coefficients) for both liquid and gaseous CO_2 that are in reasonable agreement with classical simulations as well as with experiments.

The 'combustion' ReaxFF simulations yield structures for pure H_2 that are in reasonable agreement with classical simulations, albeit the agreement is better for the gaseous phase compared to liquid H_2. In fact, the classical model employed here was derived to study gaseous hydrogen. In the liquid phase, both 'combustion' ReaxFF and classical simulations yield radial distribution functions that differ substantially compared to theoretical predictions from the literature, most likely because quantum effects are not considered either in the Frost model or in the 'combustion' ReaxFF model. The results for the self-diffusion coefficients show that 'combustion' ReaxFF predictions are reasonable for the gaseous phase, but rather poor for the liquid phase.

To explain the differences just summarised between 'combustion' ReaxFF and classical simulations we first consider the bond length and bond angle parameters as implemented in

the various force fields. It is worth pointing out that all classical force field models considered, except OPLS, are rigid, while in ReaxFF simulations both bond lengths and angles can vary during a simulation. In **Figure 4.9**, we quantify the probability density distribution of the H–C–H angle in CH_4, the H–O–H angle in H_2O, and the O–C–O angle in CO_2 as obtained for ReaxFF and OPLS simulations. The results show that, compared to the expected geometries of the simulated molecules, 'combustion' ReaxFF simulations predict smaller O–C–O angles in CO_2 (178.5° for both the liquid and the gas), similar angles for CH_4 (109.5° for both liquid and gas) and larger angles for H_2O (109.5° in the gas phase and 115.5° in the liquid phase). Perhaps these differences explain the ability, or lack thereof, of the 'combustion' ReaxFF parameterisation to estimate structure and dynamics of the pure fluids considered here.

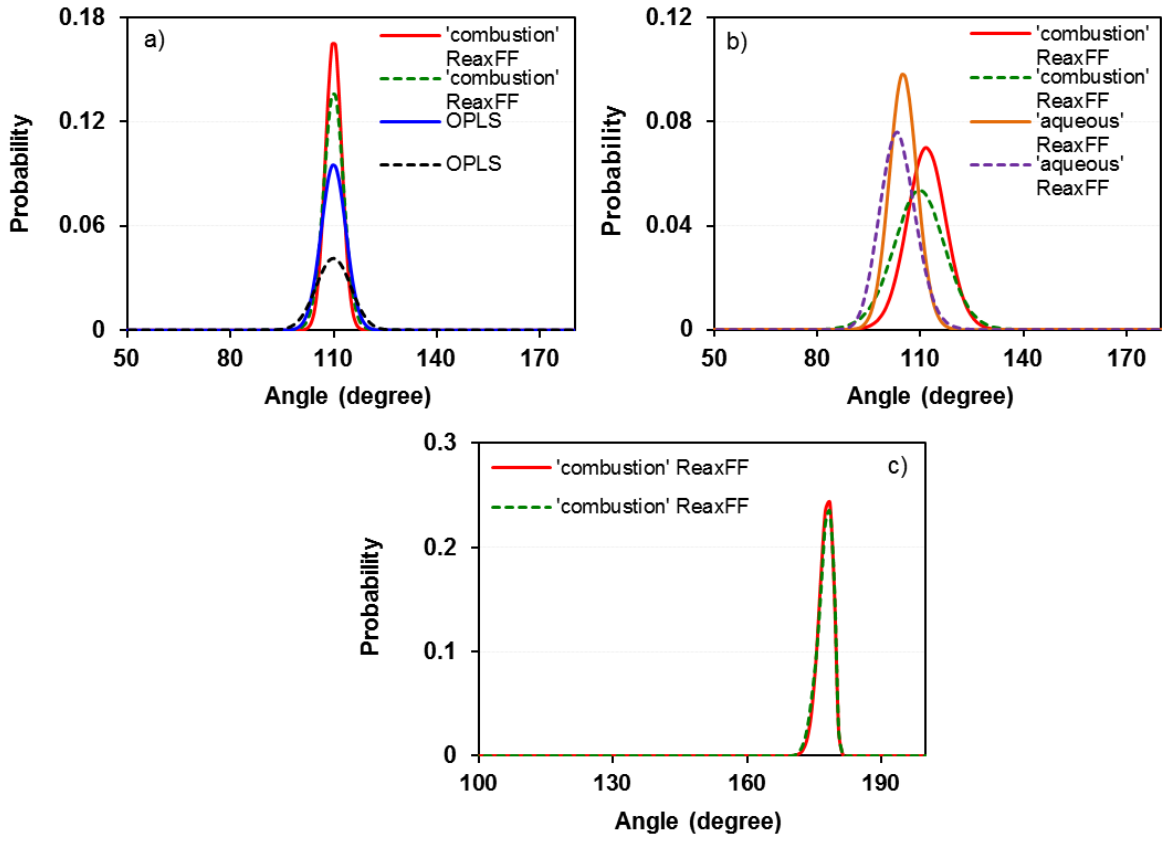

Figure 4.9. Probability density distribution for the angle for molecules studied using 'combustion' ReaxFF, 'aqueous' ReaxFF and OPLS model: CH_4 (a) H_2O (b) and CO_2 (c). Solid and dashed lines represent molecules in liquid and gas phase, respectively.

Regarding water, our results show that the 'combustion' ReaxFF yields unrealistic predictions for the properties of bulk water, both in the liquid and in the vapour phases. However, the 'aqueous' ReaxFF parameterisation yields a structure for pure water that is in

very good agreement with that predicted by classical force fields, and self-diffusion coefficients that are also in very good agreement with classical simulations. The ReaxFF parameter sets are classified into two major groups (i.e. the ReaxFF branches), intra-transferable with one another: the combustion versus the aqueous branch. The O/H parameters proposed by these two data-sets differ significantly. The ‘combustion’ ReaxFF was originally developed for applications at temperatures above the water boiling point, where combustion reactions typically occur. On the other hand, the O/H parameters from the ‘aqueous’ ReaxFF were developed to describe liquid water, thus explaining the success of ‘aqueous’ ReaxFF simulations in reproducing SPC/E simulation results. It is somewhat unexpected that, based on our simulation results, the ‘combustion’ ReaxFF parameterisation yields poor predictions for structure and diffusion of water even in the gaseous phase. As shown in **Figure 4.6** this is may be due to water association, suggesting that the temperature is still too low for ‘combustion’ ReaxFF simulations of water to be successful.

In conclusion, comparing reactive and classical simulations we found that the ReaxFF parameterisation can be helpful at predicting structure and dynamics of pure fluids, but the agreement with both classical simulations and experiments depends strongly on the fluid considered and on the thermodynamics conditions simulated. It is encouraging that the ‘aqueous’ ReaxFF parameterisation yields results in excellent agreement with those predicted using some of the most widely implemented models for bulk water.

Chapter 5. Partial CO_2 Reduction in Amorphous Cylindrical Silica Nanopores

The material presented in this Chapter was published in 2019 in volume 123, pages 26358–26369 of The Journal of Physical Chemistry C.

5.1. Introduction

It is known that pore confinement affects the structure of fluids [200-204], their transport properties [85, 90, 205-207], and mutual solubility [208-214]. It has also been shown that confinement can affect the equilibrium composition of a reactive system. The effects of confinement on chemical reaction equilibria for model, reversible reactions in slit-shaped pores were first reported by Borówko et al. [215, 216], while Turner et al. [217-220] reported molecular-level simulation studies for realistic, reversible reactions in carbon micropores and carbon nanotubes. Santiso et al. [221] implemented plane wave pseudopotential density functional theory to simulate the rotational isomerization of 1,3-butadiene and the decomposition of formaldehyde in slit-shaped pores formed by two parallel graphene sheets. Their results showed that confinement affects the potential energy profile for the isomerization of 1,3-butadiene, whereas the proximity of the pore surface reduces somewhat the activation energy. Turner et al. [222] predicted the rate constant for the hydrogen iodide decomposition reaction [$2HI \rightarrow H_2 + I_2$] in slit-shaped carbon pores and in carbon nanotubes by combining the transition-state theory formalism with reactive Monte Carlo (RxMC) simulations [35, 36]. The results suggested that the reaction rate in (8,8) carbon nanotubes increased by a factor of 47 compared to that observed for bulk fluids at the same thermodynamic conditions. These results illustrate the large effects that confinement and fluid−wall intermolecular forces can exert on the rate of a chemical reaction and on the equilibrium composition of a reactive system.

Building on this literature, Peng et al. [223] simulated the ammonia synthesis reaction in MCM-41 and pillared clays. Hansen et al. [224] quantified the influence of silicalite-1 pores on the reaction equilibria of propene metathesis reactions. Lísal et al. [225] studied the NO dimerization reaction in carbon slit nanopores in equilibrium with a bulk reservoir. In general, it has been reported that reaction rates in confinement differ from those in bulk

because the favorable wall−fluid interactions can increase the reactant density and enhance the formation of transition-state complexes. Such effects depend on pore size, pore chemistry, and pore morphology [218]. For example, Furmaniak et al. [226] showed that, within activated carbons, the decreasing pore size may increase or decrease the reaction yield, depending on the relative adsorption energy of reactants and products. The computational studies just summarized focused on pore size effects on the equilibrium conversion by employing the RxMC algorithm, widely used to simulate chemically reacting systems [220].

The present research builds on the recent results reported by Le et al. [34]. In their analysis, the CO_2 methanation reaction ($CO_2 + 4H_2 \leftrightarrow CH_4 + 2H_2O$, Reaction 1.1) was considered to occur in contact with slit-shaped pores carved out of β-cristobalite silica crystal. Reaction 1.1 was studied in either the bulk phase or for the bulk phase in equilibrium with a silica nanopore at moderate pressures 10–50 bar in the range of temperatures 200–700^{o}C. The reaction equilibrium composition was found to strongly depend on nanopore size and chemical features of the pore surface, and several scenarios were identified according to which the equilibrium CH_4 mole fraction in confinement exceeded that expected in bulk systems. The kinetics of the reaction were not considered.

In Chapter 4, we found that the ReaxFF parameterization can predict structural and transport properties of nonreactive pure fluids (CH_4, CO_2, H_2O, and H_2) [227]. However, our results showed that the agreement with both classical simulations and experiments depends strongly on the fluid considered and on the thermodynamics conditions simulated. A better understanding of the effect of confinement on both the composition and the kinetics of reactive systems could benefit many sectors, including the chemical industry, which makes large use of silica-based micro- and mesoporous materials as catalysts. Synthetic zeolites, for instance, are widely used for petroleum refining and other applications by the petrochemical industry [228, 229]. As another example, mesoporous MCM-41 materials have recently been successfully applied as a catalyst for the three-component Strecker reaction [230]. Within this background, the main objective of the present study is to investigate, using the ReaxFF MD simulation approach, whether silica nanopores could promote the CO_2 methanation reaction (Reaction 1.1) at conditions consistent with those in prior RxMC simulations conducted by Le et al. [34]. This investigation is motivated by the observation that the equilibrium composition of systems that undergo Reaction 1.1 is expected to favor CH_4 production at low T, but due to the significant kinetic limitations of the eight-electron reduction of CO_2 to CH_4

[231], active catalysts are required for conducting such a reaction industrially at acceptable rates and yields. A series of catalysts based on group VIII metals such as Ru [232], Ni [233, 234], Pd [235], and Co [236] supported on porous materials such as TiO_2, Al_2O_3, CeO_2, MgO, and zeolite have been tested and applied for CO_2 methanation [237-240]. None of these catalysts nor iron-rich saponite clays are considered in this Chapter. It should also be noted that the time scales that can be investigated using the ReaxFF formalism are extremely short (usually nanoseconds) compared to typical experimental setups, and especially so when compared to chemical transformations that might occur in the subsurface during geological times. It has been estimated that full conversion of CO_2 to CH_4 may take decadal time scales at 300 °C, or thousands of years at 200 °C during experimental serpentinization [241].

The rest of this Chapter is organized as follows: in the first section, we first outline the chosen ReaxFF and then describe the simulation methodology implemented, including details on the solid support used to conduct the simulations. In the next section, we present the results, starting from the expected equilibrium conversion for the CO_2 methanation (Reaction 1.1) based on thermodynamics calculations, followed by a detailed discussion of the reactive MD simulation results, first in the bulk and then in the amorphous silica nanopores. A discussion follows where we relate the present results to the prior RxMC calculations [34]. Finally, we summarize our main conclusions.

5.2. Computational details

5.2.1. Reactive force field (ReaxFF) parameterization

We have chosen a recently published ReaxFF potential, which was developed for the Si/C/H/O system involved in the oxidation of SiC [59]. This parameter set is the combination of existing ReaxFF descriptions for hydrocarbons [61] and silicon/ silicon oxides [242, 243]. The ReaxFF parameters used were extracted from previously used Si/C, Si/O, Si/Si, and Si/H quantum mechanics data for silicon [244], silicon oxide [242], and poly(dimethylsiloxane) ReaxFF applications [245]. Details on the training of these datasets are provided by Newsome and co-workers [59]. It has been reported that the chosen Si/C/H/O parameters are capable of describing reactions among hydrocarbons, as well as their reactions with silicon carbide, silicon oxides, diamond, and graphite materials [59].

5.2.2. Simulation methodology

All of the molecular dynamics (MD) simulations reported here were conducted using the ReaxFF reax/c code as implemented in the LAMMPS package, version 20180818 [146, 147].

The system was simulated as confined within a realistic cylindrical pore of diameter ~16 Å carved out of amorphous silica. A detailed description of the procedure implemented during the preparation of the cylindrical silica pore has been presented in a previous study [246], in which we studied the transport properties of confined water−propane systems, using nonreactive force fields. In **Figure 5.1A**, we provide a schematic of the pore, which is found within a 56.9 Å × 56.9 Å × 56.9 Å simulation box with periodic boundary conditions along the three directions. The pore is parallel to the X axis of the simulation box. Because of periodic boundary conditions, the pore is infinitely long along the X direction. The surface of the cylindrical pore was saturated with hydroxyl groups and hydrogen atoms, yielding a hydroxyl density of 3.8/nm^2. This is consistent with experimental measurements on flat amorphous silica surfaces [101]. The atoms within the silica substrate were fixed throughout the simulations, except for those atoms at the pore surface in contact with the fluid molecules.

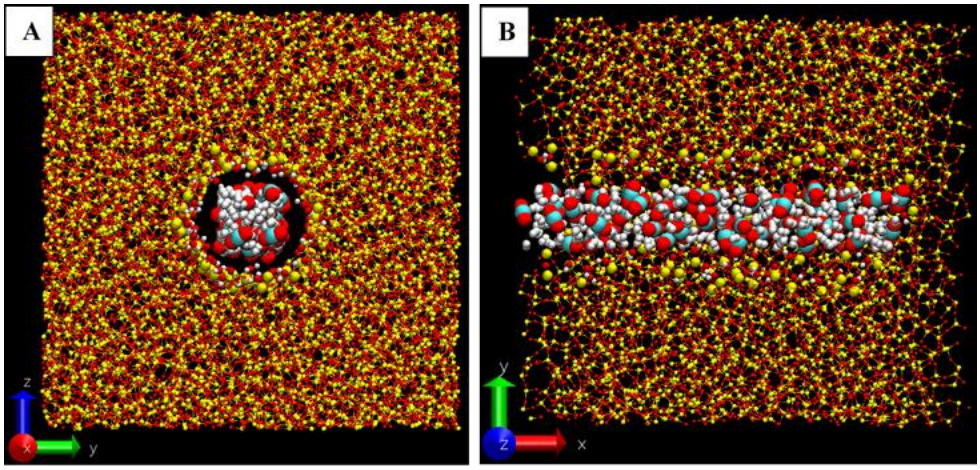

Figure 5.1. Snapshots of the initial system configuration from axial view (A) and side view (B). The yellow, red, cyan and white spheres represent Si, O, C and H atoms respectively.

In all simulations, a feed gas composed of CO_2 and H_2 was inserted in the pore, and then ReaxFF simulations were conducted to determine changes in system composition as simulation time progressed. Experimental evidence demonstrates that the H_2/CO_2 ratio should not be lower than 4 to obtain high CH_4 selectivity and avoid carbon deposition during methanation [247]. Therefore, in all cases considered here, the feed gas consists of CO_2 and H_2 with a molar ratio of $H_2/CO_2 = 4$. This highly reducing composition was previously used

to study the effect of confinement on the equilibrium composition implementing the RxMC approach [34]. A snapshot for the initial configuration of a system containing 50 CO_2 and 200 H_2 molecules confined in the amorphous silica cylindrical pore is shown in **Figure 5.1B**. Increasing the density of the reactants within the pore is expected to favor CO_2 methanation, based on the results from the simulations conducted implementing the RxMC approach [34] and also based on Le Chatelier's principle.

The simulations were conducted within the constraints of constant number of atoms, constant volume, and constant temperature, implementing the Nosé-Hoover thermostat with a temperature damping constant of 100 fs. The cutoff distance for electrostatic and van der Waals interactions is 10 Å. Although it is highly recommended to use tail corrections when simulating fluids in microporous materials [248], the ReaxFF formalism as implemented in the present study was not trained to fit long-range London dispersion forces. In addition, Liu et al. [249] reported that the dispersion corrections have a negligible effect on the description of chemical reactions.

The system temperature was set within the range from 400 to 1000 K. The simulations were performed at 100 K temperature intervals, to investigate how the reaction products vary as a function of temperature. A time step of 0.25 fs was necessary to conserve the system energy at the chosen temperatures. At each temperature, we conducted 15 independent simulations to quantify the statistical reliability of the collected data. Each of the 15 simulations has a unique starting configuration and was initially equilibrated at low temperature and then heated to the target temperature. The total simulation time for each system was determined by the extent of carbon dioxide reduction: simulations were terminated when no further change in system composition was observed within a simulated time of 5 ns. The kinetics of decomposition was studied by averaging the results from 15 simulations.

The bond, species, and trajectory data extracted from the simulation output files were analyzed to track the number of molecular species generated during the simulations. A bond order cutoff of 0.3 was used for all bond types to identify the molecular species formed during the simulations. It has been shown that the bond order cutoff does not affect the final products obtained during an MD simulation but only the formation of intermediates [39]. If the cutoff is too small, the simulation could identify too many bonds, affecting the computational efficiency; on the other hand, too large a cutoff will yield fragmented

molecules within the simulation. The 0.3 value has been widely used in the literature, yielding reliable results [41, 250, 251].

5.3. Results and discussion

5.3.1. Thermodynamic analysis: Bulk system

The methanation of CO_2 as represented by Reaction 1.1 ($CO_2 + 4H_2 \leftrightarrow CH_4 + 2H_2O$) is a reversible and strongly exothermic reaction ($\Delta H = -165$ kJ/ mol), which is favored at low temperature, high pressure, and high hydrogen fugacity [252]. The CO_2 methanation is the combination of the endothermic reverse water gas shift reaction (Reaction 5.1) and of the exothermic CO methanation (Reaction 5.2) [253], which are explicitly described as

$$H_2 + CO_2 \rightarrow CO + H_2O \qquad \Delta H = 41.2 \text{ kJ/mol} \qquad (5.1)$$

$$3H_2 + CO \rightarrow CH_4 + H_2O \qquad \Delta H = -206.1 \text{ kJ/mol} \qquad (5.2)$$

$$\frac{dlnK}{dT} = \frac{\Delta h^{o}_{rxn}}{RT^2} \qquad (5.3)$$

The thermodynamic equilibrium for the three Reactions 1.1, 5.1 and 5.2 can be quantified via the calculation of the equilibrium constants (K) by van't Hoff equation [254].

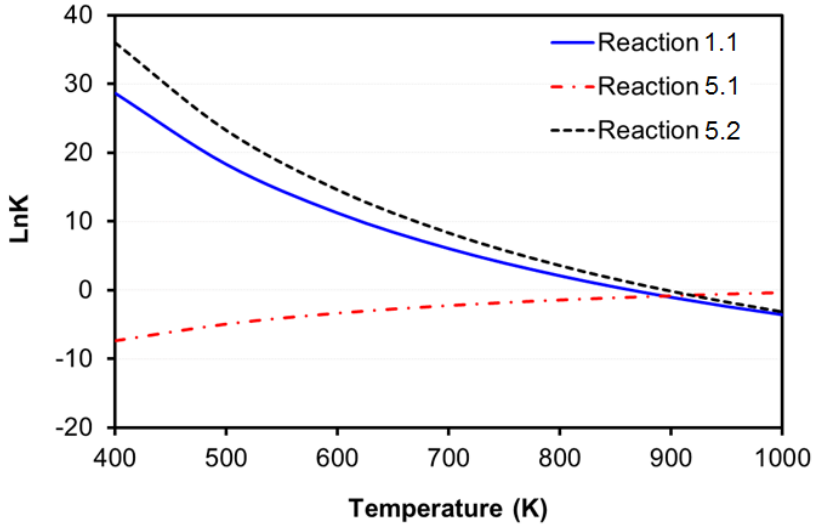

Figure 5.2. Equilibrium constants K calculated as a function of temperature for Reactions 1.1, 5.1 and 5.2 using Equation 5.3 and standard enthalpy of reaction data from literature.

The van't Hoff equation, shown in Equation 5.3, uses as input data the standard enthalpy of reaction, $\Delta h_{rxn}°$, for each of the molecular compounds, which is a function of temperature.

Obtaining the thermodynamic parameters for the reacting components from the literature [255], we calculated the equilibrium constants as a function of temperature. The results, shown in **Figure 5.2**, are consistent with those reported by Gao et al. [247]. It should be noted that in the prior work Le et al. [34] calculated equilibrium quotients from the RxMC simulation results, rather than equilibrium constants, because the reaction was occurring within narrow pores, which affects the equilibrium composition and not the equilibrium constant. The results in **Figure 5.2** are consistent with those reported previously [34], when Reaction 1.1 occurs in the bulk. The results in **Figure 5.2** show that both CO_2 and CO methanation reactions (Reaction 1.1 and 5.2, respectively) have high equilibrium constants in the temperature range of 400− 800 K, while the water gas shift reaction (Reaction 5.1) is characterized by lower K's at all temperatures. Gao et al. [247] obtained the equilibrium composition for CO_2 methanation implementing the total Gibbs free-energy (G_T) minimization method [256-258]:

$$G_T = \sum_{i=1}^{N} n_i \mu_i \tag{5.4}$$

where n_i and μ_i are the molar content and the chemical potential of species *i*, respectively. μ_i can be defined as:

$$\mu_i = \Delta G_{fi}^0 + RT \ln\left(\frac{f_i}{f_i^0}\right) \tag{5.5}$$

where ΔG_{fi}^0 is the standard Gibbs free energy of species *i*, *R* and *T* and are the ideal gases constant and operating temperature, respectively. f_i and f_i^0 are the fugacity and standard fugacity of species *i*, respectively. For the reaction equilibrium in the gas phase:

$$f_i = y_i P \varphi_i \tag{5.6}$$

$$f_i^0 = P^0 \tag{5.7}$$

where y_i and φ_i are the molar fraction and fugacity coefficient of species *i* in the gas mixture, respectively. *P* is the total pressure of the system, P^0 is standard pressure. After considering the restraints related to conservation of the total amount of individual chemical elements, the constrained function to be minimized (f_{obj}) is given as:

$$f_{obj} = \sum_{i=1}^{N} \left[n_i \left(\Delta G_{fi}^0 + RT \ln\left(\frac{y_i \varphi_i P}{P^0}\right)\right)\right] + \sum_{j=1}^{m} \lambda_j \left(b_j - \sum_{i=1}^{N} n_i a_{ji} \right) \tag{5.8}$$

Where λ_i is a Lagrange multiplier, b_j and a_{ji} are the total amount of element *j* in the mixture and the number of atoms of element *j* in species *i*, respectively.

We used the Aspen Plus V10 software to calculate the system composition as a function of temperature when Reaction 1.1, 5.1 and 5.2 occur. The Gibbs reactor model (RGibbs) was used to calculate the compositions of the species considered in equilibrium at a given pressure and temperature. The specification of the reactions involved and their stoichiometry is not required beforehand with the method applied. The species considered for the simulations included methane, carbon dioxide, hydrogen, carbon monoxide, water. The Soave-Redlich-Kwong (SRK) method available in the Aspen Plus database was used to estimate the species properties. In **Figure 5.3**, we report the equilibrium product mole fraction percent in the temperature range from 400 to 1000 K. The results in **Figure 5.3c** demonstrate that at moderate temperatures (400−800 K) CO methanation is favored in the bulk. At these conditions, the products mainly contain CH_4 and H_2O. When the temperature exceeds 800 K, the conversion of CO_2 into CH_4 is difficult to be achieved. In contrast, the conversion of CO_2 via Reaction 5.1 (the water gas shift reaction) increases with an increase in temperature (**Figure 5.3b**). This is due to the endothermic nature of Reaction 5.1, which is favored at high temperature. Reactions 5.1 and 5.2 may simultaneously occur during CO_2 methanation, Reaction 1.1. Thus, irrespective of pressure, lower temperature favors CH_4 formation. However, it is well known that, due to kinetic barriers, the use of a catalyst is essential to carry out the reaction at low temperatures [231].

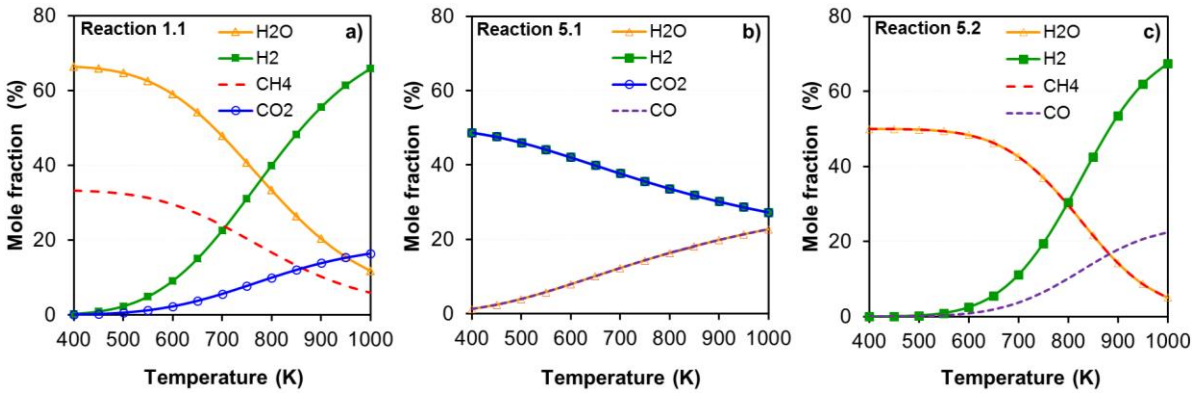

Figure 5.3. Equilibrium product composition of CO_2 methanation (a), water gas shift reaction (b) and CO methanation (c) calculated at 1 atm with a stoichiometric H_2/CO_2 molar ratio of 4.

5.3.2. ReaxFF simulations of CO_2 reduction in bulk

To check whether the chosen ReaxFF parameters can adequately describe CO_2 reduction and, in particular, its transformation into CH_4, we tracked Reaction 1.1 in the bulk phase. To overcome the time-scale limitations expected when implementing ReaxFF, we conducted this simulation at 2000 K. Although the high temperature is unfavorable for CO_2 methanation, increasing the temperature is necessary to speed up the reaction; this is a common practice to observe reactions in the nanosecond time scale in the absence of catalysts [259, 260]. The reactant's initial density considered in these simulations is consistent with those used for the simulations in the nanopores, discussed in Section 5.3.3, yielding a simulation box of dimensions 22 × 22 × 22 $Å^3$. Periodic boundary conditions were implemented in all directions. The initial configuration contained 50 CO_2 and 200 H_2 molecules. The same methodology was implemented to conduct ReaxFF simulations in the bulk (this section) and within the nanopore (Section 5.3.3).

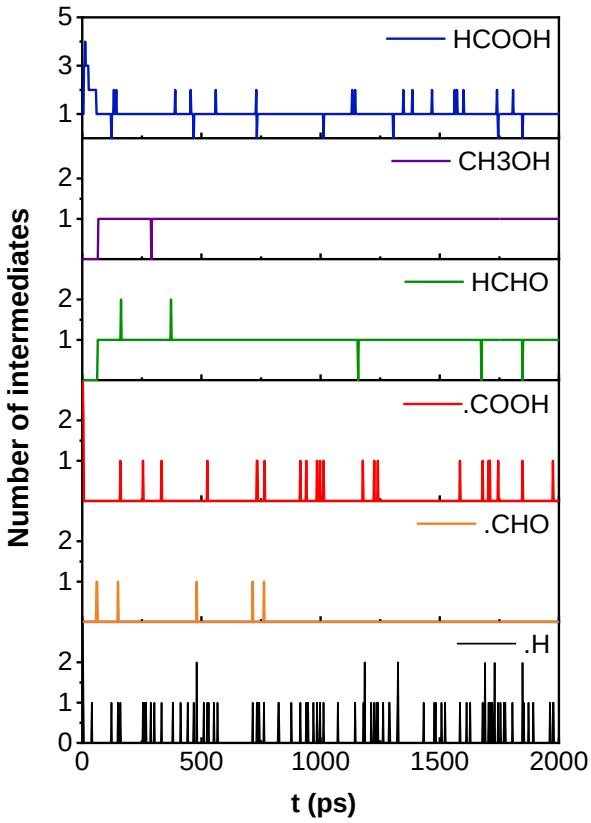

Figure 5.4. Main intermediates observed during the first 2 ns of partial CO_2 reduction (Reaction 1.1) conducted in the bulk phase at 2000 K. The results shown here are from a single simulation, while the data shown later for the overall composition are the averages from 15 simulations.

The system composition as a function of simulation time is shown in **Figure 5.4**. Analyzing the results, we observed some intermediates present for relatively long times: 1 CH_3OH and 1−2 HCHO and CH_2O_2 molecules were found during the first 2 ns of the simulations. These compounds remained in the simulated bulk systems at steady states. It should be noted that CH_2O_2 and HCHO play a key role in processes such as the oxidation of organic molecules and combustion [261, 262], and CH_3OH is one of the important intermediates observed during the conversion of $\bullet CH_3$ radicals into HCHO molecules in the gas explosion process [143].

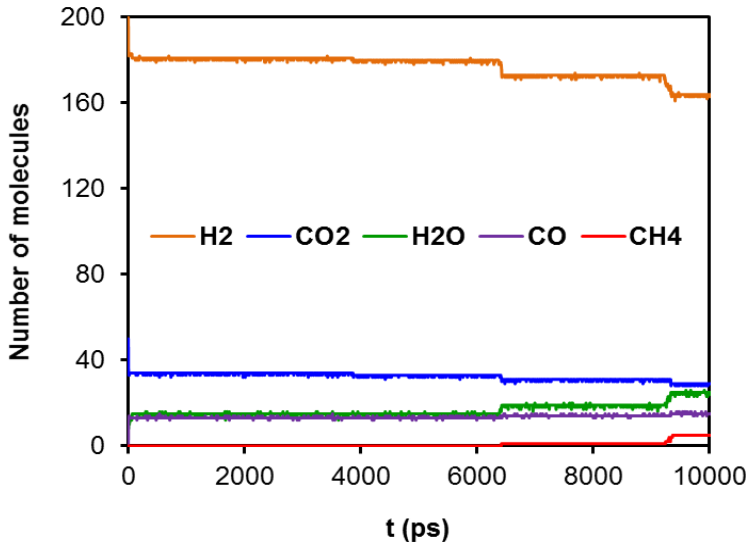

Figure 5.5. Evolution over the time of major reactants and products in the bulk reactive system simulated at 2000 K. Note that these results are from a single simulation.

The distribution of major reactants and products as a function of simulation time for the bulk Reaction 1.1 is reported in **Figure 5.5**. Although small amounts of CH_4 were produced, the simulation results suggest that, at the conditions considered, the water gas shift reaction (Reaction 5.1) dominates, because of the high temperature (2000 K). Differences between the results of **Figure 5.5** and those predicted by **Figure 5.3** are largely ascribed to the fact that for the thermodynamics calculations of **Figure 5.3**, oxygen-containing compounds such as formaldehyde, methanol, formic acid, and others were not considered. The product composition shown in **Figure 5.5** reflects the high CO content, which is also consistent with the thermodynamics calculations shown in **Figure 5.3**. In our simulations, the number of both CO and CH_4 molecules increased as the reaction proceeded. However, the amount of CO was found to be much larger than that of CH_4. Our results show that the negligible amount of CH_4 remained almost unchanged after ~71 ns of simulations.

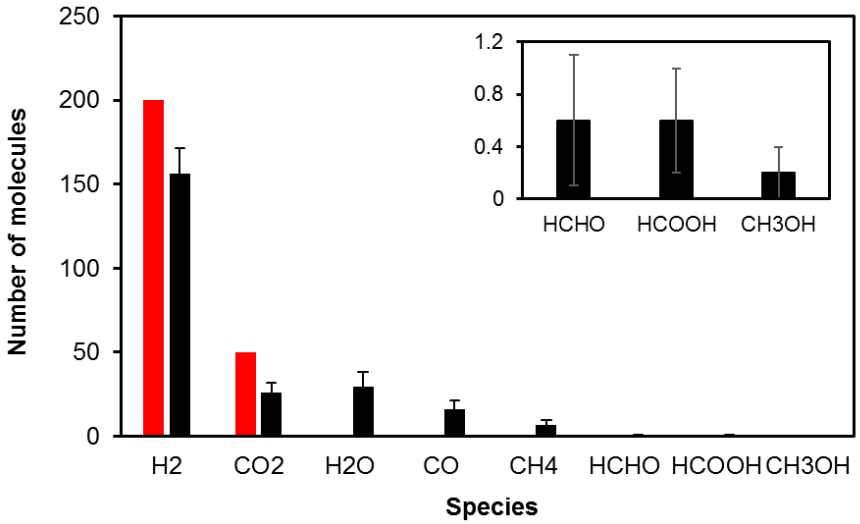

Figure 5.6. System composition obtained at 2000 K from the CO_2 reduction initiated from a system containing 50 CO_2 and 200 H_2 molecules in the bulk phase. The results are ensemble averages collected from 15 independent simulations. The initial composition is represented in red. In the inset we expand the results for HCHO, HCOOH and CH_3OH.

In **Figure 5.6**, we summarize the compositions of the bulk system, as predicted by the ReaxFF MD simulations conducted at 2000 K. Besides CH_4 and CO, which are the main products, some byproducts are present, albeit in small amounts. It should be noted that the results in **Figure 5.6** reflect the averages obtained from 15 independent bulk simulations (each of up to 100 ns). Each simulation was interrupted when the system composition did not change for at least 60 ns. Once stable system compositions were achieved, each simulation was continued for an additional 10−20 ns to further ensure that the final composition would not change. The results, shown in **Figure 5.6**, yield an average CH_4 mole fraction of ~2%, which is larger than that of less than 0.01% predicted from the total Gibbs free-energy minimization method shown in **Figure 5.3a**. These results confirm that the ReaxFF parameterization is able to describe CO_2 reduction. The deviation in system composition predicted by the ReaxFF approach compared to that by the thermodynamic analysis is possibly due to the fact that the ReaxFF allows the formation of several intermediates, which are not considered in the thermodynamic analysis of Section 5.3.1.

5.3.3. ReaxFF simulations of partial CO_2 reduction in nanopores

In **Figure 5.7**, we report typical simulation output data as observed within a silica pore, wherein the evolution of the system composition is plotted as a function of the simulation time. This simulation was conducted at 700 K, because thermodynamic analysis displayed in

Figure 5.3 indicated that at this temperature, methane production is thermodynamically favored, and this temperature may be high enough to overcome possible kinetic barriers.

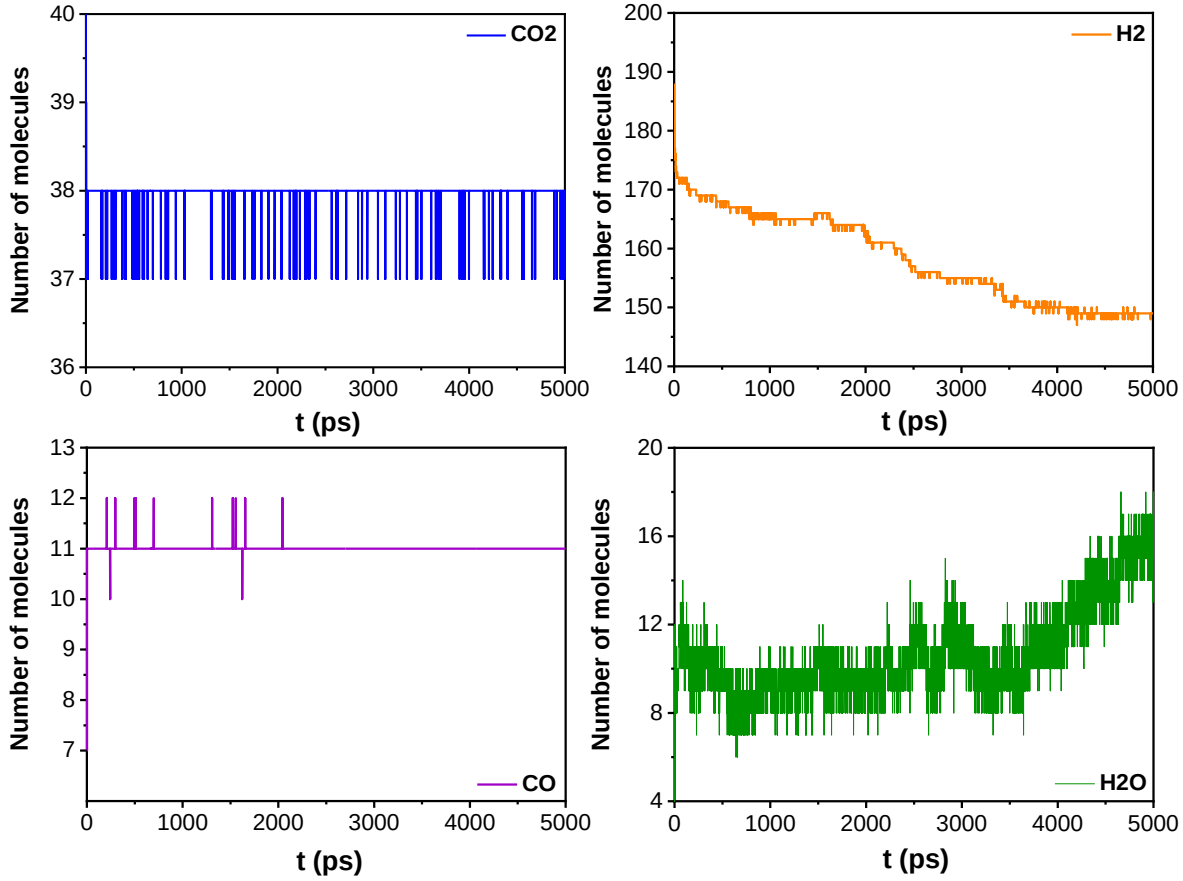

Figure 5.7. Representative results for the changes in system composition as a function of simulation time during the ReaxFF MD simulations of the partial CO_2 reduction within silica nanopores. Only CO, CO_2, H_2, and H_2O are monitored in this figure. The simulation was conducted at 700 K within an amorphous cylindrical silica nanopore. The figure only shows results from one simulation, not the average of the 15 simulations conducted at 700 K, which are reported below.

However, as shown in **Figure 5.7**, no CH_4 was found within the time scale of the simulations. The number of CO_2 molecules decreased gradually from 50 to 38, while 11 CO molecules were formed within the first 5 ns of the simulation. The number of CO_2 and CO molecules in the system remained almost constant after 5 ns. Meanwhile, the number of H_2 molecules decreased steadily; 51 H_2 molecules were consumed when the reaction proceeded to 5 ns. The number of H_2O molecules produced during the reaction increased slightly; 14 H_2O molecules were obtained at the end of the 5 ns simulation. The results suggest that, within the silica nanopore, CO_2 is reduced to CO quickly at the beginning of the simulation, but then the

reaction ceases, at least within the time frame accessed by our simulations, while H_2 continues to be consumed, in part, to yield H_2O.

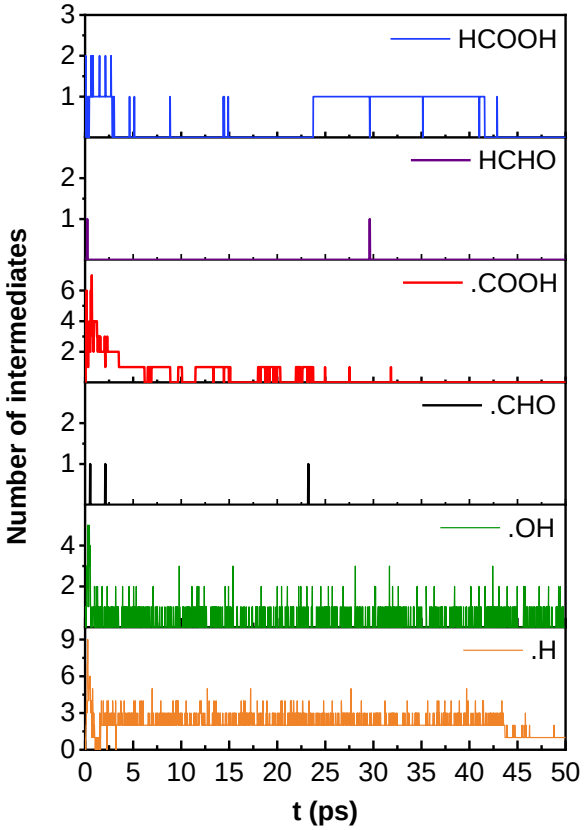

Figure 5.8. Intermediates system composition as a function of simulation time within the first 50 ps of the simulation conducted at 700 K in a silica nanopore. Note that these results are from a single simulation.

In the initial stages of the simulations, we observed numerous intermediate species, including •COOH, •CHO, HCHO, and CH_2O_2, which were present for short simulation times and only in small quantities (see **Figure 5.8**). In light of the recent report by Muchowska et al. [33], we find it interesting that some of the intermediates shown in **Figure 5.8** represent fragments of carboxylic acids, formate, and other metabolic precursors. It is possible that, in the presence of iron-based catalysts, the spontaneous reduction of CO_2 within the system considered here could yield prebiotic precursors of core metabolic pathways. However, in our system, no catalyst was present. Returning to the analysis of the system composition as a function of simulation time (**Figure 5.8**), we note that •OH and •H free radicals were observed throughout the simulations. The decomposition of CO_2 into CO generated short-lived •O radicals, which combined with •H radicals to form •OH radicals. The dissociation of H_2 produced •H radicals. Free •OH and •H radicals were also generated from the dissociation of

silanol groups on the silica surface. The amount of •OH radicals remained low (1 or 2 after 5 ps), but 20 •H radicals were observed when the simulation was interrupted at 5 ns (no additional CO production was observed when slightly longer simulations, up to 7 ns, were conducted). During the course of our simulations, it was observed that most of the •H free radicals reacted with •OH to yield H_2O molecules.

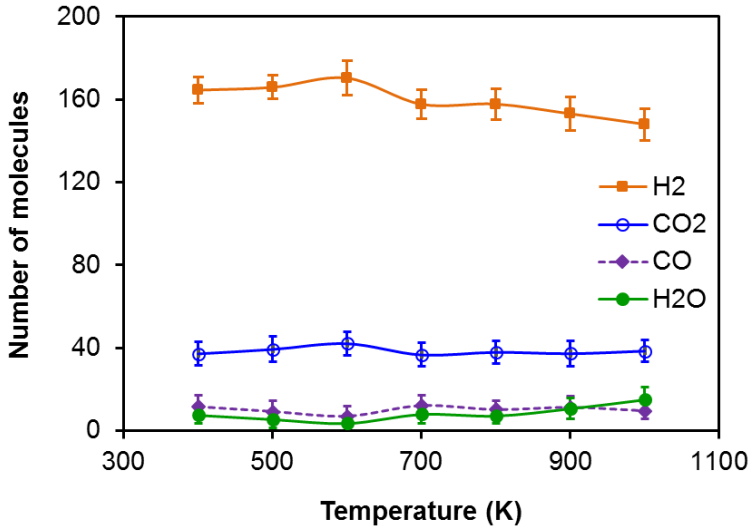

Figure 5.9. Molar composition at steady states as obtained from the MD simulation of the hydrogenation of CO_2 implementing the ReaxFF approach for systems confined in the cylindrical silica pores shown in **Figure 5.1**. In all cases, the initial system contains 50 CO_2 and 200 H_2 molecules. The simulations are conducted for 5 ns. System compositions during the last 1 ns of the simulations are used as ensemble averages. Error bars (vertical lines) are estimated as 1 standard deviation from the average.

We conducted similar simulations within a range of temperature from 400 to 1000 K. At each temperature, the system composition was found to become stable after a transient period. In **Figure 5.9**, we report the composition of the reactive systems once the composition did not change further (within the simulation times allowed by the ReaxFF simulations within the computing resources available to us). For none of the simulations conducted, which initially contained 50 CO_2 and 200 H_2 molecules, methane generation was observed. The reactive systems were found to contain CO, H_2O, and an excess amount of CO_2 and H_2. Our results show that as the temperature increases from 400 to 600 K, the amount of unreacted CO_2 increased, while the amount of CO and H_2O present within the system decreased. The amount of unreacted H_2 did not change significantly in this temperature range, which supports the hypothesis that the CO_2 methanation did not occur as the temperature fell below 600 K. When the systems were heated up to 700 K, the excess reactant amount decreased, while that

of the main products increased. At higher temperatures, the quantities of excess CO_2 and CO produced no longer changed significantly, up to 1000 K, indicating that the increase in temperature did not promote the formation of CO. In contrast, the amount of H_2O increased constantly as the temperature increased. An analysis of the molecular composition based on the simulation results shown in **Figure 5.9** suggests that partial CO_2 reduction to CO occurs at temperatures of 700 K and above, although increasing the temperature above 700 K does not seem to strongly enhance the extent of the reduction.

Our results, summarized in **Figure 5.9**, suggest that the silica substrate does not function as a catalyst for Reaction 1.1. At first, this result appears to be at odds with the prior findings, in which Le et al. [34], using the RxMC approach, found that confinement can shift the equilibrium composition of Reaction 1.1 toward methane generation. The predicted shift in the equilibrium composition toward enhanced methane formation within silica nanopores was due to the fact that the hydrophilic pore surface effectively removed water, one of the products, from the reactive environment, and that confinement effectively enhanced the pressure of the reacting system. Based on Le Chatelier's principle, both these phenomena shift the equilibrium composition to higher CH_4 production. The RxMC approach did not consider the kinetics of the reaction, as only the equilibrium composition was sampled. The present study employs the ReaxFF formalism, which tracks the reaction kinetics, although reaching equilibrium might require prohibitive computing resources. The absence of CH_4 from the reaction products could simply be due to the fact that silica is not a catalyst for Reaction 1.1. Future efforts shall explore the evolution of CO_2 reduction within iron-rich saponite clays, which were considered essential for the abiotic production of aromatic amino acids in a recent experiment by Ménez et al. [32].

To ensure that the ReaxFF MD simulations yield a structure of the confined fluid mixture similar to the one observed in the prior Monte Carlo simulations [34], in **Figure 5.10**, we report density profiles for H_2O, as well as other compounds, within the amorphous cylindrical silica pore. The density profile obtained for water (shown in the inset of **Figure 5.10**) is characterized by two pronounced peaks, which are near to the pore surface, indicating the strong adsorption of water on the surface. This is consistent with the prior results from Le et al. [34], although water is present in small amounts in the systems considered here. The positions of CO_2 and H_2 density peaks are approximately identical, which is consistent with those reported in the previous Monte Carlo simulations [34]. While H_2 and CO occupy the

entire pore volume yielding a more or less homogeneous distribution, CO_2 is found preferentially in proximity of the silica pore surface, where it can form hydrogen bonds with the −OH groups on the surface. It should be pointed out that the density profiles suggest that H_2 is somewhat depleted in the pore center, possibly because of its preferential adsorption on the pore surface. It is discussed later that this partition could directly affect the reaction mechanism.

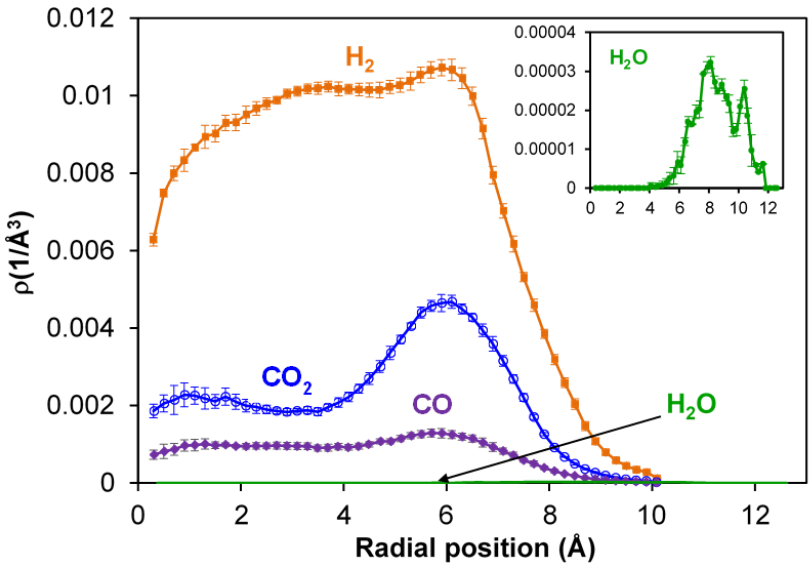

Figure 5.10. Density profiles of CO_2, H_2, CO, and H_2O during the last 1 ns of the CO_2 methanation reaction at 700 K. In this graph, radial position = 0 corresponds to the center of the cylindrical pore. We report the atomic density profiles of the molecular center of mass. Note that the molecules found at radial distances larger than 0.8 nm correspond to a few molecules that penetrated the amorphous material, sometimes in correspondence of enhanced surface roughness. Error bars are estimated as 1 standard deviation from the average.

Returning to **Figure 5.9**, the results, affected by rather large uncertainty, show very weak dependence on temperature. The results seem to suggest that CO_2 methanation did not occur within the silica nanopores when the temperature was below 700 K, within the constraints of our simulations. This could be due to several factors. It could be that computational limitations prevent us from achieving equilibrium. It could also be that, at the conditions considered, the reverse water gas shift (Reaction 5.1) dominates. Increasing the temperature does not affect this scenario because, as documented in **Figure 5.2**, Reaction 5.1 is characterized by lower K within the entire temperature range considered. The results in **Figure 5.3** suggest that low temperature promotes CO_2 methanation, but, as is the case for industrial processes, it could be that such a reaction is kinetically limited, and therefore no CH_4 generation was found in our simulations.

Comparing the composition of the reactive system in the bulk at 2000 K (**Figure 5.4**−**Figure 5.6**) versus that observed within the silica pores (**Figure 5.8** and **Figure 5.9**), it is noted that key intermediates such as •COOH, •CHO, HCHO, and CH_2O_2 are present throughout the process in the bulk but are only present for a short transient time (∼50 ps) when the reaction occurs in the silica pore. Therefore, the lack of CH_4 formation in confinement could be due to the inability of these intermediates to persist in proximity to the silica substrate.

Although the results in **Figure 5.9** do not reveal the formation of CH_4, they show that CO_2 is partially reduced to CO within the nanopores during our simulations. This observation could be of practical interest. It is in fact known that surface oxygen vacancies are the dominant defect in crystalline and amorphous silica [263]. Surface oxygen vacancies promote the adsorption and activation of CO_2, even in the absence of H_2 [264, 265]. For example, Jiang et al. [266] recently reported on the one-step thermolysis of CO_2 in the presence of metal oxide surfaces. They found that porous silica oxide materials with large specific surface areas (for example, SBA-15, MCM-41, commercial SiO_2) enhance the rate of CO_2 splitting into CO and O_2. It was suggested that the surface oxygen vacancies in the redox metal could act as a catalyst for this reaction.

To test whether similar phenomena could occur for the system considered here, we conducted an additional test in which we removed H_2 from the reactive system within the amorphous silica pores and ran ReaxFF simulations at the conditions described in **Figure 5.9**. We conducted these simulations in the temperature range of 400−1000 K. A typical evolution of the system composition is reported in **Figure 5.11**, which refers to a simulation conducted at 700 K. At the beginning of the simulation (0−3 ps), we observed some free radicals (•O, •H, •OH, and •COOH) released in relatively large amounts. However, after 100 ps, the quantities of •O, •H, and •OH no longer increased and no •COOH free radicals were observed. We observed that for the systems considered, the formation of CO was associated with the production of H_2O molecules, albeit in small amounts, rather than O_2. The amount of CO obtained at the end of the simulations as a function of temperature is shown in **Figure 5.12**. The results demonstrate that an appreciable amount of CO molecules formed even at much lower temperatures than those considered by Jiang et al. [266] for the direct thermolysis of CO_2, in the absence of H_2. The hydrogen atoms required for the formation of H_2O were obtained from the silica surface.

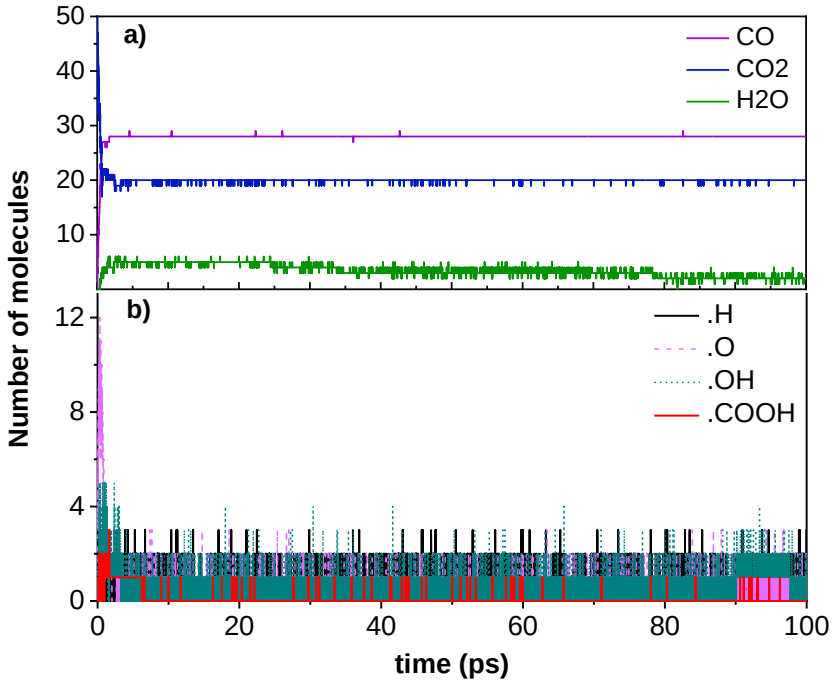

Figure 5.11. Evolution over time of a) reactants and products and b) major intermediates for the partial reduction of CO_2 within cylindrical silica pores at 700 K.

To visually quantify the effect of temperature on the results, we plot in **Figure 5.12** the amount of CO obtained at simulation completion as a function of temperature. The results indicate that CO production increases as the temperature increases within the SiO_2 nanopores of **Figure 5.1**. It is interesting to note that the quantity of CO obtained from the direct partial reduction of CO_2 in confinement appears to be much larger than that obtained from the CO_2 methanation (i.e., see **Figure 5.9**). Therefore, our results seem to suggest that the presence of hydrogen in large amounts could hinder CO formation within silica nanopores. This could be a consequence of the fact that increasing the density within the silica nanopore by the addition of H_2 reduces the collision rate of CO_2 against the silica surface (i.e., see density profiles in **Figure 5.10**). This observation is clearly at odds with the general recommendation to maintain the H_2/CO_2 ratio larger than 4 to achieve high CH_4 selectivity in CO_2 methanation reaction and avoid carbon deposition during methanation [247], although it should be pointed out that those recommendations are valid in the presence of catalytic materials.

While it is not surprising that amorphous silica is not an effective catalyst for CO_2 reduction, the analysis of the simulation results can reveal the mechanisms responsible for this observation. We refer to the density profiles of H_2 and CO_2 within the silica nanopores tracked during the 700 K simulations, which are shown in **Figure 5.10**. It can be seen that

although CO_2 and H_2 molecules distribute along the radial direction, perpendicular to the pore wall, the quantity of H_2 molecules residing close to the surface is much larger than that of CO_2, which supports the hypothesis that H_2 prevents CO_2 collisions with the surface.

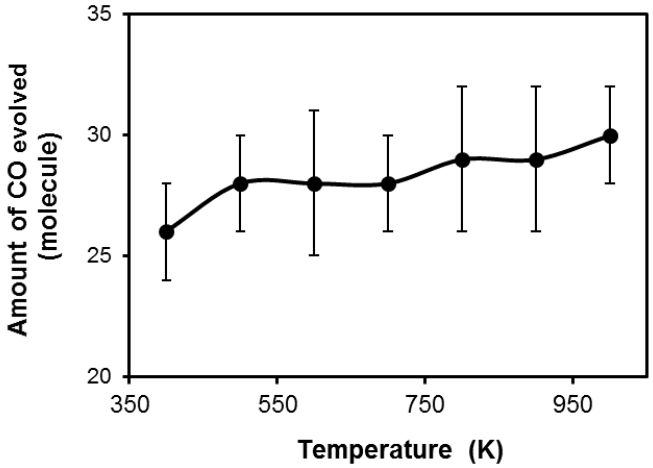

Figure 5.12. Amount of CO obtained from the partial reduction of CO_2 within cylindrical silica pores. In all cases, the initial system contains 50 CO_2 molecules, and the simulations are conducted for 5 ns. System compositions during the last 1 ns of the simulations are used as ensemble averages. Error bars are estimated as 1 standard deviation from the average.

To gain mechanistic insights into CO_2 dissociation, as described by the ReaxFF MD simulations, we performed a bond order analysis [267]. The CO_2 molecules collide with the defective silica surface, which initiates the decomposition of CO_2 to CO molecules and generates •O free radicals. When only CO_2 molecules are present within the pore, their collision with the surface yields the dissociation of silanol groups from silica, generating •H and •OH free radicals. This creates the possibility for •H radicals to combine with •OH radicals, yielding H_2O. Both CO_2 splitting and CO oxidation ($CO + ½ O_2 = CO_2$) occur simultaneously. In addition, CO molecules can contact •OH radicals to yield short-lived •COOH species, which are detected in the initial stages of our simulations. This radical is very active and has been considered a precursor for CO formation [142]. As mentioned earlier, silica provides oxygen vacancies, which promote the CO_2 splitting into CO. It is possible that CO is not reactive enough under our simulation conditions to react with H_2 and yield CH_4.

5.4. Conclusions

It is known that confinement has an effect on many physical properties of fluids. In particular, Cole et al. has considered the possibility that confinement affects the equilibrium

distribution of oxidized versus reduced carbon [268]. In the prior contribution [34], Le et al. employed the RxMC approach to quantify the equilibrium composition of a system in which CO_2 came in contact with large amounts of H_2 in the presence of narrow hydrophilic silica-based pores. The results showed that, for the most part, because the pore surface effectively removed H_2O from the products, the system composition was biased toward producing more CH_4 than it would have been expected based on thermodynamics calculations conducted in the bulk. This Chapter probes the specific question−can the CO_2 reduction be driven entirely inside cylindrical amorphous silica nanopores? The results confirm that amorphous silica is not a catalyst for the reaction, as is widely known. A better catalytic substrate choice would be TiO_2, Fe_3O_4, an FeNi bimetallic, or a Mg, Fe olivine with some trace or minor Cr, Ni, or Co at the pore surface. All of these phases exist in oceanic crustal rocks. Future studies should consider these materials, in an attempt to connect simulation studies with experimental observations for methane seeps in marine hydrothermal vents [28, 29], aromatic amino acids formed abiotically at depth [32], and intermediates of the biological Krebs cycle observed during CO_2 reduction [33].

In summary, ReaxFF molecular dynamics simulations were employed to assess the potential partial reduction of CO_2 within cylindrical pores carved out of amorphous silica. Simulating the CO_2 methanation in the bulk phase at 2000 K shows the formation of CH_4 molecules, with a product composition generally consistent with thermodynamics calculations. ReaxFF MD simulations of pure CO_2 within the silica pores showed evidence of its partial reduction at moderate temperatures, yielding large amounts of CO. Analysis of these simulations showed that CO is produced directly from the collision of CO_2 with the silica surface, on which defective sites could enhance CO_2 activation. When the ReaxFF MD simulations were conducted for CO_2 in the presence of excess H_2 within the silica nanopores, partial reduction was observed, but no CH_4 was obtained at the conditions considered because the silica support reduces the concentration of some important intermediates, which seem to promote CO_2 reduction in the bulk. The results presented, and, in particular, the analysis of the reaction pathway, could be helpful for designing catalytic processes for the one-step thermolysis of CO_2. To be of relevance for quantifying the catalytic reduction of CO_2 in the presence of excess H_2, the study should be extended to materials containing appropriate catalysts, for example, an Fe olivine with minor amounts of transition or noble metals at the pore surface.

Chapter 6. Supercritical CO_2 Effects on Calcite Wettability: A Molecular Perspective

The material presented in this Chapter was published in 2020 in volume 124, pages 18532–18543 of The Journal of Physical Chemistry C.

6.1. Introduction

Geologic carbon sequestration (GCS) into natural formations (e.g., deep saline aquifers, unmineable coal beds, and depleted oil/gas reservoirs) is one among several technologies that could contribute to reduce anthropogenic CO_2 from the atmosphere. GCS involves the capture of CO_2 from emitters, or perhaps directly from air, followed by injection of the captured CO_2 into geological reservoirs for long-term storage. Geologic CO_2 storage in deep saline aquifers presents several advantages compared to other kinds of subsurface repositories [269, 270]. It has been estimated that deep saline aquifers offer the largest potential capacity for CO_2 storage, up to 10,000 Gt CO_2 [270, 271]. Such potential repositories are widely distributed, and they are frequently located close to stationary point-source CO_2 emission sites [271].

The injection of CO_2 into subsurface reservoirs results in chemical and physical processes that could govern the long-term storage potential and its security [270, 272]. When injection ceases, supercritical CO_2 could be trapped as an immiscible free phase and as a solute in the aqueous phase within the porous rocks [273]. Various physicochemical storage mechanisms have been identified that could prevent the upward migration, and ultimately the leakage, of the injected CO_2. Such processes include structural trapping [274], residual trapping [275], dissolution trapping [276], and mineral trapping [277]. These mechanisms, and especially structural and residual trapping, are strongly influenced by the wettability characteristics of the mineral phases that come in contact with aqueous brines and injected CO_2 [274, 278, 279]. Wettability describes the adhesion, or spread, of a fluid on a solid substrate in the presence of other immiscible fluids. Increased CO_2 wettability of cap rocks at storage conditions substantially lowers the structural trapping capacity [274, 278], and the residual trapping of CO_2 in mixed-wet rocks is significantly reduced relative to trapping in water-wet systems [279, 280]. These examples demonstrate the vital importance of wettability of the

reservoir rocks in estimating storage capacity of formation and assessing its longevity (i.e., the potential of CO_2 leakage to the surface). Moreover, wettability also affects morphology and interfacial areas [281], capillary pressure, and transport and distribution of reservoir fluids [282].

The three-phase contact angle at the CO_2/brine/mineral interface, θ, is often used to evaluate wettability of a rock surface. The contact angle is described by the Young's equation [283] given in Equation 6.1:

$$\cos\theta = \frac{\gamma_{S1} - \gamma_{S2}}{\gamma_{12}} \tag{6.1}$$

In Equation 6.1, γ_{S1} and γ_{S2} are the interfacial tensions between the solid surface and the two fluids, while γ_{12} is the interfacial tension between the two fluids. Depending on the balance between intermolecular forces, the contact angle ranges from 0 to 180°. Complete wetting is defined when $\theta = 0°$, partial wetting when $0 < \theta < 180°$, and nonwetting is defined when $\theta = 180°$ [284]. A schematic of the contact angle θ considered in this work for the CO_2–water–mineral system is shown in **Figure 6.1**.

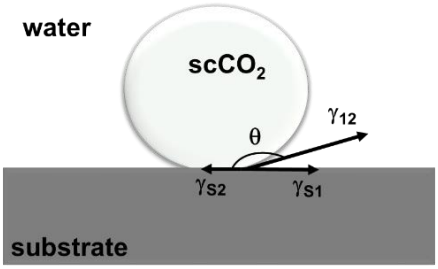

Figure 6.1. Schematic illustrating the contact angle as measured through the CO_2 phase. In this example, the mineral substrate is preferentially wet by water.

A number of studies measured contact angles as a function of pressure, temperature, surface chemistry, and brine composition, by either experiments or molecular dynamics simulations [285-294]. For example, Dickson et al. [285] developed a high-pressure apparatus to measure CO_2/water/solid contact angles on glass substrates with different hydrophilicities as quantified by the silanol (SiOH) surface density. As the CO_2 pressure increased from atmospheric pressure to 61.2 bar at 296 K, the results showed that θ increased from 71 to 99° on the substrate with 37% SiOH, and from 98 to 141° on the substrate with 12% SiOH. Wang et al. [288] measured contact angles on quartz, calcite, microcline, kaolinite, illite, and

phlogopite, in a CO_2 environment under conditions relevant to GCS. The results show that all the minerals are water-wet ($\theta < 30°$). These studies reported that the temperature and pressure dependence of contact angles exhibits no clear trend for all surfaces, while both pH and ionic strength are good predictors of contact angle. Concerning simulations, Chen et al. [295] found a good agreement between MD simulations and experimental results when they studied water contact angles on quartz in the presence of CO_2 at GCS conditions. The water contact angle was found to increase as the ionic strength increased; pressure and temperature were found to have weak effect on the contact angle. Other MD simulations suggest that, for water on three silica surfaces [290], the dependence of θ on pressure and temperature is controlled by the silanol number density on solid surfaces.

Porous sandstone and carbonate formations are considered as potential sites for CGS. Most carbonate minerals are composed of limestone and dolostone. Because calcite is the major component in limestone and widely present in geological systems, it is among the most studied minerals. Numerous experiments quantified the wettability of systems composed of calcite, CO_2, and brine [286-288, 296-298]. However, the experimental results are somewhat inconsistent regarding the wetting behavior of calcite as a function of changes in temperature, pressure, and brine composition. For example, Arif et al. [296] measured the water contact angle in calcite/CO_2/brine systems as a function of pressure, temperature, and salinity for a wide range of conditions. They found that the contact angle increased with pressure and brine salinity and decreased with temperature. On the contrary, Espinoza and Santamarina [286] measured the contact angle at ambient temperature in a wide range of pressures, up to 20 MPa. They reported that the contact angles remained nearly constant as pressure increased and that dissolved NaCl had no significant effect on the measurements. The findings of Arif et al. [296] seem to be consistent with data obtained by Bikkina et al. [287], who reported a slight increase of water contact angle as the pressure increased from 1.38 to 5.52 MPa. However, this group reported a reduction in the contact angle at higher pressures (8.27–20.68 MPa). In contrast, Wang et al. [288] reported little dependence of the contact angle on pressure and temperature. It should however be recognized that surface roughness and the possible presence of organics on natural substrates, both of which are difficult to quantify, are likely to strongly affect contact angle measurements.

Given this inconsistency in the available results, the objective of this study is to develop a molecular-level understanding regarding the wettability of calcite at GCS conditions. To this

end, MD simulations are employed at atomistic resolution. Our results complement those recently reported by Silvestri et al. [299], who performed NVT simulations to compute the contact angle of cylindrical and spherical water droplets on the calcite $[10\bar{1}4]$ surface in a CO_2 atmosphere at 323 K and 20 MPa. Our work adopts two synergistic approaches. The first concerns the validation of the model implemented to simulate water, to ensure its suitability to describe the system of interest (the water−calcite interface). The second is a systematic investigation concerning the wettability of CO_2/brine/calcite systems as a function of pressure, temperature, and salinity. The remainder of this Chapter is structured as follows. In the first section, we provide a summary of the main features of the chosen force fields, the details of the system setup, and an overview of the simulation methodology implemented. In the next section, we present the MD simulation results, starting from the assessment of the force fields, followed by the wettability studies. We summarize our concluding remarks in the last section.

6.2. Simulation method and algorithms

6.2.1. Molecular models and force fields

The calcite slab was obtained from a calcite crystal terminated at the plane $[10\bar{1}4]$ [300]. In the first instance, the calcite surface was modelled using the force field developed by Xiao et al. [301]. This force field has been previously used to study the hydration layer structure near calcite surfaces and the calcium-mediated adhesion of nanomaterials [302, 303]. In our implementation, calcium and carbon atoms were kept rigid, while the oxygen atoms were allowed to move. The force field proposed by Raiteri et al. [304] was also considered to describe calcite, for comparison.

We implemented the elementary physical model with the intramolecular bond stretch and angle bend parameters developed by Cygan et al. [305] (EPM2) to describe CO_2. EPM2 is a flexible three-site model, which is able to describe accurately the interfacial behavior and the vibrational state of CO_2 at supercritical conditions [305]. For simulations conducted by implementing the force field developed by Raiteri et al. [304] to describe calcite, we used the set of force field parameters proposed by Silvestri et al. [306] to describe the CO_2−calcite interactions. In this approach, the interactions between CO_2 and calcite were described by Buckingham and Coulomb potentials.

Although a number of different force field models are available for water, no single model accurately captures all its physical properties. To select the water model suitable for the present investigation, we conducted equilibrium MD simulations for a thin film of water supported on calcite. The following water models were compared: the SPC/E [108], the SPC [153], the SPC flexible (SPC-FW) [307], the TIP3P [155], and the TIP4P/2005 [158]. Each model has advantages and disadvantages. The SPC/E model yields good results for structure and dynamics of bulk liquid water at ambient conditions [161, 227, 308] and for static dielectric constant over a very wide range of temperatures and densities [309], but it under-estimates water viscosity [310] and fails to reproduce experimental vapor pressure, as well as other thermodynamic properties at critical and supercritical conditions [311]. The SPC model is successful at reproducing the liquid−vapor coexistence curve and vapor pressure [312, 313], but it over-predicts the diffusion coefficient [314]. The SPC/Fw yields a better prediction of viscosity, diffusion coefficient, and dielectric constant at ambient conditions than SPC/E [313, 314], but it does not predict accurately isobaric heat capacity. The TIP4P/2005 model provides a good description of vapor−liquid equilibria densities [315], surface tension [316], and viscosity [317], but it fails in reproducing simultaneously the vapor and the liquid phases of water [315], as well as its dielectric constant [160]. The TIP3P model is commonly used to describe water interactions with biological molecules. However, it provides poor descriptions of water properties when compared to other models [160, 308]. A discussion is presented below that explains why the SPC/E water model was implemented to investigate the contact angle in calcite/brine/CO_2 systems as a function of T, P, and system composition.

The model proposed by Joung and Cheatham [318] was implemented for quantifying the properties of monovalent NaCl ions. This model yields reasonable estimates for the solubility of NaCl in water at room temperature (5.1 mol_{NaCl}/kg_{H2O}) when compared to experiments (6.15 mol_{NaCl}/kg_{H2O}) [319]. In all simulations conducted here, the NaCl concentration was maintained below the solubility limit as predicted by the respective models.

In all simulations conducted by implementing the force field developed by Xiao et al. [301] to describe calcite, non-bonded dispersive interactions were modeled by the 12-6 Lennard-Jones potential and electrostatic forces by implementing the Coulombic potential. The cut-off distance for interatomic interactions was fixed at 12 Å, and the long-range electrostatic interactions were calculated using the Particle-Particle Particle-Mesh solver [65]. The LJ

parameters for all cross interactions between different atoms were determined by applying Lorentz−Berthelot mixing rules [112].

6.2.2. Simulation setup

The simulation box was periodic in the three directions for all simulations in this study and contained a slab of calcite supporting one thin film of fluid.

To validate the water models, we performed simulations with 4558 water molecules placed on the calcite surface, which yielded a water film of ~30 Å in thickness. In these simulations, the X, Y, and Z dimensions of the simulation box were 97.14, 90.0, and 158.9 Å, respectively. In our model, the solid substrate was placed with its surface parallel to the XY plane. Along the Z direction, perpendicular to the solid surface, the box contained a slab of calcite of thickness 14.1 Å to provide the free-standing calcite support. The Z direction of the simulation box is elongated because a layer of the gas phase is allowed on top of the liquid film. Based on our prior work, this prevents boundary conditions to affect the results.

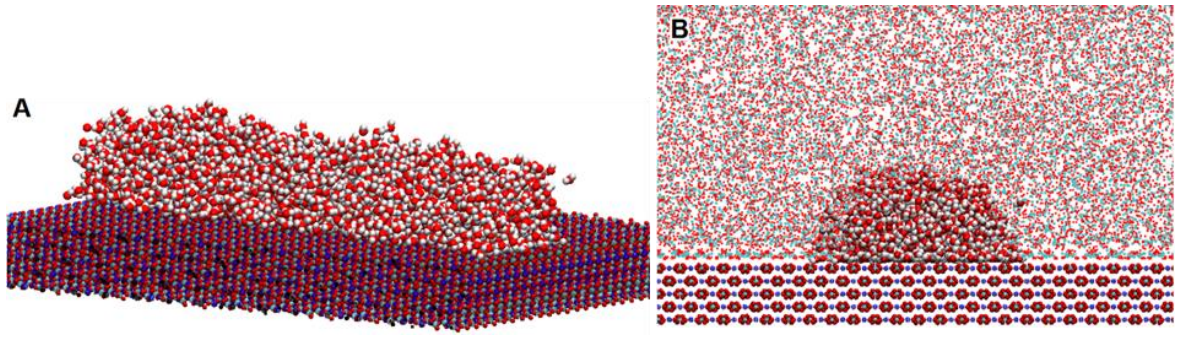

Figure 6.2. Initial configuration of one H_2O droplet on the calcite surface (a) and in the presence of CO_2 (b). Ca = blue; C = cyan; O = red; and H = white.

To study the wettability of calcite, we simulated systems in which a fluid droplet was placed on the substrate, and it was then surrounded by the other fluid. Both water droplets surrounded by CO_2, and CO_2 droplets surrounded by water were simulated. To avoid line-tension effects, we simulated cylindrical droplets, placed on the box parallel to the X direction [292, 320]. One initial configuration of the water droplet surrounded by CO_2 is shown in **Figure 6.2**. To generate the droplet, we first performed MD simulations of 2,000 water molecules placed on calcite. The simulations were carried out in the NVT ensemble, with a box size 97.14 × 180 × 100 $Å^3$. In this setup, the Y axis of the simulation box is elongated compared to the X axis. Because the cylindrical droplet is aligned parallel to the X

axis, an elongated Y axis prevents periodic boundary conditions from affecting the results. The final configuration of this simulation (**Figure 6.2a**) was then simulated in the presence of 10,426 CO_2 molecules, as shown in **Figure 6.2b**. The subsequent simulations were conducted in the NPT ensemble, wherein the pressure was controlled in the direction perpendicular to the calcite surface. To study CO_2 droplets, we used a similar procedure, within a box of initial box size 97.14 × 180 × 110 $Å^3$. The Z size of the simulation box was slightly increased compared to the prior simulations for computational reasons. As these simulations progressed, the length of the Z axis of the box decreased to ~104 Å to maintain the desired pressure. We explored the behavior of both pure water and NaCl brine at varying concentrations. The fluid phase compositions, as well as pressure, temperature, and brine composition for each system simulated within the approach exemplified in **Figure 6.2** are provided in **Table 6.1**.

Table 6.1. Composition and thermodynamic conditions of the CO_2/brine/calcite systems simulated

	Number of molecules			Temperature (K)	Pressure (MPa)
	H_2O	CO_2	NaCl		
H_2O droplet in CO_2	2,000	10,426		303 & 323	7 & 20
1.0 M NaCl droplet in CO_2	2,000	10,426	36	323	20
2.0 M NaCl droplet in CO_2	2,000	10,426	72	323	20
3.0 M NaCl droplet in CO_2	2,000	10,426	108	323	20
CO_2 droplet in H_2O	45,000	2,200		323	20
CO_2 droplet in 0.1 M NaCl	45,000	2,200	81	323	20
CO_2 droplet in 0.3 M NaCl	45,000	2,200	243	323	20
CO_2 droplet in 0.75 M NaCl	45,000	2,200	608	323	20
CO_2 droplet in 1.5 M NaCl	45,000	2,200	1,215	323	20

6.2.3. Algorithms

The assessment of water models was conducted by performing MD simulations using the package GROMACS (version 5.1.4) [113, 114] in the canonical ensemble (NVT), where the number of particles (*N*), the simulation volume (*V*), and the temperature (*T*) are kept constant.

The equations of motion were integrated by implementing the leapfrog algorithm [115] with a time step of 1.0 fs. The temperatures of calcite and that of the fluid phases were maintained constant at 298 K using two separate Nosé-Hoover thermostats [75, 76]. This allowed us to maintain the correct kinetic energy distribution between the solid and fluid [116]. Both

thermostats had a relaxation time constant of 100 fs. The total simulation time for each system was 30 ns. The system was considered equilibrated when atomic water density profiles oscillated around a constant value, and both system energy and temperature fluctuated within 10% of their respective average values. Each simulation was repeated three times to assess the reliability of the results. The last 2 ns of the simulations were used for production, and the simulated trajectories were used to extract the results presented in Section 6.3.1.

The simulations conducted to quantify the wettability of calcite were performed using the open-source LAMMPS code, version 20180818 [146]. These simulations were carried out in the NPT ensemble (constant number of atoms, constant pressure, and constant temperature). The pressure was coupled in the Z direction, perpendicular to the calcite surface, using the Nosé-Hoover barostat [321] with a relaxation time of 100 ps. The simulations were terminated when the droplet shape did not change and both fluids appeared stable within a simulated time of 12 ns. Each simulation was repeated three times to assess the reliability of the results.

6.2.4. Contact angle analysis

To identify the profile of a water droplet, the atomic density across the CO_2–water interface was fitted with the sigmoidal function [322]:

$$\rho(z) = \frac{1}{2}\rho_l\left[1 - \tanh\left(\frac{z - z_0}{d}\right)\right] \quad (6.2)$$

In Equation 6.2, ρ_l is the water liquid density, d is the width of the CO_2–water interface and z_0 is the position of the surface where the water density ρ_0 is halfway between the water bulk density and water density in the CO_2 phase.

Water contact angles were extracted from 2D density profiles obtained for the simulated water droplets fitted with Equation 6.2. The iso-density contours at $\rho = \rho_0$ were used to determine the contact angle for all of the systems considered. Once the droplet contours were known, a circular function was fit to them. Because density fluctuations occur near the calcite surface due to the water–calcite interactions, the region located within ~10 Å from the calcite surface was excluded from the fitting. The base of droplet was defined at the third hydration layer away from the calcite surface. The slopes of the tangent lines on both sides of droplet were averaged to extract the contact angle.

6.3. Simulation results

6.3.1. Assessment of water models

Among other phenomena that occur when a mineral surface is exposed to an aqueous solution, the formation of the hydration layer and its molecular structure is the most fundamental. Because the molecular structure within the hydration layer is of direct relevance to the wettability behavior, the suitability of the water models for the present study is assessed based on their ability to replicate experimental atomic density profiles at the calcite−water interface. For these simulations, the calcite substrate was modeled by implementing the force field developed by Xiao et al. [301].

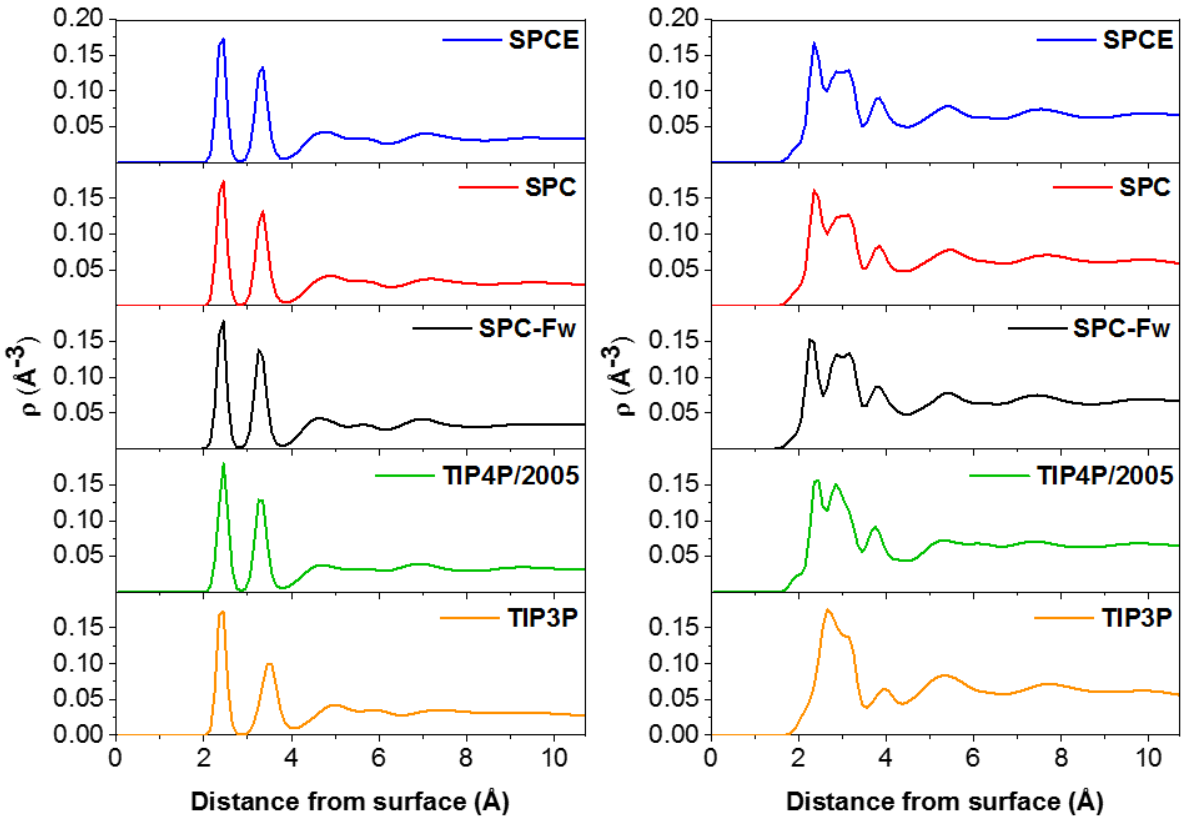

Figure 6.3. Atomic density profiles along the Z direction, vertical from the surface, for the oxygen (A) and hydrogen (B) atoms of water molecules. The reference position (i.e., z = 0) is defined by the z-position of the plane of Ca atoms on the calcite surface. In these simulations, calcite is described by implementing the force field proposed by Xiao et al. [301].

In **Figure 6.3**, we present the atomic density profiles of O and H atoms of water as a function of the vertical distance from the calcite surface. The results provide evidence for the formation of two well-defined water layers near the surface when implementing each of the water models considered. In **Table 6.2**, we summarize the positions of the two hydration

layers above the [10$\bar{1}$4] calcite surface as predicted in this study, as well as results from earlier publications. The positions of the two hydration layers were determined by the distance between the calcium carbonate plane and that formed by water O atoms. Overall, the location of the first water layer in this study is in general agreement with previous experimental and MD simulation results. The five models implemented here to simulate water consistently predict the location of the first layer at 2.45 Å from the calcium atoms in the surface. This result is in agreement with the experimental X-ray scattering findings reported by Fenter et al. [323], who found the presence of the oxygen atoms of water molecules at 2.50 ± 0.12 Å above the surface calcium ions. The five water models considered yield somewhat different positions for the second hydration layer. The result obtained from the TIP3P model is in good agreement with the X-ray scattering experiments reported by Geissbühler et al. [324], but results from the SPC/E and SPC models are more consistent with X-ray reflectivity [323], surface diffraction [325], and surface X-ray scattering data [324].

Table 6.2. Comparison of water structure results obtained at the calcite surface

Technique		**First layer (Å)**	**Second layer (Å)**
X-ray reflectivity [323]		2.50 ± 0.12	–
X-ray reflectivity [326]		2.14 ± 0.02	3.44 ± 0.12
Surface diffraction [325]		2.35 ± 0.10	3.24 ± 0.12
Surface X-ray scattering [324]		2.3 ± 0.1	3.45 ± 0.2
Ab initio simulation [327]		2.47	–
Quantum MD [328]		2.4	3.2
MD simulations from literature [329]		2.41	3.5
MD simulations from literature [306]		2.43	3.63
MD simulations (this work, Xiao et al.'s force field [301])	SPC/E	2.45	3.35
	SPC	2.45	3.35
	SPC/Fw	2.45	3.25
	TIP4P/2005	2.45	3.25
	TI3P	2.45	3.45
MD simulations (this work, Raiteri et al.'s force field [304])	SPC/E	2.19	3.31

The simulation results for the density profiles of H atoms present more pronounced differences when different water models are implemented. The H density profiles obtained when using either the SPC or SPC/E water models are very similar. Of the models that yield results consistent with experiments, the SPC/E one was chosen for the present study because

it is (a) computationally efficient, (b) reliable for assessing equilibrium structure and dynamics of liquid water, and (c) suitable for estimating the properties of aqueous electrolyte solutions. It should be pointed out that Nielsen et al. [330] found that the SPC/E model of water, when combined with the EPM2 model of CO_2, slightly overpredicts the water−CO_2 interfacial tension compared to experiments and underpredicts the expected surface excess of CO_2. For completeness, it is worth pointing out that, in general, no combination of force fields based on the LJ 12-6 functional form was found to be able to adequately represent properties of both coexisting phases of CO_2/H_2O binary mixtures [331, 332]. Using the EPM2−SPC/E combination, Vlcek et al. [333] optimized the cross-term interaction parameters to accurately reproduce experimental mutual solubilities of water and CO_2 at supercritical CO_2 conditions. Orozco et al. [332] recently reported that the parameters optimized by Vlceket et al. yield excellent predictions for solubilities in the H_2O-rich phase but not in the CO_2-rich one. These limitations were found not to be related to the cross-term parameters but instead to the inherent limitations of the implemented model [334].

6.3.2. Calcite wettability

To quantify calcite wettability at conditions representative of GCS, cylindrical water droplets surrounded by CO_2 were simulated on calcite at elevated *P* and *T* conditions. The chosen conditions represent shallow (303 K and 7 MPa) and deep formations (323 K and 20 MPa), representative of injection sites [288]. The amount of water in our simulations is intentionally much smaller than that of CO_2, in an attempt to replicate conditions near the well bore, where CO_2 is injected. Although as the simulations progress, CO_2 molecules dissolve within the water droplet, we did not attempt to quantify the CO_2 solubility as a function of, for example, salt content in the aqueous phase.

To understand the contact angle dependency on salinity, we investigated NaCl brines at increasing concentration (1, 2 and 3 M). Experimental results suggest that the water contact angle changes with temperature, pressure, and salinity. Our simulations, using the parameters reported by Xiao et al. [301] in combination with the SPC/E water model and the flexible version of the EPM2 model reported by Cygan et al. [305], however, show that water and brine in the presence of CO_2 completely spread on calcite. This prevented us from estimating the contact angle using our approach. The evolution of the water and NaCl brine droplets supported on calcite as a function of simulation time is illustrated **Figure 6.4a** and **c**. Complete wetting was observed after ∼24 ns of simulations. It seems that the simulation

results are not consistent with reported macroscopic experimental observations because of the strong interactions between H_2O and calcite. This could be because the force field implemented here to study calcite [301] was originally developed to mainly study the mechanical properties of $CaCO_3$, as well as the interaction of $CaCO_3$ with water and proteins. To test this hypothesis, we conducted additional simulations implementing the force field developed by Raiteri et al. [304] to describe calcite and the set of force field parameters developed by Silvestri et al. [306] to model the interactions between CO_2 and calcite. Water is modeled with the SPC/E formalism in these simulations.

We report in **Appendix B** details regarding these simulations. In **Figure B.2** of **Appendix B**, we report the density profiles of water obtained implementing both the force field parameters developed by Xiao et al. [301] and those by Raiteri et al. [304]. In **Appendix B**, we also display the simulation results reported by Reischlet et al. [335]. The distances between the water oxygen atoms in the first, second, and third water layers predicted by our simulations implementing the force field developed by Raiteri et al. [304] are ~2.19, 3.31, and 4.81 Å, respectively, from the calcium carbonate plane on the calcite substrate. The first and second of these values are at shorter distances compared to those predicted when the force field developed by Xiao et al. [301] was implemented (i.e., see **Table 6.2**). However, they agree reasonably well with experimental results from surface X-ray scattering [324] and surface diffraction [325], respectively. The positions of the three hydration layers, as reported by Reischlet et al. [335] are 2.43, 3.63, and 4.91 Å, respectively, which are also in good agreement with the experimental data shown in **Table 6.2**. Our analysis suggests that the force field developed by Raiteri et al. [304] yields an interfacial water structure that is similar to the one predicted by implementing the force field proposed by Xiao et al. [301]. While there are some differences, in general both sets of predictions are in reasonable agreement with available experiments.

We therefore used the force field parameters proposed by Raiteri et al. [304] and Silvestri et al. [306] in combination with the SPC/E water model to predict the contact angle. To quantify the effect of droplet size on the predicted contact angle, a series of simulations were conducted using water droplets of different initial radii. Details for the simulated systems are summarized in **Table B.1** of **Appendix B**. **Figure 6.4c** shows one of the final configurations of one water droplet without salt simulated on the calcite surface in the presence of CO_2.

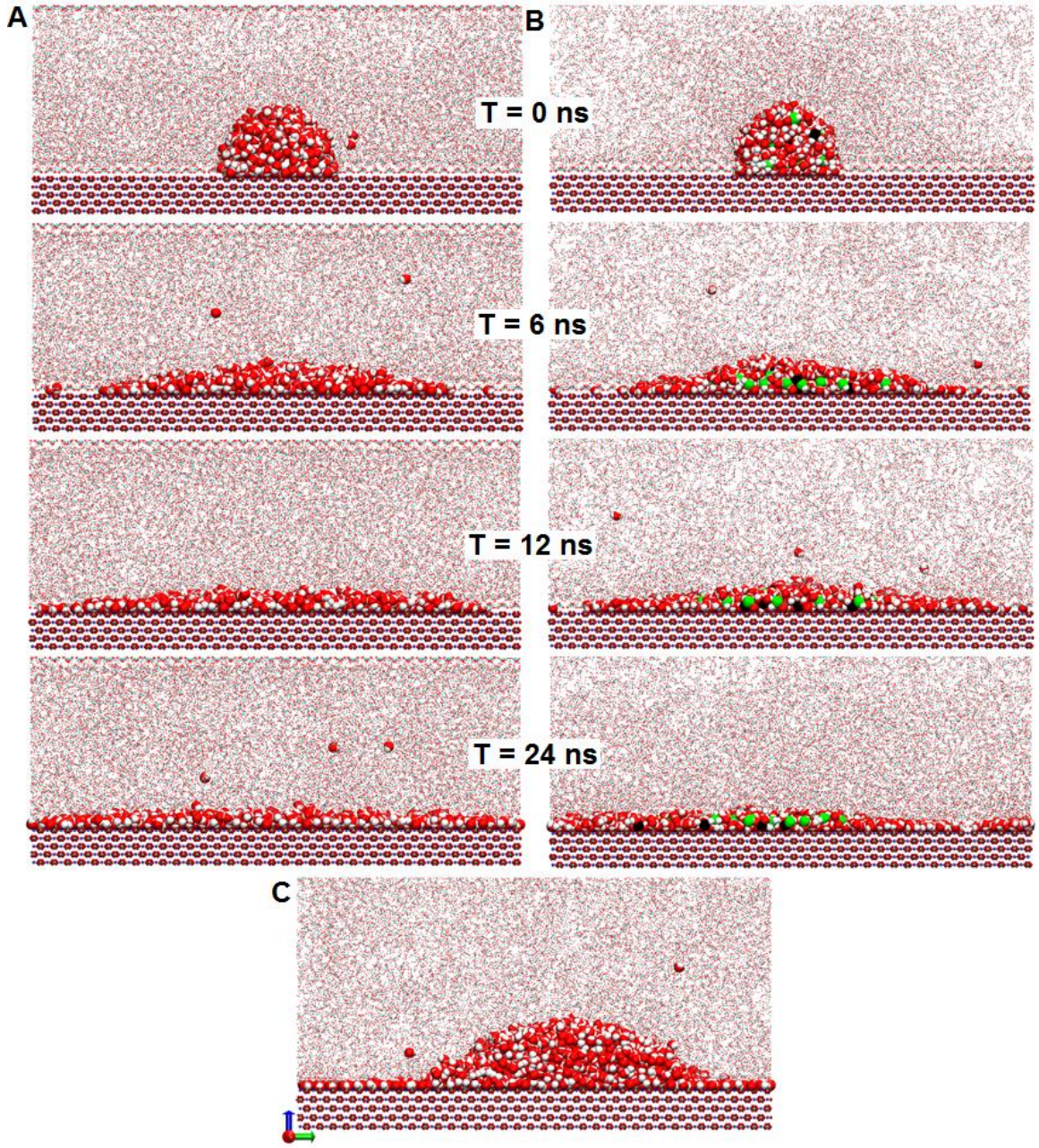

Figure 6.4. Sequence of simulation snapshots for (A) one water droplet containing no salt and (B) one water droplet containing 3 M NaCl salt as a function of simulation time. These simulations are conducted with the force field proposed by Xiao et al. [301] to describe calcite. (C) Snapshot of one pure water droplet after equilibration from simulations conducted by implementing the force field proposed by Raiteri et al. [304] to describe calcite and the set of force field parameters proposed by Silvestri et al. [306] to describe the CO_2−calcite interactions. These results were obtained simulating 5,000 H_2O molecules in the presence of 10,426 CO_2 molecules. All droplets are simulated in the presence of CO_2. The simulations were conducted at 323 K and 20 MPa. Ca = blue; C = cyan; O = red; H = white, Na^+= black; and Cl^-= green.

The corresponding 2D density profile and tangent lines for contact angle prediction are presented in **Figures B.3** and **B.4** of **Appendix B**. The contact angle for the CO_2-saturated water droplet on the calcite surface in the presence of CO_2 at 323 K and 20 MPa is found to converge to ~46° as the droplet size increases (see **Figure B.5** in **Appendix B**). By comparison, Silvestri et al. [299] recently reported water contact angles on calcite of 38° at 323 K and 20 MPa. Our simulation results strongly deviate from the experimental data reported by Arif et al. [296], who measured advancing (θ_a) and receding (θ_r) contact angles for CO_2/water/calcite systems and found that θ_a ~90° and θ_r ~80°. However, our simulations are somewhat consistent with the experimental data reported by Wang et al. [288], who reported the contact angle for water on calcite of ~26.2° at 323 K and 20 MPa.

Our analysis suggests that the force field parameters developed by Raiteri et al. [304] and Silvestri et al. [306] should be reliable for the prediction of the water contact angle for CO_2/water/calcite systems. However, force field developed by Xiao et al. [301] provides water density profiles near the calcite substrate that are in very good agreement with available experiments, as discussed in Section 6.3.1, and some experimental data report very different values for the contact angle. Therefore, it remains possible that the sources for the discrepancy between simulated and experimental contact angles are due to other effects, including the possibility that experimental calcite substrates are not perfect single crystal structures such as those simulated here. Further studies are required to clarify this situation and to test whether impurities such as organics might affect the contact angles. It should be pointed out that the force field parameters proposed by Silvestri et al. [306] have not yet been extended to include interactions with salt ions.

Even though injected supercritical CO_2 is typically the non-wetting phase in the presence of brine in many sedimentary rocks, it is of interest to quantify how CO_2 behaves on wet surfaces. For example, Wang et al. [297] investigated experimentally the adhesion of CO_2 on several homogeneous mineral surfaces, including calcite, under reservoir P and T conditions (323 K and 20 MPa). They reported that the addition of salt increased significantly CO_2 adhesion. The relationship between wettability, adhesion, and water layer structure was studied by Buckley et al. [336]. They suggested that the wettability of the mineral surface could be altered by introducing acids/bases to the system to break the electrical double layer structure and provide a strong charge imbalance at the surface. Liu et al. [328] performed extensive quantum MD simulations to investigate the mechanisms responsible for wettability

alteration of calcite. Density profiles of water and NaCl salt ions normal to the surface were calculated, as well as those of other ions such as Ca^{2+}, Mg^{2+}, and SO_4^{2-}. They found that Na^+ and Cl^- ions render the surface less water-wet, while Ca^{2+}, Mg^{2+}, and SO_4^{2-} render the surface more water-wet. To complement these simulations and in an attempt to connect to experiments, we assessed the affinity between CO_2 droplets and calcite in the presence of an aqueous-rich phase of various composition (see **Table 6.1**). Although the force field parameters developed by Raiteri et al. [304] and Silvestri et al. [306] yield water contact angles on calcite, in the presence of CO_2, which are in accordance with some experiments, those force fields do not yet allow for the inclusion of salt ions. For completeness, we conducted simulations for CO_2 droplets surrounded by pure water near calcite implementing the force field parameters developed by Raiteri et al. [304] and Silvestri et al. [306] in combination with the SPC/E water model. The results (**Figure 6.5**) how that the CO_2 droplet remains very close to the second hydration layer on calcite, which is consistent with the observations reported by Silvestri et al. [306], suggesting that strong interactions are present between CO_2 and hydration water on calcite. The effects of NaCl brine concentrations on the CO_2 droplet implementing the force fields developed by Raiteri et al. [304] and Silvestri et al. [306] were not considered in this study.

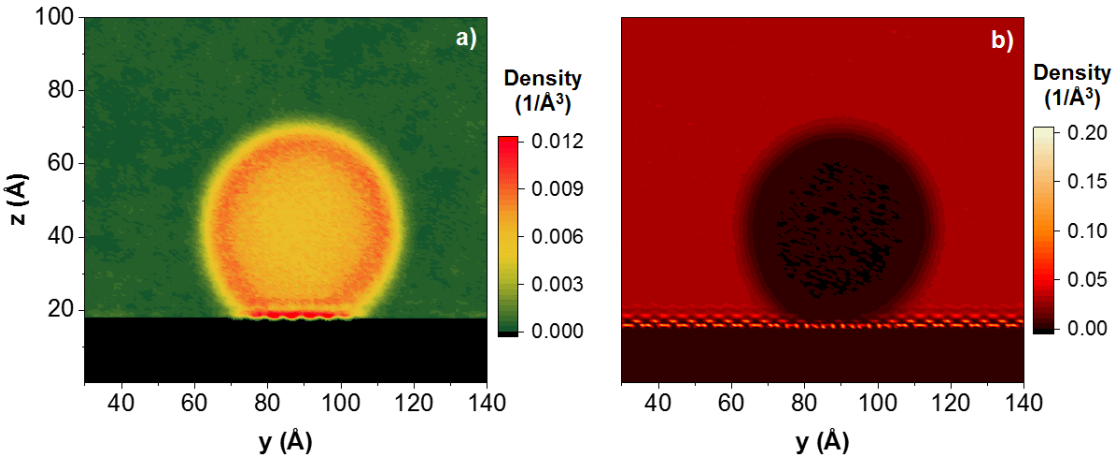

Figure 6.5. 2D density profiles of the CO_2 and H_2O averaged over the 2 ns of production run. The CO_2 droplet was surrounded by pure water. The simulations were conducted at 323 K and 20 MPa. Results are obtained for (a) CO_2 and (b) H_2O. The color bar expresses density in the units of $1/Å^3$. These simulations are conducted with the force field proposed by Raiteri et al. [304] to describe calcite and the set of force field parameters proposed by Silvestri et al. [306] to describe the CO_2–calcite interaction.

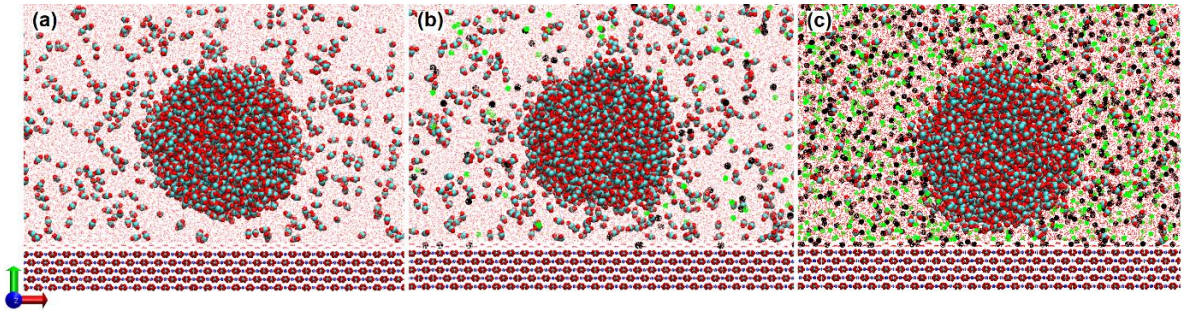

Figure 6.6. Snapshots of CO_2 droplets on the calcite surface in the presence of (a) pure water, 0.1 M NaCl brine and (c) 1.5 M NaCl brine. Small red dots represent H_2O molecules, and cyan, black, and green spheres represent carbon atoms, Na^+ and Cl^- ions, respectively. These simulations are conducted with the force field proposed by Xiao et al. [301] to describe calcite.

Because our results, combined with experimental data from literature, do not conclusively rule out that the force field proposed by Xiao et al. [301] yields reliable results and because this force field allows us to investigate the effect of NaCl concentration, we used this force field to quantify the effect of NaCl concentration. The resultant snapshots for the final configurations of cylindrical CO_2 droplets near calcite in the presence of different NaCl brines are shown in **Figure 6.6**.

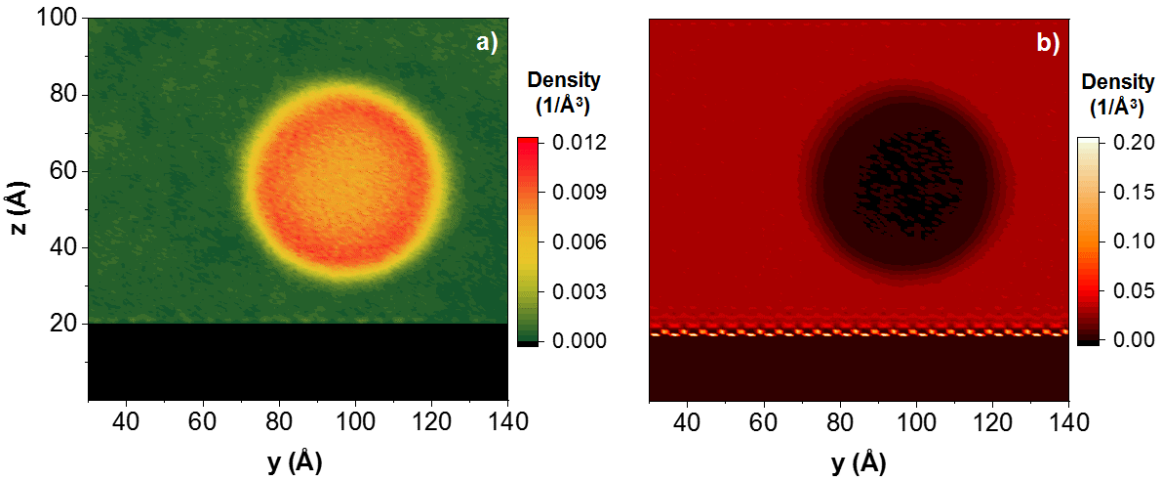

Figure 6.7. 2D density profiles of the CO_2 and H_2O averaged over the 2 ns of production run. The CO_2 droplet was surrounded by pure water. The simulations were conducted at 323 K and 20 MPa. Results are obtained for a) CO_2 and b) H_2O. The color bar expresses density in the units of $1/Å^3$. These simulations are conducted with the force field proposed by Xiao et al. [301] to describe calcite.

To complement and better quantify the results from simulation snapshots shown in **Figure 6.6**, we calculated 2D density profiles of CO_2 and the surrounding fluids at various conditions

within the plane perpendicular to the axis of the cylindrical droplet. For example, in **Figure 6.7**, we display the 2D density profiles of CO_2 and H_2O when the CO_2 droplet was surrounded by pure water at 323 K and 20 MPa. It can be seen that the CO_2 droplet did not adhere to calcite, possibly because of the extremely low contact angle predicted for water on calcite by our simulations, as displayed in **Figure 6.4a** and **b**.

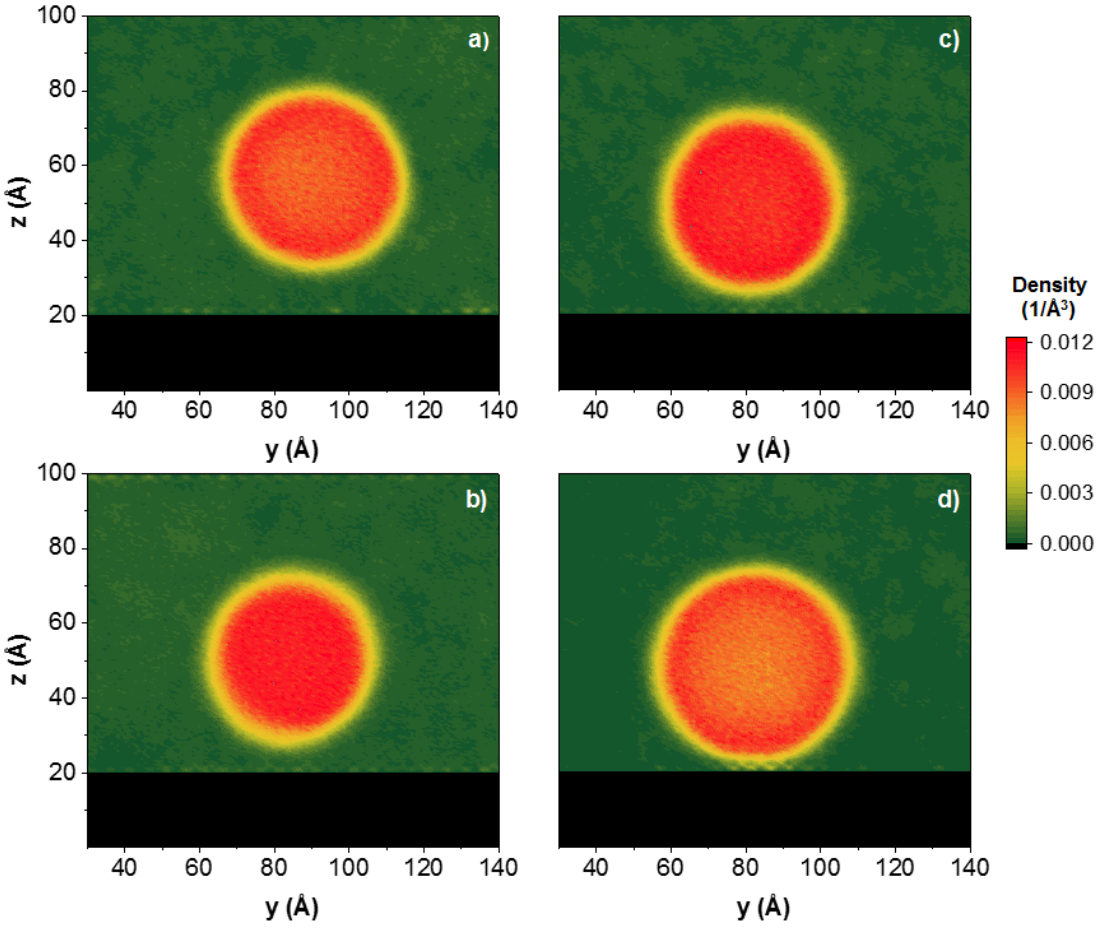

Figure 6.8. 2D density profiles of CO_2 droplets near calcite in the presence of NaCl brine at increasing salt concentration: (a) 0.1 M, (b) 0.3 M, (c) 0.75 M, and (d) 1.5 M. The simulations are conducted at 323 K and 20 MPa and the last 2 ns of the simulations are used for data analysis. The color bar expresses density in the unit of $1/Å^3$. These simulations are conducted with the force field proposed by Xiao et al. [301] to describe calcite.

The observations from **Figure 6.7** can be compared to similar ones obtained as the brine composition changes. In **Figure 6.8**, we report the 2D density profiles for CO_2 droplets near calcite in the presence of brines of different NaCl concentrations. Although the CO_2 droplets did not adhere to the calcite surface, as NaCl concentration increases from 0.1 to 1.5 M, the CO_2 droplet seems to become more affine to calcite with a slight tendency to approach the surface. This suggests that as NaCl concentration increases, the calcite surface becomes less

water-wet, potentially because the salt ions affect the interfacial hydrogen bond network. This is consistent with the results reported by Liu et al. [328], who suggested that the calcite surface becomes less water-wet because of the weak adhesion between the surface and NaCl brine. Liu et al. [328] reported that the calcite surface becomes oil-wet in the presence of 0.6 M NaCl brine.

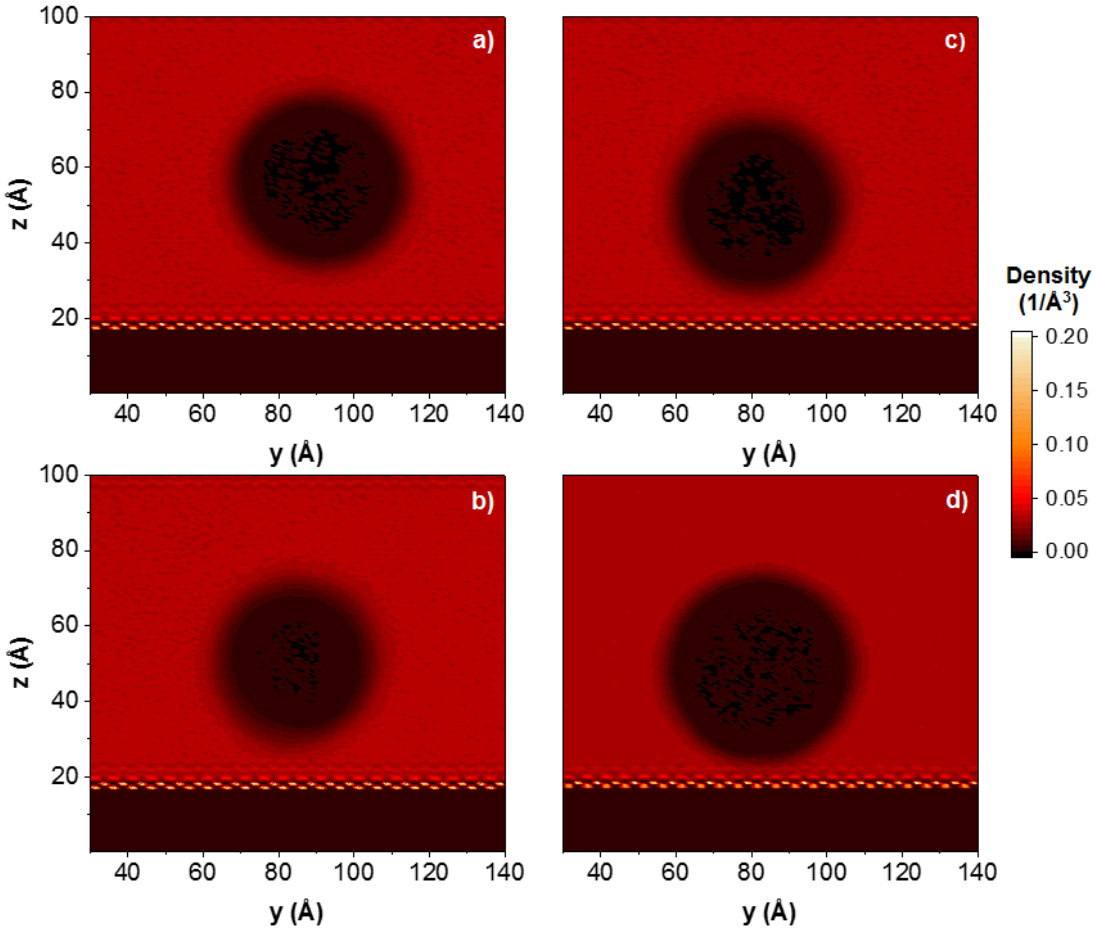

Figure 6.9. 2D density distributions of water oxygen atoms averaged over the final 2 ns of simulation conducted at 323 K and 20 MPa on the calcite surface in the presence of NaCl brine at increasing salt concentrations (a) 0.1, (b) 0.3, (c) 0.75, and (d) 1.5 M. The color bar expresses density in the unit of $1/Å^3$. These simulations are conducted with the force field proposed by Xiao et al. [301] to describe calcite.

The results in **Figure 6.8** demonstrate that salinity plays an important role in controlling the interactions between CO_2 droplets and calcite surfaces. In **Figure 6.9**, we also report the 2D densities of H_2O within the plane perpendicular to the axis of the cylindrical CO_2 droplet. The results show clearly that adding salt brings the CO_2 droplet closer to the calcite surface. In the remainder of this section, we attempt to use simulation results to identify the driving forces for the results just summarized.

In **Figure 6.10**, we show the density profiles of water and NaCl salt ions normal to the surface. The results show that water molecules formed two layers strongly adsorbed to the calcite surface, consistent with the results shown in **Figure 6.3**. The hydration layers affect the ability of the NaCl ions to directly interact with calcite. The ions density distributions reveal that Na^+ ions prefer to accumulate closer to the surface when compared to the Cl^- anions. Na^+ ions exhibit one pronounced density peak centered at ~3.00 Å, which is in between the O density peaks representative of the first and second hydration layers. In contrast, the Cl^- ions occur as two density peaks at ~5.00 and 7.35 Å.

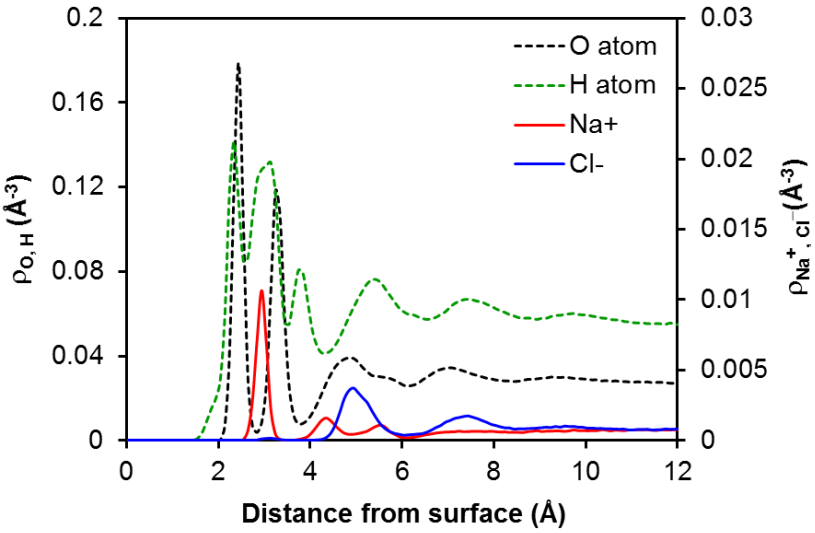

Figure 6.10. Z-density profiles of water and NaCl salt ions along the surface normal. The CO_2 droplet was surrounded by 1.5 M NaCl brine. The results were averaged over the last 2 ns of simulations conducted at 323 K and 20 MPa. The location of the calcite surface (at z = 0) is defined by the position of the plane of the surface Ca atoms. The results for other concentrations are shown in **Appendix B**. These simulations are conducted with the force field proposed by Xiao et al. [301] to describe calcite.

The height of the first Na^+ peak indicates that these ions strongly adsorb near the calcite/brine interface. This is supported by the planar density distributions obtained for the ions in the plane perpendicular to the droplet, shown in **Figure 6.11**. These results suggest the highest density of Na^+ ions is colocated with the first adsorbed layer on calcite, consistent with the results in **Figure 6.10**. Similarly, the Cl^- density is highest within the surface hydration region, above the positive Stern layer formed by Na^+ ions on the first water monolayer on the surface [337]. It should be noted that these results are in contrast with those obtained from aqueous NaCl solutions simulated on a model silica crystalline surface [202, 338]. In those studies, when the surface non-bridging oxygen atoms were fully protonated, Cl^- ions were

found to preferentially adsorb closer to the model silica surface than Na^+ ones. Both the structure of interfacial water and the availability of surface sites on which the ions can preferentially adsorb are responsible for these differences.

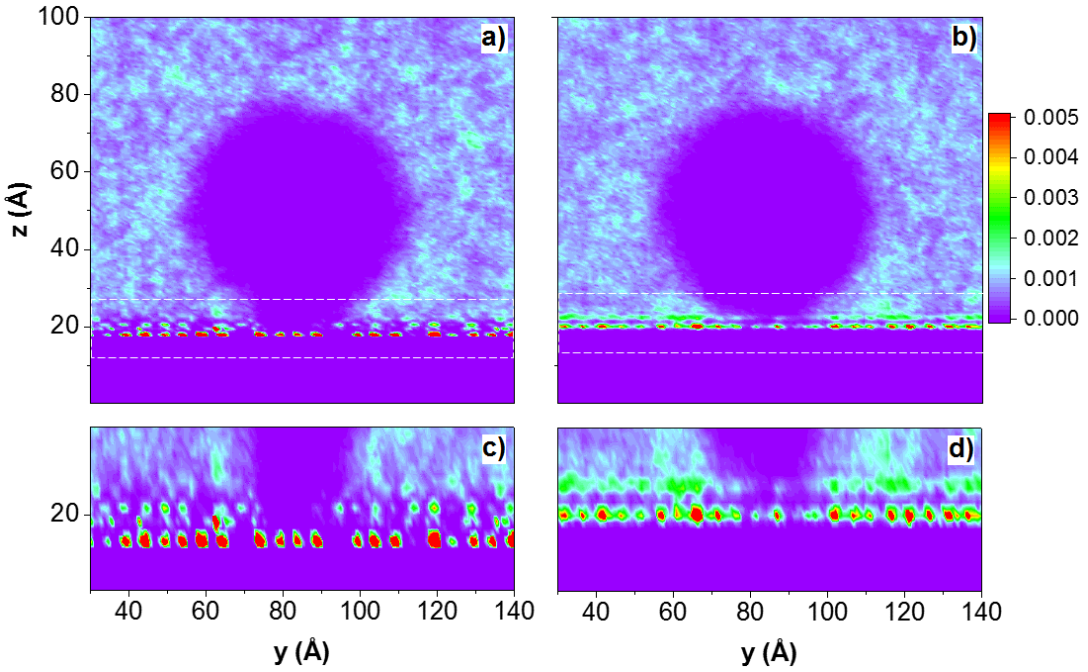

Figure 6.11. 2D density profiles of (a) Na^+ and (b) Cl^- ions surrounding the CO_2 droplet. The CO_2 droplet was surrounded by 1.5 M NaCl brine. The simulations are conducted at 323 K and 20 MPa, and the last 2 ns of the simulations are used for data analysis. Note the accumulation of ions, in particular Na^+, near the calcite substrate. The color bar expresses density in the unit of $1/Å^3$. In panels (c) and (d), we report expanded views of the interfacial region from panels (a,b), respectively. These simulations are conducted with the force field proposed by Xiao et al. [301] to describe calcite.

To further investigate the effects of NaCl on the interfacial properties of the system, we examined the surface density distribution of water oxygen atoms within the first two hydration layers and how they are affected by the presence of NaCl ions. The hydration layers are identified from the position of the O density peaks in **Figure 6.10**.

In **Figure 6.12**, we provide the surface density distribution of oxygen atoms within the first hydration layer, located at 2.9 Å from the plane of surface calcium atoms, and oxygen atoms within the second hydration layer, located 1 Å further from the first layer. The oxygen atoms in the first hydration layer yield a well-organized structure. It is likely that the pronounced structure of the first hydration layer is responsible for both the extremely low contact angle observed for water in our simulations (see **Figure 6.4a** and **b**) and also for not allowing the

CO_2 droplets to adhere directly on the surface. Density distributions at different salt contents are shown **Appendix B**.

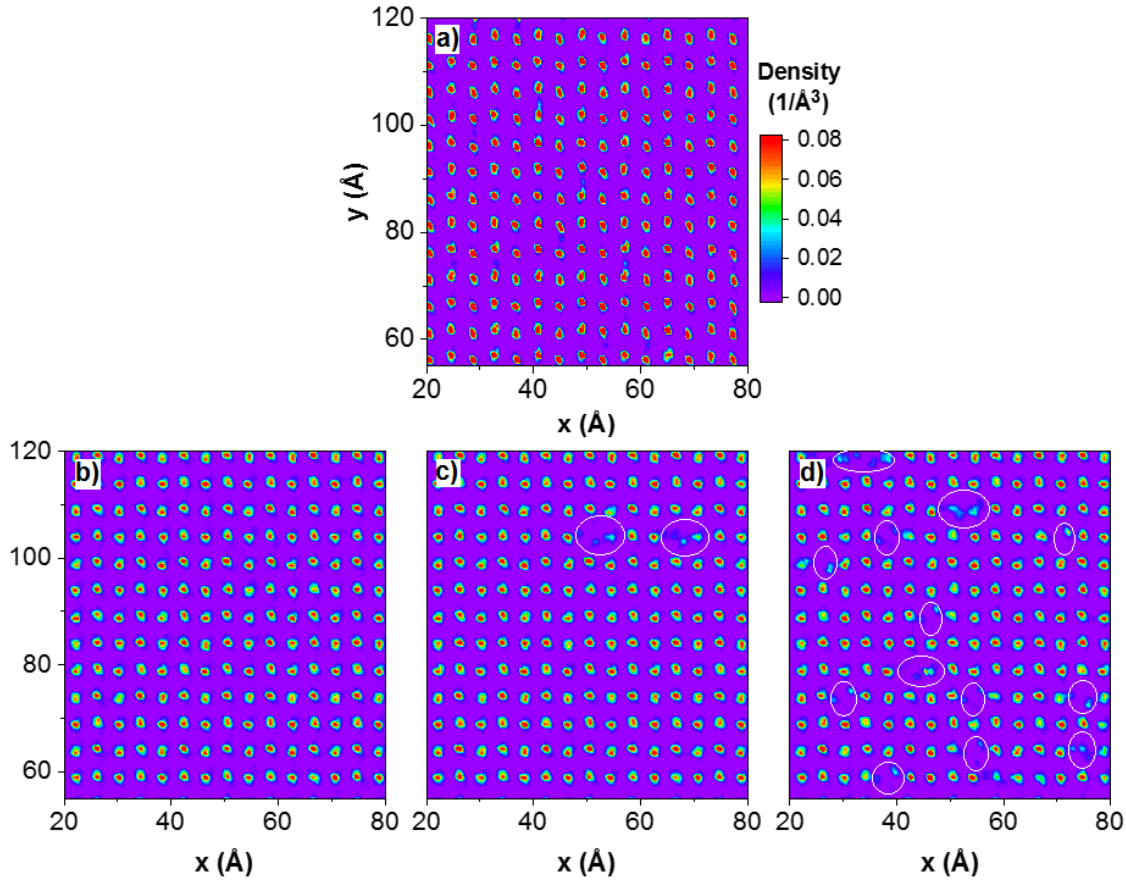

Figure 6.12. Surface density distribution of oxygen atoms within (a) the first and (b−d) the second hydration layer parallel to the X−Y plane. The figure shows the result of the first hydration layer obtained for the system in which the CO_2 droplet was surrounded by 1.5 M NaCl brine. Because the surface density distribution of oxygen atoms within the first hydration layer is similar for all systems, only one representative is shown for brevity in panel (a). The results of the second hydration layer were obtained for systems in which CO_2 droplet surrounded by pure water (b) and by NaCl brine at increasing salt concentrations: (c) 0.1 and (d) 1.5 M. The results for other concentrations are shown in **Appendix B**. The color bar expresses density in the unit of $1/Å^3$. These simulations are conducted with the force field proposed by Xiao et al. [301] to describe calcite.

The oxygen density distributions in the second hydration layer, shown in the bottom panels of **Figure 6.12**, indicate that NaCl ions strongly disrupts the arrangement of water molecules, as demonstrated by the missing accumulation of oxygen atoms within the regions highlighted by circles in panel (c) and panel (d). To complete the structural analysis of water molecules on the calcite surface, we also investigated the surface density distribution of hydrogen atoms within two hydration layers. These results are reported in **Appendix B**. In general, NaCl ions

affect the distribution of hydrogen atoms in both hydration layers, which suggests that the interfacial water structure is modified.

6.4. Conclusions

The wettability of the calcite surface was probed using atomistic MD simulations. Two force fields were compared to model the solid substrate and several to model water. In general, the models reproduced reasonably well the structure of the first two hydration layers of water formed on calcite as observed experimentally. However, when the force field parameterization proposed by Xiao et al. [301] was implemented, the strong water-wetting behavior predicted for the calcite surface prevented direct observation of the water contact angle as a function of temperature, pressure, and salinity. In fact, within the limits of our simulations, complete wetting of the calcite surface by pure water or NaCl brine solutions was observed, which seems at odds with available experimental data. When the simulations are conducted for one aqueous super-critical CO_2 droplet near calcite, the results strongly suggest that brine composition alters the affinity between a CO_2 droplet and calcite. In particular, NaCl ions disturb the hydration layers on calcite, which directly affects the affinity between the CO_2 droplet and the wet calcite surface. The simulation results suggest that increasing NaCl salt concentration allows the supercritical CO_2 droplet to more closely approach the surface.

When the force fields proposed by Raiteri et al. [304] and Silvestri et al. [306] were implemented to model calcite, the simulation results showed a contact angle for pure water, surrounded by CO_2, of ~46°. This value is in agreement with some experimental data reported in the literature, but others report contact angles as high as 80−90°. The set of force field parameters proposed by Silvestri et al. [306] has not yet been extended to investigate NaCl, and therefore, we could not quantify the effect of salt content on wetting properties. When a super-critical CO_2 droplet was simulated near calcite in the presence of pure water, the results suggested strong adhesion between the CO_2 droplet and the second hydration layer on calcite.

These results strongly suggest that force fields need to be improved to quantitatively capture the wetting properties of brine/CO_2/calcite systems via atomistic molecular simulations. However, the results suggest that ions dissolved in water can have a strong effect on the wetting properties. Further studies are required to fully quantify the effect of salt type and

concentration, as well as the effect of impurities. Once these effects are quantified, a better understanding of the important role played by brines in controlling the CO_2 wettability of caprocks is expected, which will yield more reliable predictions concerning structural trapping capacity and containment security in geological carbon sequestration.

Chapter 7. Summary and Outlook

7.1. Summary

Due to strong geometrical constraints imposed by nanoporous matrices, confined fluids are known to exhibit peculiar behaviour that deviates from the bulk. Understanding the behaviour of fluids in confinement could help in the design of new techniques for industrial processes involving porous materials, including catalysis, separation, and adsorption.

This thesis provided molecular level insights into structure, dynamics and reactivity of various fluids confined within amorphous silica cylindrical pores resembling those of MCM-41 materials by the means of equilibrium molecular dynamics simulations. When possible, all simulation results were compared to experimental data and/or theoretic reports from literature.

In **Chapter 3**, we used equilibrium molecular dynamics simulations to study fluid systems composed of propane and water, at different compositions, confined within cylindrical pores of diameter ~16 Å carved out of amorphous silica. The simulations are conducted within a single cylindrical pore. In the simulated system all the dangling silicon and oxygen atoms were saturated with hydroxyl groups and hydrogen atoms, respectively, yielding a total surface density of 3.8 $-OH/nm^2$. Simulations were performed at 300 K, at different bulk propane pressures, and varying the composition of the system. The structure of the confined fluids was quantified in terms of the molecular distribution of the various molecules within the pore as well as their orientation. This allowed us to quantify the hydrogen bond network and to observe the segregation of propane near the pore center. Transport properties were quantified in terms of the mean square displacement in the direction parallel to the pore axis, which allows us to extract self-diffusion coefficients. The diffusivity of propane in the cylindrical pore was found to depend on pressure, as well as on the amount of water present. It was found that the propane self-diffusion coefficient decreases with increasing water loading because of the formation of water bridges across the silica pores, at sufficiently high water content, which hinder propane transport. The rotational diffusion, the lifespan of hydrogen bonds, and the residence time of water molecules in contact with the silica substrate were quantified from the simulated trajectories using the appropriate autocorrelation functions. The simulation results were in qualitative agreement with experimental

quasielastic neutron scattering data, providing insights into transport properties of confined hydrocarbon in subsurface geologic environments.

In **Chapter 4**, equilibrium MD simulations implementing reactive force fields were conducted to elucidate the reliability of ReaxFF formalism in predicting bulk properties of selected common pure fluids, including CH_4, H_2O, CO_2 and H_2 when they do not undergo reactions. The 'combustion' ReaxFF was chosen as reactive force field. In the case of water, we also considered the 'aqueous' ReaxFF model. The results were compared to data obtained implementing popular classical force fields. In the gas phase, it was found that simulations conducted using the 'combustion' ReaxFF formalism yield structural properties in reasonably good agreement with classical simulations for CO_2 and H_2, but not for CH_4 and H_2O. In the liquid phase, 'combustion' ReaxFF simulations reproduce reasonably well the structure obtained from classical simulations for CH_4, degrade for CO_2 and H_2, and are rather poor for H_2O. In the gas phase, the simulation results are compared to experimental second virial coefficient data. The 'combustion' ReaxFF simulations yield second virial coefficients that are not sufficiently negative for CH_4 and CO_2, and slightly too negative for H_2. The 'combustion' ReaxFF parameterisation induces too strong an effective attraction between water molecules, while the 'aqueous' ReaxFF yields a second virial coefficient that is in reasonable agreement with experiments. The 'combustion' ReaxFF parameterisation yields acceptable self-diffusion coefficients for gas-phase properties of CH_4, CO_2 and H_2. In the liquid phase, the results are good for CO_2, while the self-diffusion coefficient predicted for liquid CH_4 is slower, and that predicted for liquid H_2 is about nine times faster than those expected based on classical simulations. The 'aqueous' ReaxFF parameterisation yields good results for both the structure and the diffusion of both liquid and vapour water.

In **Chapter 5**, equilibrium MD simulations implementing Si/C/H/O ReaxFF were conducted to investigate the possibility of CO_2 reduction within a cylindrical nanopore carved out of amorphous silica. Within the constraints of our simulations, which were conducted for 5 ns, no CH_4 molecules were detected in the temperature range of 400−1000 K, suggesting that the silica pore hinders the complete CO_2 reduction. This is consistent with the fact that silica is not an effective catalyst for CO_2 methanation. Our simulations, in agreement with literature reports, suggest that the silica pore surface facilitates the partial reduction of CO_2 to CO, which, within the conditions of our study, is found to be a stable product within the silica nanopores simulated. Analysis of the reaction products suggests that, although C−C bonds

did not form, fragments reminiscent of carboxylic acids and formate were observed. Because these compounds are part of the biological Krebs cycle, our results suggest that confinement could provide prebiotic precursors of core metabolic pathways. Our results could be useful for further developing applications in which catalysts are designed to promote CO_2 activation, for example, the one-step thermolysis of CO_2.

In **Chapter 6**, equilibrium MD simulations implementing different force fields available for water and solid substrate were conducted to investigate the wettability of the calcite surface at GCS conditions. The systems in which cylindrical water droplets surrounded by CO_2, and cylindrical CO_2 droplets surrounded by water were simulated. Several force fields are considered, achieving good agreement with experimental data for the structure of interfacial water but only partial agreement in terms of contact angles. In general, the results suggest that, at the conditions chosen, water strongly wet calcite, resulting in water contact angles either too low to be determined accurately with the algorithms implemented here or up to ~46°, depending on the force field implemented. These values are in agreement with some, but not all experimental data available in the literature, some of which report contact angles as high as 90°. One supercritical CO_2 droplet was simulated in proximity of the wet calcite surface. The results show pronounced effects due to salinity, which are also dependent on the force field implemented to describe the solid substrate. When the force field predicts complete water wettability, increasing NaCl salinity seems to slightly increase the calcite affinity for CO_2, monotonically as the NaCl concentration increases, because of the preferential adsorption of salt ions at the water−rock interface. When the other force field was implemented, it was not possible to quantify salt effects, but the simulations suggested strong interactions between the supercritical CO_2 droplet and the second hydration layer on calcite.

7.2. Outlook

7.2.1. Fluid behaviour under confinement

As mentioned in Chapter 3, the structure and dynamics of propane-water mixtures were investigated within only a 16 Å diameter cylindrical silica pore. More studies are needed to investigate the effect of the pore size and the pore geometry on the results presented. Future studies should also consider the presence of other compounds (e.g., benzene, H_2S and fatty acid) to better understand the fluid behaviour within narrow subsurface formations.

Regarding carbon dioxide methanation within silica pores, more simulations with different compositions of the confined fluids should be conducted to validate the observations reported in Chapter 5. Coating the substrate surface with proper catalytic sites (e.g., metals and oxides) could help to gain fundamental insights into the CO_2 methanation reaction.

Because of their inherent interfacial and confinement effects, nanoporous materials play a central role in a variety of geochemical phenomena in subsurface, including adsorption, fluid mobility, weathering, and flow of CO_2. Therefore, future studies should take into account different types of substrates which are representative of terrestrial rocks.

7.2.2. Interfacial interactions from a molecular perspective

Besides the confinement effects, the interactions occurring at the interfaces (i.e., fluid–fluid and rock–fluid interactions) also affect the distribution and flow behaviour of fluids. Fundamental insights into interfacial interactions are needed to reliably predict and control the macroscopic properties (e.g., wettability, adhesion, capillary pressure, and permeability) quantifying fluid flow and distribution through rock matrix, and ultimately reservoir quality. A process where understanding chemical and physical interactions at the solid-fluid interfaces is of interest is carbon capture and geologic storage. Due to a dramatic increase in atmospheric levels of carbon dioxide – a potent greenhouse gas, CO_2 sequestration efforts have been made in recent years. One of the most attractive approaches is the geologic carbon sequestration (GCS) into natural formations. A more comprehensive understanding of wettability of reservoir rocks at a molecular level can be helpful for optimizing CO_2 storage capacity and planning capture/storage strategies.

In rock aquifers, aside from CO_2, the organic compounds (e.g., pesticides, chlorinate solvents and hydrocarbons) are found to exist as coatings on mineral surfaces. Understanding the interactions between organic compounds and mineral surfaces is also helpful for various industrial and environmental applications, such as oil recovery, CO_2 storage and contamination remediation. Therefore, the structure and the adsorption of different organic molecules on surfaces should be fully investigated. Additionally, building on our prior simulation results, the question we will seek to understand is whether these organic compounds affect interfacial tension and wettability.

Appendix A

Supporting Information for Chapter 4 & Chapter 5

ReaxFF parameters

39 ! Number of general parameters

```
  50.0000    ! Overcoordination parameter
   9.5469    ! Overcoordination parameter
  26.5405    ! Valency angle conjugation parameter
   1.5105    ! Triple bond stabilisation parameter
   6.6630    ! Triple bond stabilisation parameter
   0.0000    ! C2-correction
   1.0588    ! Undercoordination parameter
   4.6000    ! Triple bond stabilisation parameter
  12.1176    ! Undercoordination parameter
  13.3056    ! Undercoordination parameter
 -70.1292    ! Triple bond stabilization energy
   0.0000    ! Lower Taper-radius
  10.0000    ! Upper Taper-radius
   2.8793    ! Not used
  33.8667    ! Valency undercoordination
   6.0891    ! Valency angle/lone pair parameter
   1.0563    ! Valency angle
   2.0384    ! Valency angle parameter
   6.1431    ! Not used
   6.9290    ! Double bond/angle parameter
   0.3989    ! Double bond/angle parameter: overcoord
   3.9954    ! Double bond/angle parameter: overcoord
  -2.4837    ! Not used
   5.7796    ! Torsion/BO parameter
  10.0000    ! Torsion overcoordination
   1.9487    ! Torsion overcoordination
  -1.2327    ! Conjugation 0 (not used)
   2.1645    ! Conjugation
   1.5591    ! vdWaals shielding
   0.1000    ! Cutoff for bond order (*100)
   2.1365    ! Valency angle conjugation parameter
   0.6991    ! Overcoordination parameter
  50.0000    ! Overcoordination parameter
```

1.8512 ! Valency/lone pair parameter
0.5000 ! Not used
20.0000 ! Not used
5.0000 ! Molecular energy (not used)
0.0000 ! Molecular energy (not used)
2.6962 ! Valency angle conjugation parameter

7 ! Nr of atoms; cov.r; valency; a.m; Rvdw; Evdw; gammaEEM; cov.r2; # alfa; gammavdW; valency; Eunder; Eover; chiEEM; etaEEM; n.u.; cov r3; Elp; Heat inc.; n.u.; n.u.; n.u.; n.u.; ov/un; val1; n.u.; val3, vval4

C	1.3825	4.0000	12.0000	1.9133	0.1853	0.9000	1.1359	4.0000
	9.7602	2.1346	4.0000	33.2433	79.5548	5.8678	7.0000	0.0000
	1.2104	0.0000	199.0303	8.6991	34.7289	13.3894	0.8563	0.0000
	-2.8983	2.5000	1.0564	4.0000	2.9663	0.0000	0.0000	0.0000
H	0.7853	1.0000	1.0080	1.5904	0.0419	1.0206	-0.1000	1.0000
	9.3557	5.0518	1.0000	0.0000	121.1250	5.3200	7.4366	1.0000
	-0.1000	0.0000	62.4879	1.9771	3.3517	0.7571	1.0698	0.0000
	-15.7683	2.1488	1.0338	1.0000	2.8793	0.0000	0.0000	0.0000
O	1.2477	2.0000	15.9990	1.9236	0.0904	1.0503	1.0863	6.0000
	10.2127	7.7719	4.0000	36.9573	116.0768	8.5000	8.9989	2.0000
	0.9088	1.0003	60.8726	20.4140	3.3754	0.2702	0.9745	0.0000
	-3.6141	2.7025	1.0493	4.0000	2.9225	0.0000	0.0000	0.0000
N	1.2333	3.0000	14.0000	1.9324	0.1376	0.8596	1.1748	5.0000
	10.0667	7.8431	4.0000	32.2482	100.0000	6.8418	6.3404	2.0000
	1.0433	13.7673	119.9837	2.1961	3.0696	2.7683	0.9745	0.0000
	-4.3875	2.6192	1.0183	4.0000	2.8793	0.0000	0.0000	0.0000
S	1.9401	2.0000	32.0600	2.0629	0.2095	1.0316	1.5483	6.0000
	9.9553	4.9055	4.0000	52.9998	112.1416	6.5181	8.2345	2.0000
	1.4601	9.6977	71.1843	5.7487	23.2859	12.7147	0.9745	0.0000
	-11.0200	2.7266	1.0338	6.2998	2.8793	0.0000	0.0000	0.0000
Si	2.0291	4.0000	28.0600	2.0043	0.1247	0.8218	1.5023	4.0000
	13.0000	2.0618	4.0000	11.8211	136.4845	1.8038	7.3852	0.0000
	-1.0000	0.0000	126.5182	3.6038	8.5961	0.2368	0.8563	0.0000
	-3.5163	4.2105	1.0338	6.2998	2.5791	0.0000	0.0000	0.0000
X	-0.1000	2.0000	1.0080	2.0000	0.0000	1.0000	-0.1000	6.0000
	10.0000	2.5000	4.0000	0.0000	0.0000	8.5000	15.0000	0.0000
	-0.1000	0.0000	127.6226	8.7410	13.3640	0.6690	0.9745	0.0000

-11.0000 2.7466 1.0338 6.2998 2.8793 0.0000 0.0000 0.0000

19 !Nr of bonds; Edis1; LPpen; n.u.; pbe1; pbo5; 13corr; pbo6; pbe2; pbo3; pbo4; Etrip; pbo1; pbo2; ovcorr

1 1 156.5953 100.0397 80.0000 -0.8157 -0.4591 1.0000 37.7369 0.4235
0.4527 -0.1000 9.2605 1.0000 -0.0750 6.8316 1.0000 0.0000

1 2 170.2316 0.0000 0.0000 -0.5931 0.0000 1.0000 6.0000 0.7140
5.2267 1.0000 0.0000 1.0000 -0.0500 6.8315 0.0000 0.0000

2 2 156.0973 0.0000 0.0000 -0.1377 0.0000 1.0000 6.0000 0.8240
2.9907 1.0000 0.0000 1.0000 -0.0593 4.8358 0.0000 0.0000

1 3 160.4802 105.1693 23.3059 -0.3873 -0.1613 1.0000 10.8851 1.0000
0.5341 -0.3174 7.0303 1.0000 -0.1463 5.2913 0.0000 0.0000

3 3 60.1463 176.6202 51.1430 -0.2802 -0.1244 1.0000 29.6439 0.9114
0.2441 -0.1239 7.6487 1.0000 -0.1302 6.2919 1.0000 0.0000

1 4 134.1215 140.2179 79.9745 0.0163 -0.1428 1.0000 27.0617 0.2000
0.1387 -0.3681 7.1611 1.0000 -0.1000 5.0825 1.0000 0.0000

3 4 130.8596 169.4551 40.0000 0.3837 -0.1639 1.0000 35.0000 0.2000
1.0000 -0.3579 7.0004 1.0000 -0.1193 6.8773 1.0000 0.0000

4 4 157.9384 82.5526 152.5336 0.4010 -0.1034 1.0000 12.4261 0.5828
0.1578 -0.1509 11.9186 1.0000 -0.0861 5.4271 1.0000 0.0000

2 3 180.4373 0.0000 0.0000 -0.8074 0.0000 1.0000 6.0000 0.5514
1.2490 1.0000 0.0000 1.0000 -0.0657 5.0451 0.0000 0.0000

2 4 231.8173 0.0000 0.0000 -0.3364 0.0000 1.0000 6.0000 0.4402
8.8910 1.0000 0.0000 1.0000 -0.0327 6.5754 0.0000 0.0000

1 5 129.1942 74.3656 55.2528 0.1066 -0.5211 1.0000 18.9617 0.5950
0.2950 -0.2398 8.0314 1.0000 -0.1019 5.6754 1.0000 0.0000

2 5 151.3159 0.0000 0.0000 -0.4644 0.0000 1.0000 6.0000 0.5950
9.4365 1.0000 0.0000 1.0000 -0.0303 7.0100 1.0000 0.0000

3 5 0.0000 0.0000 0.0000 0.5563 -0.4038 1.0000 49.5611 0.6000
0.4259 -0.4577 12.7569 1.0000 -0.1100 7.1145 1.0000 0.0000

4 5 0.0000 0.0000 0.0000 0.4438 -0.2034 1.0000 40.3399 0.6000
0.3296 -0.3153 9.1227 1.0000 -0.1805 5.6864 1.0000 0.0000

5 5 96.1871 93.7006 68.6860 0.0955 -0.4781 1.0000 17.8574 0.6000
0.2723 -0.2373 9.7875 1.0000 -0.0950 6.4757 1.0000 0.0000

1 6 90.6281 6.3660 0.0000 0.3176 -0.5558 1.0000 17.2117 0.5577
0.7223 -0.2118 7.7440 1.0000 -0.1039 5.4442 1.0000 0.0000

2	6	137.1002	0.0000	0.0000	-0.1902	0.0000	1.0000	6.0000	0.4256
		17.7186	1.0000	0.0000	1.0000	-0.0377	6.4281	0.0000	0.0000
3	6	230.7615	93.6959	43.3991	-0.3617	-0.3000	1.0000	36.0000	0.3161
		0.9856	-0.3882	4.6686	1.0000	-0.3960	4.5499	1.0000	0.0000
6	6	72.8867	50.0318	30.0000	0.9983	-0.3000	1.0000	16.0000	0.1000
		1.0538	-0.0447	10.6176	1.0000	-0.1452	8.0404	0.0000	0.0000

11 ! Nr of off-diagonal terms; Ediss; Ro; gamma ;rsigma; rpi; rpi2

1	2	0.1219	1.4000	9.8442	1.1203	-1.0000	-1.0000
2	3	0.0344	1.6800	10.3247	0.9013	-1.0000	-1.0000
2	4	0.1059	1.8290	9.7818	0.9598	-1.0000	-1.0000
1	3	0.1131	1.8523	9.8442	1.2775	1.1342	1.0621
1	4	0.1447	1.8766	9.7990	1.3436	1.1885	1.1363
3	4	0.1048	2.0003	10.1220	1.3173	1.1096	1.0206
1	5	0.1997	2.0109	9.8603	1.6611	1.3423	-1.0000
2	5	0.0938	1.8133	9.6519	1.3629	-1.0000	-1.0000
1	6	0.0250	1.7695	12.4753	1.5866	1.4409	-1.0000
2	6	0.0291	1.6805	12.5137	1.3429	-1.0000	-1.0000
3	6	0.1958	1.7958	11.1207	1.6105	1.1632	-1.0000

71 ! Nr of angles; at1; at2; at3; Thetao, o; ka; kb; pv1; pv2

1	1	1	67.2326	22.0695	1.6286	0.0000	1.7959	15.4141	1.8089
1	1	2	65.2527	14.3185	6.2977	0.0000	0.5645	0.0000	1.1530
2	1	2	70.0840	25.3540	3.4508	0.0000	0.0050	0.0000	3.0000
1	2	2	0.0000	0.0000	6.0000	0.0000	0.0000	0.0000	1.0400
1	2	1	0.0000	3.4110	7.7350	0.0000	0.0000	0.0000	1.0400
2	2	2	0.0000	27.9213	5.8635	0.0000	0.0000	0.0000	1.0400
1	1	3	49.5561	7.3771	4.9568	0.0000	0.7533	15.9906	1.0010
3	1	3	77.1171	39.8746	2.5403	-24.3902	1.7740	-42.9758	2.1240
1	1	4	66.1305	12.4661	7.0000	0.0000	3.0000	50.0000	1.1880
3	1	4	73.9544	12.4661	7.0000	0.0000	3.0000	0.0000	1.1880
4	1	4	64.1581	12.4661	7.0000	0.0000	3.0000	0.0000	1.1880
2	1	3	65.0000	14.2057	4.8649	0.0000	0.3504	0.0000	1.7185
2	1	4	74.2929	31.0883	2.6184	0.0000	0.0755	0.0000	1.0500
1	2	4	0.0000	0.0019	6.3000	0.0000	0.0000	0.0000	1.0400
1	3	1	74.3994	44.7500	0.7982	0.0000	3.0000	0.0000	1.0528
1	3	3	77.9854	36.6201	2.0201	0.0000	0.7434	67.0264	3.0000
1	3	4	82.4890	31.4554	0.9953	0.0000	1.6310	0.0000	1.0783
3	3	3	80.7324	30.4554	0.9953	0.0000	1.6310	50.0000	1.0783
3	3	4	84.3637	31.4554	0.9953	0.0000	1.6310	0.0000	1.0783

4	3	4	89.7071	31.4554	0.9953	0.0000	1.6310	0.0000	1.1519
1	3	2	71.5018	21.7062	0.4735	0.0000	0.5186	0.0000	1.1793
2	3	3	84.9468	23.3540	1.5057	0.0000	2.6374	0.0000	1.3023
2	3	4	75.6201	18.7919	0.9833	0.0000	0.1218	0.0000	1.0500
2	3	2	77.0645	10.4737	1.2895	0.0000	0.9924	0.0000	1.1043
1	4	1	66.0330	22.0295	1.4442	0.0000	1.6777	0.0000	1.0500
1	4	3	103.3204	33.0381	0.5787	0.0000	1.6777	0.0000	1.0500
1	4	4	104.1335	8.6043	1.6495	0.0000	1.6777	0.0000	1.0500
3	4	3	74.1978	42.1786	1.7845	-18.0069	1.6777	0.0000	1.0500
3	4	4	74.8600	43.7354	1.1572	-0.9193	1.6777	0.0000	1.0500
4	4	4	75.0538	14.8267	5.2794	0.0000	1.6777	0.0000	1.0500
1	4	2	69.1106	25.5067	1.1003	0.0000	0.0222	0.0000	1.0369
2	4	3	81.3686	40.0712	2.2396	0.0000	0.0222	0.0000	1.0369
2	4	4	83.0104	43.4766	1.5328	0.0000	0.0222	0.0000	1.0500
2	4	2	70.8687	12.0168	5.0132	0.0000	0.0222	0.0000	1.1243
1	2	3	0.0000	25.0000	3.0000	0.0000	1.0000	0.0000	1.0400
1	2	4	0.0000	0.0019	6.0000	0.0000	0.0000	0.0000	1.0400
1	2	5	0.0000	0.0019	6.0000	0.0000	0.0000	0.0000	1.0400
3	2	3	0.0000	0.0148	6.0000	0.0000	0.0000	0.0000	1.0400
3	2	4	0.0000	0.0019	6.0000	0.0000	0.0000	0.0000	1.0400
4	2	4	0.0000	0.0019	6.0000	0.0000	0.0000	0.0000	1.0400
2	2	3	0.0000	9.7025	6.0000	0.0000	0.0000	0.0000	1.0400
2	2	4	0.0000	0.0019	6.0000	0.0000	0.0000	0.0000	1.0400
1	1	5	73.9923	24.7559	1.8287	0.1463	0.0059	0.0000	1.0600
1	5	1	86.7521	36.5756	2.0199	0.1463	0.0058	0.0000	1.0600
2	1	5	75.1310	24.8619	1.8104	0.0000	0.0050	0.0000	1.0600
1	5	2	85.3326	36.9451	2.1403	0.0000	0.0388	0.0000	1.0706
1	5	5	86.0081	37.0451	2.1403	0.1463	0.1070	0.0000	1.0098
2	5	2	92.9959	36.9602	2.0403	0.0000	0.0050	0.0000	1.0200
2	5	5	83.2918	36.9451	2.0199	0.0000	0.0050	0.0000	1.0600
2	2	5	0.0000	0.0019	6.0000	0.0000	0.0000	0.0000	1.0400
6	6	6	71.6771	13.0081	3.6376	0.0000	0.2384	0.0000	1.3185
2	6	6	89.1207	11.7566	1.1579	0.0000	0.0100	0.0000	1.2975
2	6	2	26.3763	5.5393	0.9656	0.0000	2.3381	0.0000	1.1704
3	6	6	85.6335	17.1826	6.5759	0.0000	0.4105	0.0000	1.6398
2	6	3	59.6558	6.8748	7.0452	0.0000	4.0000	0.0000	1.0400
3	6	3	72.7359	17.5203	2.4434	0.0000	0.0100	0.0000	1.7374
6	3	6	18.3653	5.7702	3.4915	0.0000	4.0000	0.0000	1.9438
2	3	6	57.5894	40.0000	8.0000	0.0000	3.8263	0.0000	1.0534
3	3	6	54.5893	38.8349	7.6245	0.0000	2.7656	0.0000	3.0000
2	2	6	0.0000	47.1300	6.0000	0.0000	1.6371	0.0000	1.0400
6	2	6	0.0000	31.5209	6.0000	0.0000	1.6371	0.0000	1.0400

3	2	6	0.0000	31.0427	4.5625	0.0000	1.6371	0.0000	1.0400
1	1	6	63.8858	35.1811	0.6236	0.0000	2.6344	0.0000	2.3890
1	6	1	71.6429	31.1160	0.5107	0.0000	0.0100	0.0000	1.9113
6	1	6	63.2523	33.3810	2.2952	0.0000	0.0201	0.0000	1.7191
1	6	6	70.9876	29.7098	1.0210	0.0000	0.0100	0.0000	1.8242
2	1	6	96.9319	10.9008	1.4627	0.0000	2.4557	0.0000	1.5109
1	6	2	73.9320	16.6559	3.0433	0.0000	0.7961	0.0000	1.4005
1	3	6	91.5678	5.9243	2.4284	0.0000	2.9840	0.0000	1.0400
1	6	3	96.3796	36.5757	0.8505	0.0000	3.6964	0.0000	1.6527
3	1	6	42.5553	40.0000	1.5855	0.0000	1.0802	0.0000	1.1584

34 ! Nr of torsions; at1; at2; at3; at4; V1; V2; V3; V2(BO); vconj; n.u; n

1	1	1	1	-0.2500	11.5822	0.1879	-4.7057	-2.2047	0.0000	0.0000
1	1	1	2	-0.2500	31.2596	0.1709	-4.6391	-1.9002	0.0000	0.0000
2	1	1	2	-0.1770	30.0252	0.4340	-5.0019	-2.0697	0.0000	0.0000
1	1	1	3	-0.7098	22.2951	0.0060	-2.5000	-2.1688	0.0000	0.0000
2	1	1	3	-0.3568	22.6472	0.6045	-4.0088	-1.0000	0.0000	0.0000
3	1	1	3	-0.0528	6.8150	0.7498	-5.0913	-1.0000	0.0000	0.0000
1	1	3	1	2.0007	25.5641	-0.0608	-2.6456	-1.1766	0.0000	0.0000
1	1	3	2	-1.1953	42.1545	-1.0000	-8.0821	-1.0000	0.0000	0.0000
2	1	3	1	-0.9284	34.3952	0.7285	-2.5440	-2.4641	0.0000	0.0000
2	1	3	2	-2.5000	79.6980	1.0000	-3.5697	-2.7501	0.0000	0.0000
1	1	3	3	-0.0179	5.0603	-0.1894	-2.5000	-2.0399	0.0000	0.0000
2	1	3	3	-0.5583	80.0000	1.0000	-4.4000	-3.0000	0.0000	0.0000
3	1	3	1	-2.5000	76.0427	-0.0141	-3.7586	-2.9000	0.0000	0.0000
3	1	3	2	0.0345	78.9586	-0.6810	-4.1777	-3.0000	0.0000	0.0000
3	1	3	3	-2.5000	66.3525	0.3986	-3.0293	-3.0000	0.0000	0.0000
1	3	3	1	2.5000	-0.5332	1.0000	-3.5096	-2.9000	0.0000	0.0000
1	3	3	2	-2.5000	3.3219	0.7180	-5.2021	-2.9330	0.0000	0.0000
2	3	3	2	2.2500	-6.2288	1.0000	-2.6189	-1.0000	0.0000	0.0000
1	3	3	3	0.0531	-17.3983	1.0000	-2.5000	-2.1584	0.0000	0.0000
2	3	3	3	0.4723	-12.4144	-1.0000	-2.5000	-1.0000	0.0000	0.0000
3	3	3	3	-2.5000	-25.0000	1.0000	-2.5000	-1.0000	0.0000	0.0000
0	1	2	0	0.0000	0.0000	0.0000	0.0000	0.0000	0.0000	0.0000
0	2	2	0	0.0000	0.0000	0.0000	0.0000	0.0000	0.0000	0.0000
0	2	3	0	0.0000	0.1000	0.0200	-2.5415	0.0000	0.0000	0.0000
0	1	1	0	0.0000	50.0000	0.3000	-4.0000	-2.0000	0.0000	0.0000
0	3	3	0	0.5511	25.4150	1.1330	-5.1903	-1.0000	0.0000	0.0000
0	1	4	0	-2.4242	128.1636	0.3739	-6.6098	-2.0000	0.0000	0.0000
0	2	4	0	0.0000	0.1000	0.0200	-2.5415	0.0000	0.0000	0.0000
0	3	4	0	1.4816	55.6641	0.0004	-7.0465	-2.7831	0.0000	0.0000

0	4	4	0	-0.3244	27.7086	0.0039	-2.8272	-2.0000	0.0000	0.0000
4	1	4	4	-5.5181	8.9706	0.0004	-6.1782	-2.0000	0.0000	0.0000
0	1	5	0	0.1515	29.0501	0.0792	-4.5064	-1.0200	0.0000	0.0000
0	5	5	0	-0.0054	0.1000	0.1715	-2.2256	-1.0000	0.0000	0.0000
0	2	5	0	0.0000	0.0000	0.0000	0.0000	0.0000	0.0000	0.0000

9 ! Nr of hydrogen bonds; at1; at2; at3; Rhb; Dehb; vhb1

3	2	3	1.9682	-4.4628	1.7976	3.0000
3	2	4	2.0000	-6.0000	1.7976	3.0000
4	2	3	1.2000	-2.0000	1.7976	3.0000
4	2	4	1.2979	-6.0000	1.7976	3.0000
3	2	5	1.5000	-2.0000	1.7976	3.0000
4	2	5	1.5000	-2.0000	1.7976	3.0000
5	2	3	1.5000	-2.0000	1.7976	3.0000
5	2	4	1.5000	-2.0000	1.7976	3.0000
5	2	5	1.5000	-2.0000	1.7976	3.0000

Appendix B

Supporting Information for Chapter 6

In **Table B.1**, we report the system compositions considered to investigate the size effects on the water contact angle. The simulations were performed in the NPT ensemble at 323 K and 20 MPa for 30 ns. To estimate the error, the last 6 ns of simulation results were divided into three blocks and then the contact angle was calculated for each block. SPC/E [108] and EPM2 [305] force fields were used to model water and CO_2, respectively. To model calcite, we implemented the force field of Raiteri et al. [304]. The water–CO_2 cross terms were determined by applying Lorentz−Berthelot mixing rules. The interactions between CO_2 and calcite were described by implementing the set of force field parameters developed by Silvestri et al. [306]

The density profiles of NaCl salt ions along the surface normal at different concentrations are shown in **Figure B.1**.

In **Figure B.2**, we present the atomic density profiles of O and H atoms of water as a function of the vertical distance from the calcite surface. The simulations implementing the force field developed by Raiteri et al. [304] to describe calcite in combination with the SPC/E water were conducted in NVT ensemble at 298 K for 30 ns. We also report in **Figure B.2** results obtained for water molecules on the calcite plane $[10\bar{1}4]$ surface as reported by Reischlet et al. [335]

In **Figure B.3**, we present the water density profile of the system M5 (see **Table B.1**) in the direction normal to the calcite surface. The CO_2–water interface was determined by fitting the density profile with hyperbolic tangent function of Equation 6.2.

Figure B.4 shows the 2D atomic density profile of the H_2O droplet in the presence of CO_2 and an illustration presenting the contact angle estimation. The result was obtained from the simulations of the system M5 (see **Table B.1**).

Figure B.5 shows the predicted water contact angle as a function of the droplet initial radius.

Figure B.6 and **Figure B.7** show the surface density distributions of oxygen atoms within the first and second hydration layer, respectively. The first hydration layer is located at 2.9 Å

from the plane of surface Ca atoms; the second hydration layer is located 1 Å further from the first layer. Panel (a) shows the result obtained for system in which the CO_2 droplet was surrounded by pure water. Panel (b), (c), (d), and (e) show results obtained for systems in which the CO_2 droplet was surrounded by NaCl brine at increasing salt concentration. Similar results are shown in **Figure B.8** and **Figure B.9** for hydrogen atoms within the first and second hydration layer, respectively.

Table B.1. Composition of water–CO_2–calcite systems simulated to investigate the size effects on water contact angle

System	Radius (Å)	Number of molecules	
		H_2O	CO_2
M1	15	2,000	10,426
M2	23	3,000	10,426
M3	30	5,000	10,426
M4	38	6,500	10,426
M5	45	8,000	10,426

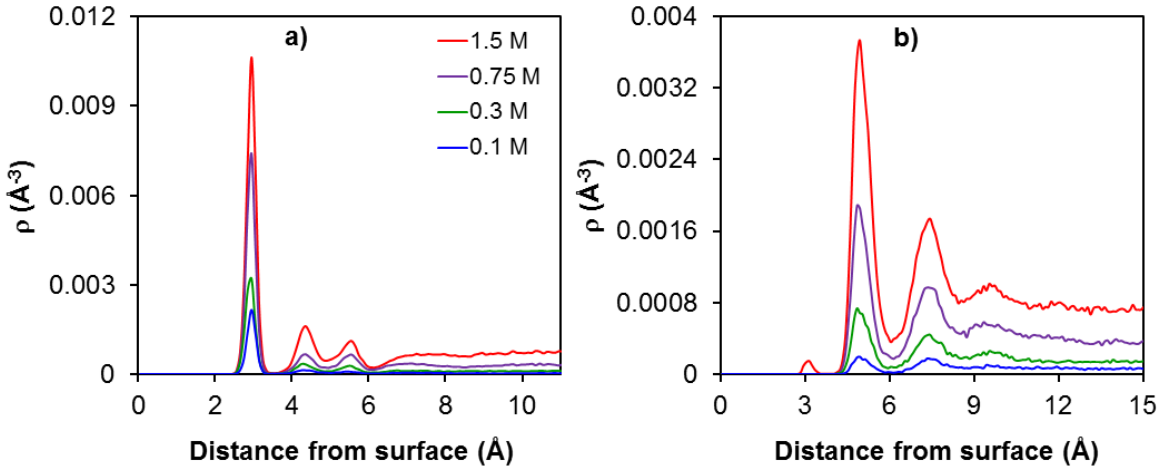

Figure B.1. Z-density profiles of NaCl salt ions along the surface normal. The CO_2 droplet was surrounded by NaCl brine at increasing salt concentration: (a) 0.1 M, (b) 0.3 M, (c) 0.75 M, and (d) 1.5 M. The results were averaged over the last 2 ns of simulations conducted at 323 K and 20 MPa. The location of the calcite surface (at z = 0) is defined by the position of the plane of the surface Ca atoms.

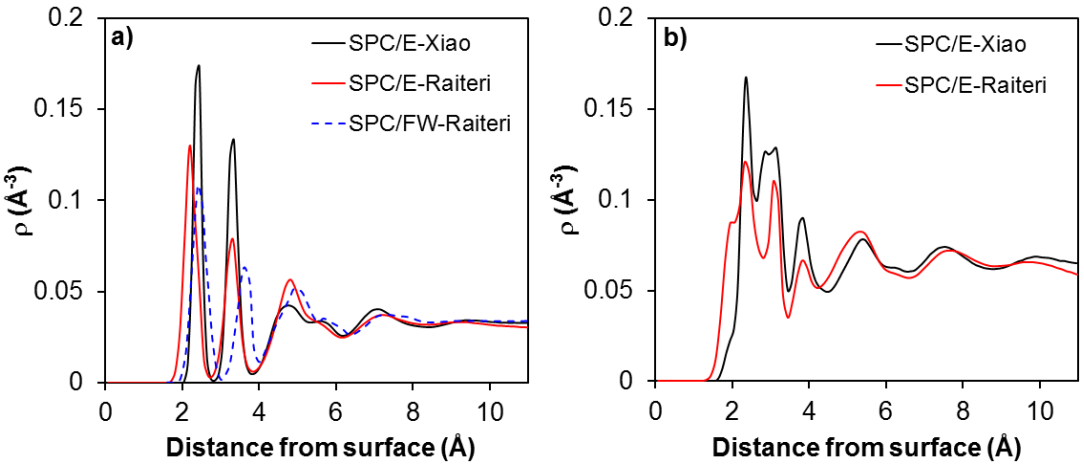

Figure B.2. Atomic density profiles along the Z direction, vertical from the surface, for the oxygen (a) and hydrogen (b) atoms of water molecules. Solid lines represent results obtained for water on the calcite surface considered here while the dash line in panel (a) represents result obtained for O atoms reported by Reischlet et al. [335] The reference position (i.e., z = 0) is defined by the z-position of the plane of Ca atoms on the calcite surface.

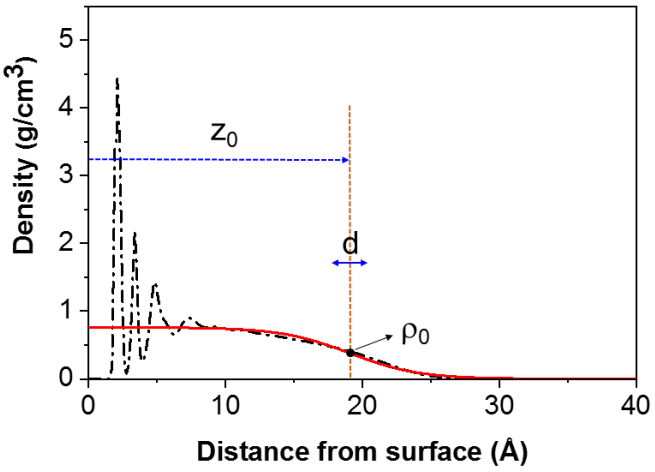

Figure B.3. Z-density profile of water along the surface normal. The dash line represents the data and the solid line gives the fit with the hyperbolic tangent function of Equation 6.2. The location of the calcite surface (at z = 0) is defined by the position of the plane of the surface Ca atoms.

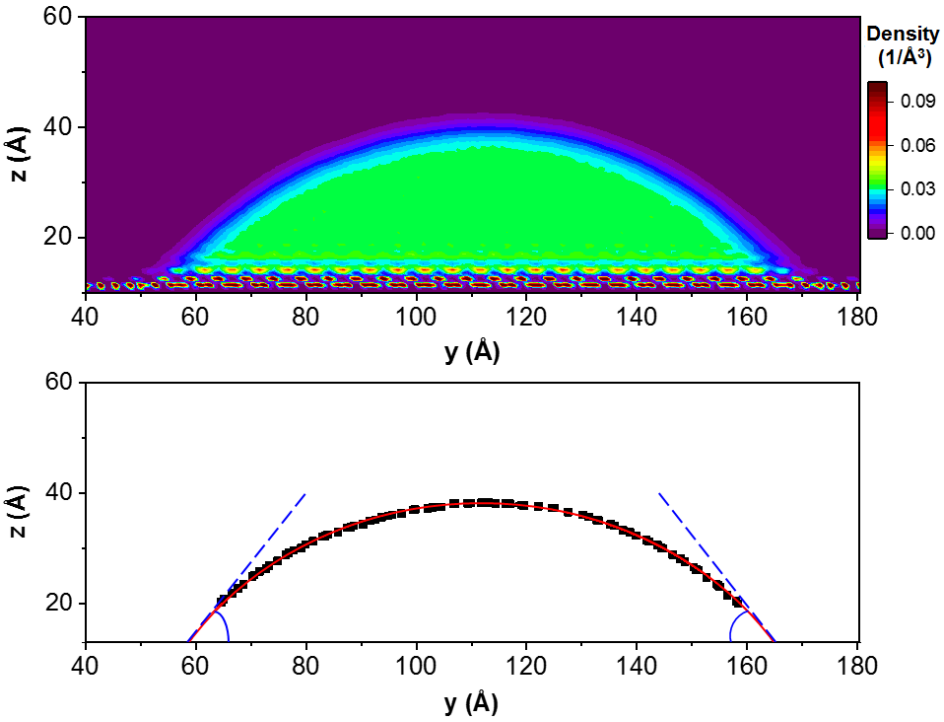

Figure B.4. Top: 2D density distribution of water oxygen atoms averaged over the final 6 ns of simulation conducted at 323 K and 20 MPa on the calcite surface in the presence of CO_2. The color bar expresses density in the unit of $1/Å^3$. Bottom: illustration of water contact angle prediction.

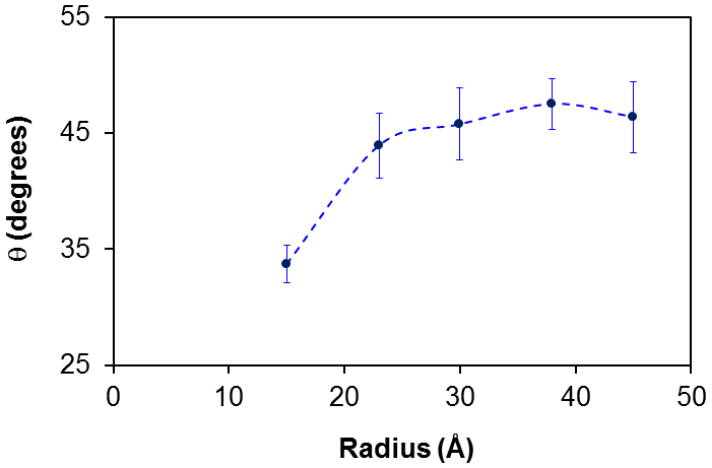

Figure B.5. Water contact angle on calcite in the presence of CO_2 at 323 K and 20 MPa as a function of initial droplet radius. Error bars are estimated as one standard deviation from the average.

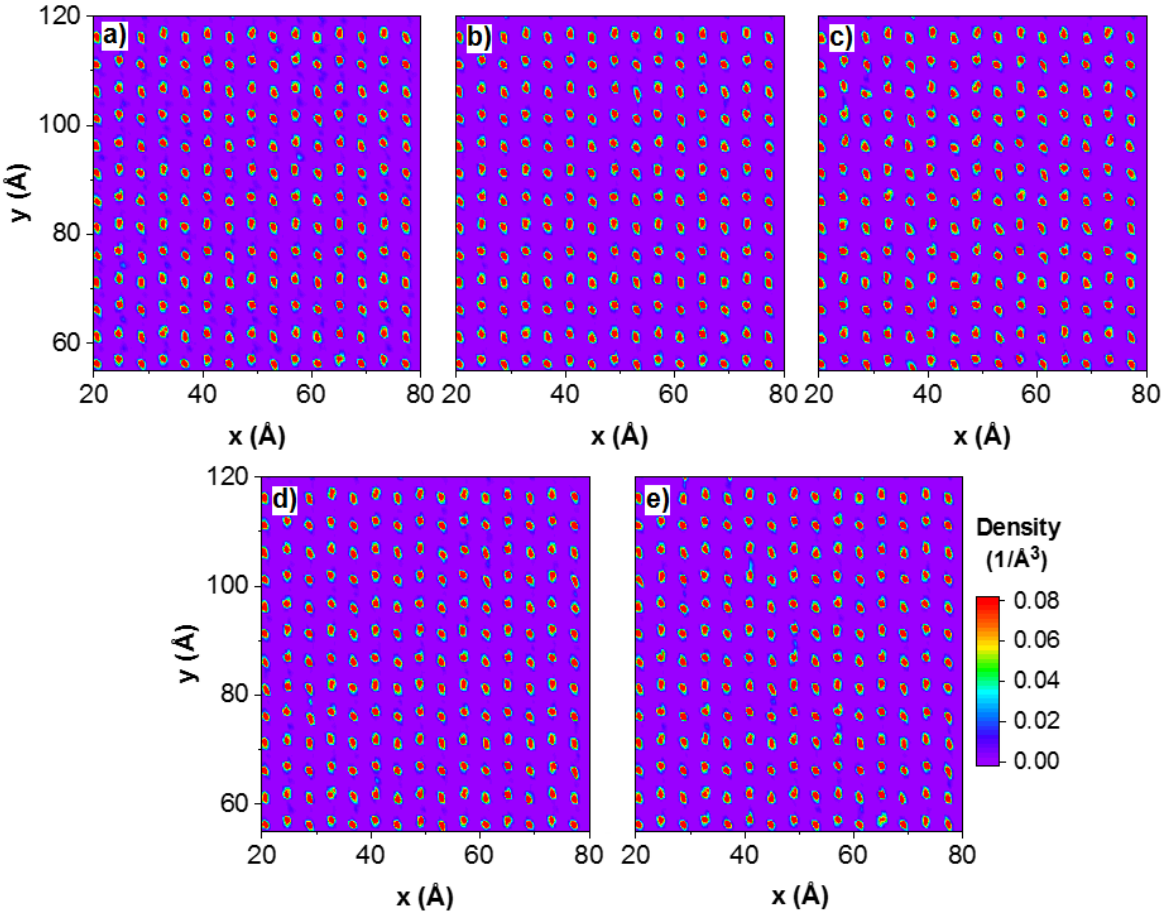

Figure B.6. Surface density distribution of oxygen atoms within the first hydration layer on calcite. The results were obtained for systems in which the CO_2 droplet was surrounded by pure water (a) and by NaCl brine at increasing salt concentration: (b) 0.1 M, (c) 0.3 M, (d) 0.75 M, and (e) 1.5 M. The color bar expresses density in the unit of $1/Å^3$.

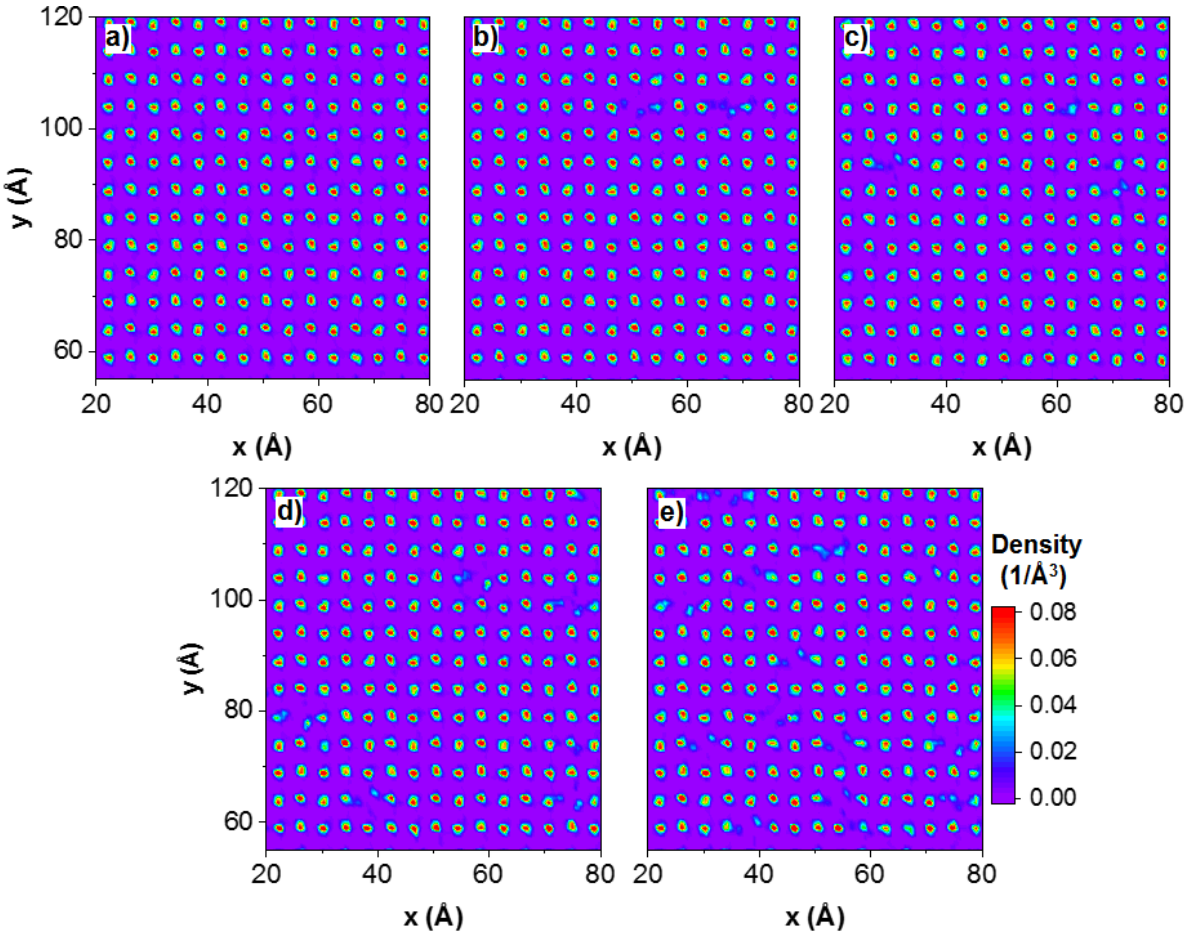

Figure B.7. Surface density distribution of oxygen atoms within the second hydration layer on calcite. The results were obtained for systems in which the CO_2 droplet was surrounded by pure water (a) and by NaCl brine at increasing salt concentration: (b) 0.1 M, (c) 0.3 M, (d) 0.75 M, and (e) 1.5 M. The color bar expresses density in the unit of $1/Å^3$.

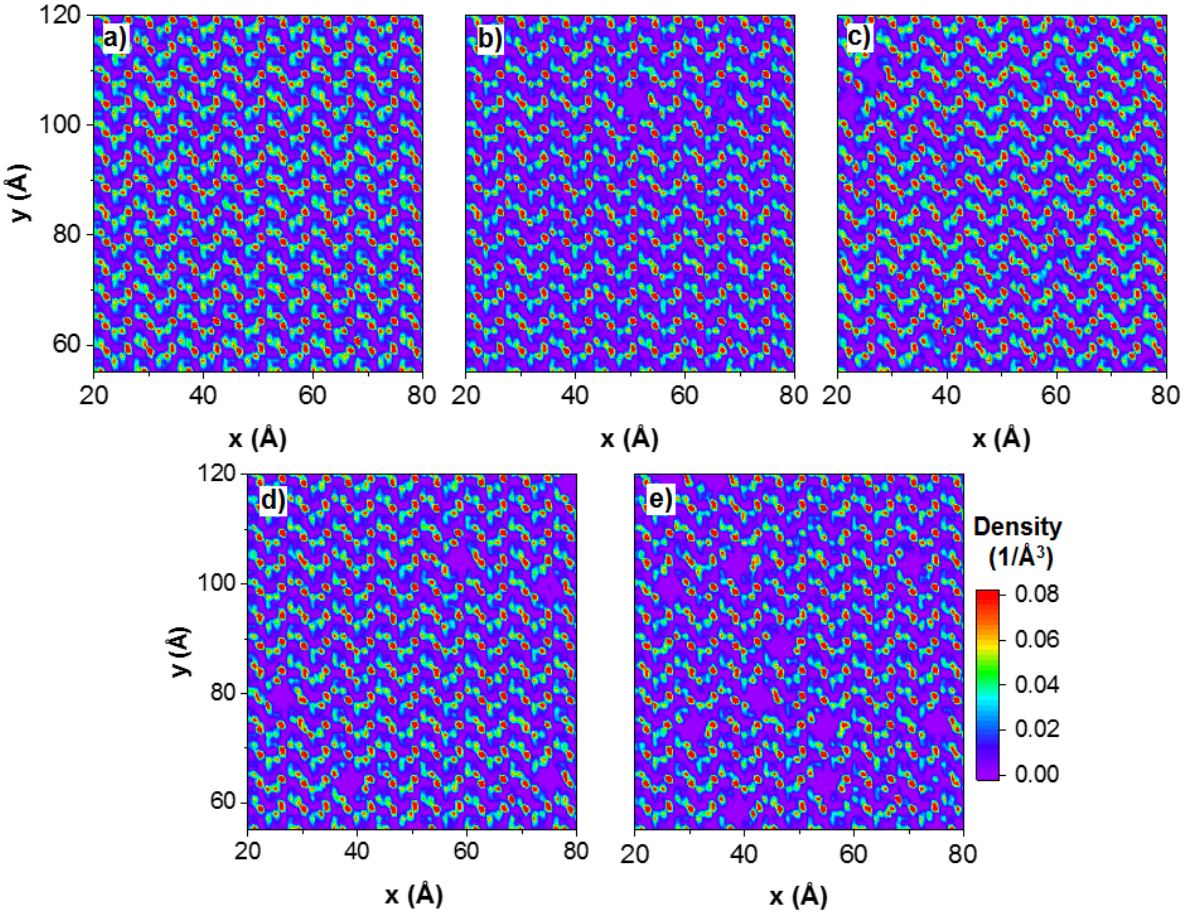

Figure B.8. Surface density distribution of hydrogen atoms within the first hydration layer on calcite. The results were obtained for systems in which the CO_2 droplet was surrounded by pure water (a) and by NaCl brine at increasing salt concentration: (b) 0.1 M, (b) 0.3 M, (c) 0.75 M, and (e, f) 1.5 M. The color bar expresses density in the unit of $1/Å^3$.

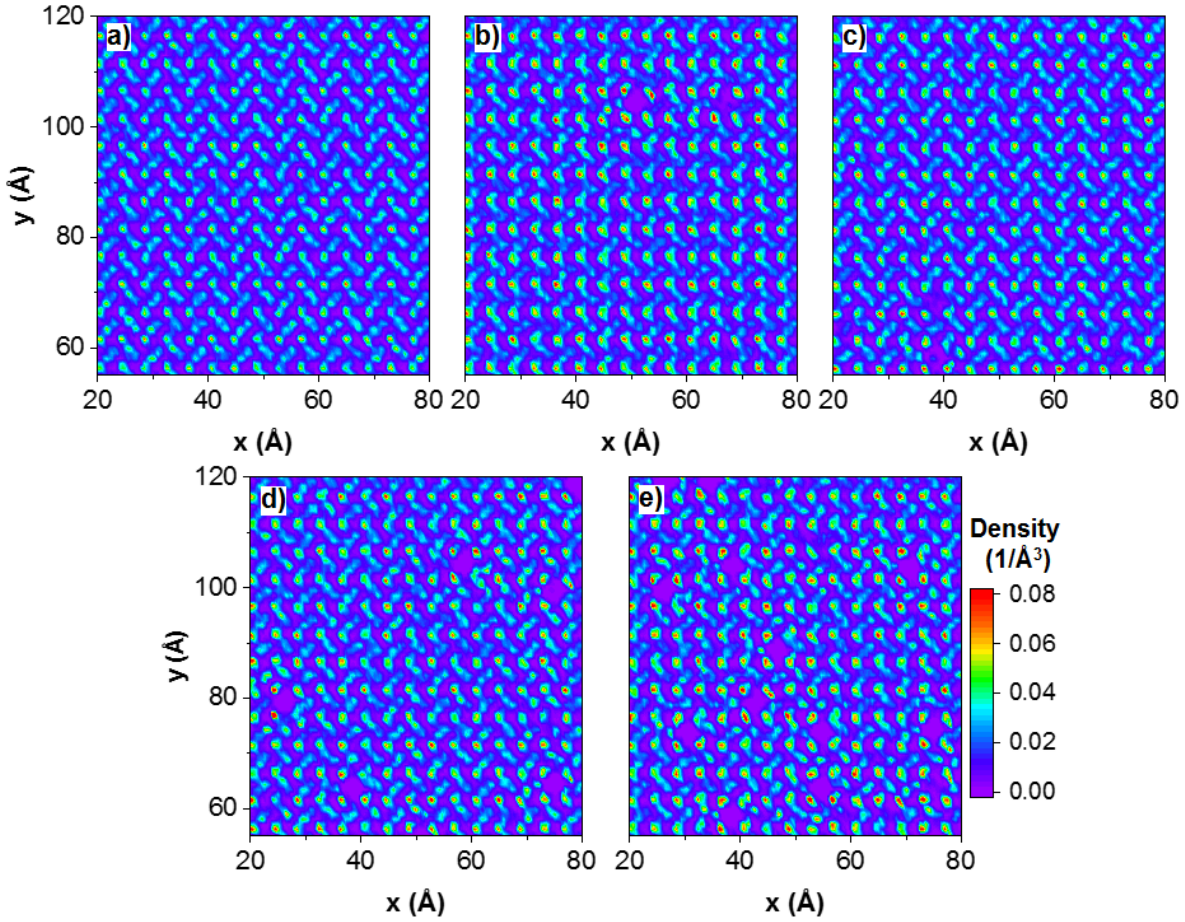

Figure B.9. Surface density distribution of hydrogen atoms within the second hydration layer on calcite. The results were obtained for systems in which the CO_2 droplet was surrounded by pure water (a) and by NaCl brine at increasing salt concentration: (b) 0.1 M, (b) 0.3 M, (c) 0.75 M, and (e, f) 1.5 M. The color bar expresses density in the unit of $1/Å^3$.

Bibliography

[1] Hugo K Christenson. Confinement effects on freezing and melting. *Journal of Physics: Condensed Matter*, 13(11):R95–R133, 2001.

[2] Denis Morineau, Yongde Xia, and Christiane Alba-Simionesco. Finite-size and surface effects on the glass transition of liquid toluene confined in cylindrical mesopores. *The Journal of Chemical Physics*, 117(19):8966–8972, 2002.

[3] L. A. Pozhar, E. P. Kontar, and Michael Z.-C. Hu. Transport properties of nanosystems: Viscosity of nanofluids confined in slit nanopores. *Journal of Nanoscience and Nanotechnology*, 2(2):209–227, 2002.

[4] Thu Le, Stephanie Ogbe, Alberto Striolo, and David R. Cole. N-octane diffusivity enhancement via carbon dioxide in silica slit-shaped nanopores – a molecular dynamics simulation. *Molecular Simulation*, 42(9):745–752, 2016.

[5] Carlos A. Grande and Alírio E. Rodrigues. Adsorption equilibria and kinetics of propane and propylene in silica gel. *Industrial & Engineering Chemistry Research*, 40(7):1686–1693, 2001.

[6] Thu Le, AlbertoStriolo, and David R.Cole. Propane simulated in silica pores: Adsorption isotherms, molecular structure, and mobility. *Chemical Engineering Science*, 121:292–299, 2015.

[7] Babak Fazelabdolabadi, and Aliasghar Alizadeh-Mojarad. A molecular dynamics investigation into the adsorption behavior inside {001} kaolinite and {1014} calcite nano-scale channels: the case with confined hydrocarbon liquid, acid gases, and water. *Applied Nanoscience*, 7:155–165, 2017.

[8] Roger F. Cracknell, Keith E. Gubbins, Michael Maddox, and David Nicholson. Modeling fluid behavior in well-characterized porous materials. *Accounts of Chemical Research*, 28(7):281–288, 1995.

[9] Lev D Gelb, K E Gubbins, R Radhakrishnan, and M Sliwinska-Bartkowiak. Phase separation in confined systems. *Reports on Progress in Physics*, 62(12):1573–1659, 1999.

[10] C Alba-Simionesco, B Coasne, G Dosseh, G Dudziak, K E Gubbins, R Radhakrishnan, and M Sliwinska-Bartkowiak. Effects of confinement on freezing and melting. *Journal of Physics: Condensed Matter*, 18(6):R15–R68, 2006.

[11] T. J. Bandosz, M. J. Biggs, K. E. Gubbins, Y. Hattori, Y. Iiyama, K. Kaneko, J. Pikunic, K. T. Thomson. Chemistry and physics of carbon. Ljubisa R. Radovic (ed.), volume 28. Marcel Dekker: New York, pages 41–228, 2003.

[12] A. D. McNaught, A. Wilkinson. IUPAC compendium of chemical terminology. Blackwell Scientific Publications: Oxford, UK, 1997.

[13] Jaison Jeevanandam, Ahmed Barhoum, Yen S. Chan, Alain Dufresne, Michael K. Danquah. Review on nanoparticles and nanostructured materials: history, sources, toxicity and regulations. *Beilstein Journal of Nanotechnology*, 9:1050−1074, 2018.

[14] Dimitrios Argyris, Naga Rajesh Tummala, Alberto Striolo, and David R. Cole. Molecular structure and dynamics in thin water films at the silica and graphite surfaces. *Journal of Physical Chemistry C*, 112(35):13587−13599, 2008.

[15] Dimitrios Argyris, David R. Cole, and Alberto Striolo. Hydration structure on crystalline silica substrates. *Langmuir*, 25(14):8025−8035, 2009.

[16] S. Alireza Bagherzadeh, Peter Englezos, Saman Alavi, and John A. Ripmeester. Influence of hydrated silica surfaces on interfacial water in the presence of clathrate hydrate forming gases. *Journal of Physical Chemistry C*, 116(47):24907−24915, 2012.

[17] Anh Phan, David R. Cole, and Alberto Striolo. Aqueous methane in slit-shaped silica nanopores: High solubility and traces of hydrates. *Journal of Physical Chemistry C*, 118(9):4860−4868, 2014.

[18] Thu Le, Alberto Striolo, and David R. Cole. CO_2-C_4H_{10} mixtures simulated in silica slit pores: Relation between structure and dynamics. *Journal of Physical Chemistry C*, 119(27):15274−15284, 2015.

[19] Siddharth Gautam, Thu Le, Alberto Striolo, and David Cole. Molecular dynamics simulations of propane in slit shaped silica nano-pores: direct comparison with quasielastic neutron scattering experiments. *Physical Chemistry Chemical Physics*, 19(48):32320−32332, 2017.

[20] P. Gallo, and M. Rovere. Glass transition and layering effects in confined water: A computer simulation study. *The Journal of Chemical Physics*, 113(24):11324−11335, 2000.

[21] Denis Morineau, Régis Guégan, Yongde Xia, and Christiane Alba-Simionesco. Structure of liquid and glassy methanol confined in cylindrical pores. *The Journal of Chemical Physics*, 121(3):1466−1473, 2004.

[22] Katsuhiro Shirono and Hirofumi Daiguji. Molecular simulation of the phase behavior of water confined in silica nanopores. *Journal of Physical Chemistry C*, 111(22):7938−7946, 2007.

[23] Anatoli A. Milischuk and Branka M. Ladanyi. Structure and dynamics of water confined in silica nanopores. *The Journal of Chemical Physics*, 135(17):174709, 2011.

[24] Hui Yan, and Shiling Yuan. Molecular dynamics simulation of the oil detachment process within silica nanopores. *Journal of Physical Chemistry C*, 120(5):2667−2674, 2016.

[25] W. Richard Bowen, and Julian S. Welfoot. Modelling the performance of membrane nanofiltration – critical assessment and model development. *Chemical Engineering Science*, 57(7):1121−1137, 2002.

[26] Tsuneji Sano, Keiko Doi, Hitoshi Hagimoto, Zhengbao Wang, Toshiya Uozumi, and Kazuo Soga. Adsorptive separation of methylalumoxane by mesoporous molecular sieve MCM-41. *Chemical Communications*, 733–734, 1999.

[27] GiselaGerstberger and Reiner Anwander. Screening of rare earth metal grafted MCM-41 silica for asymmetric catalysis. *Microporous and Mesoporous Materials*, 44–45:303–310, 2001.

[28] N. G. Holm. Marine hydrothermal systems and the origin of life: Report of SCOR working group 91: Kluwer, 1992.

[29] John Marsden. The molecular origins of life: Assembling pieces of the puzzle. André Black (ed.). Cambridge University Press, 1998.

[30] Judith B. Moody. Serpentinization: a review. *Lithos*, 9:125–138, 1976.

[31] N. H. Sleep, A. Meibom, Th. Fridriksson, R. G. Coleman, and D. K. Bird. H_2-rich fluids from serpentinization: Geochemical and biotic implications. *Proceedings of the National Academy of Sciences of the United States of America*, 101(35):12818–12823, 2004

[32] Bénédicte Ménez, Céline Pisapia, Muriel Andreani, Frédéric Jamme, Quentin P. Vanbellingen, Alain Brunelle, Laurent Richard, Paul Dumas, and Matthieu Réfrégiers. Abiotic synthesis of amino acids in the recesses of the oceanic lithosphere. *Nature*, 564:59–63, 2018.

[33] Kamila B. Muchowska, Sreejith J. Varma, and Joseph Moran. Synthesis and breakdown of universal metabolic precursors promoted by iron. *Nature*, 569:104–107, 2019.

[34] Thu Le, Alberto Striolo, C. Heath Turner, and David R. Cole. Confinement effects on carbon dioxide methanation: A novel mechanism for abiotic methane formation. *Scientific Reports*, 7:9021, 2017.

[35] J. Karl Johnson, Athanassios Z. Panagiotopoulos, and Keith E. Gubbins. Reactive canonical Monte Carlo: A new simulation technique for reacting or associating fluids. *Molecular Physics*, 81(3):717–733, 1994.

[36] W. R. Smith, and B. Triska. The reaction ensemble method for the computer simulation of chemical and phase equilibria .I. Theory and basic examples. *The Journal of Chemical Physics*, 100(4):3019–3027, 1994.

[37] Thomas P Senftle, Sungwook Hong, Md Mahbubul Islam, Sudhir B Kylasa, Yuanxia Zheng, Yun Kyung Shin, Chad Junkermeier, Roman Engel-Herbert, Michael J Janik, Hasan Metin Aktulga, Toon Verstraelen, Ananth Grama, and Adri C T van Duin. The ReaxFF reactive force-field: development, applications and future directions. *npj Computational Materials*, 2:15011, 2016.

[38] You Han, Dandan Jiang, Jinli Zhang, Wei Li, Zhongxue Gan, and Junjie Gu. Development, applications and challenges of ReaxFF reactive force field in molecular simulations. *Frontiers of Chemical Science and Engineering*, 10(1):16–38, 2016.

[39] Kimberly Chenoweth, Adri C. T. van Duin, and William A. Goddard. ReaxFF reactive force field for molecular dynamics simulations of hydrocarbon oxidation. *Journal of Physical Chemistry A*, 112(5):1040−1053, 2008.

[40] Satyam Agrawalla, and Adri C. T. van Duin. Development and application of a ReaxFF reactive force field for hydrogen combustion. *Journal of Physical Chemistry A*, 115(6):960−972, 2011.

[41] Lianchi Liu, Chen Bai, Huai Sun, and William A. Goddard, III. Mechanism and kinetics for the initial steps of pyrolysis and combustion of 1,6-dicyclopropane-2,4-hexyne from ReaxFF reactive dynamics. *Journal of Physical Chemistry A*, 115(19):4941−4950, 2011.

[42] Fidel Castro-Marcano, Amar M. Kamat, Michael F. RussoJr., Adri C.T. van Duin, and Jonathan P. Mathews. Combustion of an Illinois No. 6 coal char simulated using an atomistic char representation and the ReaxFF reactive force field. *Combustion and Flame*, 159(3):1272−1285, 2012.

[43] Alejandro Strachan, Adri C. T. van Duin, Debashis Chakraborty, Siddharth Dasgupta, William A, III. Goddard. Shock waves in high-energy materials: The initial chemical events in nitramine RDX. *Physical Review Letters*, 91(9):098301, 2003.

[44] Luzheng Zhang, Adri C. T. van Duin, Sergey V. Zybin, and William A. Goddard III. Thermal decomposition of hydrazines from reactive dynamics using the ReaxFF reactive force field. *Journal of Physical Chemistry B*, 113(31):10770−10778, 2009.

[45] Qi An, Yi Liu, Sergey V. Zybin, Hyungjun Kim, and William A. Goddard, III. Anisotropic shock sensitivity of syclotrimethylene trinitramine (RDX) from compress-and-shear reactive dynamics. *Journal of Physical Chemistry C*, 116(18):10198−10206, 2012.

[46] N. Ning, F. Calvo, A. C. T. van Duin, D. J. Wales, and H. Vach. Spontaneous self-assembly of silica nanocages into inorganic framework materials. *Journal of Physical Chemistry C*, 113(2):518−523, 2009.

[47] Akbar Bagri, Cecilia Mattevi, Muge Acik, Yves J. Chabal, Manish Chhowalla, and Vivek B. Shenoy. Structural evolution during the reduction of chemically derived graphene oxide. *Nature Chemistry*, 2:581−587, 2010.

[48] U. Khalilov, G. Pourtois, A. C. T. van Duin, and E. C. Neyts. Self-limiting oxidation in small-diameter Si nanowires. *Chemistry of Materials*, 24(11):2141−2147, 2012.

[49] Christopher R. Iacovella, William R. French, Brandon G. Cook, Paul R. C. Kent, and Peter T. Cummings. Role of polytetrahedral structures in the elongation and rupture of gold nanowires. *ACS Nano*, 5(12):10065−10073, 2011.

[50] Dimitry Papkov, Allison M. Beese, Alexander Goponenko, Yan Zou, Mohammad Naraghi, Horacio D. Espinosa, Biswajit Saha, George C. Schatz, Alexander Moravsky, Raouf Loutfy, Sonbinh T. Nguyen, and Yuris Dzenis. Extraordinary improvement of the graphitic structure of continuous carbon nanofibers templated with double wall carbon nanotubes. *ACS Nano*, 7(1):126−142, 2013.

[51] W. Somers, A. Bogaerts, A.C.T. van Duin, and E.C. Neyts. Interactions of plasma species on nickel catalysts: A reactive molecular dynamics study on the influence of temperature and surface structure. *Applied Catalysis B: Environmental*, 154–155:1–8, 2014.

[52] Thomas P. Senftle, Adri C.T.van Duin, and Michael J. Janik. Determining *in situ* phases of a nanoparticle catalyst *via* grand canonical Monte Carlo simulations with the ReaxFF potential. *Catalysis Communications*, 52:72–77, 2014.

[53] Chaoyang Zhang, Yushi Wen, and Xianggui Xue. Self-enhanced catalytic activities of functionalized graphene sheets in the combustion of nitromethane: Molecular dynamic simulations by molecular reactive force field. *ACS Applied Materials & Interfaces*, 6(15):12235–12244, 2014.

[54] Zheng-Zhe Lin. Graphdiyne as a promising substrate for stabilizing Pt nanoparticle catalyst. *Carbon*, 86:301–309, 2015.

[55] Adri C. T. van Duin, Boris V. Merinov, Seung Soon Jang, and William A. Goddard. ReaxFF reactive force field for solid oxide fuel cell systems with application to oxygen ion transport in yttria-stabilized zirconia. *Journal of Physical Chemistry A*, 112(14):3133–3140, 2008.

[56] Dmitry Bedrov, Grant D. Smith, and Adri C. T. van Duin. Reactions of singly-reduced ethylene carbonate in lithium battery electrolytes: A molecular dynamics simulation study using the ReaxFF. *Journal of Physical Chemistry A*, 116(11):2978–2985, 2012.

[57] Boris V. Merinov, Jonathan E. Mueller, Adri C. T. van Duin, Qi An, William A. Goddard, III. ReaxFF reactive force-field modeling of the triple-phase boundary in a solid oxide fuel cell. *Journal of Physical Chemistry Letters*, 5(22):4039–4043, 2014.

[58] Susanna Monti, Adri C. T. van Duin, Sung-Yup Kim, and Vincenzo Barone. Exploration of the conformational and reactive dynamics of glycine and diglycine on TiO_2: Computational investigations in the gas phase and in solution. *Journal of Physical Chemistry C*, 116(8):5141–5150, 2012.

[59] David A. Newsome, Debasis Sengupta, Hosein Foroutan, Michael F. Russo, and Adri C. T. van Duin. Oxidation of silicon carbide by O_2 and H_2O: A ReaxFF reactive molecular dynamics study, Part I. *Journal of Physical Chemistry C*, 116(30):16111–16121, 2012.

[60] Jaro.aw Meller. Molecular Dynamics. John Wiley and Sons: New York, 2001.

[61] Adri C. T. van Duin, Siddharth Dasgupta, Francois Lorant, and William A. Goddard. ReaxFF: A reactive force field for hydrocarbons. *Journal of Physical Chemistry A*, 105(41):9396–9409, 2001.

[62] Wilfried J. Mortier, Swapan K. Ghosh, and S. Shankar. Electronegativity equalization method for the calculation of atomic charges in molecules. *Journal of the American Chemical Society*, 108(15):4315–4320, 1986.

[63] Denis Donnelly, and Edwin Rogers. Symplectic integrators: An introduction. *American Journal of Physics*, 73(10):938–945, 2005.

[64] Loup Verlet. Computer "experiments" on classical fluids. I. Thermodynamical properties of Lennard-Jones molecules. *Physical Review*, 159(1):98–103, 1967.

[65] R. W. Hockney, J. W. Eastwood. Computer Simulation Using Particles. McGraw-Hill: New York, 1981.

[66] W. F. van Gunsteren, and H. J. C. Berendsen. Algorithms for macromolecular dynamics and constraint dynamics. *Molecular Physics*, 34(5):1311–1327, 1977.

[67] Berk Hess, Henk Bekker, Herman J. C. Berendsen, and Johannes G. E. M. Fraaije. LINCS: A linear constraint solver for molecular simulations. *Journal of Computational Chemistry*, 18(12):1463–1472, 1997.

[68] Shuichi Miyamoto, and Peter A. Kollman. Settle: An analytical version of the SHAKE and RATTLE algorithm for rigid water models. *Journal of Computational Chemistry*, 13(8):952–962, 1992.

[69] P. P. Ewald. Die Berechnung optischer und elektrostatischer Gitterpotentiale. *Annalen der Physik*, 369(3):253–287, 1921.

[70] Tom Darden, Darrin York, and Lee Pedersen. Particle mesh Ewald: An *N*.Log(*N*) method for Ewald sums in large systems. *The Journal of Chemical Physics*, 98(12):10089–10092, 1993.

[71] Philippe H. Hünenberger. Thermostat algorithms for molecular dynamics simulations. *Advanced Computer Simulation*, 173:105–149, 2005.

[72] Efrem Braun, Seyed Mohamad Moosavi, and Berend Smit. Anomalous effects of velocity rescaling algorithms: The flying ice cube effect revisited. *Journal of Chemical Theory and Computation*, 14(10):5262–5272, 2018.

[73] Stephen C. Harvey, Robert K.-Z. Tan, and Thomas E. Cheatham III. The flying ice cube: Velocity rescaling in molecular dynamics leads to violation of energy equipartition. *Journal of Computational Chemistry*, 19(7):726–740, 1998.

[74] H. J. C. Berendsen, J. P. M. Postma, W. F. van Gunsteren, A. DiNola, and J. R. Haak. Molecular dynamics with coupling to an external bath. *The Journal of Chemical Physics* 81(8):3684–3690, 1984.

[75] Shūichi Nosé. A molecular dynamics method for simulations in the canonical ensemble. *Molecular Physics*, 52(2):255–268, 1984.

[76] William G. Hoover. Canonical dynamics: Equilibrium phase-space distributions. *Physical Review A*, 31(3):1695–1697, 1985.

[77] M. Parrinello, and A. Rahman. Polymorphic transitions in single crystals: A new molecular dynamics method. *Journal of Applied Physics*, 52(12):7182–7190, 1981.

[78] Shuichi Nosé, and M.L. Klein. Constant pressure molecular dynamics for molecular systems. *Molecular Physics*, 50(5):1055–1076, 1983.

[79] William G. Hoover. Constant-pressure equations of motion. *Physical Review A*, 34(3):2499–2500, 1986.

[80] Hans C. Andersen. Molecular dynamics simulations at constant pressure and/or temperature. *The Journal of Chemical Physics*, 72(4):2384–2393, 1980.

[81] David Robert Cole, D. R. Grszkiewicz, M.S. Simonson, J. M. Chialvo, A. A. Melnichenko, Y. B. Wignall, G. D Lynn, G. W. Lin, J. S. Habenschuss, A. Gu, Bongiwe More, K L. Burchell, T. D. Striolo, A. Leng, Y. Cummings, P. T. Cooper, W. T. Schilling, M. Gubbins, and K. E. Frielinghaus. Influence of nanoscale porosity on fluid behavior. In book: Water–rock interactions. Taylor & Francis, pages 740–753, 2004.

[82] Natalia Pérez-Hernández, Trung Quan Luong, Martín Febles, Carlos Marco, Hans-Heinrich Limbach, Martina Havenith, Cirilo Pérez, María Victoria Roux, Ricardo Pérez, and Julio D. Martín. The mobility of water molecules through hydrated pores. *Journal of Physical Chemistry C*, 116(17):9616–9630, 2012.

[83] Ji Zang, Suchitra Konduri, Sankar Nair, and David S Sholl. Self-diffusion of water and simple alcohols in single-walled aluminosilicate nanotubes. *ACS Nano*, 3(6):1548–1556, 2009.

[84] Siddharth Gautam, and David Cole. Molecular dynamics simulation study of meso-confined propane in TiO_2. *Chemical Physics*, 458:68–76, 2015.

[85] Siddharth Gautam, Tingting Liu, Gernot Rother, Niina Jalarvo, Eugene Mamontov, Susan Welch, Julie Sheets, Michael Droege, and David R. Cole. Dynamics of propane in nanoporous silica Aerogel: A quasielastic neutron scattering study. *Journal of Physical Chemistry C*, 119(32):18188–18195, 2015.

[86] V. K. Sharma, S. Gautam, S. Mitra, Mala N. Rao, A. K. Tripathi, S. L. Chaplot, and R. Mukhopadhyay. Dynamics of adsorbed hydrocarbon in nanoporous zeolite framework. *Journal of Physical Chemistry B*, 113(23):8066–8072, 2009.

[87] Shuichi Takahara, Masatsugu Nakano, Shigeharu Kittaka, Yasushige Kuroda, Toshinori Mori, Hideaki Hamano, and Toshio Yamaguchi. Neutron scattering study on dynamics of water molecules in MCM-41. *Journal of Physical Chemistry B*, 103(28):5814–5819, 1999.

[88] Qingyin Zhang, Kwong-Yu Chan, and Nicholas Quirke. Molecular dynamics simulation of water confined in a nanopore of amorphous silica. *Molecular Simulation*, 35(15):1215–1223, 2009.

[89] Alan K Soper. Density profile of water confined in cylindrical pores in MCM-41 silica. *Journal of Physics: Condensed Matter*, 24(6):064107, 2012.

[90] S. M. Chathoth, L. He, E. Mamontov, and Y.B. Melnichenko. Effect of carbon dioxide and nitrogen on the diffusivity of methane confined in nano-porous carbon aerogel. *Microporous and Mesoporous Materials*, 148(1):101–106, 2012.

[91] Sumant Patankar, Siddharth Gautam, Gernot Rother, Andrey Podlesnyak, Georg Ehlers, Tingting Liu, David R. Cole, and David L. Tomasko. Role of confinement on adsorption and

dynamics of ethane and an ethane–CO_2 mixture in mesoporous CPG silica. *Journal of Physical Chemistry C*, 120(9):4843–4853, 2016.

[92] Siddharth Gautam, Gernot Rother, Niina Jalalrvo, Tingting Liu, Eugene Mamontov, Sheng Dai, Zhen-An Qiao, and David R. Cole. Effect of water on the dynamics of propane confined in nanoporous MCM-41-S. *Abstracts of American Conference on Neutron Scattering*:F7.03, 2016.

[93] Siddharth Gautam, Tran Thi Bao Le, Gernot Rother, Niina Jalarvo, Tingting Liu, Eugene Mamontov, Sheng Dai, Zhen-An Qiao, Alberto Striolo, and David Cole. Effects of water on the stochastic motions of propane confined in MCM-41-S pores. *Physical Chemistry Chemical Physics*, 21(45):25035–25046, 2019.

[94] Sabine Leroch., and Martin Wendland. Simulation of forces between humid amorphous silica surfaces: A comparison of empirical atomistic force fields. *Journal of Physical Chemistry C*, 116(50):26247–26261, 2012.

[95] Ersan Demiralp, Tahir Çağin, William A. Goddard, III. Morse stretch potential charge equilibrium force field for ceramics: Application to the quartz-stishovite phase transition and to silica glass. *Physical Review Letters*, 82(8):1708–1711, 1999.

[96] A. Takada, P. Richet, C.R.A. Catlow, and G.D. Price. Molecular dynamics simulations of vitreous silica structures. *Journal of Non-Crystalline Solids*, 345–346:224–229, 2004.

[97] Norman T Huff, Ersan Demiralp, Tahir Çagin, and William A Goddard III. Factors affecting molecular dynamics simulated vitreous silica structures. *Journal of Non-Crystalline Solids*, 253(1–3):133–142, 1999.

[98] Vo Van Hoang. Molecular dynamics simulation of amorphous SiO_2 nanoparticles. *Journal of Physical Chemistry B*, 111(44):12649–12656, 2007.

[99] B. W. H. van Beest, G. J. Kramer, and R. A. van Santen. Force fields for silicas and aluminophosphates based on *ab initio* calculations. Physical Review Letters, 64(16):1955–1958, 1990.

[100] S. Tsuneyuki, M. Tsukada, H. Aoki, and Y. Matsui. First-principles interatomic potential of silica applied to molecular dynamics. *Physical Review Letters*, 61(7):869–872, 1988.

[101] Andrew S. D'Souza, and Carlo G. Pantano. Mechanisms for silanol formation on amorphous silica fracture surfaces. *Journal of the American Ceramic Society*, 82(5):1289–1293, 1999.

[102] Raja Kirthi Kalluri, Deepthi Konatham, and Alberto Striolo. Aqueous NaCl solutions within charged carbon-slit Pores: Partition coefficients and density distributions from molecular dynamics simulations. *Journal of Physical Chemistry C*, 115(28):13786–13795, 2011.

[103] L. Sarkisov, and P. A. Monson. Modeling of adsorption and desorption in pores of simple geometry using molecular dynamics. *Langmuir*, 17(24):7600–7604, 2001.

[104] Roger F. Cracknell, Peter Gordon, and Keith E. Gubbins. Influence of pore geometry on the design of microporous materials for methane storage. *Journal of Physical Chemistry*, 97(2):494–499, 1993.

[105] Ding-Yu Peng, and Donald B. Robinson. A new two-constant equation of state. *Industrial & Engineering Chemistry Fundamentals*, 15(1):59–64, 1976.

[106] K. A. M Gasem, W Gao, Z Pan, and R. L Robinson Jr. A modified temperature dependence for the Peng–Robinson equation of state. *Fluid Phase Equilibria*, 181(1–2):113–125, 2001.

[107] Randall T. Cygan, Jian-Jie Liang, and Andrey G. Kalinichev. Molecular models of hydroxide, oxyhydroxide, and clay phases and the development of a general force field. *Journal of Physical Chemistry B*, 108(4):1255–1266, 2004.

[108] H. J. C. Berendsen, J. R. Grigera, and T. P. Straatsma. The missing term in effective pair potentials. *Journal of Physical Chemistry*, 91(24):6269–6271, 1987.

[109] Bertrand Guillot. A reappraisal of what we have learnt during three decades of computer simulations on water. *Journal of Molecular Liquids*, 101(1–3):219–260, 2002.

[110] Marcus G. Martin, and J. Ilja Siepmann. Transferable potentials for phase equilibria. 1. United-atom description of n-alkanes. *Journal of Physical Chemistry B*, 102(14):2569–2577, 1998.

[111] Ulrich Essmann, Lalith Perera, Max L. Berkowitz, Tom Darden, Hsing Lee, and Lee G. Pedersen. A smooth particle mesh Ewald method. *The Journal of Chemical Physics*, 103(19):8577–8593, 1995.

[112] Michael P. Allen, and Dominic J. Tildesley. Computer simulation of liquids. Oxford University Press: UK, 2004.

[113] David Van Der Spoel, Erik Lindahl, Berk Hess, Gerrit Groenhof, Alan E. Mark, and Herman J. C. Berendsen. GROMACS: Fast, flexible, and free. *Journal of Computational Chemistry*, 26(16):1701–1718, 2005.

[114] Berk Hess, Carsten Kutzner, David van der Spoel, and Erik Lindahl. GROMACS 4: Algorithms for highly efficient, load-balanced, and scalable molecular simulation. *Journal of Chemical Theory and Computation*, 4(3):435–447, 2008.

[115] R.W Hockney, S. P Goel, and J. W Eastwood. Quiet high-resolution computer models of a plasma. *Journal of Computational Physics*, 14(2):148–158, 1974.

[116] Joseph E. Basconi, and Michael R. Shirts. Effects of temperature control algorithms on transport properties and kinetics in molecular dynamics simulations. *Journal of Chemical Theory and Computation*, 9(7):2887–2899, 2013.

[117] A. Kinaci, J. B. Haskins, and T. Çağın. On calculation of thermal conductivity from Einstein relation in equilibrium molecular dynamics. *The Journal of Chemical Physics*, 137(1):014106, 2012.

[118] R. Battino. in IUPAC Solubility Data Series. H. L. Clever and C. L. Young (ed.). Pergamon Press: Oxford, 1986.

[119] Andrew L. Ferguson, Pablo G. Debenedetti, and Athanassios Z. Panagiotopoulos. Solubility and molecular conformations of n-alkane chains in water. *Journal of Physical Chemistry B*, 113(18):6405−6414, 2009.

[120] R. Mancinelli, S. Imberti, A. K. Soper, K. H. Liu, C. Y. Mou, F. Bruni, and M. A. Ricci. Multiscale approach to the structural study of water confined in MCM41. *Journal of Physical Chemistry B*, 113(50):16169−16177, 2009.

[121] R. Mancinelli, F. Bruni, and M. A. Ricci. Controversial evidence on the point of minimum density in deeply supercooled confined water. *Journal of Physical Chemistry Letters*, 1(8):1277−1282, 2010.

[122] J. Martí. Analysis of the hydrogen bonding and vibrational spectra of supercritical model water by molecular dynamics simulations. *The Journal of Chemical Physics*, 110(14):6876−6886, 1999.

[123] Huajie Feng, Wei Gao, Jingjing Nie, Jing Wang, Xiaojuan Chen, Liuping Chen, Xin Liu, Hans-Dietrich Lüdemann, and Zhenfan Sun. MD simulation of self-diffusion and structure in some n-alkanes over a wide temperature range at high pressures. *Journal of Molecular Modeling*, 19(1):73−82, 2013.

[124] A. Greiner-Schmid, S. Wappmann, M. Has, and H.-D. Lüdemann. Self-diffusion in the compressed fluid lower alkanes: Methane, ethane, and propane. *The Journal of Chemical Physics*, 94(8):5643−5649, 1991.

[125] Tuan A. Ho, and Alberto Striolo. Water and methane in shale rocks: Flow pattern effects on fluid transport and pore structure. *AIChE Journal*, 61(9):2993−2999, 2015.

[126] Tuan A. Ho, Dimitrios Argyris, Dimitrios V. Papavassiliou, Alberto Striolo, Lloyd L. Lee, and David R. Cole. Interfacial water on crystalline silica: a comparative molecular dynamics simulation study. *Molecular Simulation*, 37(3):172−195, 2011.

[127] Dimitrios Argyris, David R. Cole, and Alberto Striolo. Dynamic behavior of interfacial water at the silica surface. *Journal of Physical Chemistry C*, 113(45):19591−19600, 2009.

[128] Tuan A. Ho, and Alberto Striolo. Polarizability effects in molecular dynamics simulations of the graphene-water interface. *The Journal of Chemical Physics*, 138(5): 054117, 2013.

[129] Anh Phan, David R. Cole, and Alberto Striolo. Preferential adsorption from liquid water−ethanol mixtures in alumina pores. *Langmuir*, 30(27):8066−8077, 2014.

[130] Jnanojjal Chanda, and Sanjoy Bandyopadhyay. Hydrogen bond lifetime dynamics at the interface of a surfactant monolayer. *Journal of Physical Chemistry B*, 110(46):23443−23449, 2006.

[131] Marcus G. Martin, and J. Ilja Siepmann. Novel configurational-bias Monte Carlo method for branched molecules. Transferable potentials for phase equilibria. 2. United-atom description of branched alkanes. *Journal of Physical Chemistry B*, 103(21):4508–4517, 1999.

[132] Collin D. Wick, Marcus G. Martin, and J. Ilja Siepmann. Transferable potentials for phase equilibria. 4. United-atom description of linear and branched alkenes and alkylbenzenes. *Journal of Physical Chemistry B*, 104(33):8008–8016, 2000.

[133] Bin Chen, Jeffrey J. Potoff, and J. Ilja Siepmann. Monte Carlo calculations for alcohols and their mixtures with alkanes. Transferable potentials for phase equilibria. 5. United-atom description of primary, secondary, and tertiary alcohols. *Journal of Physical Chemistry B*, 105(15):3093–3104, 2001.

[134] Nusrat Lubna, Ganesh Kamath, Jeffrey J. Potoff, Neeraj Rai, and J. Ilja Siepmann. Transferable potentials for phase equilibria. 8. United-atom description for thiols, sulfides, disulfides, and thiophene. *Journal of Physical Chemistry B*, 109(50):24100–24107, 2005.

[135] Kevin D. Nielson, Adri C. T. van Duin, Jonas Oxgaard, Wei-Qiao Deng, and William A. Goddard. Development of the ReaxFF reactive force field for describing transition metal catalyzed reactions, with application to the initial stages of the catalytic formation of carbon nanotubes. *Journal of Physical Chemistry A*, 109(3):493–499, 2005.

[136] Chenyu Zou, and Adri Van Duin. Investigation of complex iron surface catalytic chemistry using the ReaxFF reactive force field method. *JOM*, 64(12):1426–1437, 2012.

[137] Yun Kyung Shin, Hyunwook Kwak, Alex V. Vasenkov, Debasis Sengupta, and Adri C.T. van Duin. Development of a ReaxFF reactive force field for Fe/Cr/O/S and application to oxidation of butane over a pyrite-covered Cr_2O_3 catalyst. *ACS Catalysis*, 5(12):7226–7236, 2015.

[138] W. Goddard III , B. Merinov , A. van Duin , T. Jacob , M. Blanco , V. Molinero, S. S. Jang, and Y. H. Jang. Multi-paradigm multi-scale simulations for fuel cell catalysts and membranes. *Molecular Simulation*, 32(3–4):251–268, 2006.

[139] Muralikrishna Raju, Sung-Yup Kim, Adri C. T. van Duin, and Kristen A. Fichthorn. ReaxFF reactive force field study of the dissociation of water on titania surfaces. *Journal of Physical Chemistry C*, 117(20):10558–10572, 2013.

[140] Liangliang Huan, Keith E. Gubbins, Licheng Li, and Xiaohua Lu. Water on Titanium dioxide surface: A revisiting by reactive molecular dynamics simulations. *Langmuir*, 30(49):14832–14840, 2014.

[141] C. G. Aimoli, E. J. Maginn, and C. R. A. Abreu. Transport properties of carbon dioxide and methane from molecular dynamics simulations. *The Journal of Chemical Physics*, 141(13):134101, 2014.

[142] Alister J. Page, and Behdad Moghtaderi. Molecular dynamics simulation of the low-temperature partial oxidation of CH_4. *Journal of Physical Chemistry A*, 113(8):1539–1547, 2009.

[143] Zhenghua He, Xi-Bo Li, Li-Min Liu, and Wenjun Zhu. The intrinsic mechanism of methane oxidation under explosion condition: A combined ReaxFF and DFT study. *Fuel*, 124:85–90, 2014.

[144] Zheng-Hua He, Xi-Bo Li, Wen-Jun Zhu, Li-Min Liu, and Guang-Fu Ji. Effect of water on gas explosions: combined ReaxFF and *ab initio* MD calculations. *RSC Advances*, 4(66):35048–35054, 2014.

[145] Tao Cheng, Andrés Jaramillo-Botero, William A Goddard, III, and Huai Sun. Adaptive accelerated reaxFF reactive dynamics with validation from simulating hydrogen combustion. *Journal of the American Chemical Society*, 136(26):9434–9442, 2014.

[146] Steve Plimpton. Fast parallel algorithms for short-range molecular dynamics. J*ournal of Computational Physics*, 117(1):1–19, 1995.

[147] H. M. Aktulga, J. C. Fogarty, S. A. Pandit, and A. Y. Grama. Parallel reactive molecular dynamics: Numerical methods and algorithmic techniques. *Parallel Computing*, 38(4–5):245–259, 2012.

[148] Andrew R Leach. Molecular modelling: Principles and applications. Prentice Hall, 2001.

[149] William L. Jorgensen, David S. Maxwell, and Julian Tirado-Rives. Development and testing of the OPLS all-atom force field on conformational energetics and properties of organic liquids. *Journal of the American Chemical Society*, 118(45):11225–11236, 1996.

[150] Jonathan G. Harris, and Kwong H. Yung. Carbon dioxide's liquid-vapor coexistence curve and critical properties as predicted by a simple molecular model. *Journal of Physical Chemistry*, 99(31):12021–12024, 1995.

[151] Jeffrey J. Potoff, and J. Ilja Siepmann. Vapor–liquid equilibria of mixtures containing alkanes, carbon dioxide, and nitrogen. *AIChE Journal*, 47(7):1676–1682, 2001.

[152] Zhigang Zhang, and Zhenhao Duan. An optimized molecular potential for carbon dioxide. *The Journal of Chemical Physics*, 122(21):214507, 2005.

[153] H. J. C. Berendsen, J. P. M. Postma, W. F. van Gunsteren, and J. Hermans. Interaction models for water in relation to protein hydration. in Intermolecular Forces: Proceedings of the Fourteenth Jerusalem Symposium on Quantum Chemistry and Biochemistry Held in Jerusalem, Israel. Pullman B (ed.). Dordrecht: Springer Netherlands, pages 331–42, 1981.

[154] Houston Frost, Tina Düren, and Randall Q. Snurr. Effects of surface area, free volume, and heat of adsorption on hydrogen uptake in metal-organic frameworks. *Journal of Physical Chemistry B*, 110(19):9565–9570, 2006.

[155] William L. Jorgensen, Jayaraman Chandrasekhar, Jeffry D. Madura, Roger W. Impey, and Michael L. Klein. Comparison of simple potential functions for simulating liquid water. *The Journal of Chemical Physics*, 79(2):926–935, 1983.

[156] Alice Glättli, Xavier Daura, and Wilfred F. Van Gunsteren. A novel approach for designing simple point charge models for liquid water with three interaction sites. *Journal of Computational Chemistry*, 24(9):1087–1096, 2003.

[157] J. L. F. Abascal, E. Sanz, R. García Fernández, and C. Vega. A potential model for the study of ices and amorphous water: TIP4P/Ice. *The Journal of Chemical Physics*, 122(23):234511, 2005.

[158] J. L. F. Abascal, and C. Vega. A general purpose model for the condensed phases of water: TIP4P/2005. *The Journal of Chemical Physics*, 123(23):234505, 2005.

[159] C Vega, J L F Abascal, E Sanz, L G MacDowell, and C McBride. Can simple models describe the phase diagram of water? *Journal of Physics: Condensed Matter*, 17(45):S3283–S3288, 2005.

[160] C. Vega, J. L. F. Abascal, M. M. Conde, and J. L. Aragones. What ice can teach us about water interactions: a critical comparison of the performance of different water models. *Faraday Discussions*, 141:251–276, 2009.

[161] A. K. Soper. The radial distribution functions of water and ice from 220 to 673 K and at pressures up to 400 MPa. *Chemical Physics*, 258(2–3):121–137, 2000.

[162] P. T. Cummings, H. D. Cochran, J. M. Simonson, R. E. Mesmer, and S. Karaborni. Simulation of supercritical water and of supercritical aqueous solutions. *The Journal of Chemical Physics*, 94(8):5606–5621, 1991.

[163] Ariel A. Chialvo, and Peter T. Cummings. Engineering a simple polarizable model for the molecular simulation of water applicable over wide ranges of state conditions. *The Journal of Chemical Physics*, 105(18):8274–8281, 1996.

[164] Farida Darkrim, Jean Vermesse, Pierre Malbrunot, and Dominique Levesque. Monte Carlo simulations of nitrogen and hydrogen physisorption at high pressures and room temperature. Comparison with experiments. *The Journal of Chemical Physics*, 110(8):4020–4027, 1999.

[165] J. O. Hirschfelder, C. F. Curtis, R. B. Bird. Molecular theory of gases and liquids. Wiley: New York,1954.

[166] Roger F. Cracknell. Molecular simulation of hydrogen adsorption in graphitic nanofibres. *Physical Chemistry Chemical Physics*, 3(11):2091–2097, 2001.

[167] Qingyuan Yang, and Chongli Zhong. Molecular simulation of adsorption and diffusion of hydrogen in metal-organic frameworks. *Journal of Physical Chemistry B*, 109(24):11862-11864, 2005.

[168] Fabrice Salles, Daniil I. Kolokolov, Hervé Jobic, Guillaume Maurin, Philip L. Llewellyn, Thomas Devic, Christian Serre, and Gérard Ferey. Adsorption and diffusion of H_2 in the MOF type systems MIL-47(V) and MIL-53(Cr): A combination of microcalorimetry and QENS experiments with molecular simulations. *Journal of Physical Chemistry C*, 113(18):7802–7812, 2009.

[169] A. Michels, W. de Graaff, and C.A. Ten Seldam. Virial coefficients of hydrogen and deuterium at temperatures between −175°C and +150°C. Conclusions from the second virial coefficient with regards to the intermolecular potential. *Physica*, 26(6):393–408, 1960.

[170] A. Vrij, R. Tuinier. Fundamentals of interface and colloid science. Elsevier: Amsterdam, 2005.

[171] Daniel G. Friend, James F. Ely, and Hepburn Ingham. Thermophysical properties of methane. *Journal of Physical and Chemical Reference Data*, 18(2):583–638, 1989.

[172] Y. Suehiro, M. Nakajima, K. Yamada, and M. Uematsu. Critical parameters of s for x=(1.0000, 0.7496, 0.5013, and 0.2522). *The Journal of Chemical Thermodynamics*, 28(10):1153–1164, 1996.

[173] H. Sato, K. Watanabe, J. M. H. Levelt Sengers, J. S. Gallagher, P. G. Hill, J. Straub, and W. Wagner. Sixteen thousand evaluated experimental thermodynamic property data for water and steam. *Journal of Physical and Chemical Reference Data*, 20(5):1023–1044, 1991.

[174] R. C. Reid, J. M. Prausnitz, and B. E. Poling. The properties of gases and liquids (4th ed.). McGraw Hill: New York, 1987.

[175] H. Stassen. On the pair potential in dense fluid methane. *Journal of Molecular Structure: THEOCHEM*, 464(1-3):107–119, 1999.

[176] G. Strauβ, A. Bassen, H. Zweier, H. Bertagnolli, K. Tödheide, A. K. Soper, and J. Turner. High-pressure neutron diffraction on fluid methane. *Physical Review E*, 53(4):3505–3517, 1996.

[177] S. Murad, D. J. Evans, K. E. Gubbins, W. B. Streett, and D. J. Tildesley. Molecular dynamics simulation of dense fluid methane. *Molecular Physics*, 37(3):725–736, 1979.

[178] Donald E. Williams. Nonbonded potential parameters derived from crystalline hydrocarbons. *The Journal of Chemical Physics*, 47(11):4680–4684, 1967.

[179] J. B. van Tricht, H. Fredrikze, and J. van der Laan. Neutron diffraction study of liquid carbon dioxide at two thermodynamic states. *Molecular Physics*, 52(1):115–127, 1984.

[180] Thomas Lindenau, Manfred L. Ristig, Klaus A. Gernoth, Javier Dawidowski, and Francisco J. Bermejo. The physics of liquid para-hydrogen. *International Journal of Modern Physics B*, 20(30–31):5035–5046, 2006.

[181] J. Dawidowski, F. J. Bermejo, M. L. Ristig, B. Fåk, C. Cabrillo, R. Fernández-Perea, K. Kinugawa, and J. Campo. Static structure factor of liquid parahydrogen. *Physical Review B*, 69(1):014207, 2004.

[182] Jayant K. Singh, and David A. Kofke. Mayer sampling: Calculation of cluster integrals using free-energy perturbation methods. *Physical Review Letters*, 92(22):220601, 2004.

[183] Andrew J. Schultz, David A. Kofke, and Allan H. Harvey. Molecular-based virial coefficients of CO_2–H_2O mixtures. *AIChE Journal*, 61(9):3029–3037, 2015.

[184] Shu Yang, Andrew J. Schultz, and David A. Kofke. Evaluation of second and third dielectric virial coefficients for non-polarisable molecular models. *Molecular Physics*, 115(8):991–1003, 2017.

[185] David E. Smith, and A. D. J. Haymet. Free energy, entropy, and internal energy of hydrophobic interactions: Computer simulations. *The Journal of Chemical Physics*, 98(8):6445–6454, 1993.

[186] K. Koga, and B. Widom. Thermodynamic functions as correlation-function integrals. *The Journal of Chemical Physics*, 138(11):114504, 2013.

[187] B. Widom, and Robin C. Underwood. Second osmotic virial coefficient from the two-component van der Waals equation of state. *Journal of Physical Chemistry B*, 116(31):9492–9499, 2012.

[188] K. Koga, Vincent Holten, and B. Widom. Deriving second osmotic virial coefficients from equations of state and from experiment. *Journal of Physical Chemistry B*, 119(42):13391–13397, 2015.

[189] Ohgaki Kazunari, Mizuhaya Takashi, and Katayama Takashi. The interaction second virial coefficients for seven binary systems containing carbon dioxide, methane, ethylene, ethane and propylene at 25°C. *Journal of Chemical Engineering of Japan*, 14(1):71–72, 1981.

[190] R S Dadson, E J Evans, and J H King. The second virial coefficient of carbon dioxide. *Proceedings of the Physical Society*, 92(4):1115–1121, 1967.

[191] Allan H. Harvey, and Eric W. Lemmon. Correlation for the second virial coefficient of water. *Journal of Physical and Chemical Reference Data*, 33(1):369–376, 2004.

[192] R. D. Goodwin, D. E. Diller, H. M. Roder, and L. A. Weber. Second and third virial coefficients for hydrogen. *Journal of Research of the National Bureau of Standards, Section A: Physics and Chemistry*, 68A(1):121–126, 1964.

[193] Edward B. Winn. The temperature dependence of the self-diffusion coefficients of argon, neon, nitrogen, oxygen, carbon dioxide, and methane. *Physical Review*, 80(6):1024–1027, 1950.

[194] T. Groß, J. Buchhauser, and H.-D. Lüdemann. Self-diffusion in fluid carbon dioxide at high pressures. *The Journal of Chemical Physics*, 109(11):4518–4522, 1998.

[195] R. Mills. Self-diffusion in normal and heavy water in the range 1-45.deg. *The Journal of Physical Chemistry*, 77(5):685–688, 1973.

[196] P. Clark Souers. Hydrogen properties for fusion energy. University of California Press, 1986.

[197] E. A. Mason, B. K. Annis, and M. Islam. Diffusion coefficients of T_2−H_2 and T_2−D_2: The nonequivalence of H_2 and D_2 cross sections. *The Journal of Chemical Physics*, 42(10):3364–3366, 1965.

[198] In-Chul Yeh, and Gerhard Hummer. System-size dependence of diffusion coefficients and viscosities from molecular dynamics simulations with periodic boundary conditions. *Journal of Physical Chemistry B*, 108(40):15873–15879, 2004.

[199] Manfred Holz, Stefan R. Heil, and Antonio Sacco. Temperature-dependent self-diffusion coefficients of water and six selected molecular liquids for calibration in accurate ^{1}H NMRPFG measurements. *Physical Chemistry Chemical Physics*, 2(20):4740–4742, 2000.

[200] Stuart A. Rice. Structure in confined colloid suspensions. *Chemical Physics Letters*, 479(1–3):1–13, 2009.

[201] Sang Soo Lee, Paul Fenter, Changyong Park, Neil C. Sturchio, and Kathryn L. Nagy. Hydrated cation speciation at the muscovite (001)−water interface. *Langmuir*, 26(22):16647–16651, 2010.

[202] Tuan A. Ho, D. Argyris, D. R. Cole, and A. Striolo. Aqueous NaCl and CsCl solutions confined in crystalline slit-shaped silica nanopores of varying degree of protonation. *Langmuir*, 28(2):1256–1266, 2012.

[203] Ateeque Malani, and K. G. Ayappa. Relaxation and jump dynamics of water at the mica interface. *The Journal of Chemical Physics*, 136(19): 194701, 2012.

[204] Patrice Porion, Anne Marie Faugère, Anne-Laure Rollet, Emmanuelle Dubois, Virginie Marry, Laurent J. Michot, and Alfred Delville. Influence of strong confinement on the structure and dynamics of liquids: A study of the clay/water interface exploiting ^{2}H NMR spectroscopy and spin-locking relaxometry. *Journal of Physical Chemistry C*, 122(29):16830–16841, 2018.

[205] Anh Phan, David R. Cole, R. Gregor Weiß, Joachim Dzubiella, and Alberto Striolo. Confined water determines transport properties of guest molecules in narrow pores. *ACS Nano*, 10(8):7646–7656, 2016.

[206] Luís F. M. Franco, Marcelo Castier, and Ioannis G. Economou. Anisotropic parallel self-diffusion coefficients near the calcite surface: A molecular dynamics study. *The Journal of Chemical Physics*, 145(8): 084702, 2016.

[207] Tai Bui, Anh Phan, David R. Cole, and Alberto Striolo. Transport mechanism of guest methane in water-filled nanopores. *Journal of Physical Chemistry C*, 121(29):15675–15686, 2017.

[208] Alenka Luzar, and Dusan Bratko. Gas solubility in hydrophobic confinement. *Journal of Physical Chemistry B*, 109(47):22545–22552, 2005.

[209] Dusan Bratko, and Alenka Luzar. Attractive surface force in the presence of dissolved gas: A molecular approach. *Langmuir*, 24(4):1247–1253, 2008.

[210] Volaniana Rakotovao, Rachid Ammar, Sylvain Miachon, and Marc Pera-Titus. Influence of the mesoconfining solid on gas oversolubility in nanoliquids. *Chemical Physics Letters*, 485(4–6):299–303, 2010.

[211] Yaofeng Hu, Liangliang Huang, Shuangliang Zhao, Honglai Liu, and Keith E. Gubbins. Effect of confinement in nano-porous materials on the solubility of a supercritical gas. *Molecular Physics*, 114(22):3294–3306, 2016.

[212] Filip Moučka, Martin Svoboda, and Martin Lísal. Modelling aqueous solubility of sodium chloride in clays at thermodynamic conditions of hydraulic fracturing by molecular simulations. *Physical Chemistry Chemical Physics*, 19(25):16586–16599, 2017.

[213] Greeshma Gadikota, Baptiste Dazas, Gernot Rother, Michael C. Cheshire, and Ian C. Bourg. Hydrophobic solvation of gases (CO_2, CH_4, H_2, noble gases) in clay interlayer nanopores. *Journal of Physical Chemistry C*, 121(47):26539–26550, 2017.

[214] Sakiru B. Badmos, Alberto Striolo, and David R. Cole. Aqueous hydrogen sulfide in slit-shaped silica nanopores: Confinement effects on solubility, structural, and dynamical properties. *Journal of Physical Chemistry C*, 122(26):14744–14755, 2018.

[215] M. Borówko, A. Patrykiejew, S. Sokołowski, R. Zagórski, and O. Pizio. Chemical reactions at surfaces: Application of the reaction ensamble Monte Carlo method. *Czechoslovak Journal of Physics*, 48(3):371–388, 1998.

[216] M. Borówko, and R. Zagórski. Chemical equilibria in slitlike pores.*The Journal of Chemical Physics*, 114(12):5397–5403, 2001.

[217] C. Heath Turner, J. Karl Johnson, and Keith E. Gubbins. Effect of confinement on chemical reaction equilibria: The reactions $2NO \Leftrightarrow (NO)_2$ and $N_2 + 3H_2 \Leftrightarrow 2NH_3$ in carbon micropores. *The Journal of Chemical Physics*, 114(4):1851–1859, 2001.

[218] C. Heath Turner, Jorge Pikunic, and Keith E. Gubbins. Influence of chemical and physical surface heterogeneity on chemical reaction equilibria in carbon micropores. *Molecular Physics*, 99(24):1991–2001, 2001.

[219] C. Heath Turner, and Keith E. Gubbins. Effects of supercritical clustering and selective confinement on reaction equilibrium: A molecular simulation study of the esterification reaction. *The Journal of Chemical Physics*, 119(12):6057–6067, 2003.

[220] C. Heath Turner, John K. Brennan, Martin Lísal, William R. Smith, J. Karl Johnson, and Keith E. Gubbins. Simulation of chemical reaction equilibria by the reaction ensemble Monte Carlo method: a review. *Molecular Simulation*, 34(2):119–146, 2008.

[221] Erik E. Santiso, Aaron M. George, Malgorzata Sliwinska-bartkowiak, Marco Buongiorno Nardelli, and Keith E. Gubbins. Effect of confinement on chemical reactions. *Adsorption*, 11:349–354, 2005.

[222] C. Heath Turner, John K. Brennan, J. Karl Johnson, and Keith E. Gubbins. Effect of confinement by porous materials on chemical reaction kinetics. *The Journal of Chemical Physics*, 116(5):2138–2148, 2002.

[223] Xuan Peng, Wenchuan Wang, and Shiping Huang. Monte Carlo simulation for chemical reaction equilibrium of ammonia synthesis in MCM-41 pores and pillared clays. *Fluid Phase Equilibria*, 231(2):138–149, 2005.

[224] Niels Hansen, Sven Jakobtorweihen, and Frerich J. Keil. Reactive Monte Carlo and grand-canonical Monte Carlo simulations of the propene metathesis reaction system. *The Journal of Chemical Physics*, 122(16):164705, 2005.

[225] Martin Lísal, John K. Brennan, and William R. Smith. Chemical reaction equilibrium in nanoporous materials: NO dimerization reaction in carbon slit nanopores. *The Journal of Chemical Physics*, 124(6):064712, 2006.

[226] Sylwester Furmaniak, Piotr A. Gauden, Piotr Kowalczyk, and Andrzej Patrykiejew. Monte Carlo study of chemical reaction equilibria in pores of activated carbons. *RSC Advances*, 7(85):53667–53679, 2017.

[227] Tran Thi Bao Le, Alberto Striolo, and David R. Cole. Structural and dynamical properties predicted by reactive force fields simulations for four common pure fluids at liquid and gaseous non-reactive conditions. *Molecular Simulation*, 44(10):826–839, 2018.

[228] John D. Sherman. Synthetic zeolites and other microporous oxide molecular sieves. *Proceedings of the National Academy of Sciences of the United States of America*, 96(7):3471–3478, 1999.

[229] Ana Primo, and Hermenegildo Garcia. Zeolites as catalysts in oil refining. *Chemical Society Reviews*, 43(22):7548–7561, 2014.

[230] Mohammad Eslami, Mohammad G. Dekamin, Leila Motlagh, and Ali Maleki. MCM-41 mesoporous silica: a highly efficient and recoverable catalyst for rapid synthesis of alpha-aminonitriles and imines. *Green Chemistry Letters and Reviews*, 11(1):36–46, 2018.

[231] K. Ravindranathan Thampi, John Kiwi, and Michael Grätzel. Methanation and photo-methanation of carbon dioxide at room temperature and atmospheric pressure. *Nature*, 327:506–508, 1987.

[232] Frigyes Solymosi, András Erdöhelyi, and Mária Kocsis. Methanation of CO_2 on supported Ru catalysts. *Journal of the Chemical Society, Faraday Transactions 1: Physical Chemistry in Condensed Phases*, 77(5):1003–1012, 1981.

[233] M. Krämer, K. Stöwe, M. Duisberg, F. Müller, M. Reiser, S. Sticher, and W. F. Maier. The impact of dopants on the activity and selectivity of a Ni-based methanation catalyst. *Applied Catalysis A: General*, 369(1–2):42–52, 2009.

[234] Guoan Du, Sangyun Lim, Yanhui Yang, Chuan Wang, Lisa Pfefferle, and Gary L. Haller. Methanation of carbon dioxide on Ni-incorporated MCM-41 catalysts: The influence of catalyst pretreatment and study of steady-state reaction. *Journal of Catalysis*, 249(2):370–379, 2007.

[235] Natalia M. Martin, Peter Velin, Magnus Skoglundh, Matthias Bauer, and Per-Anders Carlsson. Catalytic hydrogenation of CO_2 to methane over supported Pd, Rh and Ni catalysts. *Catalysis Science & Technology*, 7(5):1086–1094, 2017.

[236] Thien An Le, Min Sik Kim, Sae Ha Lee, and Eun Duck Park. CO and CO_2 methanation over supported cobalt catalysts. *Topics in Catalysis*, 60:714–720, 2017.

[237] Takayuki Abe, Masaaki Tanizawa, Kuniaki Watanabe, and Akira Taguchi. CO_2 methanation property of Ru nanoparticle-loaded TiO_2 prepared by a polygonal barrel-sputtering method. *Energy & Environmental Science*, 2(3):315–321, 2009.

[238] E. Jwa, S. B. Lee, H. W. Lee, and Y. S. Mok. Plasma-assisted catalytic methanation of CO and CO_2 over Ni-zeolite catalysts. *Fuel Processing Technology*, 108:89–93, 2013.

[239] Long Zhou, Qianqian Wang, Liping Ma, Jiantao Chen, Jun Ma, and Zhecheng Zi. CeO_2 promoted mesoporous Ni/γ-Al_2O_3 catalyst and its reaction conditions for CO_2 methanation. *Catalysis Letters*, 145(2):612–619, 2015.

[240] Hyun You Kim, Hyuck Mo Lee, and Jung-Nam Park. Bifunctional mechanism of CO_2 methanation on Pd-MgO/SiO_2 catalyst: Independent roles of MgO and Pd on CO_2 methanation. *Journal of Physical Chemistry C*, 114(15):7128–7131, 2010.

[241] Michael E. Berndt, Douglas E. Allen, William E. Seyfried, Jr. Reduction of CO_2 during serpentinization of olivine at 300 °C and 500 bar. *Geology*, 24(4):351–354, 1996.

[242] Adri C. T. van Duin, Alejandro Strachan, Shannon Stewman, Qingsong Zhang, Xin Xu, and William A. Goddard. $ReaxFF_{SiO}$ reactive force field for silicon and silicon oxide systems. *Journal of Physical Chemistry A*, 107(19):3803–3811, 2003.

[243] Joseph C. Fogarty, Hasan Metin Aktulga, Ananth Y. Grama, Adri C. T. van Duin, and Sagar A. Pandit. A reactive molecular dynamics simulation of the silica-water interface. *The Journal of Chemical Physics*, 132(17): 174704, 2010.

[244] Markus J Buehler, Adri C T van Duin, and William A Goddard III. Multiparadigm modeling of dynamical crack propagation in silicon using a reactive force field. *Physical Review Letters*, 96(9):095505, 2006.

[245] Kimberly Chenoweth, Sam Cheung, Adri C. T. van Duin, William A. Goddard, and Edward M. Kober. Simulations on the thermal decomposition of a poly(dimethylsiloxane) polymer using the ReaxFF reactive force field. *Journal of the American Chemical Society*, 127(19):7192–7202, 2005.

[246] Tran Thi Bao Le, Alberto Striolo, Siddharth S. Gautam, and David R. Cole. Propane-water mixtures confined within cylindrical silica nanopores: Structural and dynamical properties probed by molecular dynamics. *Langmuir*, 33(42):11310–11320, 2017.

[247] Jiajian Gao, Yingli Wang, Yuan Ping, Dacheng Hu, Guangwen Xu, Fangna Gu, and Fabing Su. A thermodynamic analysis of methanation reactions of carbon oxides for the production of synthetic natural gas. *RSC Advances*, 2(6):2358–2368, 2012.

[248] Kevin Maik Jablonka, Daniele Ongari, and Berend Smit. Applicability of tail corrections in the molecular simulations of porous materials. *Journal of Chemical Theory and Computation*, 15(10):5635–5641, 2019.

[249] Lianchi Liu, Yi Liu, Sergey V Zybin, Huai Sun, and William A Goddard, III. ReaxFF-lg: Correction of the ReaxFF reactive force field for London dispersion, with applications to

the equations of state for energetic materials. *Journal of Physical Chemistry A*, 115(40):11016–11022, 2011.

[250] Vitaly V. Chaban, Eudes Eterno Fileti, and Oleg V. Prezhdo. Buckybomb: Reactive molecular dynamics simulation. *Journal of Physical Chemistry Letters*, 6(5):913–917, 2015.

[251] Sung Jin Pai, Byung Chul Yeo, and Sang Soo Han. Development of the $ReaxFF_{CBN}$ reactive force field for the improved design of liquid CBN hydrogen storage materials. *Physical Chemistry Chemical Physics*, 18(3):1818–1827, 2016.

[252] Marc Jacquemin, Antoine Beuls, and Patricio Ruiz. Catalytic production of methane from CO_2 and H_2 at low temperature: Insight on the reaction mechanism. *Catalysis Today*, 157(1–4):462–466, 2010.

[253] Jung-Nam Park, and Eric W. McFarland. A highly dispersed Pd–Mg/SiO_2 catalyst active for methanation of CO_2. *Journal of Catalysis*, 266(1):92–97, 2009.

[254] J. M. Smith, Hendrick Van Ness, and Michael Abbott. Introduction to chemical engineering thermodynamics. McGraw-Hill: Boston, 2005.

[255] M. D. Koretsky. Engineering and Chemical Thermodynamics. John Wiley & Sons, Inc.: New York, 2013.

[256] Carlos V. Miguel, Miguel A. Soria, Adélio Mendes, and Luis M. Madeira. Direct CO_2 hydrogenation to methane or methanol from post-combustion exhaust streams – A thermodynamic study. *Journal of Natural Gas Science and Engineering*, 22:1–8, 2015.

[257] A. Catarina Faria, C. V. Miguel, and Luís M. Madeira. Thermodynamic analysis of the CO_2 methanation reaction with *in situ* water removal for biogas upgrading. *Journal of CO_2 Utilization*, 26:271–280, 2018.

[258] Joel M. Silva, M.A. Soria, and Luis M. Madeira. Thermodynamic analysis of glycerol steam reforming for hydrogen production with in situ hydrogen and carbon dioxide separation. *Journal of Power Sources*, 273:423–430, 2015.

[259] Chen Bai, Lianchi Liu, and Huai Sun. Molecular dynamics simulations of methanol to olefin reactions in HZSM-5 zeolite using a ReaxFF force field. *Journal of Physical Chemistry C*, 116(12):7029–7039, 2012.

[260] Zhiqiang Zhang, Kefeng Yan, and Jilong Zhang. ReaxFF molecular dynamics simulations of non-catalytic pyrolysis of triglyceride at high temperatures. *RSC Advances*, 3(18):6401–6407, 2013.

[261] Irene Liu, Noel W. Cant, John H. Bromly, Fred J. Barnes, Peter F. Nelson, and Brian S. Haynes. Formate species in the low-temperature oxidation of dimethyl ether. *Chemosphere*, 42(5–7):583–589, 2001.

[262] Craig A. Taatjes, Giovanni Meloni, Talitha M. Selby, Adam J. Trevitt, David L. Osborn, Carl J. Percival, and Dudley E. Shallcross. Direct observation of the gas-phase criegee intermediate (CH_2OO). *Journal of the American Chemical Society*, 130(36):11883–11885, 2008.

[263] David L. Griscom. Defect structure of glasses: Some outstanding questions in regard to vitreous silica. *Journal of Non-Crystalline Solids*, 73(1–3):51–77, 1985.

[264] Yun-xiang Pan, Chang-jun Liu, Donghai Mei, and Qingfeng Ge. Effects of hydration and oxygen vacancy on CO_2 adsorption and activation on β-Ga_2O_3(100). *Langmuir*, 26(8):5551–5558, 2010.

[265] Stijn Huygh, Annemie Bogaerts, and Erik C. Neyts. How oxygen bacancies Activate CO_2 dissociation on TiO_2 anatase (001). *Journal of Physical Chemistry C*, 120(38):21659–21669, 2016.

[266] Qingqing Jiang, Zhenpan Chen, Jinhui Tong, Min Yang, Zongxuan Jiang, and Can Li. Direct thermolysis of CO_2 into CO and O_2. *Chemical Communications*, 53(6):1188–1191, 2017.

[267] Michael R Weismiller, Chad E Junkermeier, Michael F Russo Jr, Michael R Salazar, Dmitry Bedrov, and Adri C T van Duin. ReaxFF molecular dynamics simulations of intermediate species in dicyanamide anion and nitric acid hypergolic combustion. *Modelling and Simulation in Materials Science and Engineerin*g, 23(7):074007, 2015.

[268] D. Cole, A. Striolo. in Deep Carbon: Past to Present. Orcutt B, Daniel I, Dasgupta R (ed.). Cambridge University Press, 2019.

[269] Dr. Curt M. White, Brian R. Strazisar, Evan J. Granite, James S. Hoffman, and Henry W. Pennline. Journal of the Air & Waste Management Association. Separation and capture of CO_2 from large stationary sources and sequestration in geological formations – Coalbeds and deep saline aquifers. *Journal of the Air & Waste Management Association*, 53(6):645–715, 2003.

[270] M. A. Celia, S. Bachu, J. M. Nordbotten, and K. W. Bandilla. Status of CO_2 storage in deep saline aquifers with emphasis on modeling approaches and practical simulations. *Water Resources Research*, 51(9):6846–6892, 2015.

[271] Robert G. Bruant, Jr. Jr., Michael A. Celia, Andrew J. Guswa, and Catherine A. Peters. Peer reviewed: Safe storage of CO_2 in deep saline aquifiers. *Environmental Science & Technology*, 36(11):240A–245A, 2002.

[272] C. M. Oldenburg, J. L. Lewicki. On leakage and seepage of CO_2 from geologic storage sites into surface water. *Environmental Geology*, 50(5):691–705, 2006.

[273] Christine Doughty. Investigation of CO_2 plume behavior for a large-scale pilot test of geologic carbon storage in a saline formation. *Transport in Porous Media*, 82(1):49–76, 2010.

[274] Stefan Iglauer, C. H. Pentland, and A. Busch. CO_2 wettability of seal and reservoir rocks and the implications for carbon geo-sequestration. *Water Resources Research*, 51(1):729–774, 2015.

[275] M. A. Hesse, F. M. Orr, and H. A. Tchelepi. Gravity currents with residual trapping. *Journal of Fluid Mechanics*, 611:35–60, 2008.

[276] Stefan Iglauer. Dissolution trapping of carbon dioxide in reservoir formation brine – A carbon storage mechanism. *Mass Transfer-Advanced Aspects*. Rijeka, Croatia: InTech, pages 233–262, 2011.

[277] Irina Gaus. Role and impact of CO_2–rock interactions during CO_2 storage in sedimentary rocks. *International Journal of Greenhouse Gas Control*, 4(1):73–89, 2010.

[278] Stefan Iglauer, Ahmed Zarzor Al-Yaseri, Reza Rezaee, and Maxim Lebedev. CO_2 wettability of caprocks: Implications for structural storage capacity and containment security. *Geophysical Research Letters*, 42(21):9279–9284, 2015.

[279] Samuel Krevor, Martin J. Blunt, Sally M. Benson, Christopher H. Pentland, Catriona Reynolds, Ali Al-Menhali, and Ben Niu. Capillary trapping for geologic carbon dioxide storage – From pore scale physics to field scale implications. *International Journal of Greenhouse Gas Control*, 40:221–237, 2015.

[280] Ali S. Al-Menhali, and Samuel Krevor. Pore-scale analysis of in situ contact angle measurements in mixed-wet rocks: Applications to carbon utilization in oil fields. *Energy Procedia*, 114:6919–6927, 2017.

[281] S. Iglauer, M. A. Fernø, P. Shearing, and M. J. Blunt. Comparison of residual oil cluster size distribution, morphology and saturation in oil-wet and water-wet sandstone. *Journal of Colloid and Interface Science*, 375(1):187–192, 2012.

[282] Tetsu K. Tokunaga, and Jiamin Wan. Capillary pressure and mineral wettability influences on reservoir CO_2 capacity. *Reviews in Mineralogy and Geochemistry*, 77(1):481–503, 2013.

[283] Thomas Young. III. An essay on the cohesion of fluids. *Philosophical Transactions of the Royal Society of London*, 95:65–87, 1805.

[284] Arthur W. Adamson, Alice P. Gast. Physical Chemistry of Surfaces. Wiley-Interscience: New York, 1997.

[285] Jasper L. Dickson, Gaurav Gupta, Tommy S. Horozov, Bernard P. Binks, and Keith P. Johnston. Wetting phenomena at the CO_2/water/glass interface. *Langmuir*, 22(5):2161–2170, 2006.

[286] D. Nicolas Espinoza, and J. Carlos Santamarina. Water–CO_2–mineral systems: Interfacial tension, contact angle, and diffusion—Implications to CO_2 geological storage. *Water Resources Research*, 46(7): W07537, 2010.

[287] Prem Kumar Bikkina. Contact angle measurements of CO_2−water−quartz/calcite systems in the perspective of carbon sequestration. *International Journal of Greenhouse Gas Control*, 5(5):1259–1271, 2011.

[288] Shibo Wang, Ian M. Edwards, and Andres F. Clarens. Wettability phenomena at the CO_2–brine–mineral interface: Implications for geologic carbon sequestration. *Environmental Science & Technology*, 47(1):234–241, 2013.

[289] Stefan Iglauer. CO_2–water–rock wettability: Variability, influencing factors, and implications for CO_2 geostorage. *Accounts of Chemical Research*, 50(5):1134−1142, 2017.

[290] Cong Chen, Bo Dong, Ning Zhang, Weizhong Li, and Yongchen Song. Pressure and temperature dependence of contact angles for CO_2/water/silica systems predicted by molecular dynamics simulations. *Energy & Fuels*, 30(6):5027−5034, 2016.

[291] S. Iglauer, M. S. Mathew, and F. Bresme. Molecular dynamics computations of brine–CO_2 interfacial tensions and brine–CO_2–quartz contact angles and their effects on structural and residual trapping mechanisms in carbon geo-sequestration. *Journal of Colloid and Interface Science*, 386(1):405−414, 2012.

[292] Craig M. Tenney, and Randall T. Cygan. Molecular simulation of carbon dioxide, brine, and clay mineral interactions and determination of contact angles. *Environmental Science & Technology*, 48(3):2035−2042, 2014.

[293] Muhammad Arif, Sidqi A. Abu-Khamsin, and Stefan Iglauer. Wettability of rock/CO_2/brine and rock/oil/CO_2−enriched−brine systems: Critical parametric analysis and future outlook. *Advances in Colloid and Interface Science*, 268:91−113, 2019.

[294] Mohammad Jafari, and Jongwon Jung. Direct measurement of static and dynamic contact angles using a random micromodel considering geological CO_2 sequestration. *Sustainability*, 9(12):2352, 2017.

[295] Cong Chen, Jiamin Wan, Weizhong Li, and Yongchen Song. Water contact angles on quartz surfaces under supercritical CO_2 sequestration conditions: Experimental and molecular dynamics simulation studies. *International Journal of Greenhouse Gas Control*, 42:655−665, 2015.

[296] Muhammad Arif, Maxim Lebedev, Ahmed Barifcani, and Stefan Iglauera. CO_2 storage in carbonates: Wettability of calcite. *International Journal of Greenhouse Gas Control*, 62:113−121, 2017.

[297] Shibo Wang, Zhiyuan Tao, Sara M. Persily, and Andres F. Clarens. CO_2 adhesion on hydrated mineral surfaces. *Environmental Science & Technology*, 47(20):11858−11865, 2013.

[298] Wael Abdallah, and Ahmed Gmira. Wettability assessment and surface compositional analysis of aged calcite treated with dynamic water. *Energy & Fuels*, 28(3):1652−1663, 2014.

[299] A. Silvestri, E. Ataman, A. Budi, S. L. S. Stipp, J. D. Gale, and P. Raiteri. Wetting properties of the CO_2−water−calcite system via molecular simulations: Shape and size effects. *Langmuir*, 35(50):16669−16678, 2019.

[300] Sebastien Kerisit, and Stephen C Parker. Free energy of adsorption of water and metal ions on the $\{10\bar{1}4\}$ calcite surface. *Journal of the American Chemical Society*, 126(32):10152−10161, 2004.

[301] Shijun Xiao, Scott A. Edwards, and Frauke Gräter. A new transferable forcefield for simulating the mechanics of $CaCO_3$ crystals. *Journal of Physical Chemistry C*, 115(41):20067–20075, 2011.

[302] Beibei Zhu, Xurong Xu, and Ruikang Tang. Hydration layer structures on calcite facets and their roles in selective adsorptions of biomolecules: A molecular dynamics study. *The Journal of Chemical Physics*, 139(23):234705, 2013.

[303] Hsieh Chen, Shannon L. Eichmann, and Nancy A. Burnham. Understanding calcium-mediated adhesion of nanomaterials in reservoir fluids by insights from molecular dynamics simulations. *Scientific Reports*, 9:10763, 2019.

[304] Paolo Raiteri, Raffaella Demichelis, Julian D. Gale. Thermodynamically consistent force field for molecular dynamics simulations of alkaline-earth carbonates and their aqueous speciation. *Journal of Physical Chemistry C*, 119(43):24447–24458, 2015.

[305] Randall T. Cygan, Vyacheslav N. Romanov, and Evgeniy M. Myshakin. Molecular simulation of carbon dioxide capture by montmorillonite using an accurate and flexible force field. *Journal of Physical Chemistry C*, 116(24):13079–13091, 2012.

[306] A. Silvestri, A. Budi, E. Ataman, M. H. M. Olsson, M. P. Andersson, S. L. S. Stipp, J. D. Gale, P. Raiteri. A quantum mechanically derived force field to predict CO_2 adsorption on calcite {10.4} in an aqueous environment. *Journal of Physical Chemistry C*, 121(43):24025–24035, 2017.

[307] Yujie Wu, Harald L. Tepper, and Gregory A. Voth. Flexible simple point-charge water model with improved liquid-state properties. *The Journal of Chemical Physics*, 124(2):024503, 2006.

[308] Pekka Mark, and Lennart Nilsson. Structure and dynamics of the TIP3P, SPC, and SPC/E water models at 298 K. *Journal of Physical Chemistry A*, 105(43):9954–9960, 2001.

[309] Evgeny Wasserman, Bernard Wood, and JohnBrodhol. The static dielectric constant of water at pressures up to 20 kbar and temperatures to 1273 K: Experiment, simulations, and empirical equations. *Geochimica et Cosmochimica Acta*, 59(1):1–6, 1995.

[310] S. Balasubramanian, Christopher J. Mundy, and Michael L. Klein. Shear viscosity of polar fluids: Molecular dynamics calculations of water. *The Journal of Chemical Physics*, 105(24):11190–11195, 1996.

[311] I. Shvab, and Richard J. Sadus. Intermolecular potentials and the accurate prediction of the thermodynamic properties of water. *The Journal of Chemical Physics*, 139(19):194505, 2013.

[312] Juan J. de Pablo, John M. Prausnitz, Henry J. Strauch, and Peter T. Cummings. Molecular simulation of water along the liquid–vapor coexistence curve from 25 °C to the critical point. *The Journal of Chemical Physics*, 93(10):7355–7359, 1990.

[313] Gabriele Raabe, and Richard J. Sadus. Molecular dynamics simulation of the dielectric constant of water: The effect of bond flexibility. *The Journal of Chemical Physics*, 134(23):234501, 2011.

[314] Gabriele Raabe, and Richard J. Sadus. Molecular dynamics simulation of the effect of bond flexibility on the transport properties of water. *The Journal of Chemical Physics*, 137(10): 104512, 2012.

[315] C. Vega, J. L. F. Abascal, and I. Nezbeda. Vapor-liquid equilibria from the triple point up to the critical point for the new generation of TIP4P-like models: TIP4P/Ew, TIP4P/2005, and TIP4P/ice. *The Journal of Chemical Physics*, 125(3):034503, 2006.

[316] C. Vega, and E. de Miguel. Surface tension of the most popular models of water by using the test-area simulation method. *The Journal of Chemical Physics*, 126(15):154707 2007.

[317] Miguel Angel González, and José L. F. Abascal. The shear viscosity of rigid water models. *The Journal of Chemical Physics*, 132(9): 096101, 2010.

[318] In Suk Joung, and Thomas E. Cheatham III. Determination of alkali and halide monovalent ion parameters for use in explicitly solvated biomolecular simulations. *Journal of Physical Chemistry B*, 112(30):9020–9041, 2008.

[319] J. L. Aragones, E. Sanz, and C. Vega. Solubility of NaCl in water by molecular simulation revisited. *The Journal of Chemical Physics*, 136(24):244508, 2012.

[320] David R. Heine, Gary S. Grest, Edmund B. Webb, III. Spreading dynamics of polymer nanodroplets in cylindrical geometries. *Physical Review E*, 70(1): 011606, 2004.

[321] Glenn J. Martyna, Douglas J. Tobias, and Michael L. Klein. Constant pressure molecular dynamics algorithms. *The Journal of Chemical Physics*, 101(5):4177–4189, 1994.

[322] M. J. de Ruijter, T. D. Blake, and J. De Coninck. Dynamic wetting studied by molecular modeling simulations of droplet spreading. *Langmuir*, 15(22):7836–7847, 1999.

[323] P. Fenter, P. Geissbühler, E. DiMasi, G. Srajer, L. B. Sorensen, and N. C. Sturchio. Surface speciation of calcite observed in situ by high-resolution X-ray reflectivity. *Geochimica et Cosmochimica Acta*, 64(7):1221–1228, 2000.

[324] P. Geissbühler, P. Fenter, E. DiMasi, G. Srajer, L. B. Sorensen, N. C. Sturchio. Three-dimensional structure of the calcite–water interface by surface X-ray scattering. *Surface Science*, 573(2):191–203, 2004.

[325] Frank Heberling, Thomas P. Trainor, Johannes Lützenkirchen, Peter Eng, Melissa A. Denecke, Dirk Bosbach. Structure and reactivity of the calcite–water interface. Journal of *Colloid and Interface Science*, 354(2):843–857, 2011.

[326] P. Fenter, and N. C. Sturchio. Calcite (1 0 4)–water interface structure, revisited. *Geochimica et Cosmochimica Acta*, 97:58–69, 2012.

[327] Jennifer S. Lardge, Dorothy M. Duffy, Mike J. Gillan, and Matthew Watkins. Ab Initio simulations of the interaction between water and defects on the calcite $(10\bar{1}4)$ surface. *Journal of Physical Chemistry C*, 114(6):2664–2668, 2010.

[328] Jian Liu, Omar B. Wani, Saeed M. Alhassan, and Sokrates T. Pantelides. Wettability alteration and enhanced oil recovery induced by proximal adsorption of Na^+, Cl^-, Ca^{2+}, Mg^{2+}, and SO_4^{2-} ions on calcite. *Physical Review Applied*, 10(3):034064, 2018.

[329] M. Wolthers, D. Di Tommaso, Z. Du, and N. H. de Leeuw. Calcite surface structure and reactivity: molecular dynamics simulations and macroscopic surface modelling of the calcite–water interface. *Physical Chemistry Chemical Physics*, 14(43):15145–15157, 2012.

[330] Laura C. Nielsen, Ian C. Bourg, Garrison Sposito. Predicting CO_2–water interfacial tension under pressure and temperature conditions of geologic CO_2 storage. *Geochimica et Cosmochimica Acta*, 81:28–38, 2012.

[331] Yang Liu, Athanassios Z. Panagiotopoulos, and Pablo G. Debenedetti. Monte Carlo simulations of high-pressure phase equilibria of CO_2–H_2O Mixtures. *Journal of Physical Chemistry B*, 115(20):6629–6635, 2011.

[332] Gustavo A. Orozco, Ioannis G. Economou, and Athanassios Z. Panagiotopoulos. Optimization of intermolecular potential parameters for the CO_2/H_2O mixture. *Journal of Physical Chemistry B*, 118(39):11504–11511, 2014.

[333] Lukas Vlcek, Ariel A. Chialvo, and David R. Cole. Optimized unlike-pair interactions for water–carbon dioxide mixtures described by the SPC/E and EPM2 models. *Journal of Physical Chemistry B*, 115(27):8775–8784, 2011.

[334] Evgeniy M. Myshakin, Wissam A. Saidi, Vyacheslav N. Romanov, Randall T. Cygan, and Kenneth D. Jordan. Molecular dynamics simulations of carbon dioxide intercalation in hydrated Na-Montmorillonite. *Journal of Physical Chemistry C*, 117(21):11028–11039, 2013.

[335] Bernhard Reischl, Paolo Raiteri, Julian D. Gale, and Andrew L. Rohl. Atomistic simulation of atomic force microscopy imaging of hydration layers on calcite, dolomite, and magnesite surfaces. *Journal of Physical Chemistry C*, 123(24):14985–14992, 2019.

[336] J. S. Buckley, K. Takamura, and N. R. Morrow. Influence of electrical surface charges on the wetting properties of crude oils. *SPE Reservoir Engineering*, 4(03):332–340, 1989.

[337] Mohammad Mehdi Koleini, Mohammad Fattahi Mehraban, and Shahab Ayatollahi. Effects of low salinity water on calcite/brine interface: A molecular dynamics simulation study. *Colloids and Surfaces A: Physicochemical and Engineering Aspects*, 537:61–68, 2018.

[338] Dimitrios Argyris, David R. Cole, Alberto Striolo. Ion-specific effects under confinement: The role of interfacial water. *ACS Nano*, 4(4):2035–2042, 2010.